

Development of novel Optics and Analysis Tools for enhancing Biomedical Imaging by Coherent Raman Scattering

PhD Thesis

to obtain the degree of

Doktor der Naturwissenschaften (Dr. rer. nat.)

Faculty of Physics

University of Bielefeld

submitted by

Christian Pilger

Blomberger Weg 17

32699 Extertal

Matriculation-no.: 1921909

on

June 24, 2019

1. Reviewer: Prof. Dr. Thomas Huser
2. Reviewer: Prof. Dr. Dario Anselmetti

Contents

List of Figures	VI
1. Introduction	1
2. Theoretical background	5
2.1. Introduction to Raman scattering	5
2.2. Coherent Raman scattering	10
2.2.1. Driven Raman mode	10
2.2.2. Coherent anti-Stokes Raman scattering	12
2.2.3. Detection modes	18
2.2.4. Stimulated Raman scattering	22
2.3. Concept of structured illumination for resolution enhancement	26
2.3.1. Microscopic image formation	27
2.3.2. Linear structured illumination	31
2.3.3. Non-linear structured illumination	36
3. Materials and Methods	39
3.1. Experimental setup	40
3.1.1. Solid-state laser system	40
3.1.2. Optical parametric oscillator	42
3.1.3. Spatio-temporal overlap with laser diagnostics	45
3.1.4. Acousto-optic modulator	47
3.1.5. Setup for a customized CRS-microscope	48
3.1.6. SRS modulation and detection scheme	53
3.2. Structured illumination for resolution enhancement	56
3.2.1. Generation of a striped illumination pattern	59
4. Results	62
4.1. Investigation of osteogenic differentiation in human stem cells	62
4.1.1. Exploring label-free CARS microscopy as suitable tool for visualizing the successful differentiation of ITSCs in clinical research	62
4.1.2. Design of the experiments: CARS and SHG imaging of ITSCs and control group	63
4.1.3. CARS and SHG data are compared to spontaneous Raman spectra and Alizarin Red staining	65
4.1.4. CARS and SHG imaging leads to successful visualization of the ITSCs differentiation also applicable to clinical research	65

4.2.	In vivo analysis of intracellular lipid droplets in <i>Monoraphidium neglectum</i>	71
4.2.1.	Identification and characterization of lipid rich microalgae as non-food feedstock in bio-diesel production	71
4.2.2.	Established methods for analyzing the lipid content of microalgae are laborious and partly not feasible due to rigid cell walls . . .	71
4.2.3.	Raman-based techniques speed up the analysis process of <i>M. neglectum</i>	72
4.2.4.	Design of experiments: modulation approach excludes two-photon excited fluorescence enabling CARS imaging of lipid droplets . .	73
4.2.5.	Comparing the results concerning the lipid content acquired by volumetric CARS imaging to established methods	77
4.2.6.	Studying the degree of unsaturation of fatty acids in lipid droplets of <i>M. neglectum</i> by Raman micro-spectroscopy	83
4.2.7.	Successful CARS imaging of lipid contents in <i>M. neglectum</i> under nitrogen starvation conditions indicates optimal harvesting time point enabling comparison to other types of microalgae	83
4.3.	Developing a hyperspectral CARS imaging modality	84
4.3.1.	Exploring hyperspectral CARS for enhancing the information content of samples by their spectral response	84
4.3.2.	Improving the stability of the microscopy setup enables high fidelity HS-CARS data sets	85
4.3.3.	Customized software controls entire HS-CARS scan process ensuring undistorted spectra	85
4.3.4.	Pulse length variation induces spectral distortions in hyperspectral CRS-microscopy	88
4.3.5.	Identifying the OPO parameters influencing the pulse length during wavelengths scanning	90
4.3.6.	Influence of pulse length induced distortions on HS-CARS spectra shown in methanol	93
4.3.7.	Investigating the effect of non-controlled OPO wavelengths tuning on HS-CARS spectra in U2OS cell sample	95
4.4.	Applying HS-CARS imaging to biological research questions	100
4.4.1.	Analyzing the influence of copper on the fitness parameters of <i>Caenorhabditis elegans</i>	100
4.4.2.	Volumetric CARS imaging reveals changes of the lipid storage in <i>C. elegans</i>	101

4.4.3.	Hyperspectral CARS scanning assessing false positive identification of lipid contents	104
4.4.4.	Visualizing the differentiation of primary human alveolar epithelial cells by label-free imaging techniques	106
4.4.5.	Volumetric CARS imaging enables z-sectioning and shows differentiation process over time	107
4.4.6.	Non-negative matrix factorization applied on HS-CARS scans reveals cellular compartments	111
4.5.	Resolution enhancement utilizing structured illumination in scanning-based non-linear microscopy	116
4.5.1.	Generating striped illumination pattern by addressing the galvanometric scanning mirrors	117
4.5.2.	Enhancing the resolution and contrast by striped illumination of fluorescent bead samples in two-photon excitation	118
4.5.3.	Exploiting autofluorescence signals of <i>Convallaria majalis</i> for combining z-scanning with striped illumination pattern via MAP-SIM	120
4.5.4.	Investigating the potential of a striped two-photon illumination in tissue utilizing a stained murine kidney section	125
4.5.5.	SI-CARS: investigating the potential of resolution enhancement by striped illumination patterns	128
4.5.6.	Structured illumination utilizing galvanometric scanning mirrors proves to be a versatile tool for two-photon fluorescence and CARS microscopy	133
4.6.	Developing a self-synchronized two-color fiber laser for fast, high contrast CRS-microscopy	134
4.6.1.	Utilizing highly doped ytterbium and erbium non-linear fibers for the low noise, high power two-color laser in CRS-microscopy	136
4.6.2.	Characterizing the temporal and spectral properties of the all fiber-based CRS-laser source	143
4.6.3.	All fiber-based two-color laser system enables simultaneous SRS and CARS imaging on living human cells	149
4.6.4.	Investigating the performance of the all fiber-based laser on tissue samples utilizing simultaneous SRS and CARS contrast	151
4.6.5.	Fs-laser pulses of Stokes cavity are utilized for SHG and two-photon excited fluorescence imaging broadening the range of application	154

4.6.6. Extending the range of accessible wavenumbers with a third laser cavity enabling the visualization of alkyne tagged samples in the future	156
5. Summary and outlook	159
6. List of publications	163
A. Statutory declaration	165
B. Acknowledgments	167
References	170

List of Figures

1.	Scheme of spontaneous Raman scattering	8
2.	Raman spectrum of pure methanol	9
3.	Scheme of the coherent Raman scattering	12
4.	Jablonski diagram of the FWM CARS process	13
5.	Wave vector diagram of the CARS process	16
6.	Spectral dependence of $\chi^{(3)}$	18
7.	Forward and epi-detected CARS signal strength with increasing sample thickness	20
8.	Back-scattering of forward directed CARS signals in tissues	21
9.	Principle of stimulated Raman scattering	23
10.	Broadening of a point-shaped object by the PSF	30
11.	Relation of PSF and OTF in the image formation of an optical system	30
12.	Illustration of the Moire effect	32
13.	Structured illumination in Fourier space	36
14.	Linear and non-linear SIM compared in Fourier space	38
15.	Fourier transform of SI-CARS image indicating second order frequency components	38
16.	Solid-state laser source <i>HighQ picoTRAIN</i>	42
17.	Optical parametric generation (OPG)	43
18.	Scheme of a <i>Levante Emerald</i> OPO	45
19.	Scheme of the CRS-microscope setup	47
20.	Scheme of the scanning setup	50
21.	Detection modes and optical path	52
22.	CAM/CAD simulation of the microscope and the condenser lens mount	53
23.	Customized SI-photodiode for SRS imaging	55
24.	Modulation and detection scheme of SRS imaging	56
25.	Detection scheme for SI-CARS	58
26.	Scheme of the camera trigger and striped pattern generation utilizing the AOM	61
27.	CARS and SHG imaging of the ITSCs showing the osteogenic differentiation	66
28.	CARS and SHG imaging of the ITSCs under control conditions showing no deposition of calcium hydroxyapatite or collagen fibers	67
29.	Applying CARS and SHG imaging on a human skull bone for the visualization of calcium hydroxyapatite and collagen fibers	68

30.	SHG imaging of a mouse tail fiber sample showing the presence of collagen	68
31.	Spontaneous Raman spectra of the ITSCs during the differentiation process	69
32.	Fluorescence imaging of ITSCs utilizing Alizarin Red staining	70
33.	3D imaging of ITSCs after 21 days of differentiation	70
34.	Modulation approach for eliminating undesired two-photon excited fluorescence signals investigating <i>M. neglectum</i>	75
35.	Two channel detection of CARS signal and two-photon excited fluorescence	76
36.	Frequency modulated CARS imaging reveals lipid droplet formation in <i>M. neglectum</i> under nitrogen starvation	79
37.	Cell growth parameters and gravimetrical analysis of <i>M. neglectum</i> during nitrogen starvation	80
38.	2D CARS imaging of <i>M. neglectum</i> for investigating cell growth and lipid distribution under nitrogen starvation conditions	81
39.	Volumetric CARS imaging of <i>M. neglectum</i> for monitoring cell growth and cellular lipid content	82
40.	Block diagram of the control program for hyperspectral CARS image acquisition	87
41.	HS-CARS imaging scheme: influence of the OPO operation mode on spectra due to pulse length variation	89
42.	OPO crystal temperature influences CARS intensity due to pulse length variation imaging a DMSO solution	92
43.	Detuning of OPO cavity length leads to pulse length variation and temporal mismatch resulting in CARS intensity changes	93
44.	OPO operation modes causing intensity distortions on HS-CARS spectra in methanol due to pulse length variations	94
45.	Comparison of HS-CARS to spontaneous Raman spectrum acquired on pure methanol	95
46.	OPO operation modes influence pulse length visualized in HS-CARS imaging of a U2OS cell	98
47.	Relative difference in CARS signal during hyperspectral scanning due to OPO induced pulse length variation	99
48.	3D CARS imaging studying the lipid distribution in <i>C. elegans</i> during life history trait	102
49.	Quantitative analysis of 3D CARS data determining lipid size and content of control and EC20 treatment	103
50.	PCA analysis of a hyperspectral CARS image scan of a <i>C. elegans</i> sample	105

51.	Comparison of representative CARS images illustrating the differentiation process of ATII into ATI cells over 7 days	108
52.	Repeat experiments during the differentiation process of ATII cells applying CARS imaging at different time points	109
53.	Representative CARS z-scan on ATII cells at day 1	110
54.	Representative CARS z-scan on the differentiation of ATII cells into ATI at day 3	110
55.	3D projection of volumetric CARS data at a rotation angle of 90° of ATII cell differentiation at day 2	111
56.	Hyperspectral CARS imaging of ATII differentiation process utilizing NNMF for decoding spectral information	114
57.	Investigating the signal-to-background behavior at selected ROIs utilizing NNMF analysis on hyperspectral CARS data at day 2	115
58.	Structured illumination applied on a 200nm TetraSpeck fluorescence bead sample using two-photon excitation	119
59.	Comparison of widefield images to the reconstruction in a region of interest of a 200nm bead sample	119
60.	Line plot of the 200nm bead sample: comparing widefield images to the reconstruction shows enhanced resolution and contrast	120
61.	MAP-SIM reconstruction performed on a z-scan image series of a <i>Convallaria majalis</i> sample	122
62.	ROI 1 of <i>Convallaria majalis</i> sample comparing widefield to MAP-SIM reconstruction	123
63.	ROI 2 of <i>Convallaria majalis</i> sample comparing widefield to MAP-SIM reconstruction	123
64.	Comparing the performance of FairSIM and MAP-SIM on fluorescent bead samples	124
65.	Line plot comparing reconstruction algorithms on a fluorescent bead sample	124
66.	Fluorescent 1µm bead sample imaged by fine illumination pattern investigating scattering effects	125
67.	Striped two-photon excited fluorescence imaging of a stained murine kidney tissue section comparing widefield to reconstruction	126
68.	Line plot at selected ROI of a kidney tissue section	127
69.	Zoom image of a kidney tissue section comparing widefield to reconstructed image using FairSIM	127

70.	1, $1\mu m$ polystyrene beads in DMSO solution illuminated with coarse CARS illumination pattern	129
71.	Raw data set using striped CARS illumination pattern for imaging $2\mu m$ polystyrene beads	130
72.	SI-CARS: comparison of widefield to reconstruction in $2\mu m$ polystyrene beads	130
73.	SI-CARS: line plot of ROI comparing reconstruction to widefield image	131
74.	Reconstruction parameter fitting and band separation in Fourier space using Fair-SIM	132
75.	Schematic diagram of the tunable two-color all fiber-based CRS-laser .	141
76.	Sketch of the passive self-synchronization mechanism utilized in the fiber laser setup	142
77.	Numerical simulations of the passive self-synchronization mechanism of the 1, $5\mu m$ laser cavity	143
78.	Temporal characterization of the Stokes and pump laser pulses	146
79.	Pulse train characterization of both laser wavelengths over long time period	147
80.	Radio frequency (RF) spectra for characterizing the two-color pulsed fiber laser	147
81.	Spectral characterization of the two-color fiber laser source	148
82.	Comparing SRS and spontaneous Raman spectra on pure samples	148
83.	Comparing SRS and CARS imaging performance on living human cells	150
84.	CRS-imaging of murine superior Vena cava tissue cryosection	152
85.	CRS-imaging of murine brain sections	153
86.	SHG imaging of mouse tail sample and two-photon excited fluorescence imaging of kidney and brain tissue sections	155

1. Introduction

Biomedical research has benefitted from the continuous technical developments and improvements that were made to many optical microscopy techniques over the last decades. New, highly relevant topics were addressed in order to understand the origins and early development of human diseases, such as cancer-related growth of cells [Ji et al. [2015]], acquired immunodeficiency syndromes [Hübner et al. [2009]], age-related affection of the musculoskeletal system [Croft et al. [2019]], brain- [Ji et al. [2018]] or cardiovascular-related diseases [Huang et al. [2019]], to name just a few examples. A specific enabling requirement for targeting these questions was the application of fluorescent dyes for the specific labeling of biological structures of interest in a sample [Taylor and Wang [1980]]. The introduction of immunofluorescence staining [Pawley [2006]] and genetic modification by gene transfection techniques [Kim and Eberwine [2010]] for the active expression of fluorescent dyes in living samples allowed e.g. virus tracking [Chojnacki and Eggeling [2018]] or identification of tumor cells and affected tumor tissues [Yang et al. [2017a]].

Also the spatial and temporal resolution of the applied microscopy techniques were enhanced, especially by the introduction of novel superresolution techniques, which are able to resolve structures of interest beyond the diffraction limit of light. This task was tackled by exploiting either the stochastic blinking of fluorescent dyes in a multi-image acquisition series and final post-processing [Heilemann et al. [2008]], by active engineering of the point spread function of the excitation volume [Klar and Hell [1999]] or by applying a structured illumination pattern in a multi-image acquisition scheme followed by post-processing steps [Gustafsson, M. G. L. [2000], Gustafsson, M. G. L. et al. [2000]].

All fluorescence-based microscopy techniques share the intrinsic drawback of the need for exogenous fluorescent dyes, which results in laborious preparation protocols, detrimental effects to the sample by the presence of the potentially toxic dyes [Trewin et al. [2018]] or influencing time-dependent processes, such as diffusion experiments or lifetime tracking in living cell samples based on the size and weight of the dye. All this affects the response of the sample also due to the necessarily high laser intensities in the visual part of the optical spectrum, resulting in increased phototoxicity [Wäldchen et al. [2015]]. Also there are samples of interest, where no sufficient labeling method could be found, yet, e.g. due to the presence of rigid cell walls [Bogen et al. [2013b]] or insufficient fluorescent labeling [Cheng and Xie [2015]].

An alternative solution to address these biomedical research questions can be found utilizing Raman-based imaging techniques such as label-free stimulated **R**aman scattering

(SRS) [Woodbury E. J. and Ng W. K. [1962], Ploetz et al. [2007]] and **coherent anti-Stokes Raman scattering (CARS)** [Terhune et al. [1965], Druet, S. A. J. and Taran, J. P. E. [1981]], which offer high chemical specificity and rapid imaging speeds due to their enhanced signal strength by exploiting the coherent nature of the signal. This leads to signals, which are several orders of magnitude stronger than those obtained by spontaneous Raman scattering while they do not suffer from bleaching effects as their fluorescent counterparts. **Coherent Raman scattering (CRS)** techniques are actively probing the molecular resonance of a large number of the same molecular groups by coherent laser wavelengths, which will perform a pump-probe experiment resulting in the strongly enhanced CRS-signals. Nevertheless, the molecular sensitivity of these techniques is still limited, which hinders the extensive replacement of the established fluorescent microscopy techniques with CRS-microscopy also due to the mostly diffraction limited resolution in relevant biomedical applications [Cheng and Xie [2015]]. This is also the case due to an enhanced level of complexity of the microscope setup as well as to the required cost-intensive and bulky laser systems, which also constrain the clinical use and which is part of ongoing research [König et al. [2011], Saar et al. [2011]]. To address these obstacles a state-of-the-art CRS microscope setup is developed and presented in this PhD-thesis, which utilizes novel optical and analytical tools to further enhance the reproducibility and chemical sensitivity of the CRS techniques. It covers a multimodal acquisition capability of simultaneous CARS and SRS imaging in combination with second harmonic generation (SHG) and two-photon excited fluorescence microscopy enabling high imaging speeds and volumetric scanning of the sample. In addition to that a hyperspectral scanning mode is implemented by computer-controlled wavelengths tuning, which demonstrates the enhanced sample information by sequentially addressing different molecular resonances by CARS [Fussell et al. [2013]]. This technique is further analyzed in terms of reproducibility as well as on specific properties of the laser system used for the experiments and a new level of accuracy is presented to the research community [Pilger et al. [2018]]. In collaboration with several partners the successful application of the newly constructed setup to a range of biomedical problems was investigated and is presented. To further extend the range of applications of CARS microscopy the concept of structured illumination is explored in this scanning-based microscopy technique. The special appeal of this approach is the highly cost-effective way of boosting the resolution using mostly standard components of state-of-the-art two-photon scanning and CRS-microscopes.

For paving the way of CRS microscopy to clinical application a collaborative effort with the University of Hong Kong, with the group of Prof. K. K. Y. Wong, is presented by exploiting fiber-laser technology to construct a novel, low noise all fiber-based two

color CRS laser system, which can replace the current solid-state laser setups offering similar performance. The introduced all-fiber-based laser source is characterized in its performance, which is superior to other published solutions in terms of noise level. This enables rapid, high quality CARS and SRS imaging without the need for additional noise cancellation schemes such as balanced detection devices. The fiber laser is then utilized on several biomedical samples to demonstrate the simultaneous SRS and CARS imaging capability, while also offering SHG and two-photon excited fluorescence imaging by minor changes to the laser setup. This turns it into a cost-efficient, environmentally insensitive, stable, compact and versatile tool, which can be proposed for clinical applications. This domain has additional relevance due to ongoing research on endoscopic applications using CRS-contrast, which would be a valuable match to the fiber laser source [Saar et al. [2011], Lukic et al. [2017]].

In the following thesis a short theoretical introduction is provided on coherent Raman scattering as well as on the microscopic image formation with emphasis on resolution enhancement by structured illumination techniques (section 2). Following this part the CRS setup is described introducing novel aspects, which separates it from other recent realizations (3). The results obtained with this system are presented in section 4: first, CARS and SHG imaging contrast is utilized for the investigation of the osteogenic differentiation of human stem cells, which offer promising treatment for the cure of injured bone structures (4.1). The results achieved by CARS and SHG imaging are combined with spontaneous Raman spectroscopy and then compared to established methods in this field, such as fluorescence staining and rt-PCR (reverse transcription polymerase chain reaction). Then the successful application of volumetric CARS imaging to the oleaginous microalgae *Monoraphidium neglectum* is demonstrated in vivo for investigating the lipid content under nitrogen starvation conditions (4.2). Here, an intensity modulation approach is utilized in combination with lock-in amplification for the suppression of undesired two-photon excited fluorescence of the chloroplast, which enabled a quantitative determination of the lipid content and, finally, the optimal harvesting time point.

Furthermore, the hyperspectral CARS imaging modality is introduced in (4.3): the hyperspectral control software is compared in its performance to the conventional non-controlled mode and the influence of the optical parametric oscillator as a tunable wavelength source is determined concerning its influence on the laser pulse length in the experiments (4.3.4). The hyperspectral image acquisition is contrasted to static CARS imaging for determining the fitness parameter of the soil worm *Caenorhabditis elegans* under exposition to a copper treatment (4.4.1) as well as for visualizing the differentiation process of primary human alveolar epithelial cells (4.4.4).

Subsequently, the spatial resolution enhancement based on structured illumination applied to scanning-based microscopy setups is explored in two-photon excitation mode of several fluorescent samples as well as on polystyrene bead samples with CARS contrast. Two reconstruction approaches are compared to each other for producing the final image, whose resolution and contrast is strongly enhanced.

After that the setup of the novel two-color all-fiber-based laser source is described and the source is characterized in its optical parameters with strong emphasis on the noise performance indicating superior performance as a source in SRS imaging (4.6). Then data of a range of relevant biomedical samples is presented in simultaneous acquired SRS and CARS contrast demonstrating the performance of the setup. The SHG and two-photon imaging capability is showcased by providing additional data sets proving the laser source to be a versatile multimodal imaging tool.

Finally, the thesis is summarized and future steps are indicated in section 5.

2. Theoretical background

In the following thesis coherent Raman scattering (CRS) is utilized for imaging purposes on biomedical samples. This theoretical introduction describes the two mechanisms of spontaneous Raman scattering and the coherent counterpart in sections (2.1) and (2.2). Then the two coherent effects of coherent anti-Stokes Raman scattering (CARS) (section 2.2.2) and stimulated Raman scattering (SRS) (section 2.2.4) are introduced due to their physical dependencies on the occurring light fields as well as to the different detection modes. Finally, the image formation in a microscope as well as the concept of resolution is introduced (2.3.1), while the aspect of resolution enhancement by structured illumination is discussed in (2.3).

2.1. Introduction to Raman scattering

Single atoms form a molecular bond reaching a lower energetic state due to the overlap of their specific electronic orbitals in the bond state. A molecular bond exhibits three energetic regimes corresponding to three different mechanisms in which energy can be deposited: the excitation of electronic states has the highest amount of energy deposition, which can be performed with excitation wavelengths in the range of ultraviolet to near infra-red light (corresponding to several eV).

Also vibrational states can be excited along the binding axis analogue to the harmonic oscillator, while the binding strength of the bond determines the potential of the oscillation. Typical energies are $1eV$ to meV . The rotation of the binding components along the bond axis exhibits the lowest energy regime ranging in several meV [Haken and Wolf [2006, pp. 180]].

Electromagnetic fields are able to affect the electrons of a molecule leading to polarization effects. Here, the charges of the molecular bond are separated from each other, which is possible due to the nearly instantaneous reaction of the electrons to an applied perturbation such as a light field. The nuclei are not reacting on the same time scale but several magnitudes slower. By applying the Born-Oppenheimer assumption [Born and Oppenheimer [1927]] stating that the electrons are moving in an unaltered potential of the nuclei, the reaction of the electrons on the perturbation can be described. A change of the potential due to an oscillation of the nuclei leads to an instantaneous following of the electrons [Haken and Wolf [2006, pp. 209]]. The polarization induced by an incident light field leads to a non-equilibrium position of the electrons in the potential of the nuclei. This induces a dipole moment $\mu(t)$, which can be stated with only one electron in one dimension as (derivation following [Cheng and Xie [2013, pp. 5]]):

$$\mu(t) = -e \cdot r(t) \quad (1)$$

e charge of the electron
 $r(t)$ displacement from the equilibrium position

The magnitude of the displacement $r(t)$ is defined by the coupling strength of electrons and nuclei. By summing up all N electric dipoles of one molecule or unit volume the macroscopic induced polarization $P(t)$ is found to be:

$$P(t) = N \cdot \mu(t) \quad (2)$$

Raman scattering describes the inelastic scattering of incident photons at a molecule, observed for the first time by C. V. Raman in 1928 [Raman and Krishnan [1928]]. The participating light field couples to a molecular bond and leads to an energy transfer. The visible or near infra-red light field $E(t)$ drives the oscillation of the electrons, which compose the molecular bond. The oscillatory motion contains information of the motion of the nuclei due to the adiabatic electronic potential, which is determined by the nuclear coordinates. Therefore, the motion of the involved nuclei will affect the motion of the electrons through the binding of both by the nuclear force. Describing the influence of the nuclear motion on the electronic motion in a quantitative manner far of an electronic resonance of the system, the electric dipole moment $\mu(t)$ is weighted with the polarizability $\alpha(t)$ [following Cheng and Xie [2013, pp. 10]]:

$$\mu(t) = \alpha(t) \cdot E(t) \quad (3)$$

By assuming no nuclear modes or nonlinearities, the polarizability can be approximated as a constant α_0 .

In the presence of nuclear modes the polarizability can be described in terms of the nuclear coordinate Q and can be approximated by a Taylor series [Placzek [1934]]:

$$\alpha(t) = \alpha_0 + \left(\frac{\delta\alpha}{\delta Q} \right)_0 \cdot Q(t) + \dots \quad (4)$$

The coupling strength of the nuclear and electronic coordinates is considered to be the first-order correction to the polarizability having the magnitude of $\delta\alpha/\delta Q$. Assuming the nuclear motion to behave as a classical harmonic oscillator leads to:

$$Q(t) = 2Q_0 \cdot \cos(\omega_\nu t + \phi) = Q_0 [e^{i\omega_\nu t + i\phi} + e^{-i\omega_\nu t - i\phi}] \quad (5)$$

- Q_0 amplitude of the nuclear motion
- ω_ν nuclear resonance frequency
- ϕ phase of the nuclear mode vibration

The incoming light field can be described as $E(t) = A \cdot e^{-i\omega_1 t} + A^* \cdot e^{i\omega_1 t}$ leading to the expression of the dipole moment as:

$$\mu(t) = \alpha_0 A e^{-i\omega_1 t} + A \cdot \left(\frac{\delta\alpha}{\delta Q} \right)_0 Q_0 \left\{ e^{-i(\omega_1 - \omega_\nu)t + i\phi} + e^{-i(\omega_1 + \omega_\nu)t - i\phi} \right\} + c.c. \quad (6)$$

The oscillation of the dipole moment occurs at several frequencies and leads to the radiation of photons, whose wavelengths is corresponding to the oscillation frequency of the dipole moment. The elastic scattering (also named as Rayleigh scattering [Strutt [1871], Rayleigh [1881, 1899]]) of the incident photons is represented in eq. (6) by the first term, the dipole moment oscillates with the frequency of the initial light field. The following term represents the inelastic scattering (the Raman shift). The so-called Stokes-shift is given by $\omega_S = \omega_1 - \omega_\nu$, where the energy of the radiated photons is lower than the one of the incident photons. Thus, the emitted light is red-shifted in comparison to the incident wavelength. Consequently, the anti-Stokes shift occurs as $\omega_{aS} = \omega_1 + \omega_\nu$ resulting in blue-shifted, higher energy photons (see fig. 1).

The Raman term is directly proportional to $\delta\alpha/\delta Q$, which states the change of the polarizability along the nuclear mode due to the incident light field. This change is significantly dependent on the symmetry of the nuclear mode in the molecule, which can be exploited for gathering of information about the molecular bond by Raman spectroscopy.

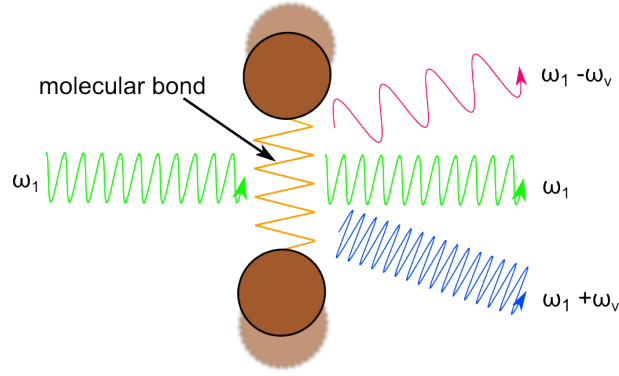


Figure 1 – Scheme of spontaneous Raman scattering

Incident photons (with the frequency ω_1 , left hand side) are scattered at a molecular bond formed by two atoms. Rayleigh scattering leads to radiated light, which is unaltered in its frequency (ω_1). Here, the dipole moment of the chemical bond oscillates with the same frequency as the light field. The frequency of the Stokes-shifted light is decreased with $\omega_1 - \omega_\nu$, energy is transferred from the light field to the molecular bond. The anti-Stokes shift occurs in analogue way at the frequency of $\omega_1 + \omega_\nu$, leading to a blue-shifted radiated light. Adapted from [Cheng and Xie [2013, p. 12]].

The amplitude of the emitted Stokes-shifted field radiating along r in the far-field is given by [Cheng and Xie [2013, p. 12]]:

$$E(\omega_S) = \frac{\omega_S^2}{4\pi\epsilon_0 c^2} |\mu(\omega_S)| \frac{e^{ikr}}{r} \cdot \sin(\theta) \quad (7)$$

- k wave vector of the radiated field
- c speed of light
- θ angle relative to the dipole axis
- r distance from the dipole location to the observation point
- $|\mu(\omega_S)|$ amplitude of the dipole oscillation at ω_S

Using the energy flux along r calculated as the time-averaged Poynting flux $S(\omega_S) = \frac{\epsilon_0 c}{2} |E(\omega_S)|^2$ the total intensity $I(\omega_S)$ emitted by a single dipole can be calculated by integrating over the unit sphere using eq. (6) as:

$$I(\omega_S) = \frac{\omega_S^4}{12\pi\epsilon_0 c^3} Q_0^2 |A|^2 \left| \frac{\delta\alpha}{\delta Q} \right|^2 \quad (8)$$

The inelastically scattered light has a ω_S^4 intensity dependency (eq. (8)). The initial intensity of the incoming light scales with $I_0 = |A|^2$ and the polarizability has the factor of $|\delta\alpha/\delta Q|^2$. These are major influences utilizing Raman spectroscopy to analyze the chemical properties of a sample of interest leading to the choice of integration times as well as the choice of the intensity and the wavelength of the excitation light field.

The frequency shift of the scattered light offers information about the chemical bond, independent of the initial frequency. Rayleigh scattering leads to coherently radiated light while Raman scattered light is incoherent due to the uncorrelated vibrations of the different molecules. Each molecule vibrates with its own independent phase ϕ [Cheng and Xie [2013, p. 13]]. The intensity of the emitted Raman photons is several magnitudes lower than that of the incident light field. In combination with the small shift of the Stokes and anti-Stokes lines a very narrow line width of the incident photons is required, which is generated by laser sources in combination with monochromators [Haken and Wolf [2006, pp. 239]]. The used spectrometer needs a high resolution in order to separate single Raman peaks from each other while the excitation wavelength is adapted to the detection range of the setup. Fig. 2 is showcasing a typical Raman spectrum of a methanol sample, while two characteristic peaks can be observed in the spectrum.

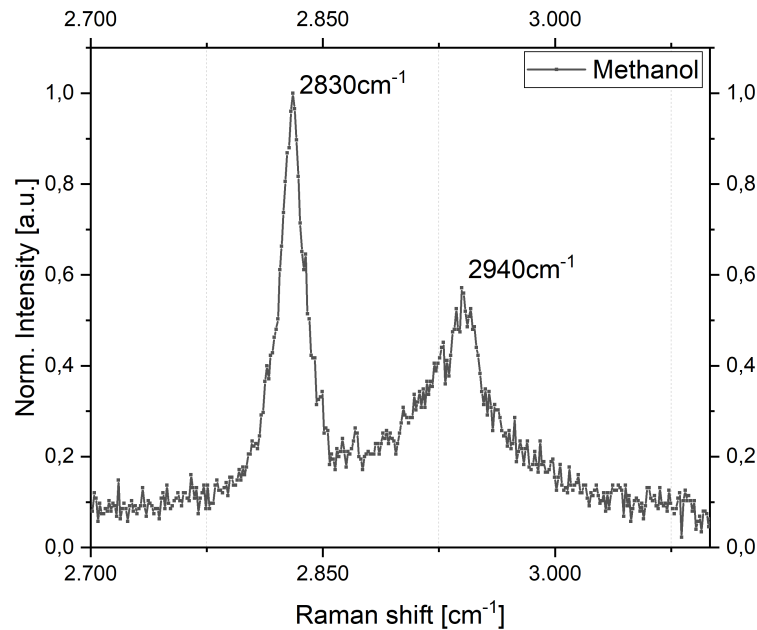


Figure 2 – Raman spectrum of pure methanol

This figure shows a normalized Raman spectrum obtained of pure methanol utilizing a cw-excitation wavelength of 785nm with a focal power of 20mW . A $60\times 1,2\text{NA}$ air objective lens focused the light into the sample. The spectrum is measured with an *Acton SpectraPro 2300i* spectrometer using a CCD camera for the detection (*Andor*, Newton 920-P-BR-DD). Two typical peaks are marked in the spectrum depicting two molecular resonances of the methanol: the symmetric and anti-symmetric $C - H$ stretching mode at 2830cm^{-1} and 2940cm^{-1} , respectively.

2.2. Coherent Raman scattering

Utilizing a classical instead of the full quantum mechanical description of coherent Raman scattering (CRS) is effectual for imaging purposes. In general the spontaneous Raman scattering is a rare event exhibiting a low strength of the Stokes and anti-Stokes signals. The difference of CRS to spontaneous Raman scattering is the actively driven nuclear oscillation of a specific molecular bond. This leads to the coherent excitation of a larger number of the same molecular group and finally to an oscillation of these molecules with one phase. Applying the two step model leads to: first, the electronic states of a molecular bond are driven by two incoming light fields, which vary in their energy. The resulting oscillation of the molecular electron cloud induces an effective force exciting the vibrational states of the bond, which finally results in a spatially coherent modulation of the refractive index of the material. The interaction of the material with a third incident light field, which experiences the modulation, is the second step in the model.

Any photons scattered at the bonds are in phase producing a coherent signal. The finally detected signal is enhanced by several orders of magnitude compared to spontaneous Raman scattering due to the constructive and destructive interference of the signal. The Raman shift is observed according to the frequency of the oscillation. Sidebands occur in the spectrum of the third light field, which can be clearly separated from the initial frequency [Cheng and Xie [2013, p. 14]].

2.2.1. Driven Raman mode

Similar to 2.1 the vibrational motion in the molecule can be described for the coherent Raman process (in a classical way) as a damped harmonic oscillator. The resonance frequency of the system is described by ω_ν along the internuclear axis Q . In contrast to spontaneous Raman scattering the molecular vibration is driven by two incident light fields E_1 and E_2 , assumed to be a plane wave (following [Cheng and Xie [2013, pp. 14]]):

$$E_j(t) = A_j e^{i\omega_j t} + A_j^* e^{-i\omega_j t} \quad j = 1, 2 \quad (9)$$

The fields apply a force on the nuclei (assuming their frequencies ω_1 and ω_2 to be much higher than the resonance frequency ω_ν):

$$F(t) = \left(\frac{\delta\alpha}{\delta Q} \right)_0 [A_1 A_2^* \cdot e^{-i\Omega t} + c.c.] \quad (10)$$

With $\Omega = \omega_1 - \omega_2$ being the difference frequency, which occurs using high intensities for the creation of non-linear effects in the electron motion. The nuclear displacement

can be described by the solution of the damped harmonic oscillator:

$$\frac{d^2Q(t)}{dt^2} + 2\gamma\frac{dQ(t)}{dt} + \omega_\nu^2Q(t) = \frac{F(t)}{m} \quad (11)$$

- γ damping constant
- m reduced mass of the nuclear oscillator
- ω_ν resonance frequency of the harmonic nuclear mode

The nuclear displacement over time can be stated from eq. (11) as:

$$Q(t) = Q(\Omega) \cdot e^{-i\Omega t} + c.c. \quad (12)$$

The amplitude at the frequency Ω is found to be:

$$Q(\omega_\nu) = \frac{1}{m} \left(\frac{\delta\alpha}{\delta Q} \right)_0 \frac{A_1 A_2^*}{\omega_\nu^2 - \Omega^2 - 2i\Omega\gamma} \quad (13)$$

Eq. (13) shows that the joint action of the incident fields drives the addressed nuclear motion at Ω . The amplitude of the vibrational mode is depending on the amplitudes of the incoming fields A_1 and A_2 as well as on the coupling strength of the nuclear motion to the polarizability along the nuclear mode due to the incident light field $\left(\frac{\delta\alpha}{\delta Q}\right)_0$. It also scales on the difference of the driving frequency Ω and the resonance frequency ω_ν of the oscillator. Matching both frequencies leads to the maximal amplitude (fig. 3).

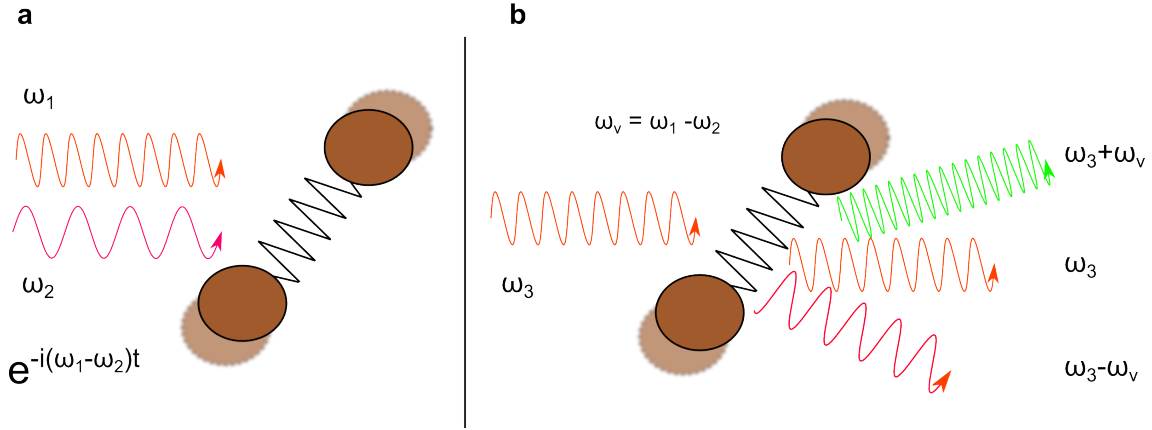


Figure 3 – Scheme of the coherent Raman scattering

In **a**) two incoming light fields with the frequency ω_1 and ω_2 are coherently driving the nuclear bond with the difference frequency $\Omega = \omega_1 - \omega_2$. **(b)** shows the interaction of the third light field with the driven molecular bond. Due to the presence of the molecular vibration the refractive index of the material is fluctuating leading to two sidebands, which are shifted in their frequencies compared to the fundamental ω_3 with the frequency of the molecular vibration ω_ν . If Ω matches the resonance of the molecular bond ω_ν , the amplitudes of the sidebands are at their maximum. Adapted from [Cheng and Xie [2013, p. 15]].

2.2.2. Coherent anti-Stokes Raman scattering

Coherent anti-Stokes Raman scattering (CARS) is a parametric **four wave mixing** process (FWM), which can be exploited for a label-free imaging contrast. An incoming pump photon ω_p excites a molecular bond to a higher virtual¹ energy state. The incoming Stokes photon ω_S de-excites the bond coherently to a certain vibrational mode, matching the molecular vibration of the bond with the frequency ω_ν . It depends on the molecular bond and is specific to the investigated material (following [Cheng and Xie [2013, pp. 26]]):

$$\omega_\nu = \omega_p - \omega_S \quad (14)$$

A second pump photon² ω_p excites the driven molecular bond to a higher virtual energy state, comparing this energy to the initial one the following relation can be stated ($|E_{virtual1}| < |E_{virtual2}|$). The relaxation of this unstable state creates the coherent blue-shifted anti-Stokes signal ω_{aS} , de-exciting the bond to the initial ground state (see fig. 4):

¹Meaning an unstable state, which lasts only a short period of time $t \sim \frac{\hbar}{\delta E}$.

²In most implementations it has the same frequency as the first pump photon while originating from the same laser source.

$$\omega_{aS} = (\omega_p - \omega_S) + \omega_p \quad (15)$$

Due to the geometry of the participating scatterers the CARS signal occurs in forward and epi-direction. Comparing CARS to spontaneous Raman scattering the signal strength is many orders of magnitude higher, still depending on the concentration of the addressed molecular group.

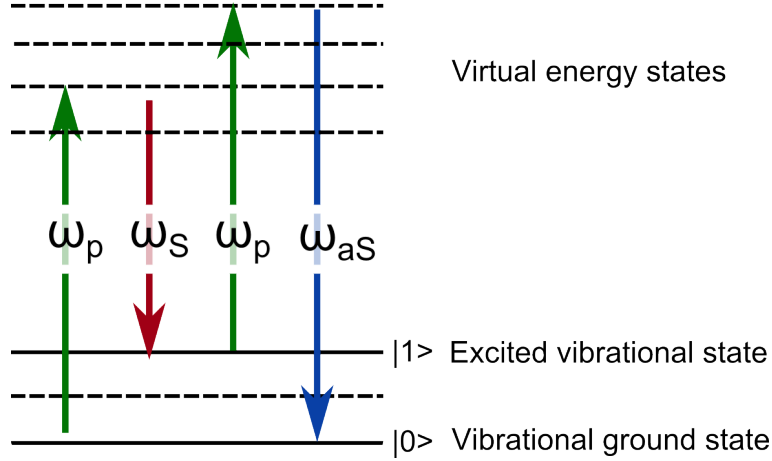


Figure 4 – Jablonski diagram of the FWM CARS process

The Jablonski energy diagram depicts the four wave mixing process of CARS. Two incoming pump photons ω_p and the probe photon (“Stokes”) ω_S coherently excite a larger number of the same molecular group. The radiated blue-shifted CARS photon ω_{aS} is strongly enhanced in its signal strength due to the introduction of constructive and destructive interference. Adapted from [Cheng and Xie [2013, p. 38]].

The third-order non-linear polarization $\mathbf{P}^{(3)}$ occurring in the material is the origin of all CRS signals, it can be defined as (following [Cheng and Xie [2013, pp. 46]]):

$$\mathbf{P} = \mathbf{P}^{(1)} + \mathbf{P}^{(3)} = \epsilon_0 \chi_e^{(1)} \mathbf{E} + \epsilon_0 \chi_e^{(3)} \mathbf{E} \cdot \mathbf{E} \cdot \mathbf{E} \quad (16)$$

The quantitative description of the signal generation in the CARS process on the macroscopic scale is possible using the Maxwell equations, which describes the spatial properties of the electric and magnetic fields. The wave equation describes the generation and propagation of the participating waves. It predicts the amplitude and phase of the non-linear electric field \mathbf{E} , having the non-linear polarization \mathbf{P} as the source term. Using eq. (16) it is found to be:

$$\nabla^2 \mathbf{E} - \frac{n^2}{c^2} \frac{\partial^2}{\partial t^2} \mathbf{E} = \frac{1}{\epsilon_0 c^2} \frac{\partial^2}{\partial t^2} \mathbf{P}^{(3)} \quad (17)$$

By the plane wave assumption with a constant amplitude and phase propagating in

forward direction the incoming fields of the FWM process can be described as [Cheng and Xie [2013, p. 50]]:

$$\mathbf{E}_j(z, t) = \frac{1}{2} \left(A_j(z) e^{i(k_j z - \omega_j t)} + A_j^*(z) e^{-i(k_j z - \omega_j t)} \right) \hat{\mathbf{x}} \quad j = 1, 2, 3 \quad (18)$$

$\hat{\mathbf{x}}$	polarization direction of the plane waves
ω_j	angular frequency
$k_j = \omega_j n_j / c$	scalar wave vector
A_j	amplitude of the incident wave
n_j	refractive index

By introducing the non-linear susceptibility $\chi_e^{(3)}(\Omega)$ with $\Omega = \omega_1 - \omega_2$ it is possible to state the third-order polarization of the non-linear Raman active material $P^{(3)}$:

$$\chi_e^{(3)} = \frac{G_\nu}{\omega_\nu - \Omega - i\gamma_\nu} \quad (19)$$

$$\mathbf{P}^{(3)}(z, t) = \frac{1}{8} \epsilon_0 \chi_e^{(3)}(\Omega) A_1(z) A_2^*(z) A_3(z) e^{i[(k_1 - k_2 + k_3)z - \omega_4 t]} \hat{\mathbf{x}} + c.c. \quad (20)$$

G_ν	spectral amplitude
γ_ν	damping constant related to the dephasing time of the vibrational level at frequency ω_ν

The induced polarization is the source of the coherent radiation, which oscillates with the angular frequency $\omega_4 = \omega_1 - \omega_2 + \omega_3$. Substituting the x -component of the forward propagating plane wave $\mathbf{E}_4(z, t)$ with the wave vector k_4 along the \hat{z} and $-\hat{z}$ directions into the wave equation [Druet, S. A. J. and Taran, J. P. E. [1981]], the slowly varying envelope approximation (SVEA) can be performed, which assumes that the change of the amplitude A_4 of the wave is incrementally small on a length scale in the regime of the optical wavelength [Potma et al. [2000]], leading to:

$$\mathbf{E}_4(z, t) = \frac{1}{2} A_4(z) e^{i(k_4 z - \omega_4 t)} \hat{\mathbf{x}} + c.c. \quad (21)$$

Starting with the left hand side of eq. (17) the following term is found:

$$\begin{aligned} \nabla^2 E_4(z, t) - \frac{n_4^2}{c^2} \frac{\partial^2}{\partial t^2} E_4(z, t) &= \frac{1}{2} \left[\left(\frac{\partial^2}{\partial t^2} + 2ik_4 \frac{\partial}{\partial z} \right) A_4(z) \right] e^{i(k_4 z - \omega_4 t)} + c.c. \\ &\approx ik_4 \frac{\partial A_4(z)}{\partial z} e^{i(k_4 z - \omega_4 t)} + c.c. \end{aligned} \quad (22)$$

Inserting the non-linear polarization $P^{(3)}$ (eq. (16)) into the wave equation for the field with the amplitude A_4 leads to:

$$\frac{\partial A_4(z)}{\partial z} = i \frac{\omega_4}{8n_4c} \chi_e^{(3)}(\Omega) A_1(z) A_2^*(z) A_3(z) e^{i\Delta kz} \quad (23)$$

$\Delta k = k_1 - k_2 + k_3 - k_4$ describes the wave vector mismatch along the z axis between the effective wave vector of the polarization field ($k_1 - k_2 + k_3$) and the wave vector of the radiating field (k_4). Assuming that the incident field amplitudes are mostly unaltered during the FWM process the amplitudes A_j are considered as constants during the signal generation. The integration of the differential equation (23) in the range of $z = 0$ to $z = L$, covering the length of the material, leads to the signal amplitude A_4 [Druet, S. A. J. and Taran, J. P. E. [1981]]:

$$A_4(L) = i \frac{\omega_4}{8n_4c} \chi_e^{(3)}(\Omega) A_1 A_2^* A_3 L \operatorname{sinc} \left(\frac{\Delta k L}{2} \right) e^{i\Delta k L/2} \quad (24)$$

With $\operatorname{sinc}(x) = \sin(x)/x$. Here, the strong influence on the amplitude of the coherent radiation by the wave vector mismatch becomes apparent. The maximal amplitude is observed when no phase mismatch between the induced non-linear polarization and the radiating field is present. In media this can not be the case, because of the inevitable dispersion of the medium, which always introduces a wave vector mismatch. Having a non-zero Δk the radiating field and the induced polarization are dephasing and, therefore, limiting the effective coherence to a length scale of $L_c = 2\pi/|\Delta k|$. This length determines an effective thickness in the sample material, where the signal amplitude can be generated.

Transferring this description of all CRS-signals to the CARS process the third-order non-linear polarization is found to be $\chi_e^{(3)}(\Omega) = \chi^{(3)}(\omega_{aS}; \omega_p, -\omega_S, \omega_p)$. The pump photons have the electric field of $E_1 = E_3$ at the frequency ω_p and the Stokes photons E_2 at ω_S ($\omega_S < \omega_p$). In the dual-color CARS process the pump beam participates two times the Stokes beam one time, generating the field E_{aS} , which is oscillating with the anti-Stokes frequency $\omega_{aS} = 2\omega_p - \omega_S$. The scalar wave vector of the field is $k_{aS} = 2k_p - k_S$ (fig. 5).

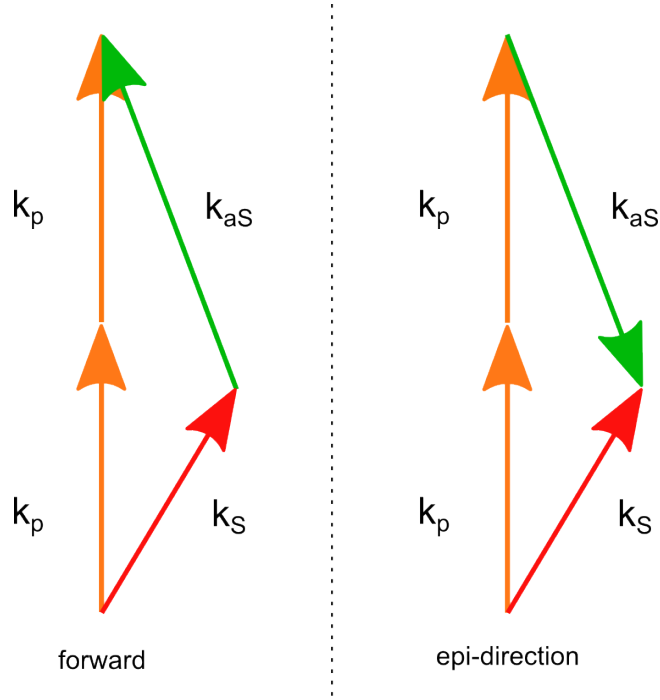


Figure 5 – Wave vector diagram of the CARS process

On the left the wave vector diagram is depicting the forward propagating CARS process with the generated wave vector of k_{aS} . On the right the epi-direction is illustrated. The pump beam wave vector (k_p) participates two times in the FWM process generating together with the Stokes beam (k_s) the. Adapted from [Evans and Xie [2008]].

Utilizing eq. (24) the intensity of the detected CARS signal can be found by deriving the squared amplitude [Cheng and Xie [2013, pp. 53]]:

$$I(\omega_{aS}) = |A_{aS}(L)|^2 \propto |\chi_e^{(3)}(\Omega)|^2 I_p^2 I_S L^2 \text{sinc}^2\left(\frac{\Delta k L}{2}\right) \quad (25)$$

Eq. (25) shows the dependencies of the CARS signal on the parameters set in the experiment. The CARS intensity scales quadratic to the pump beam intensity and linear to the Stokes beam intensity. During the imaging experiment the pump beam is set with a higher intensity than the Stokes beam for maximizing the finally detected CARS signal.

The wave vector mismatch Δk is weighted with the squared sinc-function. In the experimental realization this means that the interacting beams have to be aligned very exactly to minimize a possible mismatch. The divergence as well as the beam size have to be matched to generate a perfect overlap in the focal plane. This process is also affected by the focusing objective lens, which itself introduces chromatic aberrations. All optical lens failures have to be compensated as good as possible by introducing additional beam divergence. Any mismatch introduced by the dispersion by the medium of the sample is considered as small compared to the coherence length of the signals

in the microscope. The squared amplitude of the non-linear susceptibility $\chi_e^{(3)}$ itself is proportional to the density of the molecules, which participate in the signal generation process. Hence, the CARS signal depends quadratically to the number of molecules in the interacting focal volume and high concentrations of a molecule in the sample will induce high CARS signal strength.

The non-linear susceptibility contains a vibrationally resonant $\chi_r^{(3)}$ and a non-resonant part $\chi_{nr}^{(3)}$ and can be written as:

$$\chi_e^{(3)} = \chi_r^{(3)} + \chi_{nr}^{(3)} \quad (26)$$

Now the squared susceptibility can be found to be (following [Evans and Xie [2008]]):

$$\left| \chi_e^{(3)}(\Omega) \right|^2 = \left| \chi_r^{(3)}(\Omega) + \chi_{nr}^{(3)} \right|^2 = \left| \chi_r^{(3)}(\Omega) \right|^2 + \left| \chi_{nr}^{(3)} \right|^2 + 2\chi_{nr}^{(3)} \text{Re}[\chi_r^{(3)}(\Omega)] \quad (27)$$

Here, an intrinsic drawback of the CARS signal as contrast mechanism becomes apparent: the first term is resonant to the addressed molecular vibration and delivers the desired chemically sensitive signal. The second term represents the non-resonant background contribution, which obscures the desired resonant signals especially in the case of lower molecular concentrations. The last term refers to the mixing part of resonant and non-resonant contribution. The sensitivity of CARS is limited by the intensity of this non-resonant background.

The reason for the presence of a non-resonant background can be found by considering all possible responses of the system taking into consideration all the optical frequencies described by the third-order susceptibility. Because of the parametric nature of CARS in the $\chi^{(3)}$ process 24 quantum pathways are possible, while combining the incoming light fields in order to detect the CARS signal. 17 of this pathways do not exhibit a Raman coherence and are not fulfilling the Raman resonance condition. They are summed up to χ_{nr} . A semi-classical explanation of this behavior is the possibility of undergoing some system pathways, which contribute to the dipole radiation at ω_{aS} , but having no propagators at the resonance frequency of the molecular bond. In addition, there are so-called electronic resonances, meaning quantum pathways, which are possible if³ ω_1 or ω_{aS} is resonant to electronic states of the material or, in case of a populated vibrational state, if ω_2 has a resonance to the electronic states. In the case that no electronic resonance is present the contribution to the CARS signal of the non-resonant pathways is less than the vibrationally resonant part. In case of an electronic resonance the non-resonant signals are significantly higher than the resonant counterpart [Cheng and Xie [2013, pp. 27]].

³Referring to the driven Raman mode.

The non-linear susceptibility is strongly dependent on the difference frequency $\Omega = \omega_1 - \omega_2$ near the molecular resonance. A simulation for the spectral dependence of each part and the overall CARS signal can be found in fig. 6. The detected CARS signal is generated by the interference of all three parts. The mixing term of the resonant and the non-resonant part of the non-linear susceptibility stated in eq. (27) has a dispersive line shape, which can be observed in the CARS signal as a redshift. When comparing CARS spectra to spontaneous Raman spectra this redshift has to be considered, especially identifying the optimal combination of excitation wavelengths in the CARS process [Evans and Xie [2008]].

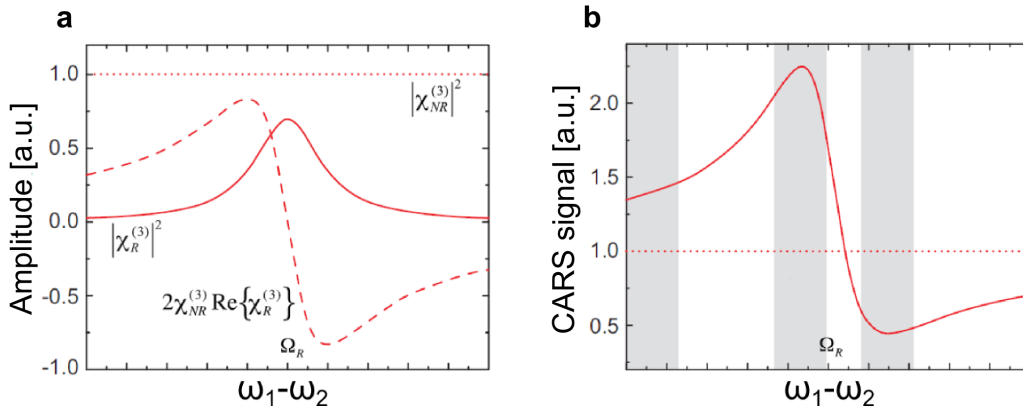


Figure 6 – Spectral dependence of $\chi^{(3)}$

a) shows the three components of the CARS signal referring to the non-linear susceptibility, while the molecular resonance $\Omega_R = \omega_1 - \omega_2$ is scanned. The constant non-resonant background $|\chi_{nr}^{(3)}|^2$ is depicted by a dotted line, the purely resonant term $|\chi_r^{(3)}|^2$ in solid line and the mixing term of both $2\chi_{nr}^{(3)}\text{Re}[\chi_r^{(3)}]$ in dashed line, respectively. b) shows the resulting total CARS signal, whose peak is red-shifted and which has a dispersive line shape arising from $2\chi_{nr}^{(3)}\text{Re}[\chi_r^{(3)}]$. The dotted line represents the non-resonant background, the solid line the combination of all signal components from (a). Adapted from [Evans and Xie [2008]].

2.2.3. Detection modes

When the CARS process is exploited as contrast mechanism for imaging two possible detection pathways can be used: the forward and epi-detection. In forward detection the CARS signal is generated in the focal plane and then propagates through the sample. Finally, it is collected by a condenser lens, filtered and detected. The epi-detection describes all back scattered CARS signals, which are collected by the same objective lens, which focused the excitation beams into the sample. The detection is performed similar to the forward direction.

One major difference of both detection modes is the strength and the origin of the signal, referring to the participating sample structures in the CARS process. This re-

sults in differences of information content of the investigated sample. As mentioned before the wave vector mismatch induced by the dispersion of the media is small for the forward propagating CARS signal and has no significant effect on the detected signal [Potma et al. [2000], Cheng and Xie [2013, p. 54]].

In epi-CARS a significant wave vector mismatch is introduced, which can be approximated as $|\Delta k| = 2|k_{aS}|$ leading to a coherence length of $L_c \approx 0,24\mu m$ in water⁴. This mismatch affects the signal generation when the investigated structures are smaller than the coherence length in their axial dimensions. If the structures are smaller than the pump wavelength the wave vector mismatch condition is satisfied in both propagation directions. With an increasing thickness D of the structure the forward CARS signal scales to $\sim D^2$ until it becomes saturated, when D exceeds the longitudinal dimension of the focal excitation volume. Depending on the size and the shape of the scatterers as well as on the optical parameters of the setup, forward CARS overwhelms the epi-signal due to the constructive interference in the forward direction (and the destructive interference in the epi-direction respectively) (see fig. 7).

The epi-CARS signal oscillates as a function of the sample thickness with a periodicity of $\lambda_{aS} \cdot 2n$ $n = 1, 2, 3, \dots$ and has an intensity which is proportional to (Volkmer et al. [2001]):

$$I_{aS}^{epi} \propto \lambda_{aS}^2 \cdot \sin^2\left(\frac{2\pi n D}{\lambda_{aS}}\right) \quad n = 1, 2, 3, \dots \quad (28)$$

⁴Using the planar wave approximation.

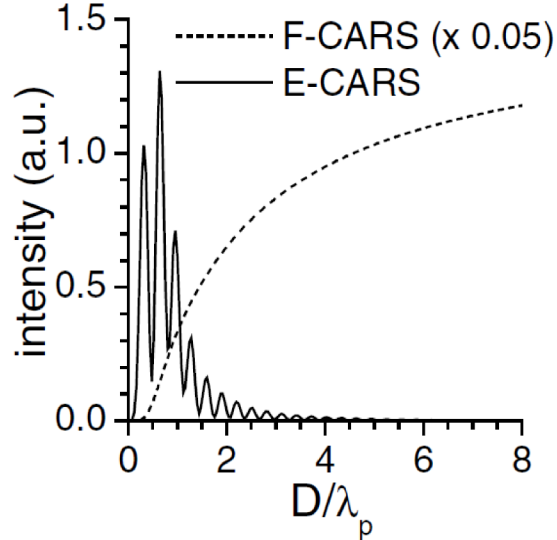


Figure 7 – Forward and epi-detected CARS signal strength with increasing sample thickness

The graph shows a simulation of the forward and epi-CARS intensities for tightly focused excitation beams as a function of the diameter D of a spherical scatterer. The following parameters are used: pump and Stokes wavelengths are at $\omega_p = 800nm$ and $\omega_S = 917nm$, respectively. The index of refraction of the medium is 1,52 and the NA of the lens is 1,4. The epi-CARS signal oscillates, the forward signal saturates, when the focal volume is filled with material. Note, that the forward CARS signal is rescaled by a factor of 0,05. From [Volkmer et al. [2001]].

When the focal excitation volume is small compared to the thickness of the sample linear scattering events of the forward CARS signal can occur, especially in tissues. Then the collected signal in epi-direction is significantly enhanced due to the loss in the forward direction. Monte-Carlo simulations based on typical tissue scattering parameters in skin samples indicate a loss of the forward CARS signal of 40 – 45%, enhancing the epi-CARS signal respectively [Saar et al. [2010]]. Utilizing a high NA objective lens 10% of the entire epi-CARS signal can be collected due to the limited cone angle of the lens. Multiple scattered, diffusive light is in most cases beyond the limit of the objective (see fig. 8).

Assuming structures in the $\sim \lambda_p/2$ regime a variation of $\chi_e^{(3)}$ is induced, which leads to an intrinsic backward radiation added to the overall CARS signal in epi-direction [Cheng and Xie [2013, pp. 70]].

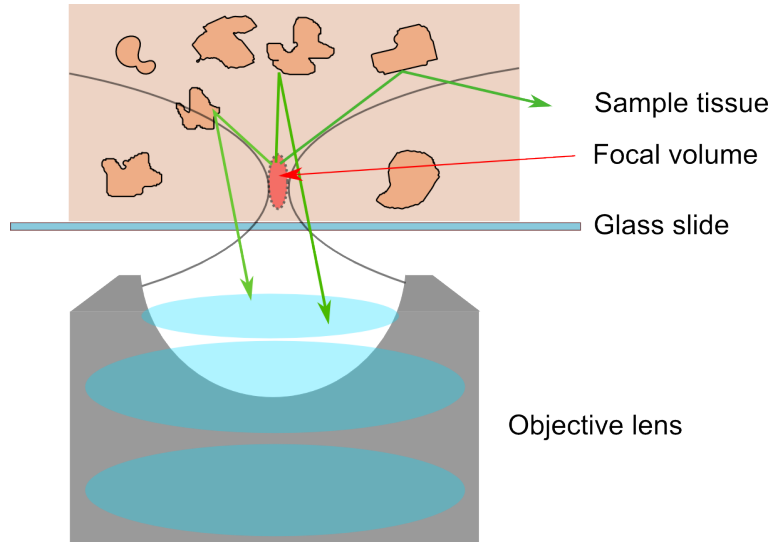


Figure 8 – Back-scattering of forward directed CARS signals in tissues

In tissues a portion of the forward-propagating CARS signal is back-scattered and contributes to the epi-CARS signal (adapted from [Cheng and Xie [2013, p. 71]]).

The geometric shape, size and position relative to the focal volume of the single scatterers play also a role for the ratio of forward and epi-CARS signals due to non-linear interference effects. The spectral properties of $\chi_e^{(3)}$ introduce a phase shift of π to the resonant signal, while probing the vibrational resonance from lower wave numbers to higher ones [Cheng et al. [2002]].

In the case of scatterers, which are small enough to be considered as single dipole emitters, an axial phase shift along the excitation beam direction introduces a wave vector mismatch, known as the Gouy phase shift. This effect is responsible for destructive and constructive interference detected in the far-field due to the position of the scatterers in the focal volume. If the focus is shifted through a sample an object located in the lower half of the focal volume will get a phase shift of π compared to the case, when it is in the upper half. This can lead to artifacts in the CARS images due to the interference effects with the non-resonant background, which has to be considered during the data interpretation [Popov et al. [2011], Cheng and Xie [2013, pp. 72]].

2.2.4. Stimulated Raman scattering

Stimulated Raman scattering (SRS) belongs to the group of coherent Raman scattering processes [Woodbury E. J. and Ng W. K. [1962]] and is used as contrast mechanism in biomedical imaging [Ploetz et al. [2007], Freudiger et al. [2008], Ozeki et al. [2009]]. The addressed molecular vibration is driven similar to the CARS-technique, whereas several differences in the signal detection as well as an additional intensity modulation of the Stokes beam are necessary. SRS is a dissipative energy transfer process in which energy is transferred between two incident light fields, the pump beam, with the frequency ω_p , and the Stokes beam with ω_S , respectively ($\omega_S < \omega_p$). Both light fields drive the molecular vibration at the resonance frequency Ω with the difference frequency $\Delta\omega = \omega_p - \omega_S$. Thereby, the molecular transition rate is enhanced because of the stimulated excitation of molecular transitions [Cheng and Xie [2013, pp. 100]]. The electronic states of the molecules are excited into a virtual state by the pump beam and de-excited by the Stokes field, transferring the molecular population from the ground state into a vibrationally excited state (see fig. 9). To satisfy the law of energy conservation a pump photon is absorbed by the molecule and a low-energetic Stokes photon is generated. This transfer of the number of photons in the two beams can be detected in the intensities of the pump beam I_p and the Stokes beam I_S after the interaction with the sample. The resulting loss in intensity SRL (stimulated Raman loss) ΔI_p and the gain SRG (stimulated Raman gain) ΔI_S are scaling to [Cheng and Xie [2013, p. 100]]:

$$\Delta I_S \propto N \cdot \sigma_{Raman} \cdot I_p \cdot I_S \quad (29)$$

$$\Delta I_P \propto -N \cdot \sigma_{Raman} \cdot I_p \cdot I_S \quad (30)$$

N number of molecules in the probe volume
 σ_{Raman} molecular Raman scattering cross section

By detecting the intensity of the pump or the Stokes beam with a suitable detector such as a large area fast silicon photo diode it is possible to measure the SRG or SRL as a function of the focus position. Because of the proportionality of the number of addressed molecules to the intensity of the detected beam $\Delta I \propto N$, thereby to the concentration of the target species, the obtained signal holds the spatial information of the chemical properties of the investigated sample. While the focus is raster scanned over the sample a two dimensional map of the chemical properties of the sample is acquired.

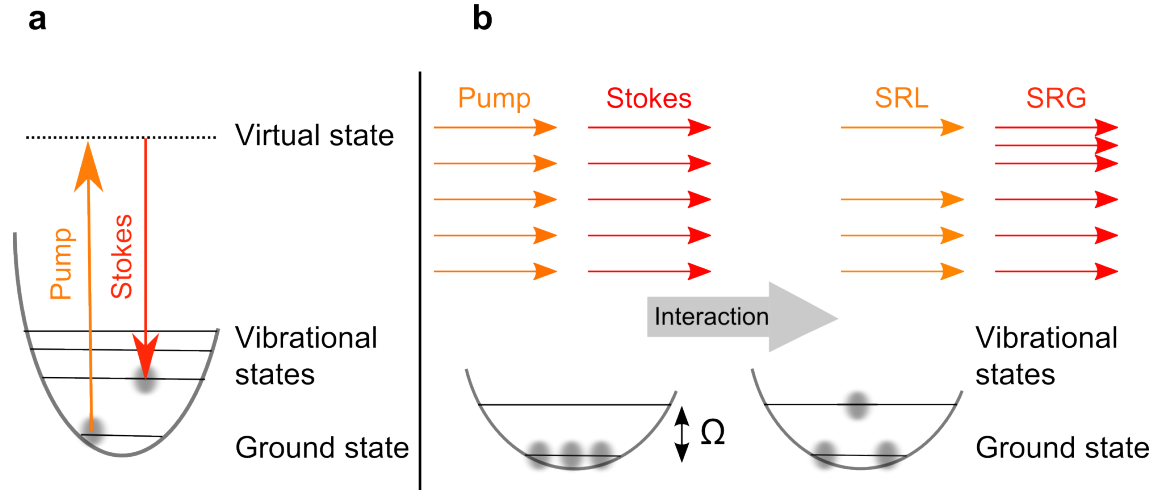


Figure 9 – Principle of stimulated Raman scattering

(a) shows the energy diagram of SRS. Here, the pump and Stokes beam coherently excite the molecular bond, transferring the molecules into the first excited vibrational state by passing through a virtual state. The selection of the addressed molecular vibration is achieved by tuning the pump and Stokes wavelengths to the molecular resonance frequency Ω , with $\Delta\omega = \omega_p - \omega_S$. (b) illustrates the energy transfer process in SRS: the gain and loss of the two participating light fields is obtained. Due to the conservation of energy the number of photons is increased after the interaction with the sample in the Stokes field, the number of pump photons decreases, respectively. Adapted from [Cheng and Xie [2013, p. 101]].

With the plane wave approximation described in chapter 2.2.2 (especially eq. (24)) the amplitude for the forward propagating stimulated Raman wave is found to be [Cheng and Xie [2013, pp. 54]]:

$$A_2^{stim} = i \frac{\omega^2}{8n_2c} \left\{ \chi_e^{(3)}(\Omega) \right\}^* A_1^* A_2 A_1 L \quad (31)$$

Due to the coherent nature of the stimulated Raman wave and the incident waves these contributions interfere at the detector (in the case of forward detection). The detected SRG intensity with frequency ω_S can be written as:

$$I(\omega_S) = \left| A_2(L) + A_2^{stim}(L) \right|^2 \quad (32)$$

$$= I_S + \left| \chi_e^{(3)} \right|^2 \cdot I_p^2 \cdot I_S \cdot L^2 + 2Im \left\{ \chi_e^{(3)}(\Omega) \right\} \cdot I_p \cdot I_S \cdot L \quad (33)$$

The first term of eq. (33) refers to the intensity of the incident Stokes beam, assuming that it is unattained during the non-linear process. The second term is the intrinsic SRS term, which is depending on the material properties as well as on the incident light fields similar to CARS. The last term is the interference term of the incident Stokes field and the stimulated Raman field at the detector. The induced amplitude A_2^{stim}

has an intrinsic $\pi/2$ phase shift relative to the incident A_2 driving field, which follows from the plane wave approximation. If the sample contains no addressed molecular content $\chi_e^{(3)}$ is purely real and the interference term disappears. Close to a resonance $\{\chi_e^{(3)}\} \neq 0$ the interference term is prominent. For the investigation of samples the interference term has to be isolated from the remaining terms of eq. (33). Assuming that the amplitude of the incident Stokes beam is bigger by several orders of magnitude compared to the stimulated Raman field ($A_2 \gg A_2^{stim}$) the forward SRG and SRL can be stated as:

$$\Delta I(\omega_S) \propto 2Im \{ \chi_e^{(3)}(\Omega) \} \cdot I_p \cdot I_S \cdot L \quad (34)$$

$$\Delta I(\omega_p) \propto -2Im \{ \chi_e^{(3)}(\Omega) \} \cdot I_p \cdot I_S \cdot L \quad (35)$$

In contrast to CARS the detected field in SRS (either SRG or SRL) is the same as the corresponding incident field, ensuring the phase matching condition automatically [Boyd [2003, pp. 451]]. The intensity gain or loss of the transmitted excitation beam is utilized as the measurand to gather information of the sample. In the parametric CARS process the signal is detected at a new optical frequency. Resulting of this difference the detected signal ΔI has to be separated from the incident beam during the SRS experiment. The rate of change in amplitude compared to the incident beam intensity ($\Delta I/I$) is in the range of $< 10^{-4}$ in both SRL and SRG [Freudiger et al. [2008]]. To separate the desired signal ΔI from the overall detected signal, a modulation of one of the incident beams with the frequency f is performed to detect the signal achieving the necessary sensitivity. Avoiding the laser noise, which is scaling to $\frac{1}{f}$, the modulation frequency is set to be in the range of $1MHz$ to $20MHz$ utilizing electro- or acousto-optic modulation devices. Higher frequencies enable shorter integration times for rapid live cell imaging [Freudiger et al. [2008], Cheng and Xie [2013, pp. 103]].

The desired SRS signal ΔI is modulated with the known frequency f and can be extracted from the larger laser intensity (e.g. I_p), which has its characteristic arbitrary fluctuations resulting from the laser source. To perform this operation a lock-in amplifier is used as a very narrow bandpass filter at the frequency f to extract the small SRS signal from the overall signal. The modulated beam has to be the complementary beam, which is filtered out behind the sample and is not detected. In case of SRG the pump beam has to be modulated, in SRL the Stokes beam respectively.

Eq. (34) and (35) state that the detected signal is depending only on the imaginary part of $\chi_e^{(3)}$ meaning that in contrast to CARS there is no non-resonant background present. Here, a higher molecular sensitivity compared to CARS can be observed (for

example $50\mu M$ investigating a retinol solution using $1s$ integration time and $40mW$ on each beam in the focus [Cheng and Xie [2013, pp. 108]].

The interpretation of data obtained by SRS for determining the molecular concentration in a sample is easier compared to CARS due to the linear concentration dependence in SRS. Spectra obtained with SRS are identical to spontaneous Raman spectra because of the absence of the dispersive line shape, which is found during hyperspectral scanning in the distribution of the CARS signal intensity. This enables a direct and easy comparison of SRS to spontaneous Raman spectra.

Using SRS for imaging the signal is the convolution of the object with the point spread function of the optical system. SRS images can be interpreted straight forward while CARS images have to be checked for coherent image artifacts, especially when images contain small structures compared to the pump and Stokes wavelengths [Cheng and Xie [2013, pp. 100]].

2.3. Concept of structured illumination for resolution enhancement

The main goal in the development of optical microscopy was to resolve structures and gain information of unknown samples, whose amount of details could not be revealed with state of the art setups. For comparing the capabilities of different approaches and systems the term resolution was introduced. The resolution is the ability of an optical imaging system to resolve two point-like objects in close proximity. Classic examples for a definition of resolution were given by Abbe (Abbe [1873], Hecht [2002] p. 215, pp. 609), Rayleigh (Rayleigh [1879]) and C. M. Sparrow (Sparrow [1916]), stating that the resolution d is limited by the diffraction limit determined by the wavelength λ of the radiation used in the experiment and the utilized optics (in the case of Abbe the following equation was stated having n : *index of refraction* and α : *the half of the acceptance angle*).

$$d = \frac{\lambda}{2n \cdot \sin\alpha} \quad (36)$$

In recent efforts the diffraction limit could be circumvented by various so-called “super-resolution” techniques using fluorescent dyes to label specific parts of the sample. Here, the **stimulated emission depletion** (STED) microscopy (theoretically predicted by Hell and Wichmann [1994] and practically demonstrated by Donnert et al. [2006]), the **photo-activated localization microscopy** (PALM) (theoretically predicted by [Betzig [1995], demonstrated by Betzig et al. [2006] and Hess et al. [2006]), the **stochastic optical reconstruction microscopy** (STORM [Rust et al. [2006]] and **direct STORM** [Heilemann et al. [2005]]) as well as the **structured illumination microscopy** (SIM) (shown independently by [Heintzmann and Cremer [1999], Frohn et al. [2000] and Gustafsson, M. G. L. [2000]]) are the main state of the art super-resolution techniques applied to biological samples. Several extensions and modifications of the mentioned techniques are scope of the ongoing research for the adaption to sample specific problems or higher resolution enhancements [Sahl et al. [2017]].

For these super-resolution microscopy techniques the classical definition of resolution, e.g. by Abbe, can not be applied straight forward. Specifying a numerical value for the resolution at a selected area in an image can not represent the overall obtained resolution of a technique as well as it may not be comparable to other techniques due to the selection of the sample or the utilized fluorescent dyes. A more convenient method is valuing the resolution of an image by estimating supported frequency bandwidth, taking into consideration that the spatial resolution is inversely related to the spatial frequency bandwidth [Nieuwenhuizen et al. [2013]] and following Mertz [2010, pp. 371]].

In the following section a brief description of the image formation in a microscope is provided, highlighting the aspects to circumvent the diffraction limit (2.3.1). Structured illumination for resolution enhancement with linear dependence on the excitation power is discussed in 2.3.2. Also the non-linear structured illumination approach is introduced illustrating the resulting effects in the Fourier transformed frequency space (2.3.3). This technique is especially important for this thesis due to the non-linear properties of the utilized striped illumination in CARS and two-photon excited fluorescence microscopy presented in the results part of the thesis.

2.3.1. Microscopic image formation

A microscope is an optical setup with a magnification M to image a sample of interest (e.g. a point-shaped object), whose point size can not be resolved by using solely a classic detector (e.g. the human eye or a camera). The microscope performs an optical imaging process which results in the magnification of the point size allowing the detector to resolve the structure (fig. 10).

This process can be described in the frequency domain by performing a Fourier transformation. The object has frequency components $I_0(X, Y)$ which will be transferred via the microscope to the detector, which itself has a limited frequency support. The whole imaging process has an overall limited range of supported frequencies, which are summed up with the **modulation transfer function** (MTF), which defines the ratio of detected image modulation to the object modulation over the whole frequency band. The cut-off-frequency describes the highest frequency which is supported by the optical system and is a useful value for estimating the resolution in modern microscopy.

The **optical transfer function** (OTF) $T(k_X, k_Y)$ describes how the frequency components of the object are transformed by the optical system to the final image. It is a spatial frequency-dependent, complex quantity having the MTF as modulus and whose phase is described by the **phase transfer function** (PTF) [Hecht [2002, pp. 552]].

The most applied transfer function is finally the **point spread function** (PSF) $H(x, y)$ determining how a point-shaped object is imaged by the microscope. The point size will be broadened due to the imperfectness of the optical components used in the microscope. Mathematically the object will be convolved with the response of the microscope resulting in the detected image I_i , given as [derivation follows Hecht [2002, pp. 554]]:

$$I_i(Y, X) = I_0(x, y) \otimes H(x, y) \quad (37)$$

The convolution theorem states that the frequency spectrum of the image irradiance distribution is the product of the frequency spectrum of the object irradiance distribu-

tion and the Fourier transform of the spread function (see fig. 11). Transforming the image (eq. (37)) into the spatial frequency domain by a Fourier transform using the convolution theorem leads to:

$$\mathcal{F}\{I_i(X, Y)\} = \mathcal{F}\{I_0(x, y)\} \cdot \mathcal{F}\{H(x, y)\} \quad (38)$$

Now the non-normalized OTF can be defined as $\Theta(k_X, k_Y) = \mathcal{F}\{H(x, y)\}$, because the multiplication with $\mathcal{F}\{H(x, y)\}$ produces the alteration in the frequency spectrum of the object, converting it into the image spectrum. Dividing $\Theta(k_X)$ by the zero spatial frequency value $\Theta(0) = \int_{-\infty}^{+\infty} H(x) dx$ the normalized spread function can be described as:

$$H_n(x) = \frac{H(x)}{\int_{-\infty}^{+\infty} H(x) dx} \quad (39)$$

Resulting in the normalized OTF:

$$T(k_X) = \frac{\mathcal{F}\{H(x)\}}{\int_{-\infty}^{+\infty} H(x) dx} = \mathcal{F}\{H_n(x)\} \quad (40)$$

For the description of the achievable resolution of an imaging system the concept of spatial bandwidth $\Delta\kappa_{\perp}$ and the spatial resolution $\Delta\rho$ is introduced [following Mertz [2010, pp. 36 and pp. 62]]. $\Delta\kappa_{\perp}$ describes the amount of lateral wave vectors supported by the OTF. A Gaussian fit over the OTF of the optical system with the determination of the **full width at half maximum** (FWHM) can be used as a value for the resolution in microscope setups.

The relation $\Delta\rho = \frac{1}{\Delta\kappa_{\perp}}$ describes the spatial resolution. The full angular width of the entrance aperture $\Delta\theta_0$ of the optical system limits the supported frequencies. For finding the classical resolution in a wide-field imaging system one can state (with $\kappa = \kappa_{\perp} + \kappa_z$):

$$\Delta\rho_0 = \frac{1}{\kappa\Delta\theta_0} \quad (41)$$

The relationship between resolution and bandwidth in the object plane (ρ_0 and $\Delta\kappa_{\perp 0}$) and the image plane (ρ_1 and $\Delta\kappa_{\perp 1}$) lead to the magnification M :

$$|M| = \frac{\Delta\rho_1}{\Delta\rho_0} = \frac{\Delta\kappa_{\perp 0}}{\Delta\kappa_{\perp 1}} \quad (42)$$

Taking the angular width of the aperture pupil of the imaging system into account given by (θ_0 denoting the half-angular width seen from the object plane $\frac{1}{2} \cdot \Delta\theta_0$ and n the index of refraction):

$$NA_0 = n \cdot \sin(\theta_0) \quad (43)$$

In the paraxial limit ($NA_0 \rightarrow n\theta_0$) eq. (43) becomes:

$$NA_0 = \frac{n\Delta\kappa_{\perp 0}}{2\kappa} = \frac{\lambda\Delta\kappa_{\perp 0}}{2} \quad (44)$$

This results in the well-known equation for the diffraction-limited resolution by Abbe [Abbe [1873]]:

$$\Delta\rho_0 = \frac{\lambda}{2NA_0} \quad (45)$$

The introduced methods above (**STED**, **(d-)STORM**, **SIM**), commonly described as *super-resolution* microscopy techniques, refer to the diffraction-limited resolution, meaning that the achieved resolution is below this intrinsic limit. All methods share the fact that the convolution of OTF and the spectral information of the sample can be deconvolved. Therefore, the PSF has to be measured or estimated for a computational deconvolution step, which can be performed by several user-friendly open-source programs.

In addition to that it is possible to actively improve the performance of the optical system by engineering the PSF. Here, the combination of two or more excitation foci can be exploited to reduce the size of the excitation light volume (e.g. STED [Donnert et al. [2006]]). The desired ideal PSF is the delta function, which can image the spatial distribution of the sample without any introduced point spreading.

Utilizing a structured illumination pattern for the imaging of a sample is another method to broaden the accessible frequency support of a microscope. Chapter 2.3.2 explains the principle of SIM microscopy, whose technique is applied to CARS-microscopy as a novel approach to enhance the resolution in this label-free microscopy technique.

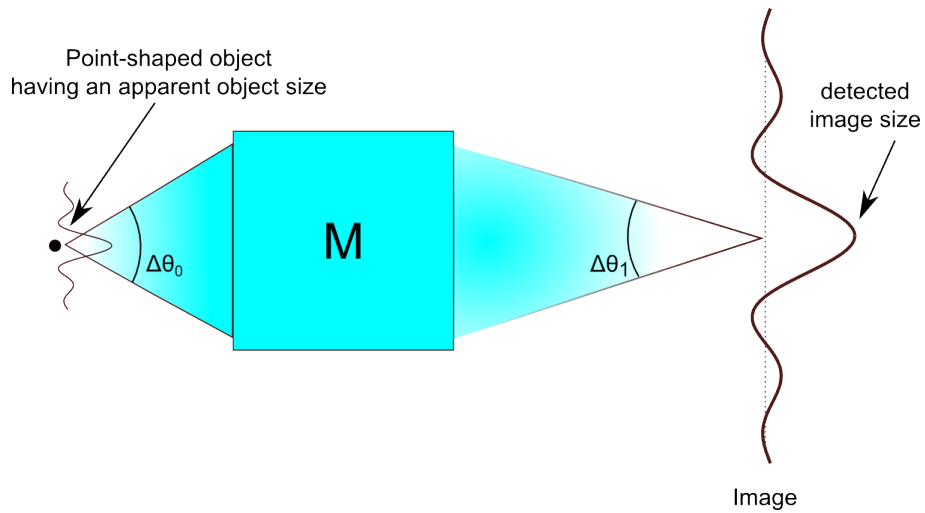


Figure 10 – Broadening of a point-shaped object by the PSF

The PSF of the microscope broadens the apparent object size of the sample. The magnification M of the optical system is the ratio of object size to image size. $\Delta\theta_0$ denotes the full angular width of the aperture pupil as seen by the object plane. Adapted from [Mertz [2010, p. 37]].

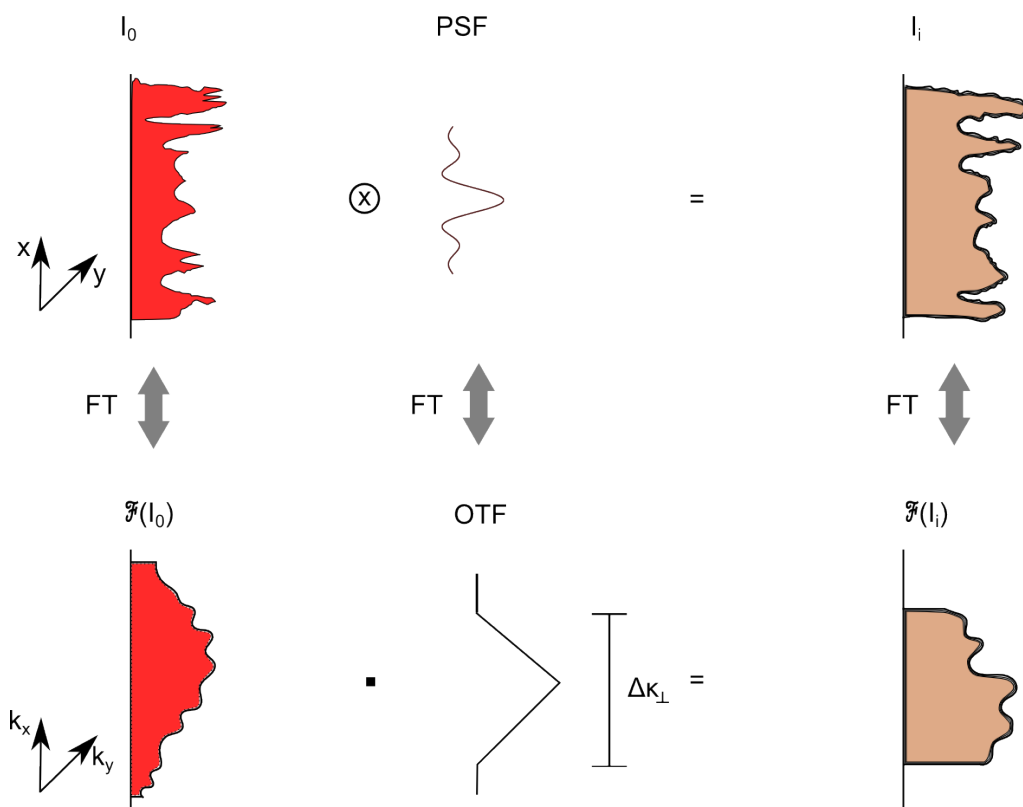


Figure 11 – Relation of PSF and OTF in the image formation of an optical system

The spatial information of the object I_0 (red) is convolved with the PSF of the optical system resulting in the image I_i (real space, brown, top row). The Fourier transform (FT, bottom) leads to the frequency domain: the finally detected frequency content is limited by the OTF support of the optical system. Adapted from [Mertz [2010, p. 39]].

2.3.2. Linear structured illumination

Structured illumination microscopy improves the spatial resolution of optical microscopy beyond the diffraction limit by utilizing striped illumination patterns [Gustafsson, M. G. L. [2000], Gustafsson, M. G. L. et al. [2000]]. In many implementations a sinusoidal stripe pattern is generated by two or three beam laser light interference effects in the focal plane along a specific angle, described by a wave vector k_{ill} and a specific phase φ . This pattern illuminates a stained sample (in fluorescence-based microscopy) leading to a striped excitation of the specimen. High signal intensities of the dyes are obtained in the regions of the peaks of the illumination pattern, whereas regions with low excitation energies (valleys of the pattern) will exhibit little to no contribution to the image and appear dark [following Schüttpelez et al. [2014]].

The principle of the method can be described referring to frequency mixing in radio wave transmission. A carrier frequency is mixed with a sample frequency to transmit the signal across the pass-band of the optical microscope. The advantage of the structured illumination is a resolution enhancement (up to all three dimensions) in the case, that the frequency of the pattern is increased to the point where it approaches the cut-off frequency. The user-selected frequency of the illumination pattern k_{ill} is mixed with the unknown frequency of the sample. Consequently, the Moire effect in two dimensions leads to additional contrast in the image (see fig. 12). This method is exploited in fluorescence-based SIM microscopy for enhancing the resolution by acquiring a series of images, which is then reconstructed via specifically designed software [Gustafsson, M. G. L. [2005], Gustafsson et al. [2008]].

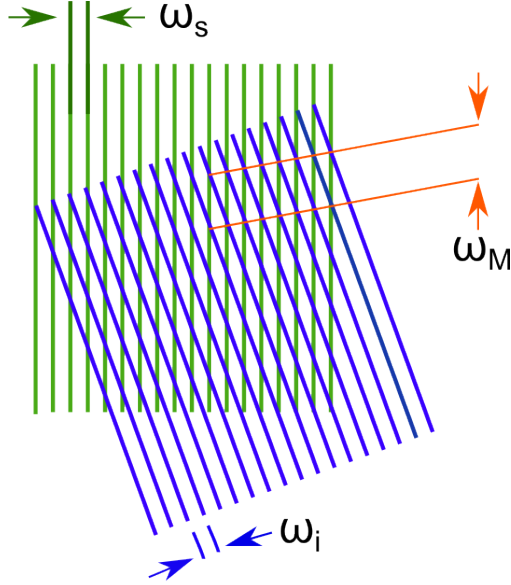


Figure 12 – Illustration of the Moire effect

The Moire effect describes the overlapping of two 2D-stripped patterns rotated by an angle to each other. The mixing frequency ω_M (orange) of the overlapped frequencies (ω_S green and blue ω_i) can be observed [Schüttpelz et al. [2014]].

Considering pure frequency mixing, the addition of two cosine functions with frequencies ω_1 and ω_2 generates a beat mode carrying two new frequencies, the sum and the difference frequency, which can be described as [Schüttpelz et al. [2014]]:

$$\cos(\omega_1 t) + \cos(\omega_2 t) = 2 \cdot \cos\left(\frac{\omega_1 t + \omega_2 t}{2}\right) \cdot \cos\left(\frac{\omega_1 t - \omega_2 t}{2}\right) \quad (46)$$

In the spatial frequency space, having now the transformed k_1 and k_2 , the additional frequency components are:

$$\cos(k_1 x) + \cos(k_2 x) = 2 \cdot \cos\left(\frac{k_1 x + k_2 x}{2}\right) \cdot \cos\left(\frac{k_1 x - k_2 x}{2}\right) \quad (47)$$

This mechanism is called heterodyning and can be exploited to expand the detectable range of frequencies, when one frequency is known. The second, unknown higher (and, therefore, undetectable) frequency can be obtained by measuring the reduced frequency of the envelope of the beat pattern. Hence, the limited pass-band can be enlarged up to twice of its original value. Expanding the pass-band any further by increasing the frequency of the beat pattern is not possible because the beat pattern itself is not supported any more and can not be detected.

Analyzing an arbitrary (e.g. widefield) image in the two-dimensional Fourier space its spatial frequencies appear as a circular pattern. Low frequencies are located near the center of the image, high frequencies at the border of the circle, having longer k vec-

tors. The OTF support of the optical system can be observed as the radius of the circle depicting the cut-off-frequency introduced above.

Applying a sinusoidal pattern on a homogeneous sample two delta peaks appear in the Fourier transform, if the frequency of the illumination pattern is lower than the OTF support. Connecting these two delta peaks by an axis indicates the pattern orientation, while the distance from the peaks to the center of the image describe the frequency of the applied pattern.

For generating a resolution enhancement as high as possible the frequency of the illumination pattern is chosen to be near the edge of the OTF support. The undetectable spatial frequencies of the sample beyond the OTF support will be mixing with the known pattern frequency. By an unmixing step the unknown frequency can be calculated in a post-processing step utilizing the known pattern frequency. The final accessible frequency range will be broadened allowing to detect spatial sample features beyond the classic OTF support only limited by the need of detecting the mixing frequency.

Shown in 2.3.1 the image I_i is the convolution of the fluorescence emission $F(\vec{r})$ and the PSF $H(\vec{r})$, meaning $I = F \otimes H$, while \vec{r} denotes the lateral coordinates (x, y) . The varying illumination pattern $P(\vec{r})$ as well as the spatial distribution of the fluorescent dyes $S(\vec{r})$ are determining $F(\vec{r})$, $F = P \cdot S$. Assuming a sinusoidal stripe pattern along a specific angle ϑ_{rot} , with the frequency k_{ill} and the phase φ the pattern can be described as [derivation follows Schüttpelz et al. [2014]]:

$$P(\vec{r}) = \frac{I_0}{2} [1 - \cos(\vec{k}_{ill} \cdot \vec{r} + \varphi)] \quad (48)$$

Having I_0 as the initial illumination intensity. The measured image $I(\vec{r})$ can now be stated as:

$$I(\vec{r}) = (S(\vec{r}) \cdot P(\vec{r})) \otimes H(\vec{r}) \quad (49)$$

Performing a Fourier transform leads to the term in reciprocal space, turning the deconvolution of the PSF and the fluorescence emission into a simple product:

$$\tilde{I}(\vec{k}) = \tilde{H}(\vec{k}) [\tilde{P}(\vec{k}) \otimes \tilde{S}(\vec{k})] \quad (50)$$

The sinusoidal illumination pattern occurs in the frequency domain as a series of delta functions δ , which can be used to simplify the equation to:

$$\tilde{P}(\vec{k}) = \frac{I_0}{2} \left[\delta(\vec{k}) - \frac{1}{2} \delta(\vec{k} - \vec{k}_{ill}) e^{-i\varphi} - \frac{1}{2} \delta(\vec{k} + \vec{k}_{ill}) e^{i\varphi} \right] \quad (51)$$

Finally the observed image in the frequency domain can be stated as the convolution

of the pattern with the fluorophore distribution:

$$\tilde{I}(\vec{k}) = \frac{I_0}{2} \vec{H}(\vec{k}) \left[\tilde{S}(\vec{k}) - \frac{1}{2} \tilde{S}(\vec{k} - \vec{k}_{ill}) e^{-i\varphi} - \frac{1}{2} \tilde{S}(\vec{k} + \vec{k}_{ill}) e^{i\varphi} \right] \quad (52)$$

In the following post-processing step for reconstructing the raw data into the final image, which has enhanced resolution, the parameters of the system's PSF as well as the properties of the illumination pattern have to be identified beforehand by a parameter estimation. Then the superresolved distribution of the fluorophores in the sample can be calculated. The PSF can be measured experimentally by imaging a sub-diffraction-limited structure such as e.g. a fluorescent quantum dot or a single fluorescent bead ($\varnothing \leq 100nm$), which is background corrected and rotationally averaged. The OTF can be stated afterwards by calculating the 2D Fourier transform of the PSF.

Typical SIM raw data contains a stack of single images described by eq. (52). For a constant pattern angle $\vartheta_{rot} = const.$ the phase φ of the pattern is shifted by translating the interference pattern across the sample for a number of images N . ($N \geq 3$ for 2D SIM and $N \geq 5$ for 3D SIM). The phase shifts are spaced evenly over 2π ($\Delta\varphi = \frac{2\pi}{N}$) (see fig. 13).

In the experiment M separate values of ϑ_{rot} are set in order to cover the focal plane, which are evenly spread across the image space ($\Delta\vartheta_{rot} = \frac{2\pi}{M}$), with $M \leq N$. The data set of $M \times N$ images is background-subtracted and intensity-corrected compensating for bleaching effects during the acquisition as well as source fluctuations. Then the data is Fourier transformed into reciprocal space. Here, a pairwise cross-correlation is utilized to identify the values of the frequency shift vector, the phase shift and the modulation depth for each image, while by linear regression the initially estimated values are optimized.

The information of the images of each angle are combined, each phase triplet is separated into three components: the central band identical to the conventional widefield image, and two side bands representing the new spatial information. The side bands are translated by a vector k_0 in reciprocal space restoring the information to the original position.

Without a final noise filtering step the obtained image would suffer due to additional noise of the high spatial frequency region. The exclusion of undesired noise is performed typically by a Wiener filter or a Richardson-Lucy deconvolution step (referring to FairSIM [Müller et al. [2016]]). In addition a suitable cutoff frequency has to be identified to exclude contributions, which only provide noise and no further sample information. This task is performed by an apodization function applied to the side band information. It is also evening out overlapping frequency components ensuring an even intensity distribution in the reconstructed image. Then the final image is obtained by

transforming back into real space. In the best case a twofold improved spatial resolution is found in the reconstructed image (compared to standard widefield imaging) [Gustafsson, M. G. L. [2000]]. For the reconstruction purpose of SIM data sets open source software packages are published recently, which utilize the image processing platform *FIJI* [Schindelin et al. [2012], Rueden et al. [2017]] in the case of FairSIM [Müller et al. [2016]] or MATLAB in the case of MAP-SIM [Křížek et al. [2015], Lukeš et al. [2014]].

For the generation of the illumination pattern in the focal plane typically the interference of two (or three in 3D SIM) laser beams is utilized, which are focused onto the back focal plane of the objective lens and finally generating two counter propagating evanescent waves in the focal plane utilizing a diffraction grating. It is rotated and laterally shifted by piezoelectric transducers, but also limits the imaging speed. More recent attempts replace the diffraction grating by active optical elements, such as e.g. spatial light modulators [Hirvonen et al. [2009], Rego and Shao [2015]] or galvanometric mirrors [Mandula et al. [2012]] allowing rapid changes in the phase and angle of the pattern. The image detection is performed by CCD or sCMOS cameras providing high sensitivity as well as high acquisition speed for live-cell imaging [Kner et al. [2009], Wu and Shroff [2018], Heintzmann and Huser [2017]].

Alternative implementations are utilizing micro-mirror arrays for the generation of point-shaped, multi-focal illumination patterns [York et al. [2012]], which are swept over the sample for an improved imaging speed in 2D SIM. Here, the optical excitation and detection pathway can be folded and manipulated by a galvanometric mirror, which affects both optical paths. This way parts of the reconstruction process are performed on a direct, optical way for an enhanced imaging speed [York et al. [2013]].

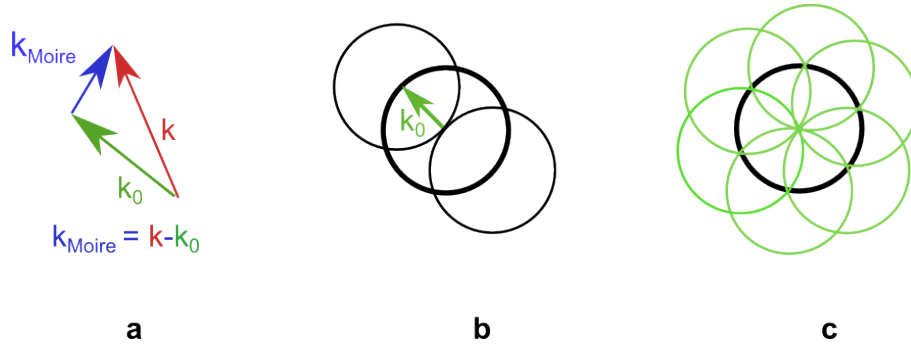


Figure 13 – Structured illumination in Fourier space

A sinusoidal structured pattern with wave vector k_0 is exploited for generating the illumination of the sample. It leads to Moire fringes at $k_{Moire} = k - k_0$ (when k is the sample's frequency content) (a). Side bands at the mixing frequencies with the vectors $k + k_0$ and $k - k_0$ appear and provide additional spatial information of classically unobservable frequency regions. The microscope can observe only frequencies which are located within the OTF support, indicated with the heavy circle (b). The observed data includes the classic widefield information of the OTF support itself as well as the additional information of the side bands, which is shifted by the vector k_0 (indicated with the light circles in b). This information has to be decoded and restored to its original position. By rotating the pattern with three or more angles the additional frequency content can be spread evenly over the frequency space, generating a new circle of observable sample information, which has up to twice the diameter of the initial OTF support (c) [adapted from Gustafsson, M. G. L. [2000]].

2.3.3. Non-linear structured illumination

The maximum resolution enhancement in a SIM experiment is limited to a factor of two while using a sinusoidal pattern with a linear excitation of the sample. Introducing a non-linearity into the imaging process the theoretical predicted improvement in resolution improvement is unlimited (Heintzmann et al. [2002]). In fluorescent-based microscopy a saturated structured illumination can generate this non-linear feature [Gustafsson, M. G. L. [2005]]. The intensity of the excitation pattern is increased to the point, where the fluorescent dye is saturated and any stronger illumination intensity does not produce a higher fluorescent signal. This is due to the rather long lifetimes of the excited states of the fluorophores. The mechanism limits the number of emitted photons per time per unit. Now the sinusoidal illumination generates flat tops at the peak intensities of the fluorescence response of the specimen. The non-linear pattern combined with an increased number of phase shifts and angles of rotation leads to an optical spatial resolution of $\sim 50nm$ in recent implementations [Rego et al. [2012]]. The higher intensities of the excitation power compared to linear SIM lead to increased bleaching effects, which are a limiting factor and disadvantages of this method. In addition the penetration depth of the generated pattern in thick, densely labeled fluorescent samples is still limited, due to scattering effects at the sample ma-

terial, which potentially lead to disturbed illumination patterns.

For increasing the accessible sample thickness the combination of line scanning with structured illumination microscopy (LS-SIM) is performed [Mandula et al. [2012]] allowing the suppression of out-of-focus light by line scanning, while still the resolution is enhanced by SIM. To introduce the non-linearity the length of k_0 is chosen to be small compared to the linear Gustafsson-SIM method. Now the non-linearity in the data sets becomes apparent analyzing the Fourier transform, while the length of multiples of k_0 is in the OTF support of the optical system. The additional peaks at integer multiples of the initial k_0 vector of the illumination pattern appear in the frequency space laterally shifted along the k_0 direction (see fig. 14 and fig. 15).

The reconstruction of the data needs exact knowledge of the position and length of the k vectors to shift the additional sample information to its origin in the final image, but also holds great potential in terms of final obtained resolution enhancement. Especially the MAP-SIM approach is capable of reconstructing non-linear excitation patterns [Lukeš et al. [2014]], which are also apparent in the line scanning-based SI-CARS approach introduced in 4.5.5. The non-linearity in the galvomirror-based scanning of specific patterns in a sample arises from the non-sinusoidal intensity distribution of the excitation pattern. Here, the OTF function (mostly determined by the objective lens) is smoothing the rather rectangular on-off-like illumination pattern, but this effect is also dependent on the fineness of the pattern. The finer the pattern the more sinusoidal it gets due to the reduced frequency support of the OTF in that particular frequency region.

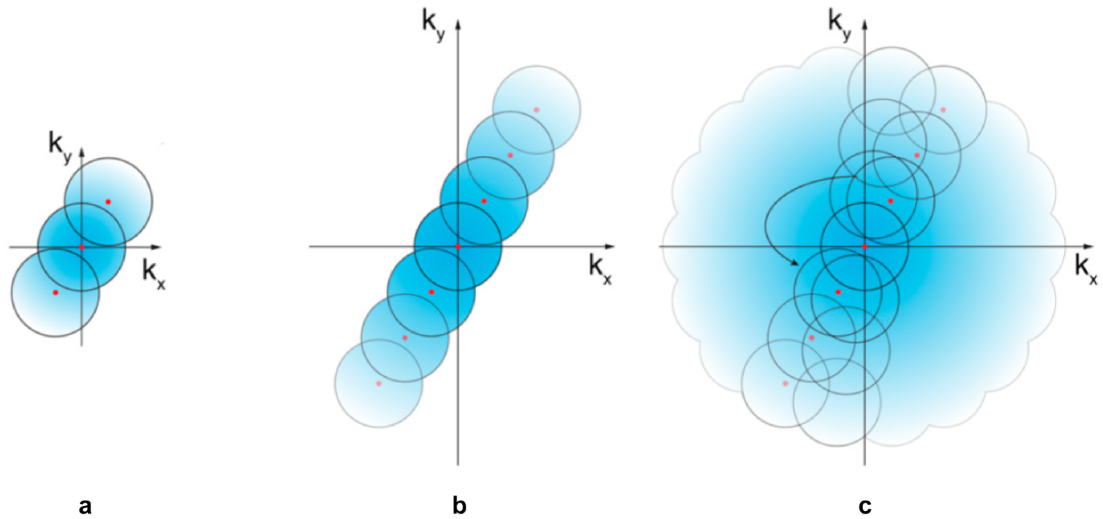


Figure 14 – Linear and non-linear SIM compared in Fourier space

In (a) the Fourier transform is depicted for a linear SIM image, two additional frequency components occur in the spectra, shifted from the origin with $\pm k_0$. In the case of non-linear SIM the illumination pattern contains spatial frequencies which are integer multiples of the initial illumination pattern, shifted with k_0 . In (b) a single angle of rotation is shown, for full resolution enhancement in all spatial directions it is shifted in smaller fractions of 2π . (c) depicts the necessity of small angular shifts: the overlap of the frequency content in higher orders of k can be accomplished by reducing the step size of the rotation angle [from Rego et al. [2012]].

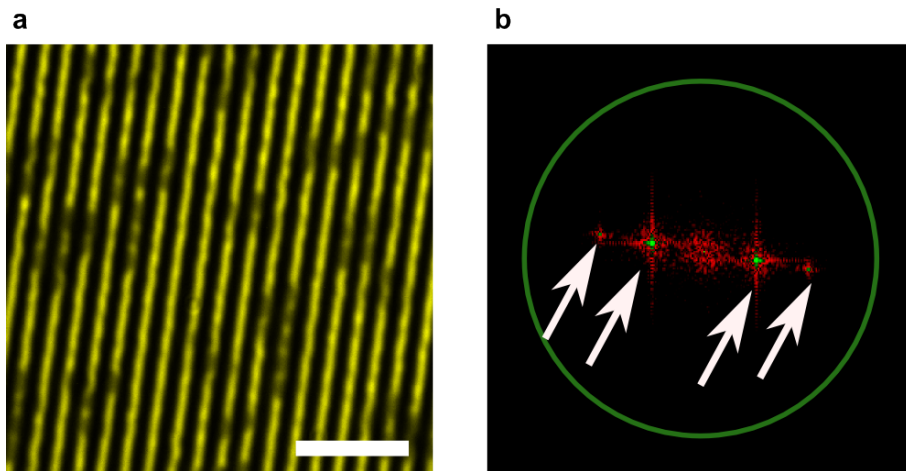


Figure 15 – Fourier transform of SI-CARS image indicating second order frequency components

a) shows a CARS image with an applied very coarse structured illumination pattern utilizing galvanometric scanning mirrors. The sample was a polystyrene bead sample ($\varnothing = 1,1\mu m$) embedded into a DMSO solution while probing the $2913cm^{-1}$ $C - H$ symmetric stretching mode of the DMSO solution generating an anti-contrast. More details are provided in 4.5.5. The scale bar depicts $5\mu m$. Fourier transform **(b)** of the single raw frame acquired by *FIJI* [Schindelin et al. [2012], Rueden et al. [2017]]. The arrows point at the frequency peaks introduced by the illumination pattern while the green circle depicts the estimated cutoff frequency. Note that the Fourier transform was rescaled for visualization purposes.

3. Materials and Methods

In the course of this thesis a state of the art CRS-setup was developed⁵. It has a variety of imaging modalities and different work modes. In order to show its capabilities the following chapter will first focus on the general instrumentation and setup, which is used in almost all shown different applications in the thesis. In order to report about the successful construction, characterization and application of the CRS-microscopic setup a selection of data is shown, originating from collaborative work where CRS-imaging was beneficial for actual research in different biomedical fields such as the study of stem cell differentiation (section 4.1), the lipid storage of algae for bio-fuels (4.2), the study of lipid storage in *C. elegans* under the influence of copper treatment (4.4.1) as well as the differentiation of primary human alveolar epithelial cells (4.4.4). Further work, which is addressing new insight into CRS-imaging and novel technical developments is presented: a study and characterization of the OPO pulse length while performing a wavelengths tuning for hyperspectral (HS) CARS and SRS imaging causing possible spectral distortions in the final data as well as presenting a controlled OPO tuning mode to perform HS-CARS with stable pulse length and, therefore, reproducible and undistorted data by a custom developed Matlab-based OPO tuning control program (section 4.3). In addition a novel imaging modality utilizing structured illumination for CARS (SI-CARS) is presented for enhancing the resolution of conventional CARS imaging beyond the diffraction limit (section 4.5). Therefore, two-photon excited fluorescence data is compared to the SI-CARS data in order to prove the applicability of structured illumination in combination with a coherent contrast mechanism. Due to the need for compact, stable, user-friendly and low cost CRS-laser sources in clinical applications a collaboration with the University of Hong Kong was forged in order to apply all fiber-based techniques for the construction of a novel laser source providing CARS- as well as SRS-imaging without balanced detection, SHG and two-photon excited fluorescence imaging in one approach (section 4.6). Furthermore, a fiber-based short pulse laser source is introduced providing fs-laser pulses with up to 500mW intensity, which is applied for SHG and two-photon excited fluorescence imaging. This source is a preliminary results of the project and was proposed as a stand-alone laser source interesting for users of two-photon excited fluorescence and SHG imaging.

⁵In collaboration with Mr. H. Hachmeister.

3.1. Experimental setup

The following section describes the CRS-microscope, which can be categorized in three main parts (fig. 19): The laser source providing a fundamental IR-wavelength for the Stokes beam (see 3.1.1) as well as a frequency doubled wavelength pumping two OPOs, which deliver tunable pump wavelengths for the CRS process (see 3.1.2). It follows the spatio-temporal overlap of the three⁶ excitation beams as well as the beam diameter and divergence adaption in combination with intensity and pulse length diagnostics. Finally, a home-built scanning microscope is utilized for the sample analysis enabling a maximum degree of freedom in the detection and manipulation modes as well as superior performance in terms of stability over long time scales.

3.1.1. Solid-state laser system

A solid-state picosecond laser (*HighQ*, picoTRAIN IC-1064-15000 / 532-10000 ps Nd:VAN) is utilized for the generation of the Stokes beam as well as to pump an double OPO system in the CRS-setup. It is located on an actively damped optical table (*TMC*) in order to avoid vibrations in the laser system as well as in the microscope. The laser source consists of an oscillator (fig. 16 blue box A), an amplification stage (red box B) and a final frequency doubling unit (green box C). The oscillator has a wavelength of $1064nm$ and can deliver up to $10,8W$ power (see fig. 16). A Nd:VAN optical crystal is placed in the folded laser cavity, where the population inversion is created by optical pumping using a laser diode array, whose light is focused into the crystal by a cylindrical lens (*HighQ* [2012]). The mode locking is performed passively with a SESAM⁷, which has a gold metalized back side soldered to a heat sink mounted in a piezo driven mirror mount. It is used for remote cavity alignment through the mirror mount performed by the user. The laser cavity itself is terminated on one side by the SESAM mirror and on the other by the metalized end facet of the Nd:VAN crystal, which directs a definite portion of the IR-beam to the amplifier stage passing an isolator. This additional amplifier stage utilizes a diode pumped amplifier crystal and delivers an output power of $16,1W$. By a motorized $\frac{\lambda}{2}$ -wave plate and a thin-film polarizer a user selected portion of the IR-beam is frequency doubled to $532nm$ through second harmonic generation by a non-linear crystal. For a high efficiency of the SHG process a temperature control is applied to the crystal, which enables a maximum output power of $10,4W$ (100% $532nm$). For meeting the need of pumping two OPOs at the same time the laser has three outputs, one for the fundamental $1064nm$ beam as

⁶In case of DR-CARS.

⁷Semiconductor saturable absorber mirror

well as two outputs for $532nm$. Again a motorized attenuator manages the energy ratio between the two outputs of the $532nm$ beam. In normal operation 10% of the infra-red power are used as the Stokes beam in the CARS experiments, the remaining portion is frequency doubled and leaves the laser at the two remaining outputs for pumping the OPOs. The polarization of the IR-beam as well as of the $532nm$ beam leaving the laser at exit 2 is horizontally polarized whereas the $532nm$ beam of exit 1 has a vertical polarization. In order to meet the requirements for the OPO, which needs vertically polarized light at its entrance window, a wave-plate is placed into the beam path of exit 2 in order to turn its polarization into vertical. The $1064nm$ laser wavelength has a pulse length of $7,4ps$, the $532nm$ frequency doubled portion has $6,2ps$ respectively. The configuration of one master oscillator as fundamental laser source is beneficial for the performed CRS-experiments in terms of temporal and spatial coherence of all beams due to the absence of any electronic synchronization mechanism among two separate excitation sources, which are reported as former configurations in the literature [Ganikhanov et al. [2006], Cheng and Xie [2013, pp. 83]].

The application of a pulsed laser system with a high pulse peak energy leads to strongly enhanced CRS signals generated in the sample. Due to the resulting moderate mean powers in biological specimens low thermal heating and non-critical photonic stress is observed. A laser system with picosecond instead of femtosecond pulse duration meets the aim of addressing a single Raman mode for a high signal-to-background ratio in CRS as well as a high spectral resolution for hyperspectral imaging. Here, the line width of the laser excitation matches well to the line width of the probed vibrational mode generating higher CRS signal intensities. Also the undesired non-resonant background in the CARS process is rather low in the regime of pulse length applied in this setup [see also Zumbusch et al. [1999], Cheng and Xie [2013, pp. 80-82]].

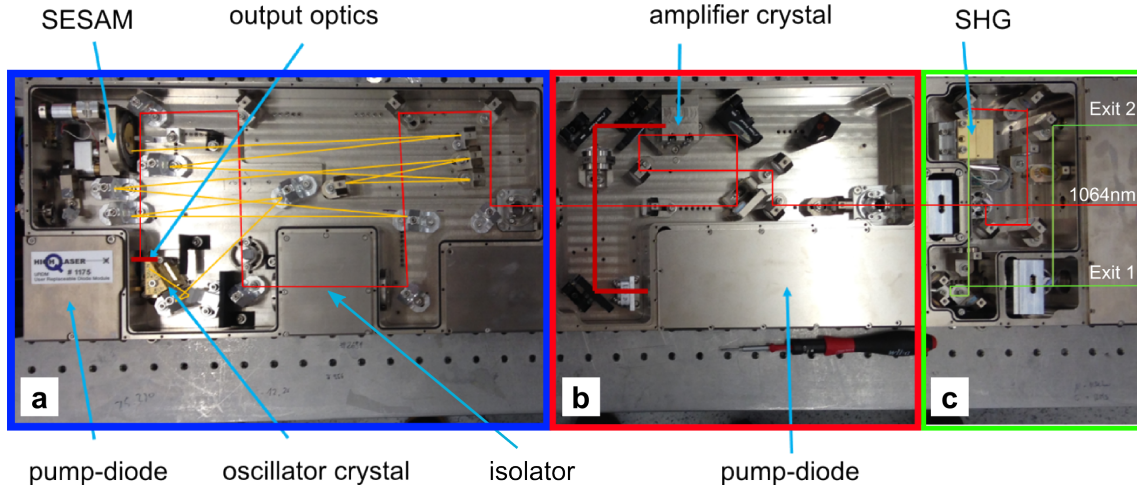


Figure 16 – Solid-state laser source *HighQ picoTRAIN*

The photograph provides an overview of the three main components of the solid-state laser system (the access covers are open for maintenance): The blue box (a) marks the master oscillator cavity with the pump diode array, Nd:VAN crystal and the SESAM mirror for passive mode locking. In the red box (b) the amplification stage can be seen. Here, the 1064nm beam is focused again into a pumped optical crystal and can be amplified to a maximal output power of $p_{1064\text{nm}} = 16,1\text{W}$. In the green box (c) the second harmonic generation (SHG) through a temperature controlled crystal with the following division by polarization dependent optical beam splitters into the different output ports takes place [HighQ [2013]].

3.1.2. Optical parametric oscillator

An optical parametric oscillator (OPO) is an array of optical components inside an optical cavity used for the conversion of high energetic photons into lower energetic photons with two defined energy levels, whereas the ratio of both generated photons is tunable in a system specific range (see fig. 17). The energy-shifted photons are named signal and idler, the shorter wavelength is defined as the signal [Cheng and Xie [2013], Ganikhanov et al. [2006]]. The conversion is performed by focusing the light into a non-linear crystal exploiting the optical parametric generation (OPG), which is a $\chi^{(2)}$ -process. Here, the law of energy conservation ($h\omega_{\text{pump}} = h\omega_{\text{signal}} + h\omega_{\text{idler}}$) as well as the phase-matching condition ($\vec{k}_{\text{pump}} = \vec{k}_{\text{signal}} + \vec{k}_{\text{idler}}$) has to be satisfied, while in this configuration the collinear non critical type I phase matching interaction is exploited in the LBO crystal [Weiner [2009, pp. 245]].

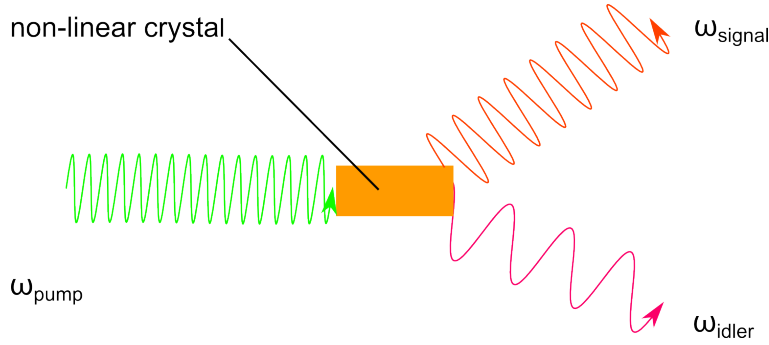


Figure 17 – Optical parametric generation (OPG)

The optical parametric conversion performed in a non-linear crystal is shown. Incoming pump photons ω_{pump} (green) are converted into the lower energetic signal ω_{signal} (orange) and idler ω_{idler} (red) wavelength (right hand side). For illustration purposes the directions of the generated beams are not congruent.

In the CRS-setup two commercial synchronously pumped OPOs (*APE*, Levante Emerald) generate tunable wavelengths used as the pump photons in the CARS and SRS process (fig. 18). Two OPOs are chosen to further extend the range of probed wavenumbers by granting more freedom of combining different wavelengths in the CRS process as well as to enable DR-CARS experiments. The solid state laser system pumps each OPO's LBO crystal (lithium triborate) with 3,5 – 4,0W of 532nm laser light. For a high efficiency the pump beam is focused by a lens into the crystal, which is placed in a folded 8-mirror cavity. The cavity length of 3,75m is matching the repetition rate of the laser source ($\sim 80MHz$). This way every 12,5ns a pump pulse enters the cavity and generates the signal and idler photons inside the crystal. All photons travel in the cavity and meet with the next pump pulse in the crystal generating a high instantaneous intensity for a high efficiency of the OPG-process. The cavity length must be tuned precisely to every desired signal wavelength as well as to the repetition rate of the incoming pulses, which is performed by a piezo-actuated delay stage (mounting mirror M2). The smallest increment the stage can travel is 85nm. The phase matching condition according to the desired signal wavelength is performed via temperature control of the crystal. Due to the type I phase matching condition the incoming vertically polarized 532nm pump photons generate the horizontally polarized signal and idler photons exiting the OPO. Their polarization is then matching the polarization of the 1064nm laser beam in the final CRS experiment, which was initially horizontally polarized [APE [2009], Powers [2011, pp. 94]]. The crystal is placed on a resistor heated mount and can be heated in the range of 105°C to 160°C in 0,1°C steps using a thermocouple for control. A look-up table allows the choice of the correct temperature. The natural bandwidth generated by the LBO crystal is in the range of $\approx 15nm$. For the desired smaller bandwidth and final tunable wavelengths selection a simplified

Lyot filter scheme is applied in the OPO's cavity. It consists of a birefringent crystal performing a wavelength-dependent polarization according to its rotation position, which is electronically actuated by a rotation mount. Finally, a polarizer selects the supported wavelength by its polarization sensitive transmission. The Lyot filter further suppresses undesired wavelengths with each pass through the filter layout, resulting in a spectral width of approximately $\Delta\lambda = 0.3nm$ (full width at half maximum).

The signal and idler photons are finally split with a short-pass filter into two exits. In the current setup only the signal photons are used for the CRS-experiments. A clean-up filter (*AHF*, FF01-855/210BP) placed inside the signal beam path eliminates the remaining pump photons and residual idler wavelengths of each OPO. A built in spectrometer and two photo-diodes measure the incoming pump beam intensity as well as the outgoing signal intensity allowing the adjustment and control of the OPO.

Both commercial OPOs are identical in their performance and can be operated simultaneously. Their tuning range is $680 - 990nm$ for the signal wavelength whereas the available range in the CRS experiment is more limited due to the dichroic mirrors installed for the spatial overlap (see fig. 19). The resulting available wavelength range is $950 - 835nm$ for OPO I and $830 - 680nm$ for OPO II. Utilizing the $1064nm$ beam as fixed Stokes pulse leads to an addressable wave number range of $\sim 1100cm^{-1}$ to $\sim 2578cm^{-1}$ (OPO I) and $\sim 2650cm^{-1}$ to $\sim 5753cm^{-1}$ (OPO II). If a broader spectral range is needed for CRS-experiments the dichroic mirrors can be replaced by 50/50 beam splitters sacrificing 50 percent of the incoming power at each passed splitter. In general the OPOs have a good long term stability of the optical cavity so that a readjustment is needed every two to three month.

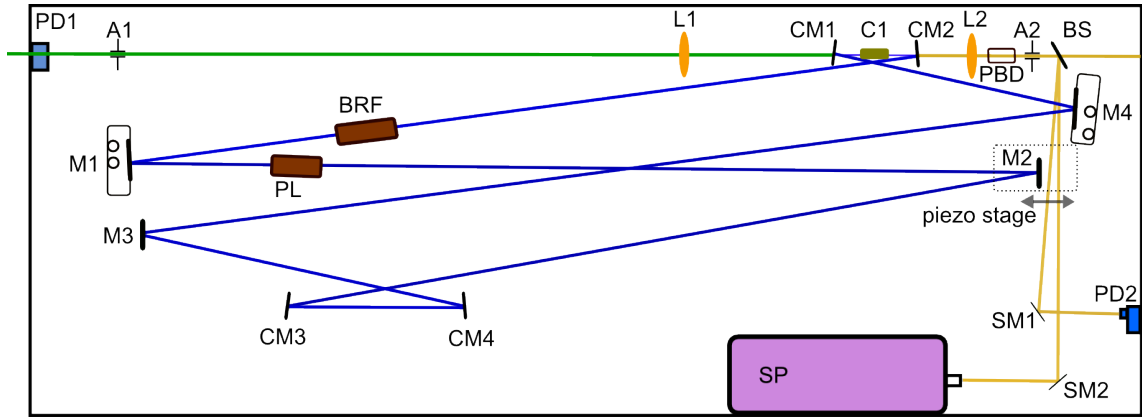


Figure 18 – Scheme of a *Levante Emerald* OPO

The 532nm pump beam (green) enters the OPO on the upper left hand side. It is focused into the LBO crystal (C1) by a 75mm lens (L1) and generates the signal and idler photons. The folded cavity beam path is shown in blue. A tunable birefringent crystal (BRF) and a polarizer (PL) form a simplified Lyot filter for defining the signal wavelength as well as the bandwidth. A small portion of the generated photons is directed into the spectrometer (SP) for wavelengths monitoring. Signal and idler beam exit the OPO on two separate ports, which contain Brewster windows (not shown).

Abbreviations: **A1,2**: apertures, **L1**: pump focus lens, **L2**: output collimator lens, **CM1-4**: concave mirrors, **M1-4**: plane mirrors, **BRF**: birefringent filter, **C1**: LBO crystal, **BS**: beam splitter, **SP**: spectrometer, **SM1,2**: beam steering mirrors, **PD1**: pump power photo detector, **PD2**: signal power photo detector, **PMD**: pump beam dump, **PL**: polarizer. Adapted from [APE [2009]].

3.1.3. Spatio-temporal overlap with laser diagnostics

Due to three different sources of laser light it is necessary to overlap all beams in spatial and temporal properties in the specimen. The temporal overlap is adjusted by two delay stages which introduce additional optical path length to each laser source. The Stokes beam is directed onto the first delay stage, which is constructed by a retro-reflector (*Thorlabs*, PS973M-B) mounted on a linear translation stage (own construction by workshop University Bielefeld) (see fig. 19). Delay stage 1 covers the temporal overlap of the 1064nm beam and OPO I. The second delay stage is home-built constructed by two dielectric mirrors (*Thorlabs*, BB1-EO3) facing each other in a 45° arrangement (using for mirror mounting *Radiant Dyes*, MNI-23025) built on a linear translation stage (*Owis*, LT60-50). The light path of OPO II is directed onto this stage in order to adjust it to the already matched temporal overlapping beams of Stokes and OPO 1. The need for the use of a mirror based delay stage instead of the retro-reflector approach arises from the change of wavelength during OPO tuning in the pump beam path. This avoids a rotation of polarization in the case of passing a retro-reflector with different wavelengths. Here, we give up the benefit of utilizing a retro-reflector in terms of alignment speed and simplicity but gain an undisturbed polarization of the pump beam in the experiments over the whole range of pump wavelengths.

The spatial overlapping of the $1064nm$ beam with the two pump beams of the OPOs is performed with a dichroic mirror 1 (DM1, *AHF*, F73-951 beam splitter). It is transmitting the $1064nm$ beam and reflecting any shorter wavelengths than $950nm$, so that the signal wavelengths of both OPOs are reflected to the microscope. The overlap of the two signal wavelengths of the two OPOs is performed in a similar way at dichroic mirror 2 (DM2, *AHF*, F43-831), which is reflecting any wavelength shorter than $831nm$. Half-wave plates (*Thorlabs*, AHWP05M-980) in combination with polarizing beam splitter cubes (*Thorlabs*, PBS252) are utilized for variable intensity attenuation by rotating the polarization of the light of each source with the half-wave plate. This way the desired intensity for the different samples can be set with an accuracy of $\sim 0,5mW$.

In order to adjust the beam diameter and control the beam divergence a magnifying telescope (focal length $f_{T1} = 45mm$ and $f_{T2} = 80mm$, all *Thorlabs*, AC254-XX-B) is implemented for each OPO (T1 and T2). Here, the second lens is mounted on a linear translation stage for precise tuning of the divergence. Finally all three beams enter the laser scanning microscope with a beam diameter of $4,3mm$ (FWHM) overlapping in time and space. For further analysis of the interacting pump and Stokes beams we implemented an automated intensity measurement setup consisting of three self constructed fast photodiodes (*Luna Optoelectronics*, PDB-C613-2), which are read out by an **analog-to-digital** (A/D) converter (*National Instruments*, PCIe-6363). A pellicle beam splitter (*Edmund Optics*, 8R/92T 25.4mm) reflects $\sim 2\%$ of each laser beam onto the photodiode. Here, great care was taken for choosing a wavelength unaffected way of beam separation. A Matlab-based custom written program was developed for recording the actual intensity of each participating laser source linking the intensity values of the excitation beams to the measured signal intensity of the specimen. In a post processing step a correction for intensity fluctuations up to $100kHz$ as well as normalization between different images can be performed (see also 4.3).

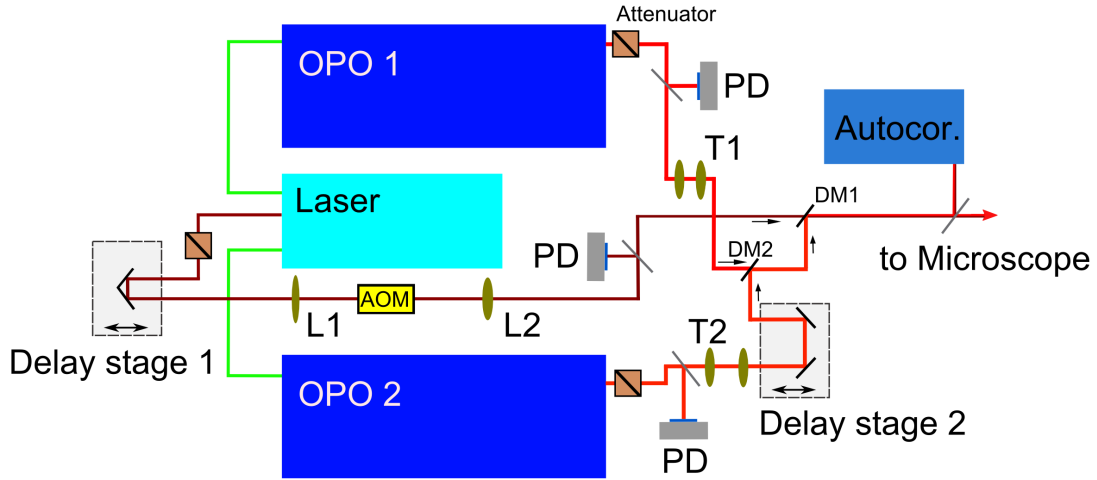


Figure 19 – Scheme of the CRS-microscope setup

The laser system (light blue) generates the 1064nm beam (depicted in dark red) as well as pumping two OPOs (dark blue), which generate the pump beams for the CRS experiments (in light red). In the middle the spatial overlap is performed with two dichroic mirrors (DM1 and DM2). Two delay stages are utilized to add optical path to Stokes and pump beam 2 in order to perform the temporal overlap of all pulsed laser lines. For intensity corrections as well as normalization in the CRS data three photodiodes (PD) detect the actual intensity of all laser sources by using a small portion of each beam separated by pellicle beam splitters. In a similar way an autocorrelator (Autocor.) is in use for recording the actual pulse length of the laser light. An AOM performs an intensity modulation of the Stokes laser for SRS as well as modulated CARS experiments.

3.1.4. Acousto-optic modulator

An acousto-optic modulator (AOM) (*Pegasus Optik*, MT 200-A0.4-1064) performs an amplitude modulation of the 1064nm Stokes beam. In this way we enable background free SRS experiments, frequency modulated CARS experiments (in order to suppress e.g. auto-fluorescence of samples) as well as it is used for fast intensity switching for the generation of a structured illumination pattern for SI-CARS. An AOM consists of an optical crystal (here TeO_2), which is coupled to a piezo-element. The piezo-driver (*AA Opto-Electronics*, A200 B4-34) applies a high radio frequency (RF) to the piezo-element (200MHz), which acts as a carrier frequency and creates an acoustical standing wave inside the crystal. The density variations lead to a local change of the refractive index in the material generating an optical grating. Incoming light is diffracted at the grating in different orders, well known from Bragg-diffraction [Pegasus Optik [2007]]. For precise alignment of the crystal to the light path it is mounted on a pivotable xyz-stage, enabling a high diffraction efficiency into the first order. All other orders are blocked exploiting the $\sim 1,3^\circ$ offset of order +1 to the zero order. The AOM's crystal is positioned into the focus of a telescope, which is consisting of the

biconvex lenses L1, $f_{L1} = 300mm$ and L2, $f_{L2} = 400mm$ (see also fig. 19). This way parallel light with the desired beam diameter is generated behind the AOM as well as the small entrance aperture of the device is matched, which allows fast rise times. For the final amplitude modulation of the Stokes beam the RF-carrier frequency is externally amplitude modulated by a signal-frequency (setting an amplitude of $0 - 5V$) applied to the driver with a waveform generator (*e.g.* *Hameg*, HMF 2550). This leads to a diffraction efficiency into the first order, which is directly proportional to the signal amplitude of the waveform generator. According to the Nyquist-criteria the maximal theoretical frequency of the light modulation is $100MHz$, meaning that for the successful transformation of the desired frequency onto the beam the carrier frequency has to be doubled at least. The optical properties of the AOM's crystal further limit the maximal modulation frequency to a value of $60MHz$.

The focus size of the telescope was chosen to $\sim 98,5\mu m$ (according to the grid spacing of $21\mu m$) ensuring a fast rise time for the experiment as well as to avoid disturbing diffraction effects in the outgoing beam [Pegasus Optik [2007]]. This results in a final restriction of the frequency to maximal $\sim 20MHz$, which is sufficient for all conducted experiments. Due to the crystal orientation in combination with the mounting mechanics a $\frac{\lambda}{2}$ -wave-plate turns the polarization of the light matching the polarization direction of the AOM. Finally the transmitted light is turned back by a second halfwave-plate. In the current installation a transmission efficiency of 76% is reached, while having a modulation depth (at $20MHz$ modulation frequency) of $\sim 75\%$.

3.1.5. Setup for a customized CRS-microscope

For CRS, SHG as well as two-photon excited fluorescence imaging a home-built scanning-microscope was developed. The decision for a customized solution instead of a commercial microscopy body was motivated by the need of a higher grade of flexibility in terms of detection pathways as well as more room for additional optical elements. For being competitive to commercial microscopes a lightproof body housing shields the inner part but also allows fast changes of sample or optical elements inside. Therefore, a frame of rectangular construction rails (*Thorlabs*, XE25L600/M) in combination with black hardboard (*Thorlabs*, TB4) was set up adding sealed cable feed through as well as blackened aluminum sheets as doors, which are removable due to a magnetic holding system. This way any disturbing room light was suppressed.

The scanning of the excitation beams over the sample in a line per line manner is performed by a set of xy-galvanometric laser scanning mirrors (*Cambridge Technology*, *Galvanometer Optical Scanner*, Model 6215H). Each mirror of the pair varies the deflection angle of the beam in one direction, according to a control voltage ($0 - 10V$) applied

at the power module of the scanning unit. The control voltage is set by a multifunctional scanning program (*ScanImage, Janelia Farm*) [Pologruto et al. [2003]], which operates an **analog-to-digital** (A/D) converter (*National Instruments, PCI-6110S* multifunction device connected to a breakout box BNC-2110). The incoming beams are further magnified by a scanning telescope after the scanning mirrors (*Thorlabs, AC508-XXX-B-ML*, with $f_{SL1} = 150mm$ and $f_{SL2} = 200mm$, magnification of 1,33) in order to fill the back focal plane of the objective ($\varnothing \approx 8mm$) enabling a high resolution through high focus quality without cutting parts of the beam during the scan process. According to the chosen integration times⁸ the maximum imaging speed reached with the galvo scanners was 8,9Hz frame rate.

A non-moving illumination of the back focal plane of the objective lens during the scanning process is important for a even and uniform illumination of the final image over the entire field of view. Especially in SRS experiments intensity losses due to beam cutting can lead to imaging artifacts. Therefore, the distances between the scanning mirrors, the telescope and the objectives' back focal plane are chosen in a special ratio (see fig. 20) [Fällman and Axner [1997]]:

$$d_1 = f_{SL1} \cdot \frac{f_{SL2} \cdot d_2 - d_3 \cdot (d_2 - f_{SL2})}{f_{SL2} \cdot (d_2 - f_{SL1}) - d_3 \cdot (d_2 - f_{SL1} - f_{SL2})} \quad (53)$$

Using $d_2 = f_{SL1} + f_{SL2}$ due to the system's afocality eq. (53) is further simplified to:

$$d_1 = f_{SL1} \cdot \frac{f_{SL1} \cdot f_{SL2} + f_{SL2}^2 - d_3 \cdot f_{SL1}}{f_{SL2}^2} \quad (54)$$

$$d_1 = \frac{f_{SL1}}{f_{SL2}} \cdot \left(f_{SL1} + f_{SL2} - d_3 \frac{f_{SL1}}{f_{SL2}} \right) \quad (55)$$

⁸128x128px and 0,5ms per line

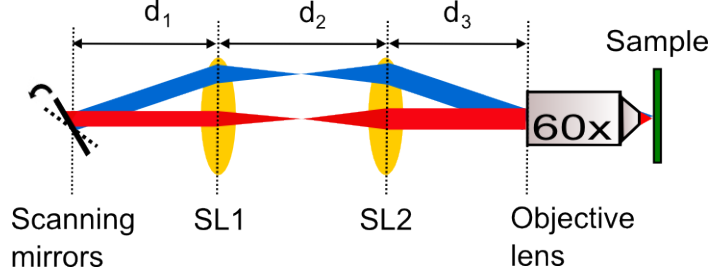


Figure 20 – Scheme of the scanning setup

The scanning telescope composed of two lenses having a focal length of $f_{SL1} = 150mm$ and $f_{SL2} = 200mm$ (both 51mm in diameter) is magnifying the raster scanned laser beams by a factor of 1,33, while it ensures a non-moving beam position at the back focal plane of the objective lens. The distances of galvo scanning unit, telescope and back-focal plane have to be set carefully according to the equation[55]. In red the radial line is shown, in blue the parallel beam, which should be congruent with the radial line at the back focal plane for all scanning angles. The parallelism of the scanning telescope was checked in an external experiment with a parallel laser beam using a long imaging distance.

For focusing the excitation beams into the sample an apochromatic water immersion objective (*Olympus*, UPLSAPO, 60 \times , NA 1,2) is used (see fig. 21). The focus is set with a linear translation stage containing a differential micrometer screw (resolution in manual translation of $\sim 0,5\mu m$ with a smallest possible incremental move of $\sim 50nm$). The transmission ratio of objective lens, scanning telescope and scanning mirrors is found to be $\frac{1}{6}$ for the 1064nm Stokes beam and $\frac{1}{3}$ for the pump beams (measured at the wavelength of 816nm).

The sample is fixed on a motorized xy-stage (*Märzhäuser*, MT mot 100 \times 100 MR) which can be addressed by the scanning control program via RS-232 for moving the sample in an image series enabling a bigger field of view. A closed-loop piezo controlled z-stage (*Märzhäuser*, S/N 222009) offers z-positioning of the sample in 1nm step size and is also connected to the imaging software. Hence, it is possible to perform a 3D-analyzation of a sample in an automated and fast manner. A dichroic mirror (BS1) (*Semrock*, FF757-Di01-25 \times 36) placed between the second lens of the scanning telescope (*SL2*) and the objective lens is used to detect epi-CARS signals or bright light from the sample. A flip mirror mount switches between epi-CARS imaging via a photomultiplier module (PMT) (*Hamamatsu Photonics*, H 9656-20) (connected to ScanImage) or a CMOS camera (*IDS Imaging*, μ -eye SE) for bright-field imaging, while the sample is illuminated from above by a halogen or LED lamp. Here, an additional lens L_{I4} with a focal length of $f_{L_{I4}} = 120mm$ focuses the desired signals onto the camera chip or, when the mirror is flipped into the beam path, onto the PMT's detector area. In forward detection a condenser lens (*Olympus*, U-AAC, NA = 1.4) is used to collect the CRS signals in standard operation. It has a high transmission for CARS signal

wavelengths as well as for the pump beam. Therefore, it is supporting the SRS experiments with sufficient intensity of pump light on the SRS detection photodiode. After the condenser lens a multichannel imaging system is constructed through a telescope ($f_{I1} = 300mm$ and $f_{I2} = 180mm$) and the beam splitter BS2 (*AHF*, T750SPXRXT) in order to separate the pump beam signal for SRS imaging from CARS, SHG and fluorescence signals, which are blue-shifted. Here, two planes are introduced in the microscope separating the wavelengths also by two lightproof optical breadboards into two branches offering space for several detectors and optical elements (fig. 22). A PMT detector array composed of three PMTs placed in a cage system offers three simultaneous acquisition channels for CARS, SHG and fluorescence signals. It is possible to exchange the optical filters and beam splitters (BS3 and BS4) very rapidly according to the desired wavelength separation. Due to the use of an additional telescope after the condenser lens the detected signals are non-moving on the detector area granting an even illuminated image. In the second area the pump beam is detected with an additional lens L_{I3} ($f_{L_{I3}} = 50mm$) on a fast silicon photodiode in combination with an electronic filter set and a lock-in amplification scheme (see section 3.1.6). The fundamental Stokes beam is filtered out by a $950nm$ short-pass filter after the lens L_{I1} in order to avoid this wavelength in any detection area. In total the microscope has four forward detection channels (including the SRS channel) and one epi-detection channel, which can be utilized all simultaneously. The typical CARS wavelengths (in the case of the CH_2 resonance it is $\lambda_{CARS} = 660nm$) are filtered by two $775nm$ short pass filters (*AHF*, F75-775) to eliminate the excitation wavelengths and by a $514nm$ long pass filter (*Semrock*, Razor Edge LP02-514 RU-25) to suppress second harmonic signals. The remaining signal is focused onto customized fast PMTs (*Hamamatsu Photonics*, H 9656-20 and H 9656-20 MOD trans-impedance $20k\Omega$, having 0-5MHz bandwidth), which are connected to the A/D converter using the PMTs current-voltage-converter. The focal position of the excitation beams in the sample and the corresponding detected signal are combined by ScanImage to the final image. The Matlab-based software provides different scanning speeds and binning factors for the user as well as zooming into full field of view by a specified magnification ratio while selecting regions of interest in the sample.

Due to the arrangement of the focusing objective lens and the condenser lens in a 4π configuration it is necessary to move the condenser lens in xyz-direction with high precision without any mechanical instabilities especially when replacing the point detectors (PMT or photodiodes) with a camera (see also section 3.2). Therefore, a customized condenser lens xyz-mount proved to be necessary (fig. 22). It was constructed based on a $60mm$ cage system utilizing a modified xy-translation stage offering $\pm 1mm$ range

(Thorlabs, CXY2) in combination with a self developed z-translation stage composed of two pairs of linear bearings (Schneeberger, RN 3-075-DR-SQ) for high stability and minimal thermal drifts. Here, a range of 25mm was realized enabling easy replacement of the sample as well as the option to replace the condenser lens with an objective lens. A differential micrometer screw again offers high precision while setting the z-position.

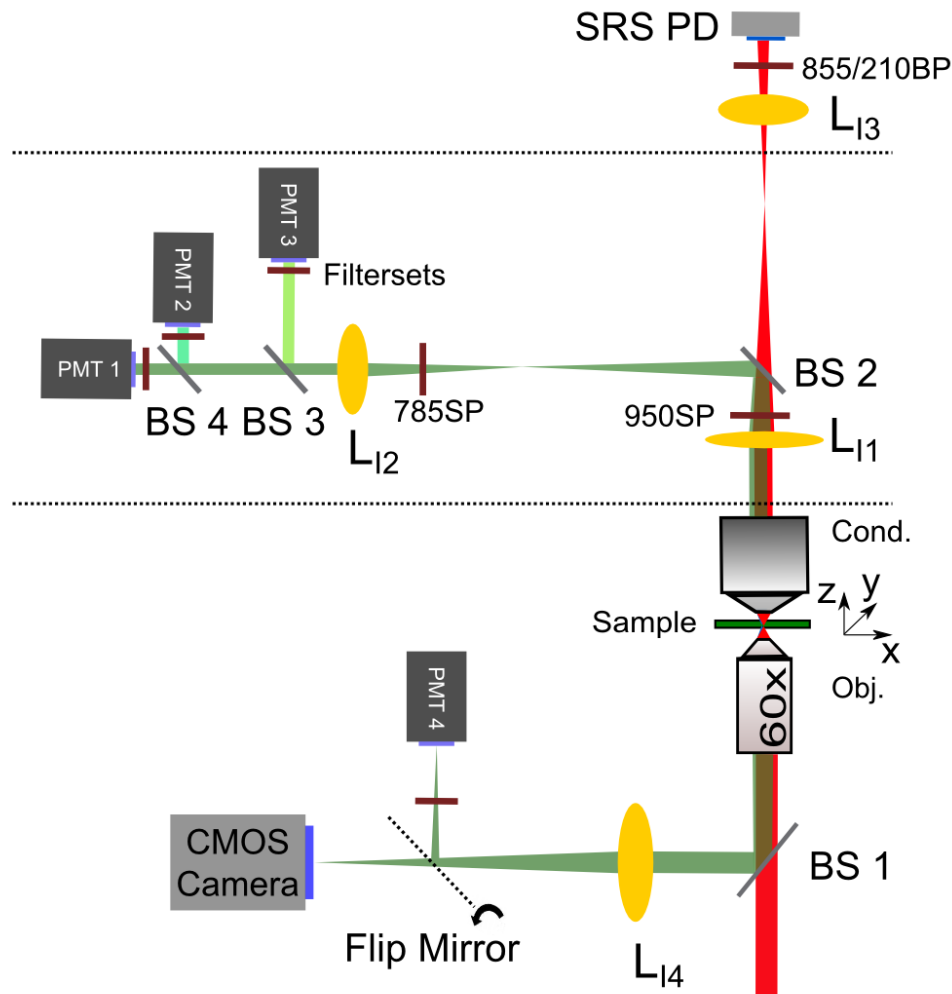


Figure 21 – Detection modes and optical path

The scanning microscope is set up in a 4π configuration of focusing objective lens (Obj.) and condenser lens (Cond.) for the analysis of the sample, which is placed in between on a motorized 3D-stage. In epi-detection a PMT for CARS or a CMOS camera for bright field imaging are set up. In forward detection two lightproof areas for SRS (upper area) and blue-shifted signals, e.g CARS, SHG or two-photon excited fluorescence are offering space for multiple detectors. In the CARS area an array of three PMTs are used to detect up to three different wavelengths at the same time. The photosensitive area of all detectors are illuminated using a diminutive telescope arrangement in order to avoid imaging artifacts due to vignetting effects during the scanning process. All optical signals can be split by beam splitters (*BS2* to *BS4*) and are finally filtered in front of the detectors by optical filter sets.

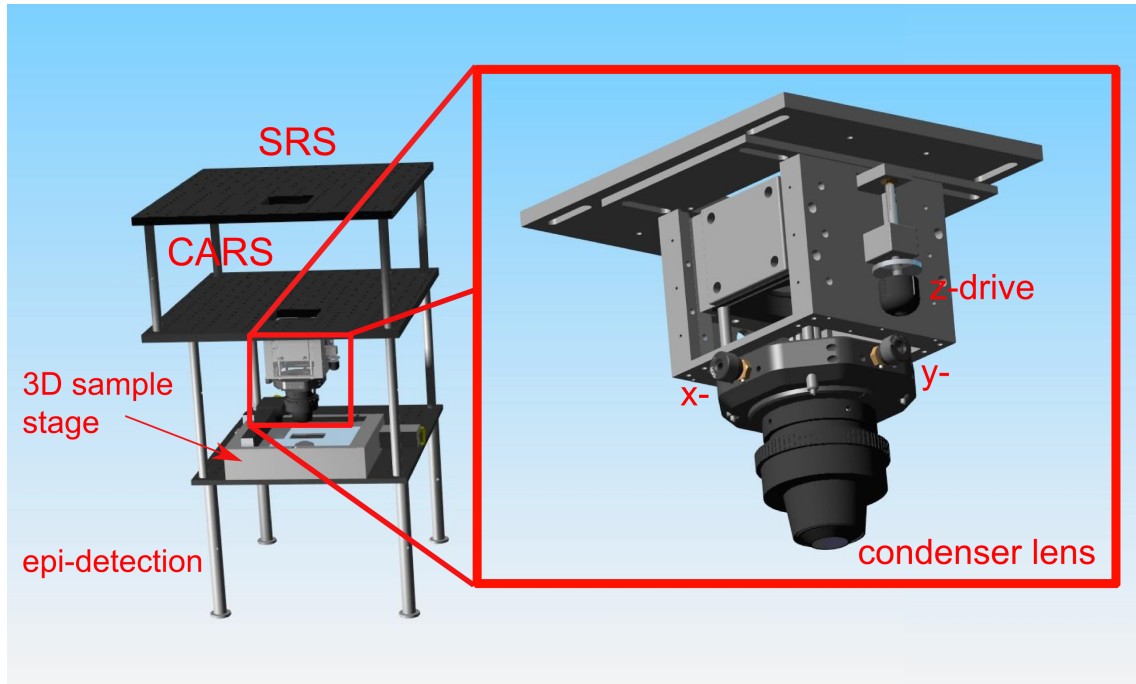


Figure 22 – CAM/CAD simulation of the microscope and the condenser lens mount

For a high flexibility of all desired detectors the microscope has three detection areas. One for epi-detection using the optical table and two forward areas constructed with optical breadboards offering space for CARS and SRS detectors. The focusing objective lens is mounted on a z-linear stage, the condenser lens is placed in a home-built XYZ-holder. It offers high stability and low tilt by using two pairs of linear bearings for the z-translation. The implemented 60mm cage system holds a modified xy-stage, which was optimized by setting in two bronze bushings. The condenser lens is screwed inside by an thread adapter, which offers additional freedom in terms of working distance of the installed collecting optics. The shown inner part of the microscope has an additional lightproof housing with several removable covers.

3.1.6. SRS modulation and detection scheme

In the case of SRS imaging the 1064nm Stokes beam is intensity modulated (in general with $5 - 20\text{MHz}$) by the AOM before it is focused into the sample (see 3.1.4). For the highest sensitivity of the setup the modulation imprinted on the Stokes beam has a fixed phase relation to the 80MHz repetition rate of the laser system and an approach to gain tunability of this phase between both frequencies is realized through a custom built frequency divider and phase shifter. The electronic seed signal of the laser system is amplified and fed into an array of home-made oscillators with phase delay loops consisting of Schmidt triggers and comparator circuits. Here, the frequency is divided to 20, 10 and 5MHz while achieving a tunability of phase from $0 - 2\pi$ regarding to the 80MHz repetition frequency. Then a commercial function generator (such as *Hameg*, HMF 2550 or *HP*, 8116A) is externally triggered by this signal (case of 5 and 10MHz) and then delivers the final frequency with an amplitude of $0 - 5\text{V}$ to the AOM driver

module. At 20MHz no additional frequency generator is needed, due to the included local sine generation in the phase shifter unit. In the interaction with the sample photons are transferred from the pump to the Stokes beam according to the current intensity of the Stokes beam (see 2.2.4). The rate of change in amplitude compared to the pump beam intensity ($\Delta I_{SRL}/I$) is in the range of $\ll 10^{-4}$, while the possible sensitivity achieved with current setups is 10^{-7} to 10^{-8} utilizing lock-in techniques (Freudiger et al. [2008]). The pump beam is transmitted to a large area photo diode (e.g. *Hamamatsu Photonics*, FDS 1010 or *Luna Optoelectronics*, PDB-C613-2) using a 950nm short pass filter (*AHF*, F37-950) to suppress the 1064nm beam and a 787nm long pass filter (*AHF*, F76-787/LP) (in case of probing the CH_2 resonance) to block out any remaining blue-shifted wavelength. The electronic signal of the photo diode is carefully filtered by a band-stop filter for the attenuation of the 80MHz native laser frequency as well as a π band-pass filter, all constructed of inductive and capacitive elements (see fig. 23). The desired signal is coupled into a lock-in amplifier (*APE*, S/N S04757 or *Zürich Instruments* HF2LI) to perform a demodulation of the SRS signal with the reference signal, which is the same as the initial modulation-frequency of the 1064nm beam, provided as a separate TTL trigger signal by the frequency generator. Tunable settings at the lock-in amplifier are the preamplification of the incoming signal, the integration time and the phase of the demodulator, which is set automatically in the case of a digital lock-in amplifier (e.g. *Zürich Instruments*, HF2LI). These parameters determine the final speed of the imaging and are strongly dependent on the signal strength. Finally, the demodulated signal is amplified with a variable gain factor selected by the user outputting it to the A/D converter, where it is transformed into an image by ScanImage. Due to the very low signal to noise level of the desired electronic SRS signal generated by the photodiode any additional noise coupling into the signal path, e.g. from other electronic equipment, has to be avoided by careful electromagnetic shielding. Also the proper connection of the earth ground to all hardware in a star-like manner (the starting point was set on the optical table) without ground loops and the separation into case ground and signal ground proved to be crucial to a successful SRS experimental result (see fig. 24).

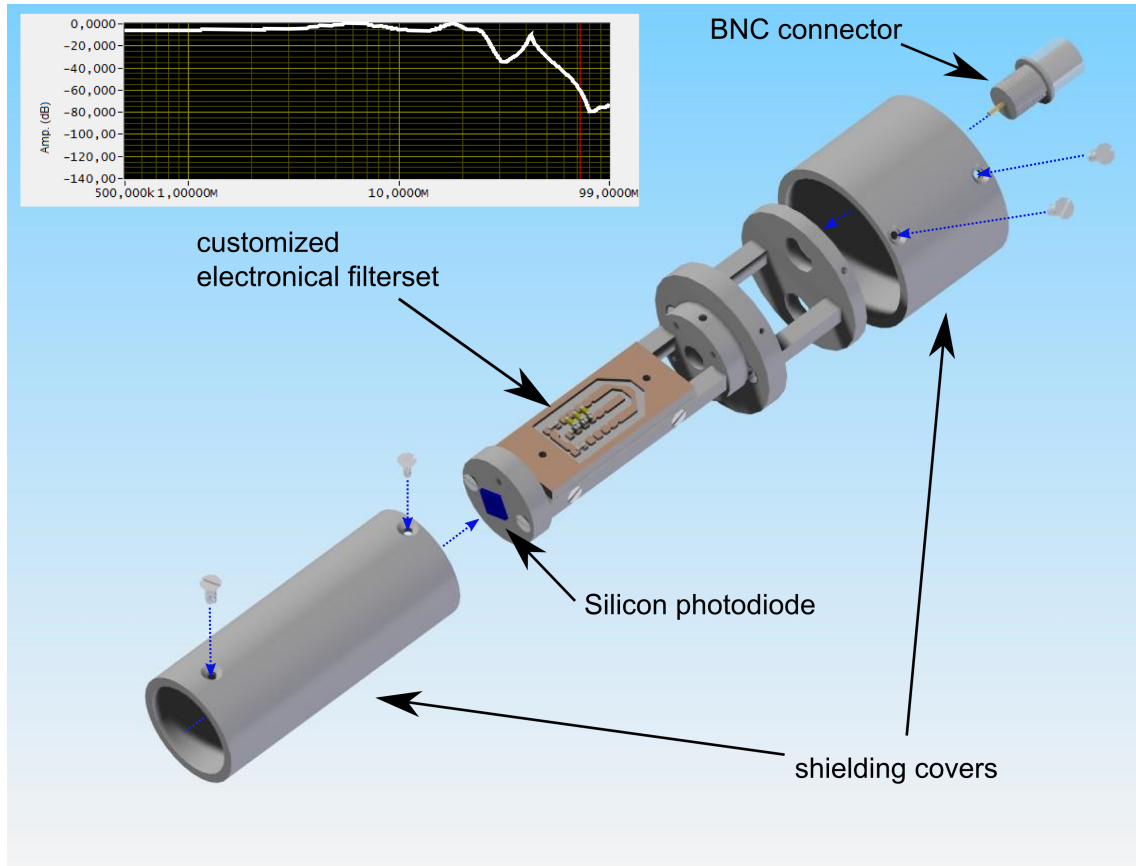


Figure 23 – Customized SI-photodiode for SRS imaging

In order to explore the optimization of the silicon photodiode detecting the pump beam for SRS imaging the shown housing was developed placing the electronic filters in close proximity to the photodiode (e.g. *Luna Optoelectronics*, PDB-C613-2). Here, the BIAS voltage delivered by a battery pack is low-pass filtered in order to avoid the flow of the signal into that branch as well as to cancel out noise collected from the connection cable (not shown). The desired modulated signal itself is passing a band-stop filter suppressing the 80MHz signal of the laser repetition rate as well as a $\sim 22\text{MHz}$ low-pass filter suppressing system noise as well as signal reflexions or higher harmonics. All characteristics were tested and fine-tuned using the frequency scanning mode of the digital lock-in amplifier (see inset). Here, the transmission of the filter was tested and optimized in order to transmit the desired signal with 20MHz with low losses as well as to suppress the laser repetition rate and any other noise. Case ground and signal ground are separated for avoiding ground loops due to the mounting. For connecting the photodiode module to the lock-in amplifier a low loss, special shielded cable was used (*SBB*, Aircell 7). The connection from the battery pack delivering the BIAS voltage is a shielded twisted pair cable (*LEMO*, AWG28/19).

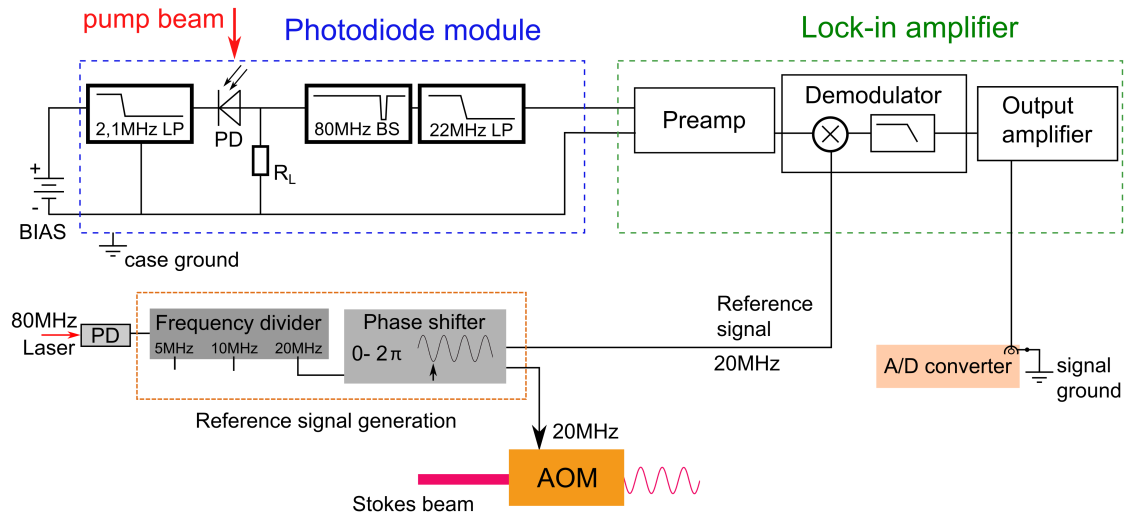


Figure 24 – Modulation and detection scheme of SRS imaging

The photodiode is provided by a low-pass filtered BIAS voltage enabling a fast rise time for the detection of the pump beam. The signal voltage is generated by the load resistor ($R_L = 50\Omega$) and then filtered by a band-stop filter and a low-pass filter, all inside the shielded photodiode module. After that the lock-in detector preamplifies the signal and demodulates it with the reference signal, which is also used for the amplitude modulation of the Stokes beam via the AOM. The imaginary as well as the real part of the demodulated signal are summed and amplified in order to be finally detected by the A/D converter card, which is operated by the imaging computer. The reference signal itself is created of the seed signal of the laser system, which has an $80MHz$ repetition rate. A frequency divider is utilized in combination with a phase shifting device to generate a phase shiftable $20MHz$ signal, which is addressed to the AOM as well as to the lock-in amplifier. Please note that the lock-in amplification scheme is simplified and thus valid for digital as well as analog systems. Also the pulsed laser characteristic is not included in the drawing.

3.2. Structured illumination for resolution enhancement

In the course of the thesis the application of structured illumination for the resolution enhancement in CARS microscopy (SI-CARS) was explored especially in the forward detection, whereas the first application of this idea was performed in the epi-detection as the task of the master's thesis [Pilger [2014]]. Here, it became apparent that the epi-direction offers too low CARS signal intensity for the detection via an sCMOS camera resulting in a beneficial resolution enhancement. Nevertheless, the application of structured illumination proved itself as a promising tool for the resolution enhancement beyond the diffraction limit. The appealing point is that in comparison to other possible approaches in a wide field arrangement the focal intensities of Stokes and pump beam are still high as well as in comparison to also focused approaches with beam profile shaping, a potential spatio-temporal mismatch of both beams is not occurring, granting the same high signal intensity as without the approach for resolution enhancement.

In addition to the SI-CARS experiments two-photon excited fluorescence is explored using the Stokes beam of the CRS-setup as excitation source. These fluorescent data sets, which are the result of incoherent image formation, were also generated to back up the prospect of resolution enhancement beyond the diffraction limit in coherent microscopy. For the implementation of SI-CARS a sCMOS camera (*Hamamatsu Photonics*, OrcaFlash4.0) was utilized as detector instead of the PMTs. It has a detector area of 2048×2048 pixels, while each pixel has the size of $6,5 \times 6,5 \mu\text{m}$. The camera's quantum efficiency is $\sim 70\%$ for the typical CARS signal wavelengths (e.g. 660nm probing the CH_2 resonance) [Hamamatsu Photonics [2012]]. For a low noise performance the sCMOS chip is cooled by a Peltier element in combination with an external water cooling system. Using optimal conditions⁹ the readout noise is $1,3\text{electrons}$,¹⁰ having a dark current of $0,15\text{electrons}/\text{pixel}$ [Hamamatsu Photonics [2012]]. In order to match the camera's optimal working condition in terms of signal intensity per pixel as well as the optimal magnification ratio of sample size to image size the detection optics for PMT had to be changed. In order to keep the effort low for switching between the standard PMT detection and the detection by the camera a flip mirror mount (*Radiant Dyes*, RD-KLS-1) was inserted in the optical path. It allows to address the camera without changing the entire beam path (see fig. 25). Only the first lens behind the collecting objective lens had to be replaced entirely (L_{I1} to L_{I5}). The condenser lens itself had to be replaced with an oil objective lens (*Olympus*, UPlanApoN $60\times$, NA 1,42), which has an infinity correction and, therefore, the better imaging performance compared to the condenser lens. The optical detection path for the camera had to be adapted as well. It is placed inside the CARS detection area of the microscope and consists of a telescope, comprised of two lenses with $f_{I5} = 180\text{mm}$ and $f_{I6} = 100\text{mm}$ (focal points set congruent, magnification of 0,56), which demagnifies the image first. Then a tube lens $f_{I7} = 300\text{mm}$ in front of the camera is forming the final image on the camera chip. In combination with the magnification ratio of the objective lens (theoretical focal length is 3mm) the total magnification ratio of these optics is 56, which leads to a imaging ratio of 116nm per pixel on the camera chip.

⁹Water cooling, water temperature of 20°C .

¹⁰Calculation: ratio of a full well capacity and the readout noise.

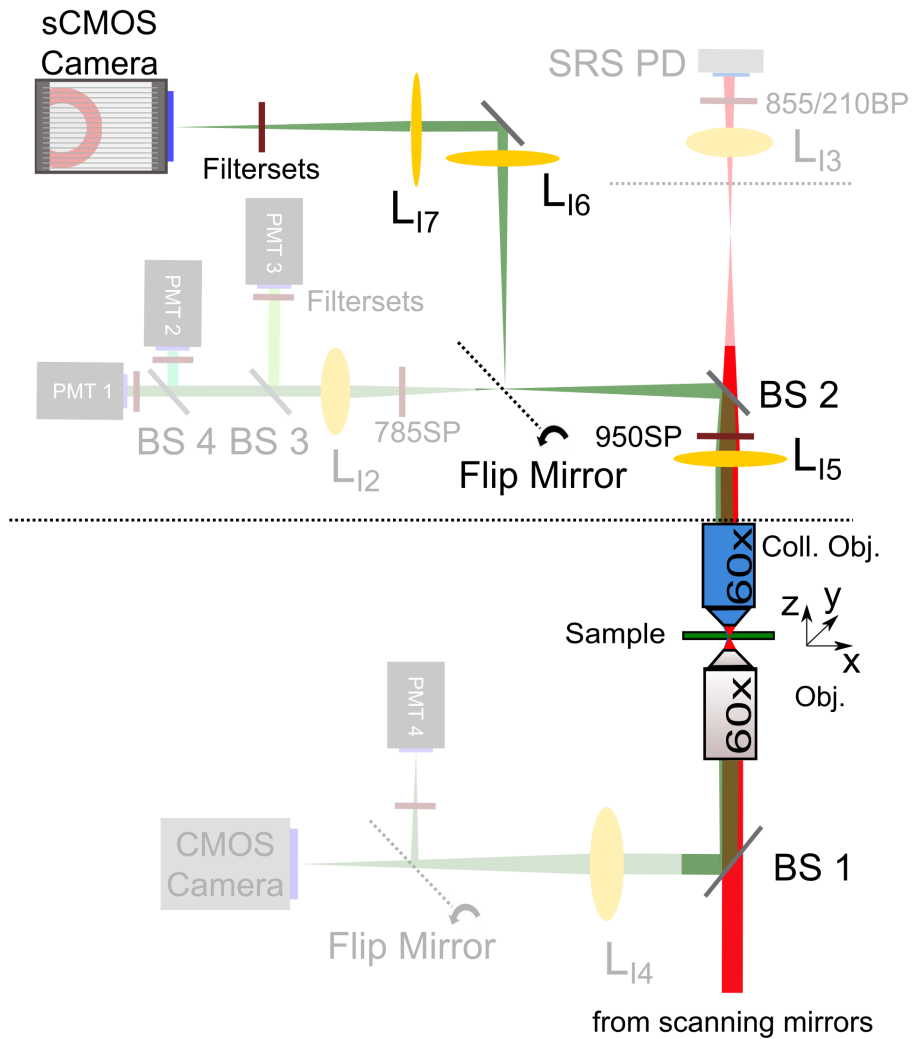


Figure 25 – Detection scheme for SI-CARS

For the structured illumination approach the condenser lens was changed to an oil immersion objective lens with high NA and 60 \times magnification. A new lens array comprised of L_{I5} , L_{I6} and L_{I7} is utilized to form the final image on the sCMOS camera with a pixel size of $116nm/px$. It is folded by three additional mirrors (not shown) in order to stay on the available space. A suitable filter set cancels out the pump and Stokes beam, while additional bandpass filters are set in to isolate the signal wavelength of interest. A flip mirror mount is implemented to enable rapid changes between PMT and camera detection, which is possible due to the large free space area built into the microscope. Due to the clear separation of all involved wavelengths and the sound lightproof housing of the detection area low noise due to undesired stray light was present on the camera.

3.2.1. Generation of a striped illumination pattern

In the standard operation of the microscope during e.g. a CARS experiment both pump and Stokes beam are raster-scanned over the sample generating a blue-shifted signal of the sample at every position. The technique to perform a striped illumination of the sample with galvanometric scanning mirrors is based on the rapid intensity switching of one of the beams (here in particular the Stokes beam) by an acousto- or electro-optical device according to the position of the focus in the sample. Due to the already used line per line scanning mode of the microscope the Stokes beam was blanked out by the AOM at certain times, generating a CARS signal only at every third scanned line. The fineness of the scanned pattern as well as the angle orientation were set by the scanning control program. The pump beam was present on the sample at every position but did not affect the experiments in any negative way. For the precise and reproducible synchronization of the position of the scanning mirrors and the modulation of the Stokes beam a trigger scheme was developed.

As the fundamental timing signal the “frame clock trigger” was exported as a 5V TTL signal provided by *ScanImage* via the second timer channel of the A/D converter card. This signal is sent to the external trigger input of the sCMOS camera after a conversion is performed by a fast level converter to a 3,3V LVCMOS trigger signal matching the camera’s hardware requirements.

For the synchronization of the Stokes beam modulation the 5V TTL trigger signal is fed into a four channel digital delay / pulse generator (*Stanford Research Systems, Inc.*, Mod. DG535), which is also used for the phase generation of the pattern. It provides four variable delay settings which are directed to the trigger input of a waveform generator (*Hameg* HMF 2550) by a external threefold toggle switch. A periodic rectangular waveform is generated by the waveform generator in the “burst” mode, while its timing is synchronized to the scanning process as well as its duration is matched to the chosen imaging parameters. Finally, the waveform is transferred to the Stokes beam intensity via the AOM (see fig. 26).

By switching the output channel of the delay generator a preset additional delay time is added to the starting point of the waveform generator. In additional measurements the delay times were determined leading to a response of the system, where three phases of the pattern were generated according to the selected channel of the delay generator. Summing up this scheme the waveform generator is triggered after the desired number of lines are scanned blocking the Stokes beam and then starts with the periodic waveform pattern releasing the Stokes beam onto the sample. For the calculation of the cycle duration of the waveform a multiple of the “true ms/line” value of the scanning program is used, which is the sum of the illumination time of one line and the moving

time of the scanning mirrors moving to the starting point of the next line. To specify the numbers of repetitions of one cycle of the waveform, the rate

$$\#cycles = \frac{\#lines/frame}{3} - 1 - \frac{1}{3} \quad (56)$$

was identified as proper value for the chosen pattern spacing. The first term refers to one period covering three lines. Due to undesired movement of the scanning mirrors at the end of the frame one cycle was subtracted as well as the first scanned line, which is the result of electronic run-times. The “rotate” setting (defined as angle of rotation ϑ_{rot}) of *ScanImage* allows the rotation of the pattern with $0, 1^\circ$ accuracy. In the final image series three angles as well as three phases per angle are utilized granting a resolution enhancement in the x- and y-direction of the field of view.

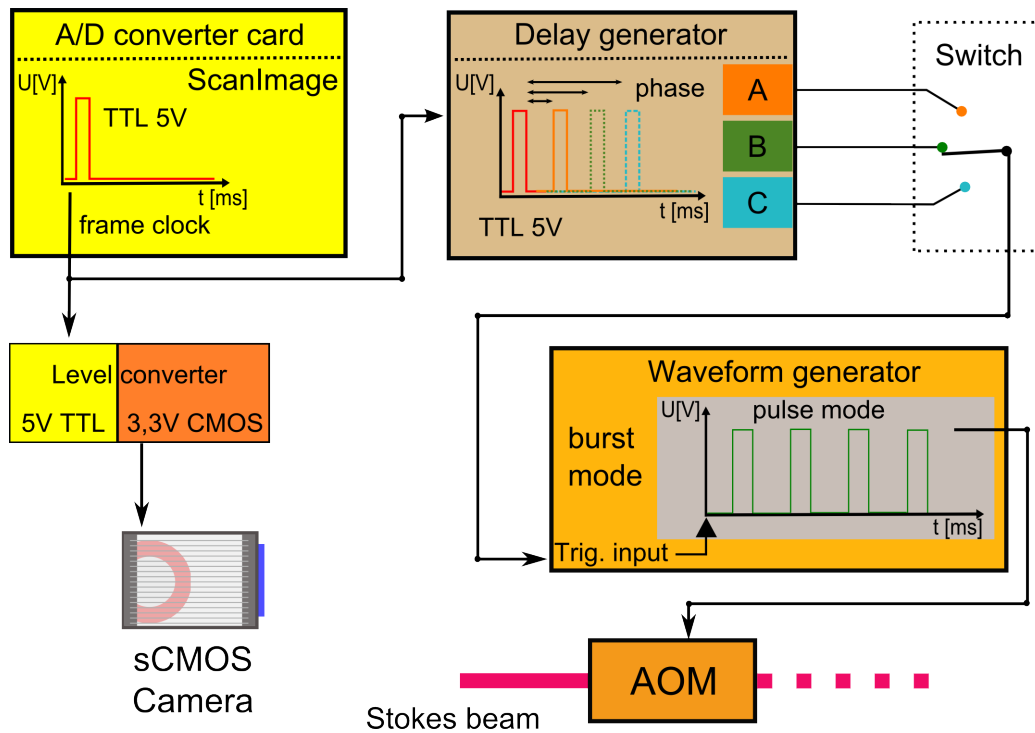


Figure 26 – Scheme of the camera trigger and striped pattern generation utilizing the AOM

The reference signal for the camera trigger as well as the AOM-based pattern generation is a 5V TTL signal provided by the A/D converter card, which is created after a frame in the imaging process is completed (left upper half). Before the camera’s external trigger is addressed a fast level converter transfers the 5V TTL signal to 3,3V CMOS logic matching the camera input (left side). The frame clock signal is also directed to a digital-delay-generator, which provides three timing delays of the original signal selectable by a switch. These are used for the phase setting of the illumination pattern by feeding them into the external trigger input of a waveform generator (right hand side up to low). The waveform generator creates a rectangular periodic waveform, whose starting point is synchronized to the position of the scanning mirror. By adding a delay the starting point is shifted to the next line of the scanning process, which should be illuminated. The periodicity as well as the duty cycles and amplitude of the waveform are set according to the chosen pattern fineness, scanning speed and desired illumination intensity set in *ScanImage*. Finally, the waveform is directed to the AOM driver module and operates the AOM rapidly blocking and unblocking the Stokes beam.

4. Results

In the following chapter the capabilities of the microscopy setup will be demonstrated by a range of selected applications on different biomedical questions, which were investigated with several collaborators who performed the preparation of the samples as well as subsidiary experiments in order to support the information provided by the CRS-experiments. Here, also hyperspectral CARS data will be shown and discussed. In the course of the thesis the influence of pulse length variations of the OPO while wavelengths tuning during hyperspectral data acquisition was investigated and a customized Matlab-based control software was developed and implemented into the scanning software, which grants undistorted spectra. Following, the results of structured illumination applied on CARS microscopy for resolution improvement are presented and compared to data of two-photon excited fluorescence. Finally, a novel all fiber based CRS laser source is introduced, which was developed in close collaboration with the research group of Prof. Kenneth K. Y. Wong at the University of Hong Kong. The source will be characterized and data on several biological specimen with CARS as well as SRS and multiphoton applications such as SHG and two-photon excited fluorescence as contrast mechanism are provided.

4.1. Investigation of osteogenic differentiation in human stem cells

4.1.1. Exploring label-free CARS microscopy as suitable tool for visualizing the successful differentiation of ITSCs in clinical research

This collaborative work was performed jointly with the research group of Prof. Christian Kaltschmidt and Prof. Barbara Kaltschmidt, faculty of biology, Bielefeld University, in the course of the bachelor thesis of Mr. Arne Hofemeier [Hofemeier [2014]]. For the cure of injured bone structures in human patients, e.g. after an accident, the use of stem cells is a new promising treatment [Meza-Zepeda et al. [2008]], which delivers new bone material to the damaged structure enabling faster recovery and minimally invasive cure [Greiner, Johannes F. W. et al. [2014], Hauser et al. [2012], Greiner et al. [2011], Seebach et al. [2010]]. In this study the osteogenic differentiation of human neural crest-derived inferior turbinate stem cells (ITSCs) was investigated with CARS and SHG microscopy [Hofemeier et al. [2016]], while spontaneous Raman scattering was utilized for supporting the CARS data as well as Alizarin Red-Staining for fluorescent light microscopy in combination with rt-PCR (reverse transcription polymerase chain reaction) in order to confirm the results. Here, the ability of CARS and SHG microscopy as label-free and, therefore, non-contaminating tool was compared to clas-

sical methods of detection such as fluorescent labeling. There is high interest for a confirmation of the successful differentiation of the stem cells without a contamination or destruction of the specimen by the analysis method, because the very same sample could be used in the therapeutic treatment of the human patient assuring the desired effect of the stem cells.

4.1.2. Design of the experiments: CARS and SHG imaging of ITSCs and control group

The ITSCs are routinely isolated during minimally-invasive surgery and were expanded in vitro. The differentiation process resulting in the production of bone material was induced by applying a chemically-defined directed differentiation medium (containing dexamethasone, β -glycerophosphate and phosphate) or topological cues of a nanoporous titanium surface on the cells. The specimen were handled in custom-built 1-fold and 4-fold dwell holders, which enabled a sealed condition of the specimen as well as the use of quartz cover slides for spontaneous Raman spectroscopy. Here, different time points were selected for analysis and the cells of a dwell were fixed with a para-formaldehyde (PFA) solution for that specific day. The starting point of the experiments was defined as “Day 0”, while four dwells were initially triggered for the differentiation with medium containing differentiation supplements. Additional four dwells called “FCS control” were kept as a control system, which were treated with standard fetal calf serum (*Sigma Aldrich*, FCS) in the course of the experiment. The selected time points for analysis were chosen to be 0, 7, 14 and 21 days of differentiation. First bright-field microscopy images were acquired for each sample on a separate spontaneous micro Raman spectroscopy setup [Oberländer [2016]]¹¹ and interesting structures were selected. Areas where biomineralization takes place can be identified due to the star-like shape of the surrounding cells, which express the calcium hydroxyapatite in combination with collagen. At these points spontaneous Raman spectra were acquired for the comparison to the following CARS and SHG imaging, while an Alizarin Red staining was performed in the end on the same sample dwell. For CARS and SHG imaging in total three different channels were acquired sequentially to collect information of the specimen utilizing the 60 \times water objective lens focusing into the sample with a total focal power of less than 30mW for CARS. The generated signals were collected by a 40 \times air objective lens (Olympus, LUMPlanFLN, NA = 0.8), while all different signal contributions were isolated with narrow-band optical filter sets (950SP, 775SP, 785SP, 514LP for all channels in common) in order to solely detect

¹¹Setup made by Dr. Elina Oberländer in the scope of her PhD-thesis, data acquisition by Mrs. Lena Nolte during her master thesis.

the desired wavelengths. The CH_2 stretching resonance at 2845cm^{-1} is predominantly connected to lipids and was probed by the 1064nm Stokes beam and a $816,7\text{nm}$ pump beam. This channel is utilized for the visualization of the ITSC cell structure, while low signal levels were assigned to the confluent cell layer and the unspecific non-resonant background, thus shown via thresholding in a separate color (see fig. 27, deep red). Higher signal levels originating from lipid accumulations, such as lipid droplets, are shown in cyan. This CARS signal occurring at 660nm was additionally filtered by a $660/40$ band-pass filter. In addition to that the PO_4^{3-} symmetric stretching mode at 959cm^{-1} was probed for the identification of calcium hydroxyapatite depositions (magenta). Here, both OPOs were utilized as laser sources directing 796nm as pump and $860,6\text{nm}$ as Stokes beam into the sample while isolating the CARS signal at $740,4\text{nm}$ by a tunable band-pass filter at $740/20\text{nm}$. In the last step SHG imaging (green) was performed with the 1064nm laser beam generating the frequency doubled signal at 532nm of the collagen secretion by applying 25mW focal power. This procedure was repeated also on the control samples in order to prove that the response of the ITSCs is depending solely on the differentiation medium (fig. 28). For backing up the claim of successfully imaging the calcium hydroxyapatite deposits via CARS an additional control experiment was performed on a human skull bone of the mastoid cortex (see fig. 29). In order to prove the applicability of SHG microscopy detecting collagen a second additional experiment was performed on a mouse tail specimen (fig. 30), which is an established sample of oriented collagen fibers. Due to the infrared wavelengths regime and rather long pulse length in the picosecond regime of the 1064nm laser source no disturbing two-photon excited autofluorescence signal was detected. For the comparison of all different signal channels the data were normalized with respect to the intensities used as excitation laser beams, signal integration time and PMT amplification factor. The images with highest contrast (day 21) was normalized to a value of 1000 and serves as overall reference for all channels and days. In addition to that small pixel shifts due to the subsequent imaging of the channels were corrected by pixel-wise manual shifting until the non-resonant signal contents present in all channels were matched via a custom-written Matlab program, which determines the best correlation between the images.

4.1.3. CARS and SHG data are compared to spontaneous Raman spectra and Alizarin Red staining

Comparing the results of spontaneous Raman spectroscopy as well as images by Alizarin Red staining to the CARS and SHG imaging, we find a Raman peak of the calcium hydroxyapatite after 14 and 21 days of differentiation (fig. 31), while no distinct spectra were present in the control cell samples. This is in compliance with the data acquired via the fluorescent staining, here characteristic calcium deposits could be identified on days 14 and 21 (fig. 32). CARS and SHG imaging were in good accordance with the prior results. Here, after 14 days of differentiation calcium hydroxyapatite deposits were identified probing the 959cm^{-1} resonance co-localized with SHG signal indicating the presence of collagen type I. At day 21 the clear increase of both signals were detected, while in an additional 3D scan of the sample at day 21 (fig. 33) also the volumetric structure of the calcium hydroxyapatite deposits and collagen was investigated. For this purpose a z-scan at 26 different positions was performed via the piezo stage using a $1\mu\text{m}$ step size, while at each z-position all three different CARS and SHG channels were acquired consecutively. The mineral deposits were observed to be localized external and superior to the cell layer surrounded by a collagen matrix formed of the collagen secretion of the ITSCs.

4.1.4. CARS and SHG imaging leads to successful visualization of the ITSCs differentiation also applicable to clinical research

In conclusion of this work the label-free and non-invasive CARS and SHG imaging modality is a notable alternative to the established methods of fluorescent staining in order to detect the successful differentiation of the ITSCs showing the similar sensitivity as the destructive counterparts while adding beneficial structural information of the sample by providing imaging data in three dimensions. Future clinical application is also in reach taking new endoscopic approaches into account [Lukic et al. [2017], Lombardini et al. [2018]], which could possibly enable investigations even in vivo. Therefore, the presented results indicate that the diagnosis of ossification-related diseases investigating bone mineralization density distributions of patients can be performed without the need of biopsies in the future.

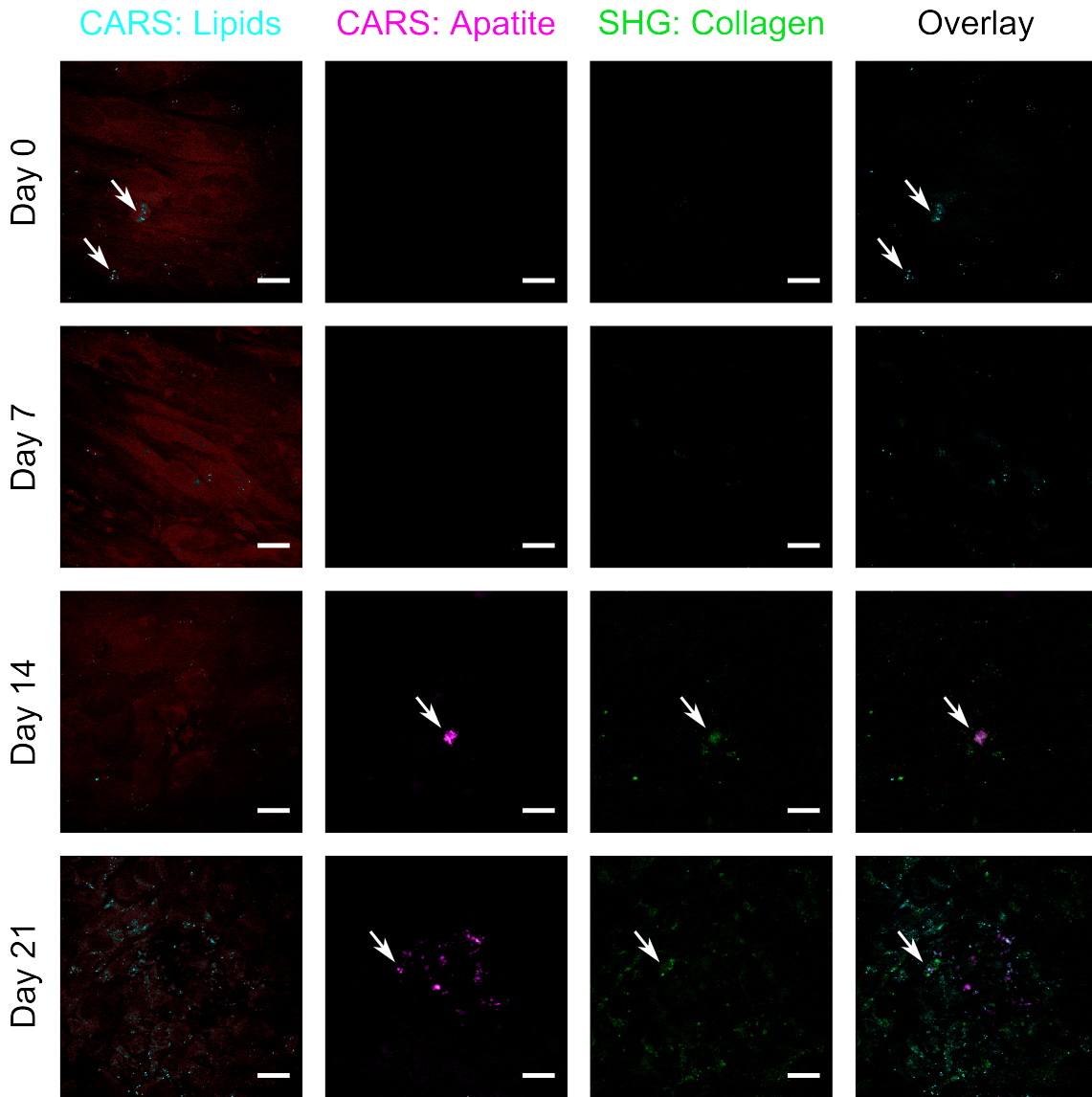


Figure 27 – CARS and SHG imaging of the ITSCs showing the osteogenic differentiation. After the induced osteogenic differentiation process of the ITSCs at day 0 only the presence of the ITSCs is visible while probing the 2845cm^{-1} CH_2 stretching resonance for the visualization of the cellular borders (red) and lipid droplets (cyan) inside the cells via thresholding. Also after 7 days of differentiation no signals were recorded probing the PO_4^{3-} stretching mode at 959cm^{-1} for calcium hydroxyapatite depositions (magenta) and SHG signals (green) indicating the presence of collagen type I secretions. At day 14 calcium hydroxyapatite depositions and also co-localized collagen secretions (arrows) were recorded, while at day 21 the signals increased in both channels and show the ongoing differentiation process with a higher amount of the depositions outside the cells compared to day 14. On the right hand side all channels are overlapped, showing the position of cells and secretions. The scale bar indicates $20\mu\text{m}$. Published in [Hofemeier et al. [2016]].

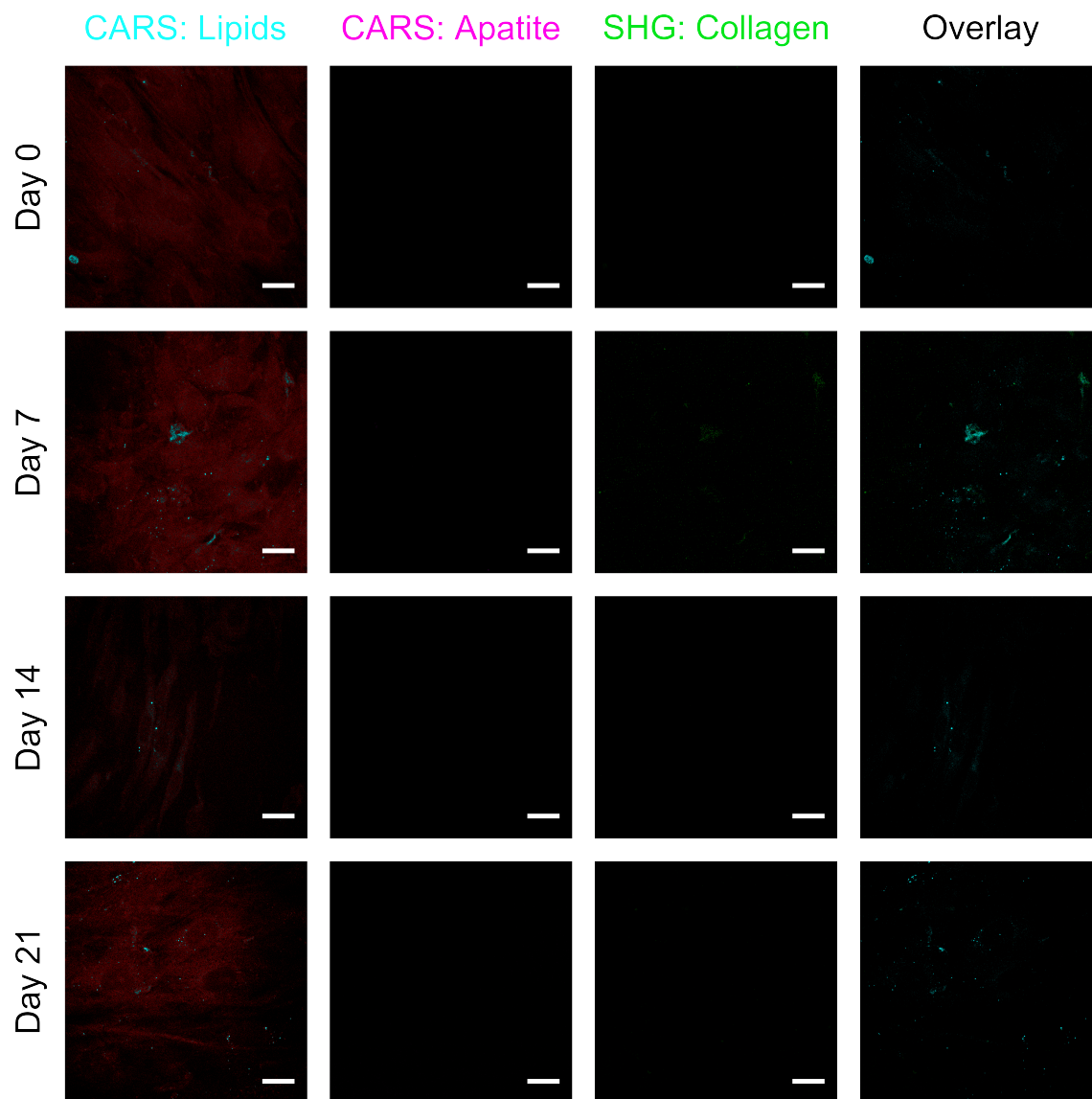


Figure 28 – CARS and SHG imaging of the ITSCs under control conditions showing no deposition of calcium hydroxyapatite or collagen fibers

The control samples, which were treated with standard fetal calf serum (*Sigma Aldrich*, FCS) instead of medium containing differentiation supplements, can also be observed via CARS probing the CH_2 resonance (red and cyan). In contrast to the triggered cells they show no signs of calcium hydroxyapatite depositions probing the PO_4^{3-} mode via CARS (magenta) and no traces of collagen due to the absence of any SHG signals (green) during the ongoing experiment. The scale bar indicates 20 μ m. Published in [Hofemeier et al. [2016]].

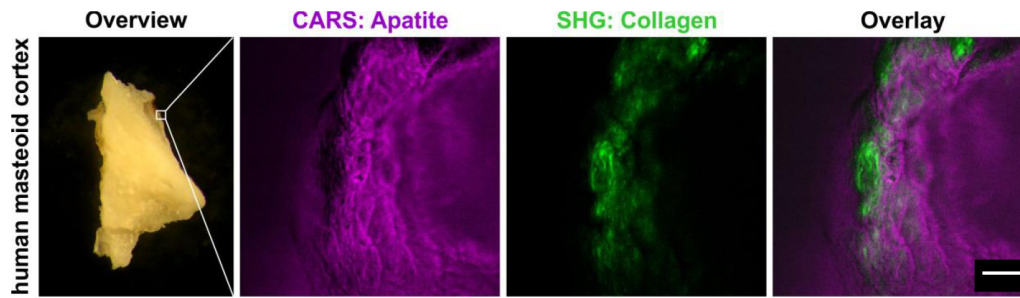


Figure 29 – Applying CARS and SHG imaging on a human skull bone for the visualization of calcium hydroxyapatite and collagen fibers

A piece of human mastoid cortex was imaged for investigating, if CARS microscopy can be utilized to show the calcium hydroxyapatite probing the 959cm^{-1} resonance (magenta) applying 20mW focal power for the $860,6\text{nm}$ pump and 6mW focal power for the Stokes beam, respectively. The SHG signal (green) is utilized for identifying collagen in the bone structure by detecting the frequency doubled signal of the 1064nm laser beam (42mW focal power were applied). By overlaying both channels we see the combined structure of the bone material, collagen structures fit into the frame formed by the calcium apatite. The imaged area of the specimen was an edge of the bone touching the cover slide. The scale bar indicates $25\mu\text{m}$. Published in [Hofemeier et al. [2016]].

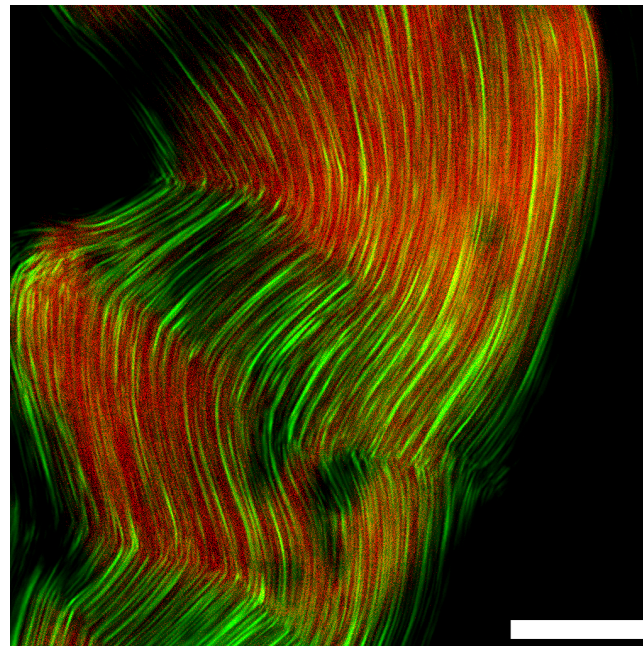


Figure 30 – SHG imaging of a mouse tail fiber sample showing the presence of collagen

For the visualization of the mouse tail fiber the CARS signal at 1662cm^{-1} (red) was probed in addition to the SHG signal (green) at 532nm utilizing 50mW focal power of the 1064nm laser beam, which shows the collagen with a typical fibrillar structure. The CARS signal is rather unspecific compared to the SHG signal. Note that for this CARS measurement two 842SP filters were replacing the 775SP and 785SP filters. The scale bar indicates $30\mu\text{m}$. Published in [Hofemeier et al. [2016]].

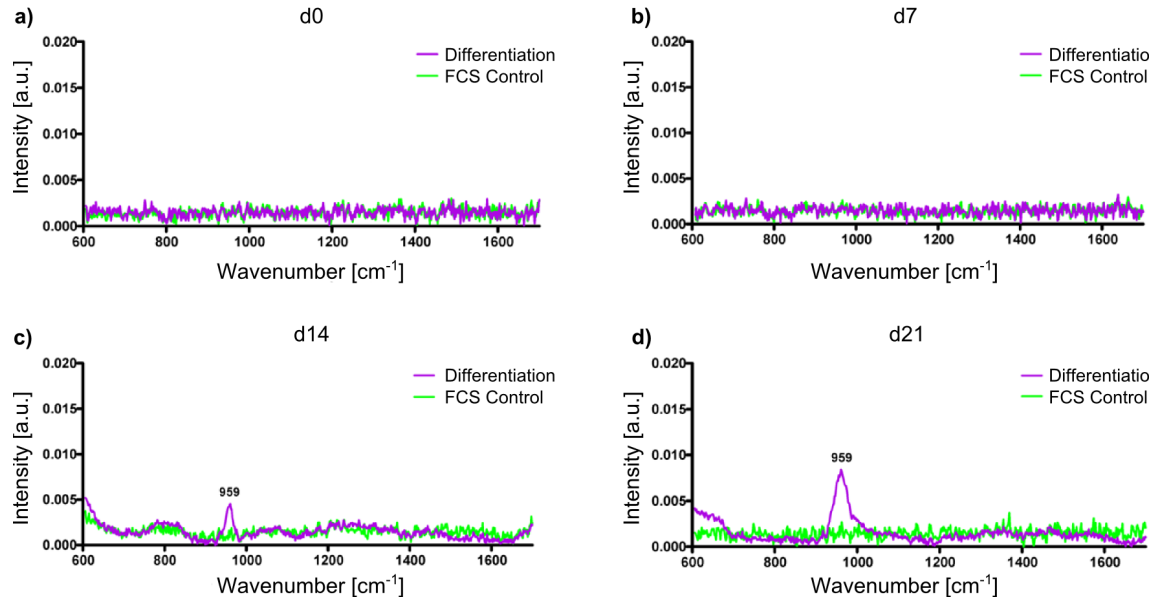


Figure 31 – Spontaneous Raman spectra of the ITSCs during the differentiation process. The differentiated as well as the control cells were imaged via bright-field microscopy on the spontaneous Raman spectroscopy setup identifying potential areas of calcium hydroxyapatite secretions. This was possible due to the characteristic star-shaped arrangement of the cells to each other at areas of deposits. In the center of the arrangement often the secretion can be found, here the spontaneous Raman spectra were acquired. **a)** shows the comparison of differentiated (purple) and FCS control (green) ITSCs at day 0, where no distinct peaks could be observed. The same behavior was found in **b)** at day 7. At day 14 (**c**) a peak at 959cm^{-1} corresponding to the PO_4^{3-} stretching mode was found in the differentiated cell sample, while no distinct spectra could be recorded for the FCS control sample. This result was detected with increased intensity of the 959cm^{-1} peak at day 21 (**d**), while again the control sample showed no traces of peaks at all. The Raman spectra were acquired using 785nm continuous wave laser light not exceeding 25mW of focal power utilizing a $60\times$ water objective lens. Adapted from [Hofemeier et al. [2016]].

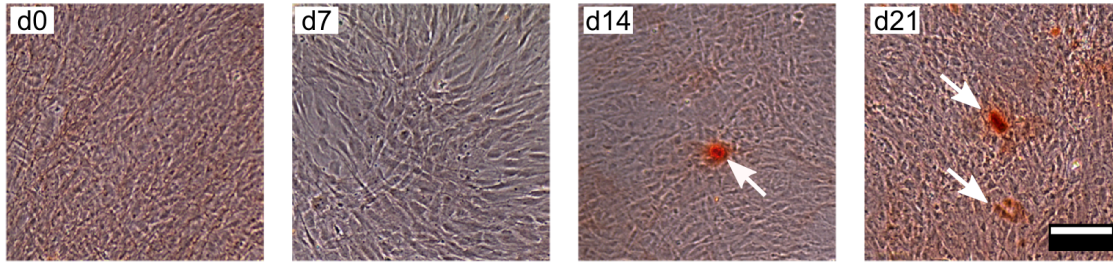


Figure 32 – Fluorescence imaging of ITSCs utilizing Alizarin Red staining

In the final step a fixation by a 4% PFA solution was performed on all samples. Then the Alizarin Red staining was applied to the samples using 1% of Alizarin Red (*Waldeck*) in ddH_2O in order to stain specifically the calcium hydroxyapatite. The samples were imaged with a combined fluorescence and bright-field microscope (*PeqLab*, AMG EVOS xl microscope). The above shown images are the combination of both imaging modalities, here showing the differentiated ITSCs from day 0 to day 21. Similar to the results of spontaneous Raman spectroscopy as well as CARS and SHG at day 14 first signals of the Alizarin Red staining are observed (white arrow) indicating the presence of calcium hydroxyapatite. At day 21 a higher signal strength in the fluorescence channel was recorded originating from larger calcium hydroxyapatite secretions. The FCS control samples exhibit no fluorescent signals (data not shown), which is in good accordance to the results of all applied techniques. The scale bar shows $100\mu m$. Adapted from [Hofemeier et al. [2016]].

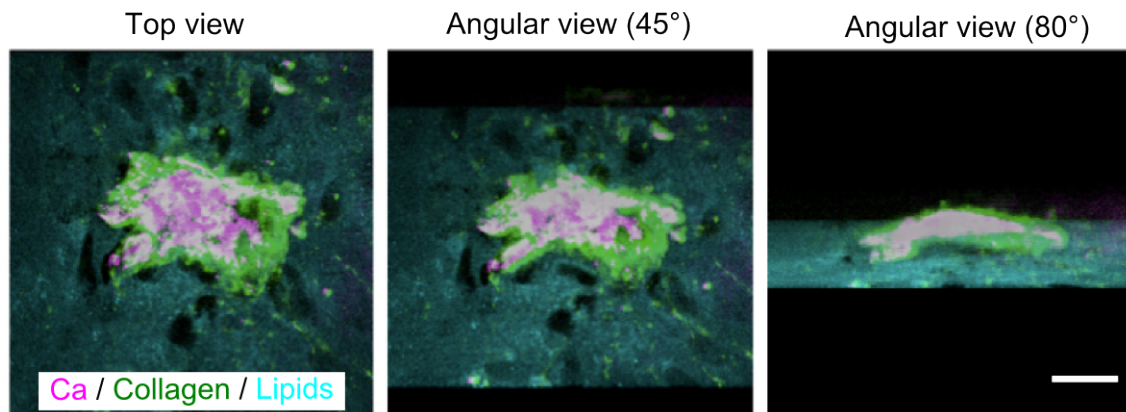


Figure 33 – 3D imaging of ITSCs after 21 days of differentiation

In a 3D scan performed on the ITSC sample after 21 days of differentiation a large crystal of calcium hydroxyapatite surrounded by the collagen matrix was imaged using a step size of the piezo stage of $1\mu m$ covering $26\mu m$ in z-direction. Each channel (lipids: cyan, calcium apatite: magenta, collagen: green) was recorded sequentially and then the z-position was altered. The imaging software *FIJI* was used for the visualization of the data, enabling different angular views. We observe that the mineral deposits are localized externally above the cell layer and are surrounded by the collagen matrix. This sample was stained with Alizarin Red when the large crystal was observed. Hence, a portion of the SHG signal can also arise from the staining, but the localization of both CARS and SHG channels are in good agreement. The scale bar depicts $25\mu m$. Published in [Hofemeier et al. [2016]].

4.2. In vivo analysis of intracellular lipid droplets in *Monoraphidium neglectum*

4.2.1. Identification and characterization of lipid rich microalgae as non-food feedstock in bio-diesel production

Facing the worldwide need for energy in respect to the turning away from fossil fuels raises an increased interest in ways to produce renewable energy sources. In the background of the worldwide climate change caused by the human induced emission of global warming gases using bio-material for the power generation in bio-gas plants or the biomass to fuel conversion holds great potential for a positive influence on the carbon footprint [Rupprecht [2009], Medipally et al. [2015]]. On the other hand the direct use of food-related bio-material or the indirect extrusion of acreage is raising new problems in the worldwide nutrition while the world population is increasing [Schenk et al. [2008]]. Hence, a non-food feedstock as a sustainable source for bio-material generated on non-agrarian used areas of the world are of high interest facing the future production of regenerative energy via biomass conversion. In this field one promising candidate meeting these requirements is the harvesting of oleaginous photosynthetic microalgae [Sheehan et al. [1998]], which can be grown in oceanic tanks where they produce lipids by the conversion of nutrients in the course of the photosynthesis [Mata et al. [2010]]. The final algal lipid yield and fatty acid content of the algae at the time of harvesting are important characteristics for the choice of the best type of microalga, which influence the economic feasibility in the production of e.g. bio-diesel utilizing the lipid content [Hu et al. [2008]]. Here, especially the ratio of neutral lipids such as triacylglycerols (TAGs), which are the main components of lipid droplets (LDs) in the cell, versus polar lipids such as membrane glycerolipids, mainly located in the cellular membrane, are a key characteristic of the successful application of microalgae in the fuel production. The TAGs are the desired form of lipids for the generation of bio-diesel and can be most easily extracted in the subsequent processing from the algae when they are accumulated in LDs.

4.2.2. Established methods for analyzing the lipid content of microalgae are laborious and partly not feasible due to rigid cell walls

The formation of the lipid droplets is dependent on the different environmental conditions of the microalgae, which affect their metabolism [Bogen et al. [2013a]]. Here, a common method to trigger the formation of LDs in microalgae is an increased illumination intensity as well as nitrogen starvation conditions. The TAGs content is routinely quantified by solvent extraction in combination with fractionation and gravi-

metrical analysis. Also HPLC (high performance liquid chromatography) or GC-MS (gas chromatography - mass spectrometry) are established tools for the quantification of the fatty acid composition of the algal lipids, but require a not negligible amount of biomass in combination with extensive work protocols and high time consumption. Faster alternatives are specific fluorescent staining, e.g. Nile Red, labeling the lipids of interest for fluorescent detection in combination with flow cytometry or fluorescent activated cell sorting. However, the major drawback of this approach are massive obstacles in the successful staining of the intracellular lipids due to the rigid cell wall of many microalgal species, which act as an impenetrable barrier for the fluorescent dyes.

4.2.3. Raman-based techniques speed up the analysis process of *M. neglectum*

Label-free alternatives such as Raman micro-spectroscopy can be utilized for the investigation of the relative degree of saturation of the lipid content. For imaging purposes CRS-microscopy is a powerful alternative to the established methods, especially when fluorescent staining is not working. Recently a proof-of-principle study using CARS microscopy was conducted on the microalga *Coccomyxa subellipsoidea* C169 [He et al. [2012]], where the CARS signal of interest had a significant overlap with the two-photon excited fluorescence of the chlorophyll hindering the analysis of the recorded data. In the diatom *Phaeodactylum tricornutum* the undesired two-photon excited fluorescence was separated from the CARS signal via time gated detection [Cavonius et al. [2015]], due to the fact that the fluorescence signal is delayed a few nanoseconds compared to the instantaneous Raman and CARS signals.

In the following collaboratively obtained results with the research group of Prof. Dr. Olaf Kruse (Bielefeld University) are presented [Jaeger et al. [2016]] concerning the analysis of the intracellular lipid droplets in the oleaginous microalga *Monoraphidium neglectum* utilizing CARS microscopy, also as a part of the PhD-thesis of Dr. D. Jäger [Jaeger [2017]]. In prior work the microalga *M. neglectum* was identified as a promising candidate for bio-fuel production but also in having a rigid cell wall, excluding fluorescent staining [Bogen et al. [2013b]]. Therefore, the label-free CARS microscopy was the selected solution circumventing the obstacles of fluorescence-based microscopy or laborious and time consuming studies via gravimetical analysis. For further quantitative determination of the degree of saturation spontaneous Raman microscopy [Oberländer [2016]]¹² was utilized on selected lipid droplets inside the algae.

¹²Work of Dr. Elina Oberlander during her PhD-thesis.

4.2.4. Design of experiments: modulation approach excludes two-photon excited fluorescence enabling CARS imaging of lipid droplets

The study evaluates the potential of CARS microscopy for imaging the LD formation in *M. neglectum* under nitrogen starvation conditions, while probing the CH_2 stretching mode at 2845cm^{-1} using $11,5\text{mW}$ focal power of the 1064nm beam as Stokes and $23,5\text{mW}$ focal power of the $816,7\text{nm}$ wavelength as pump beam. The feedstock of cells selected for the experiments were held under nutrient replete conditions and at the start of the study they were diluted to a low cell density ($\sim 4 \cdot 10^6 \frac{\text{cells}}{\text{ml}}$) and divided into three reservoirs to generate three different replicates. In a first step a strong two-photon excited autofluorescence signal, which was also present in the CARS signal occurring at 660nm , was detected over a large range of wavelengths. In order to suppress this undesired fluorescent background contribution originating from chlorophyll inside the chloroplast of the alga, the following filter set was applied: 950SP , 775SP (two times), 785SP for the suppression of the pump and Stokes laser wavelengths as well as a 514LP , $660/40\text{BP}$ and a tunable band-pass filter (*Semrock*, $TBP697/13$, $\sim 13\text{nm}$ transmission range) set to 660nm transmission for the isolation of the CARS signal. Still, the fluorescence signal was present in the CARS images, while the main source for the fluorescence excitation wavelength was identified to be the shorter, higher energetic pump wavelength at $816,7\text{nm}$ (see fig. 34 a) Stokes and b) pump beam). Due to the rather low background signal originating from the Stokes beam an intensity modulation scheme was utilized in order to divide the signals of the CARS channel into the modulated CARS signal contribution and the static fluorescence signal via lock-in demodulation (similar to [Garbacik et al. [2013]]). For this purpose the Stokes beam was intensity modulated with a frequency generator (*HAMEG*) and the AOM at 3MHz using the specifically modified high speed PMT (*Hamamatsu*, H 9656-20MOD transimpedance $20\text{k}\Omega$, $0 - 5\text{MHz}$ bandwidth¹³) for the CARS signal detection. Thus the fluorescence background was mostly eliminated from the CARS channel (fig. 34 b, d) by the demodulation using the lock-in detector (*Zurich Instruments*, HF2LI), which served as narrow band electronic filter at 3MHz using an integration time constant of $20\mu\text{s}$. The signal strength was sufficient for a typical pixel dwell time of $31,25\mu\text{s}$ recording a CARS image (see fig. 34 f). Nevertheless, an additional image with solely the Stokes beam present in the sample was acquired sequentially and subtracted from the corresponding CARS image for excluding any fluorescence contribution originating from the Stokes beam for the quantitative analysis. In order to turn the undesired fluorescence signal into an advantage a second fluorescence channel was set up utilizing

¹³The measuring resistor is changed by the manufacturer to $20\text{k}\Omega$ instead of $1\text{M}\Omega$ sacrificing sensitivity while gaining a higher bandwidth.

an $600nm$ long-pass filter (*Semrock*) in front of the band-pass and long-pass filter sets, which was detecting the chloroplasts distribution via a second PMT (see fig. 35).

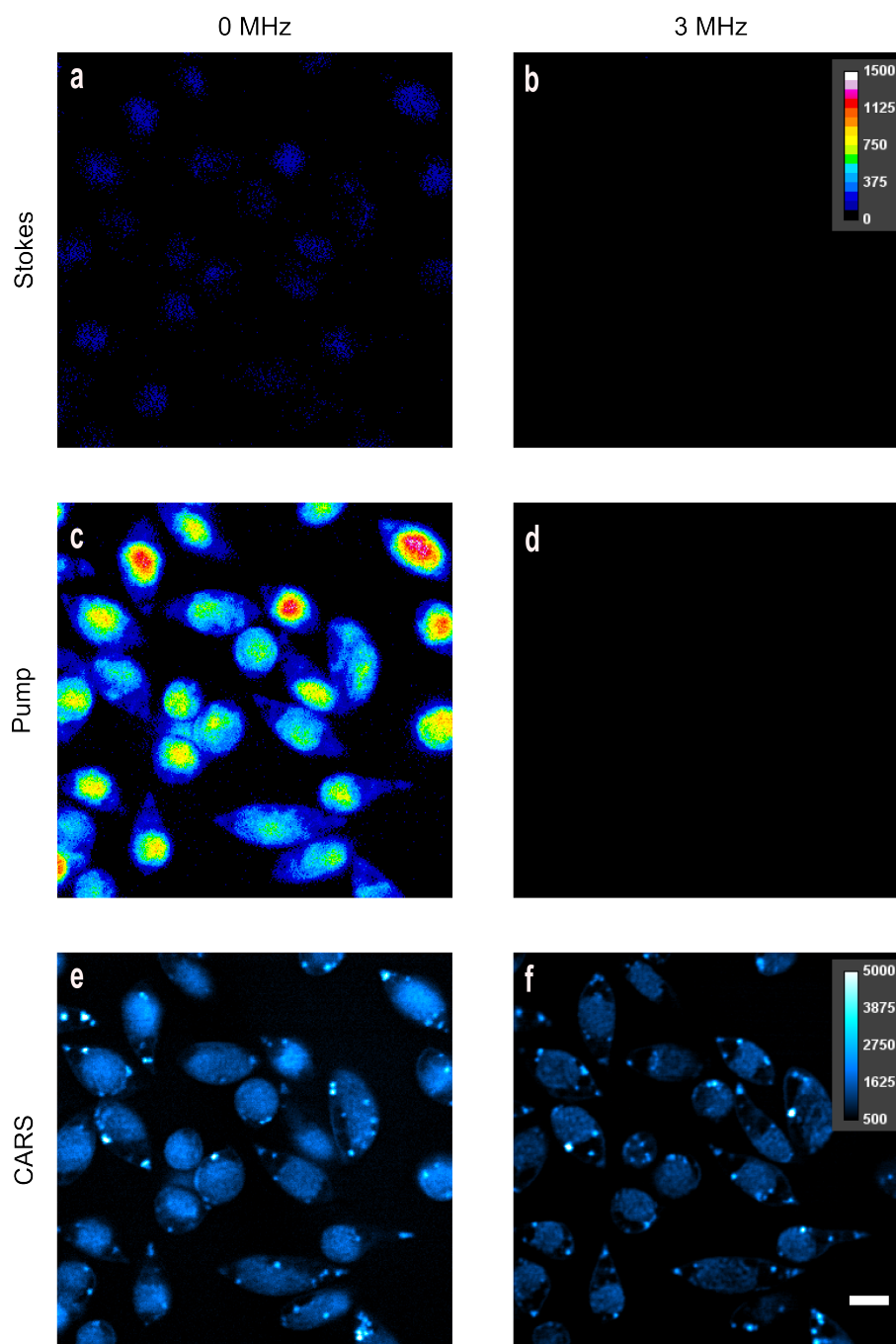


Figure 34 – Modulation approach for eliminating undesired two-photon excited fluorescence signals investigating *M. neglectum*

The left column (**a,c,e**) show the CARS channel probing 2845cm^{-1} while no modulation of the Stokes beam is performed. In **a**) solely the Stokes beam (1064nm) is directed onto the sample, in **c** the pump beam ($816,7\text{nm}$) respectively. An undesired two-photon excited fluorescence signal is visible in both channels, while its intensity is most prominent in **c**. Hence, the corresponding CARS signal (**e**) is disturbed by the fluorescence signal and has become unspecific excluding a quantitative analysis of the lipid droplets. The modulation of the Stokes beam at 3MHz in combination with the demodulation of the CARS signal by a lock-in amplifier (right column, **b, d, f**) shows significant less fluorescence signal while applying only Stokes (**b**) or pump beam (**d**). The resulting demodulated CARS signal (**f**) is specific to the lipid distribution again. For the exclusion of any artifacts due to the rather low fluorescence residuals of the Stokes beam an additional image (only Stokes beam in the sample) was acquired and subtracted from the corresponding CARS image. The data was recorded after 1 day of nitrogen starvation. Note that figures (**a - d**) as well as (**e - f**) have separate look-up tables, the scale bar depicts $5\mu\text{m}$. Published in [Jaeger et al. [2016]].

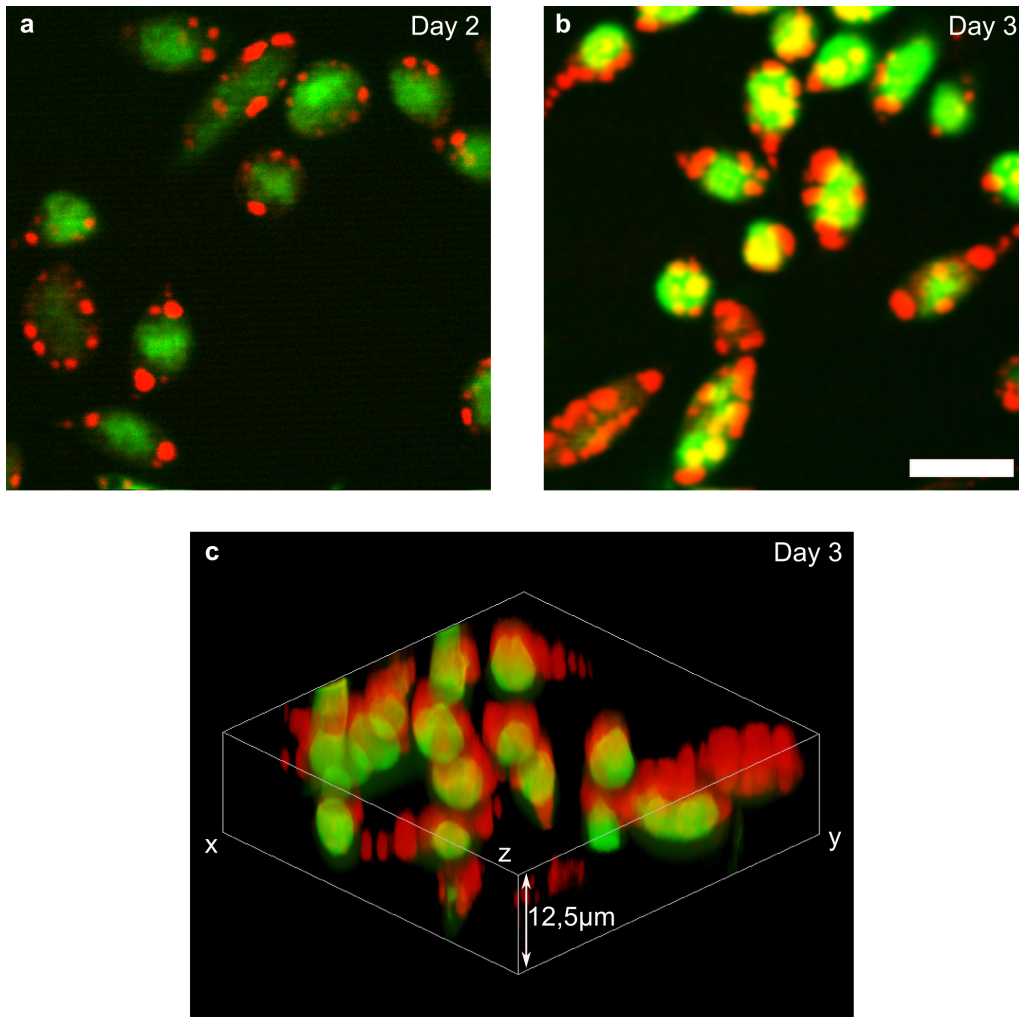


Figure 35 – Two channel detection of CARS signal and two-photon excited fluorescence. For the separation of both channels into: 1) CARS signal (red) probing the 2845cm^{-1} lipid resonance and 2) the two-photon excited autofluorescence signal (green) of the chlorophyll an additional 600LP optical filter was utilized for the detection of the fluorescent signals on a second PMT. Both channels were recorded sequentially. For the visualization of the lipid droplets and the chloroplast a z-scan was performed having a step size of 500nm covering up to $12,5\mu\text{m}$ range. The two-photon excitation was performed by the pump beam at $816,7\text{nm}$ applying 23mW focal power. A three-fold zoom was used for these images, the scale bar depicts $10\mu\text{m}$. **a)** and **b)** show a single 2D frame of days 2 and 3 respectively, while **c)** shows a full 3D scan of day 3 using the visualization tool *volume viewer* of *FIJI*. A Gaussian blur was applied on the data to smooth the 3D view. The chloroplast is visible as a large spherical component surrounded by the lipid droplets.

4.2.5. Comparing the results concerning the lipid content acquired by volumetric CARS imaging to established methods

The experiments are conducted over a time course of 8 days beginning the nitrogen starvation at day 0. On days 0, 1, 2, 4 and 8 CARS microscopy was conducted on the samples, while several microalgae were visible in one acquired image using a zoom-factor of $3\times$ for having a field of view of $48,5\mu m$ (fig. 36). For the comparison of data acquired by CARS microscopy to conventional methods the *M. neglectum* samples were investigated by cell counting, dry weight measuring (fig. 37 a) and gravimetric neutral lipid determination (fig. 37 b). The dry weight increases constantly over time while the cell density doubles after 4 days of starvation and remains constant afterwards. The lipid content of the biomass is separated by gravimetric analysis into total-, polar- and neutral- lipids, where the polar lipid content decreased continuously at the first two days and is observed as constant afterwards. The neutral lipid content increases constantly over the whole time course and reaches up to 30% of the dry weight at day 8.

Then the quantitative analysis of the cellular volume as well as the volume of the lipid droplets via CARS microscopy was explored in two different approaches: a high number of replicates was imaged by CARS imaging using arbitrary z-positions at random locations in the specimen for the counting of LDs in the cells (fig. 38 a). The number of analyzed cells per day were $n = 90$. This leads to a measure of equal or greater number of lipid droplets per cell than the number detected in the specific section. We observed an continuously increasing number of LDs, after 8 days of nitrogen starvation the mean number of LDs per cell section increased from 0 at day 0 to 15 at day 8. Also the diameter of the observed LDs is approximated from the data via assuming the LDs as circular shapes and measuring the diameter with *FIJI* [Schindelin et al. [2012], Rueden et al. [2017]] for plotting the data in respect to the days of nitrogen starvation (fig. 38 b). Here, the mean of the diameter is slightly increasing with time while the mean variation is increasing (number of investigated lipid droplets $n = 0, 468, 969, 1255, 1363$ for day 0, 1, 2, 4, 8). In addition the cell area (elliptic shapes were assumed, fig. 38 c) was estimated and via the LDs diameter the corresponding LDs areas were calculated for finally plotting the relative lipid droplets area by dividing the LDs area by the total area of the cells (fig. 38 d). A five-fold increase over the time of starvation is observed while the mean cell area remained constant. Comparing the results of CARS microscopy in terms of relative LD area to the gravimetric determined neutral lipid contents shows a strong correlation (fig. 38 e, $R^2 = 0,9981$) and indicates good agreement of both methods.

An alternative and more intuitive way of analyzing the lipid content and cellular vol-

ume of *M. neglectum* would be directly measuring the volume of the specimen instead of the area of the LDs and cells via single, arbitrarily selected z-positions. Therefore, 3D imaging was performed using the piezo-stage in the z-direction applying a step size of $500nm$ on a separate set of cells originating from the same batch of *M. neglectum*. Then the acquired data were analyzed assuming the cells volume as a ellipsoid with $Vol_{Cell} = \frac{4}{3}\pi \cdot \left(\frac{d_x}{2}\right) \left(\frac{d_y}{2}\right) \left(\frac{d_z}{2}\right)$ and the volume of the lipid droplets as a sphere $Vol_{LD} = \frac{4}{3}\pi \cdot \left(\frac{d_{xLD}}{2}\right)^3$, see also fig. 39 **a**). Here, the LD volume (fig. 39 **b**) as well as the relative LD per cell volume (fig. 39 **c**) are plotted over time and show the similar tendency as the data obtained analyzing the area instead of the volume. Finally, this results again in a strong correlation to the gravimetical neutral lipid analysis (fig. 39 **d**, $R^2 = 0,98$), but is not perfectly overlapping to the area analysis method (compare to $R^2 = 0,9981$). The reason for the slight mismatch of both methods very likely originates from the difference in the number of cell replicates, which also shows the drawback of the 3D method: a higher time consumption compared to area analysis results in the rather low number of replicates (investigated number of LDs $n = 0, 46, 121, 106, 205$ at days 0, 1, 2, 4, 8, respectively). For a statistical more solid comparison of both methods in terms of the biological conclusion a far greater number of replicates would be required in the 3D approach, which was not further pursued in the course of the study, due to the good results of the 2D method matching the gravimetical neutral lipid analysis and being very efficient in time consumption.

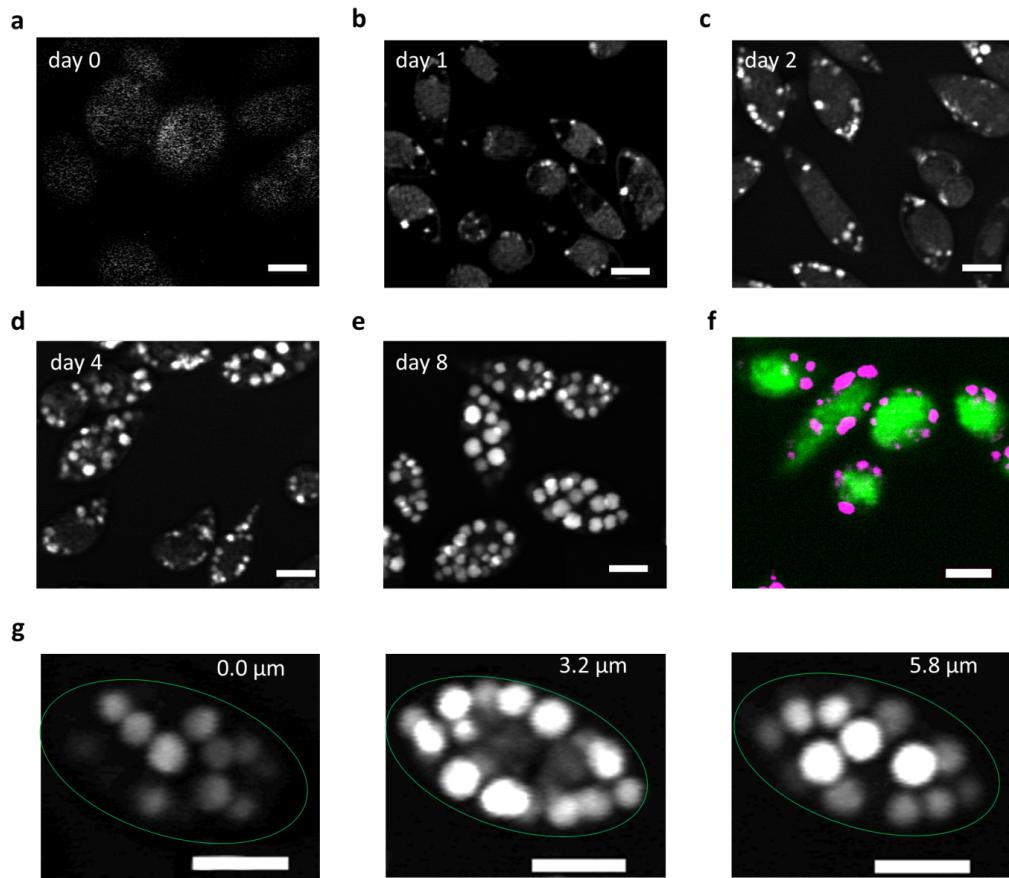


Figure 36 – Frequency modulated CARS imaging reveals lipid droplet formation in *M. neglectum* under nitrogen starvation

M. neglectum was imaged via frequency modulated CARS microscopy over 8 days of nitrogen starvation conditions (a - e). f) shows the merged signals of CARS signal (magenta) probing 2845cm^{-1} and two-photon excited fluorescence of the cup-shaped, central chloroplast (green). Increasing lipid droplet formation can be clearly observed and further analyzed by z-scanning, g) shows typical data acquired at day 8 at selected z-positions indicating the intracellular lipid droplet distribution. Note that the green circle depicts the cellular border to guide the eye. The scale bar indicates $5\mu\text{m}$. Published in [Jaeger et al. [2016]].

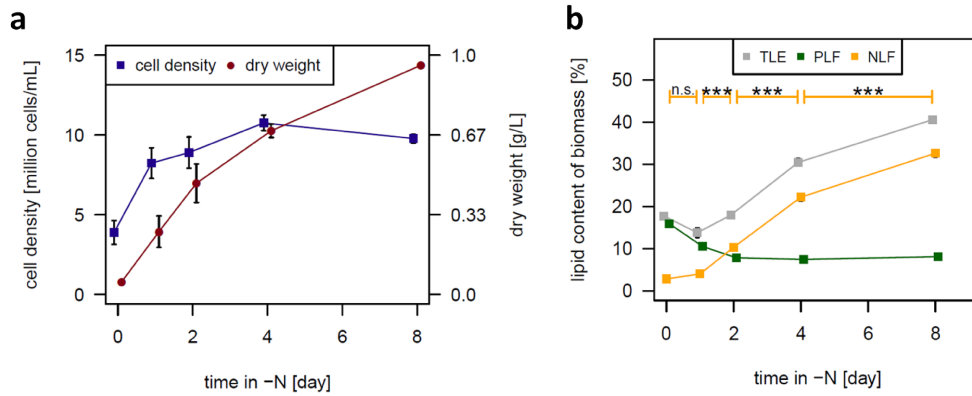


Figure 37 – Cell growth parameters and gravimetric analysis of *M. neglectum* during nitrogen starvation

a) shows the cell density (blue rectangles) determined by a cell counter (*Beckmann Coulter*, Coulter counter) and the dry biomass weight (red circles, 25ml of the cell culture were washed, dried and weighed) over eight days of nitrogen starvation conditions. The error bars represent the standard error of the mean. In **b)** the lipid content of the biomass is shown over 8 days of nitrogen starvation investigated by Folch extraction [Folch et al. [1957]] of the lipid content and then separated by gravimetric analysis into polar- (depicted in green, PLF), neutral- (yellow, NLF) and total lipids (gray, TLF). The significance was tested by a two-sided t-Test (n.s.: not significant, ***: $p < 0,001$). Published in [Jaeger et al. [2016]].

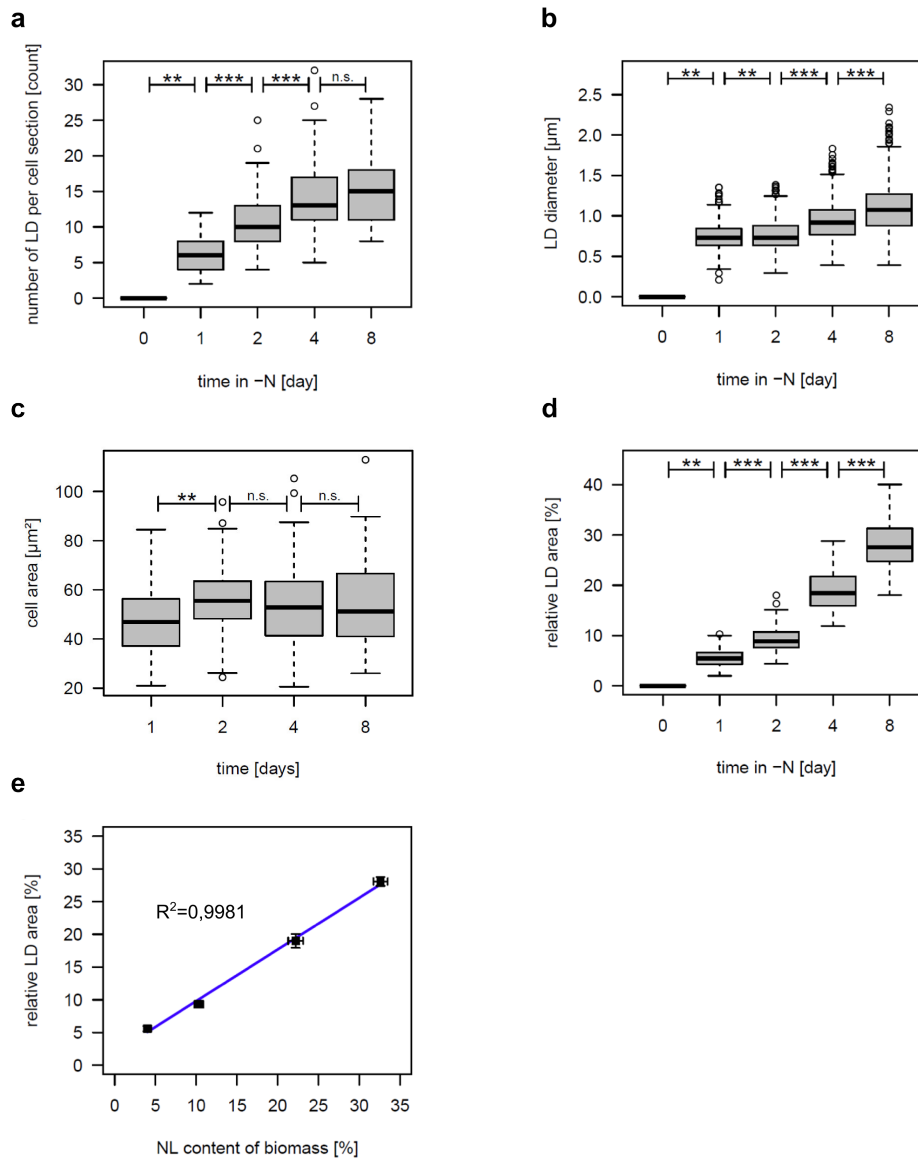


Figure 38 – 2D CARS imaging of *M. neglectum* for investigating cell growth and lipid distribution under nitrogen starvation conditions

a) shows the number of LDs per cell section at random selected z -planes over time ($n = 90$ cells per day) in a box-whisker plot. In **b)** the diameter of the LDs is measured via *FIJI* and averaged, the sample size was $n = 0, 468, 969, 1255, 1363$ for days 0, 1, 2, 4, 8. The cell area A was also measured applying $A = \pi \cdot \frac{d_x}{2} \cdot \frac{d_y}{2}$ where d_x and d_y depict the long and short diameter of the cell, respectively. **c)** shows the mean values of the cell area corresponding to days 1, 2, 4 and 8. In **d)** the relative LDs area per total cell area is plotted in respect to the days of nitrogen starvation as indicator of the TAG content. (**a** - **d**) box whisker plots: mean value indicated by the thick black lines, the gray boxes show the interval between the first and third quartile while the two whiskers mark the respective 1,5 fold interquartile ranges (open circles: outliers). The significance of changes is indicated in regard to the value of the previous time point by a two-sided Wilcoxon Rank Sum Test (n.s.: not significant, *: $p < 0,05$, **: $p < 0,01$, ***: $p < 0,001$). In **e)** the correlation of the relative LD area to the gravimetric neutral lipid content is shown (error bars represent the standard error of the mean, determination coefficient $R^2 = 0,9981$). Adapted from [Jaeger et al. [2016]].

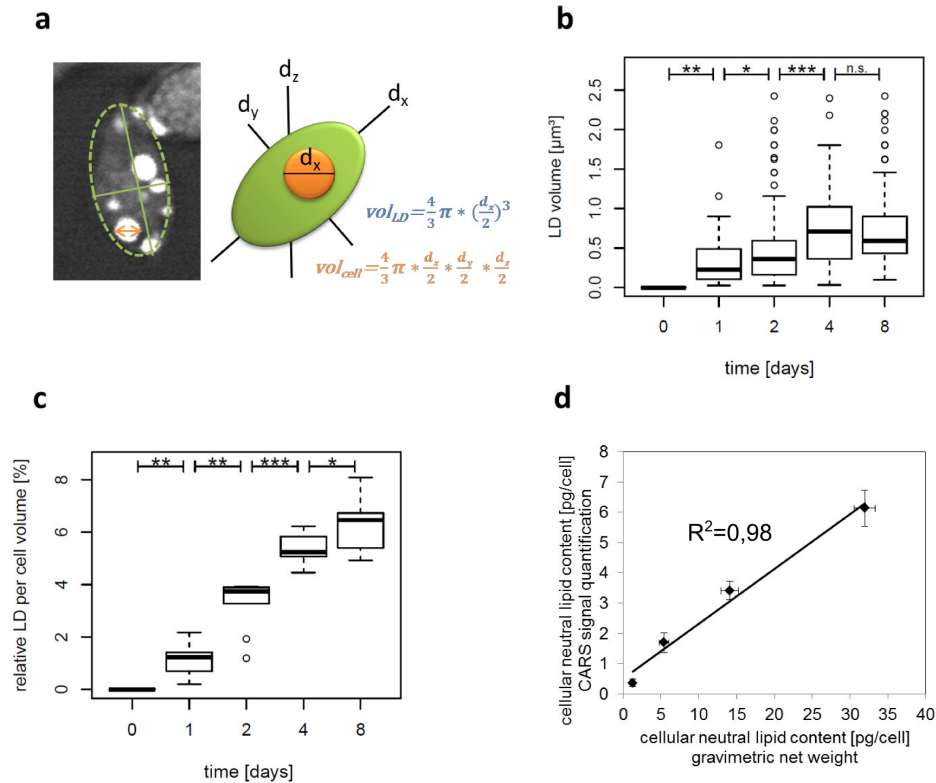


Figure 39 – Volumetric CARS imaging of *M. neglectum* for monitoring cell growth and cellular lipid content

a) illustrates the analysis strategy applied in the volumetric CARS data acquired by *z*-scanning with a step size of 500nm . The cellular volume Vol_{cell} was estimated as ellipsoid, the LDs volume Vol_{LD} as circular sphere utilizing several *z*-slices of the scanned range for the determination of the values of each cell. This analysis leads to **b)** plotting the LDs volume during the 8 days of nitrogen starvation and **c)** the relative LDs volume, respectively (cellular volume not shown). (**b** and **d**) box whisker plots: mean value indicated by the thick black lines, the gray boxes show the interval between the first and third quartile while the two whiskers mark the respective 1,5 fold interquartile ranges (open circles: outliers). The significance of changes is indicated in regard to the value of the previous time point by a two-sided Wilcoxon Rank Sum Test (n.s.: not significant, *: $p < 0,05$, **: $p < 0,01$, ***: $p < 0,001$). **d)** shows the correlation of the calculated relative LDs volume in respect to the cellular neutral lipid content determined by gravimetric analysis. The data correlates with a determination coefficient of $R^2 = 0,98$, the error bars indicate the standard error of the mean. Note that the number of investigated LDs ($n = 0, 46, 121, 106, 205$ at days 0, 1, 2, 4, 8, respectively) is much less than in the 2D approach, previously shown in fig. 38. Hence, the statistical significance and biological conclusion is less sound and these 3D results should mainly depict an alternative methodical approach. Published in [Jaeger et al. [2016]].

4.2.6. Studying the degree of unsaturation of fatty acids in lipid droplets of *M. neglectum* by Raman micro-spectroscopy

Raman micro-spectroscopy was applied to investigate the degree of unsaturation of fatty acids in the lipid droplets utilizing the label-free, non-invasive manner of the technique. Therefore, LDs were identified and analyzed by spontaneous Raman scattering for comparing the ratio of two selected peaks, namely 1660cm^{-1} ($C = C$ double bond) indicating unsaturation as well as the 1442cm^{-1} peak ($C - H_2$ vibration) as a measure of the overall lipid content. The analysis showed the ratio as a relative degree of unsaturation to be unchanged between day 4 and 8, which is in good agreement with results using GC-MS and fatty acid methyl ester derivatization. Further time points were not investigated, but the method proved as versatile tool and can be further explored in the future. The corresponding data sets will not be included into this thesis but can be found in the published manuscript [Jaeger et al. [2016]].

4.2.7. Successful CARS imaging of lipid contents in *M. neglectum* under nitrogen starvation conditions indicates optimal harvesting time point enabling comparison to other types of microalgae

Summing up the results obtained on the oleaginous microalga *M. neglectum* it was possible to utilize CARS microscopy for imaging a statistical significant number of replicates for the investigation of the relative lipid droplet content during a nitrogen starvation over eight days. Due to an intensity modulation of the Stokes beam in combination with lock-in demodulation it was possible to circumvent undesired two-photon excited fluorescence of the chloroplast, without the need of time-gated detection. Comparing the results obtained by CARS microscopy to classic approaches such as solvent extraction and gravimetric determination good agreement of the techniques is observed for the direct quantitative calculation of the TAG content. Also an optimal time point for the harvesting of the microalga *M. neglectum* could be identified to be 4 days after the start of the nitrogen starvation conditions. In addition to that the mean size of the LDs observed in *M. neglectum* was now accessible and could be related to other, already more characterized microalgae such as *C. reinhardtii* and *P. tricornutum*.

4.3. Developing a hyperspectral CARS imaging modality

4.3.1. Exploring hyperspectral CARS for enhancing the information content of samples by their spectral response

CARS microscopy is a versatile analysis tool for the investigation and visualization of one or more chemical components of a specimen, especially when the chemical components of interest are identified prior to the measurement, e.g. by spontaneous Raman spectroscopy [Huser and Chan [2015], Terjung et al. [2013]]. The received information of the images can consist of several probed CARS resonances or also SHG and fluorescence signal via wavelengths separation and modulation techniques as shown in the previous chapter. An extension of this methodical range in CARS microscopy gathering additional information of the specimen is the hyperspectral tuning of Stokes or pump beam, which are together addressing the molecular resonance [Fussell et al. [2013], Cheng and Xie [2015], Huang et al. [2018]]. In the typical technical implementation using ps-laser setups the beam delivered by the OPO is chosen for spectral tuning [Kong et al. [2013]], meaning the pump beam in the presented setup. An advantage of this method is that there is no need for prior knowledge of the chemical content of the sample and that the portions of the detected CARS signal originating from the overlay of the probed resonances can be further analyzed and interpreted by computational segmentation. Here, different methods such as principal component analysis (PCA) [Schie and Huser [2013]], non negative matrix factorization (NNMF) and other multivariate analysis tools [Miljković et al. [2010], Davis et al. [2011]] can be utilized to identify areas of similar spectral response of the sample and illustrate these with a color look-up table. The benefit of this step is an enhanced information content of the sample, which could not be achieved by probing single resonances via CARS. A drawback is the increased recording time needed of a full hyperspectral scan, e.g. probing a typical wavelength range in the lipid resonance branch ($2700 - 3100\text{cm}^{-1}$) applying typical imaging conditions elongates the recording time from $\sim 20 - 60$ seconds for one image at a fixed resonance to up to 35 minutes for the entire hyperspectral scan. The scanning time is composed of the recording time of the image at the current wavelength and the time needed for the wavelengths tuning in the OPO system, which is dominated mainly by the rather slow heat-up or cool-down of the BBO crystal temperature determining the wavelengths working range.

4.3.2. Improving the stability of the microscopy setup enables high fidelity HS-CARS data sets

Due to the long recording time high demands are set to the microscopy setup in terms of focal stability. If the sample should move during the hyperspectral scan the gathered information is inconsistent and can not be used for further analysis. Therefore, great effort was taken to optimize all parameters of the setup, which are affecting the sample drift. Here, typical values of sample drift were less than $450nm$ over $75min$ in all dimensions. For achieving these values the condenser lens 3D-translation mount was optimized by a custom made mechanism and also the technique of dipping the condenser lens into the aqueous medium of the specimen without an additional cover slip proved to be advantageous. In typical measurements a water immersion objective lens focused Stokes and pump beam into the sample. The best focal stability over long terms was achieved by applying Immersol W 2010 (*Carl Zeiss Jena GmbH*) as immersion media instead of the standard distilled water due to the lack of evaporation and thus additional forces on the specimen.

4.3.3. Customized software controls entire HS-CARS scan process ensuring undistorted spectra

For the analysis of the hyperspectral data sets it is necessary to record the applied laser power of the OPO during the wavelengths tuning due to the varying response and efficiency of the LBO crystal and the OPO cavity. Addressing this need we choose to expand the task of intensity recording also to the Stokes beam for further improvement of the image quality of all recorded data. Hence, in the course of a bachelor thesis [Anselmetti [2016]] the intensity recording of Stokes and both OPOs signal exits was performed by home-embedded Si photodiodes (*Luna Optoelectronics*, PDB-C613-2) and an additional A/D converter card (*National Instruments*, PCIe-6363) for the fast recording of the photodiode signals. For the time correlation of recorded laser intensities to the image data a custom-written Matlab program was created, which was capable to correct laser intensity fluctuations in a post-processing step up to $100kHz$, also in imaging data with fixed molecular resonance.

For the application to hyperspectral data this program was extended and further improved by implementing an auto-correlation functionality matching photodiode signals and CARS data in a more accurate manner as well as the development of control software for the hyperspectral scanning in the course of two master theses [Greife [2017], Weiß [2017]]. For the tuning of the OPO's wavelength a Matlab-based control program was designed (HyperSpectrum, see fig. 40 **a**), which controls the OPO parameters via

the RS-232 interface of the OPO controller as well as it operates the microscope imaging software. Here, the LBO crystal temperature t was precisely characterized and is set according to the desired pump wavelength for each image of the hyperspectral stack. The piezo stage of the OPO cavity determining the cavity length L_{Cav} is addressed and optimized according to each selected wavelength. Finally, the simplified Lyot filter inside the OPO cavity is adjusted for the selection of the desired signal wavelength, which is monitored by the inbuilt spectrometer of the OPO. In general all described OPO parameters are optimized for the highest possible signal output intensity of the OPO according to the selected wavelength (then described as L_{Cav}^{Opt} and t_{opt}), which is an important factor for the reproducibility of the hyperspectral data set due to possible pulse length variation of the pump pulses (which will be further explained later). When the output wavelength of the OPO has reached the required parameters the control program starts the image acquisition and awaits its end for continuing in the wavelengths tuning process with a user selectable step size between the consecutive wavelengths.

In a post-processing step the hyperspectral image stack is then intensity corrected and each image is normalized according to the applied laser intensity at the specific pump wavelength with the Matlab routine (fig. 40 **b**). For high precision of this post-processing step it proved necessary to characterize the wavelength-dependent transmission / reflectivity of the pellicle beam splitters used for recording a small portion of the pump and Stokes beam on the photodiodes. Here, a transmission curve was recorded and stored in the analysis program, which corrected the photodiode data by a wavelength-dependent weight factor.

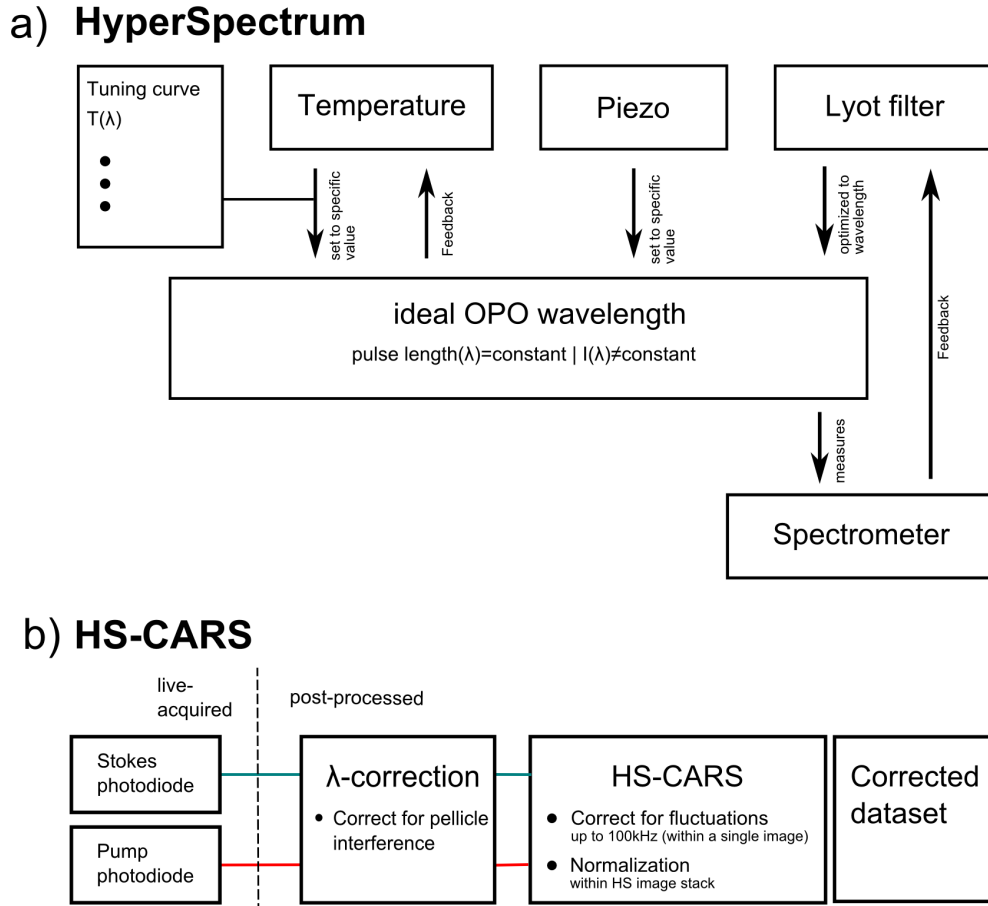


Figure 40 – Block diagram of the control program for hyperspectral CARS image acquisition. In **a)** the block diagram of the custom-written Matlab routine HyperSpectrum shows the parameters of the OPO, which are acquired and optimized during the wavelengths tuning process in a hyperspectral image acquisition. The temperature tuning curve of the LBO crystal was carefully characterized and stored in the routine. The cavity length of the OPO L_{Cav} is adapted to every target wavelength, while the tuning of the OPO's generated wavelength is performed by the Lyot filter and monitored via the inbuilt spectrometer. All parameters are optimized with HyperSpectrum in order to operate the OPO at its working point for the maximum intensity output at the specific wavelength. This leads to a constant pulse length and reproducible data acquisition. **b)** showcases the post-processing by the Matlab routine HS-CARS, which utilizes the data of the applied laser intensities of pump and Stokes beam recorded by the photodiodes for the correction of stripes in the CARS images due to laser jitter up to $100kHz$. In the second step the normalization between all single images of the hyperspectral data stack is performed, which is necessary due to variation of output power of the OPO according to the selected wavelength. For the normalization step the wavelength-dependent transmission of the pellicle beam splitters is measured and implemented into the program as additional weight factor. Published in [Pilger et al. [2018]].

4.3.4. Pulse length variation induces spectral distortions in hyperspectral CRS-microscopy

During the development of the hyperspectral CARS scanning modality as well as in additional experiments¹⁴ it became apparent, that the pulse length of the laser pulses generated by the OPO is depending on the mode of operation and several tuning parameters. Probing e.g. a molecular resonance while switching back and forth between the pump beams of identical wavelength provided by both OPOs with an acousto-optic tunable filter in a switching rate of $100kHz$ different CARS signal intensities were recorded. The effect of pulse length variation is most significant during a wavelengths tuning of the OPO e.g in a hyperspectral CARS experiment. Even by applying the same focal power or by measuring the power and recalculating the intensity change in the final images as a correction, the pulse length has a significant influence to the final CARS intensity. As seen in eq. 25 the intensity of the pump beam I_p contributes being squared to the final CARS intensity $I(\omega_{aS}) \propto I_p^2$. The pump beam intensity is composed of the constant duty cycle of the laser system (here $80MHz$) and the pulse peak energy E_{peak} , which is defined by the pulse length of the applied laser pulses. The significance of this influence on HS-CARS experiments is illustrated in fig. 41, here a U2OS cell sample is scanned probing a range of $2738 - 2947cm^{-1}$ in a step size of $4,7cm^{-1}$ while operating the OPO during the wavelengths tuning in two modes: a static OPO setting with optimized OPO parameters on one output wavelength (upper left side in fig. 41) as well as with our customized OPO control software described in chapter 4.3 (see also fig. 40), referred to as dynamic optimization. The dynamic optimization utilizes the prior analysis of the OPO and performs an active optimization of two parameters: the cavity length L_{Cav} as well as the temperature of the LBO-crystal t assuring a constant pulse length of the pump beam (depicted on the upper right side of fig. 41). In this study [Pilger et al. [2018]] the pulse length of the pump beam was recorded simultaneously during the imaging by directing a small portion of the pump beam into an autocorrelator (*APE*, pulseCheck 50) and assigning its value to the images (see also fig. 19). This way the microscopy setup was independent and undisturbed of the pulse length measurements and the time of a HS-CARS scan was unaltered. The result of the pulse length measurement indicated, that the static optimization of the OPO parameters on one wavelength leads to a variation in pulse length, whereas the dynamic optimization shows unaltered pulse length. Performing the HS-CARS measurement on a U2OS cell and comparing the spectral response in a selected area (here the nucleus) of both OPO modes shows a strong distortion of the spectrum; the

¹⁴As a part of the master thesis of Mr. Alex Weiss [Weiß [2017]].

CARS spectrum using constant pulse length (fig. 41, blue solid line) has an offset to the data using a varying pulse length (green dashed line).

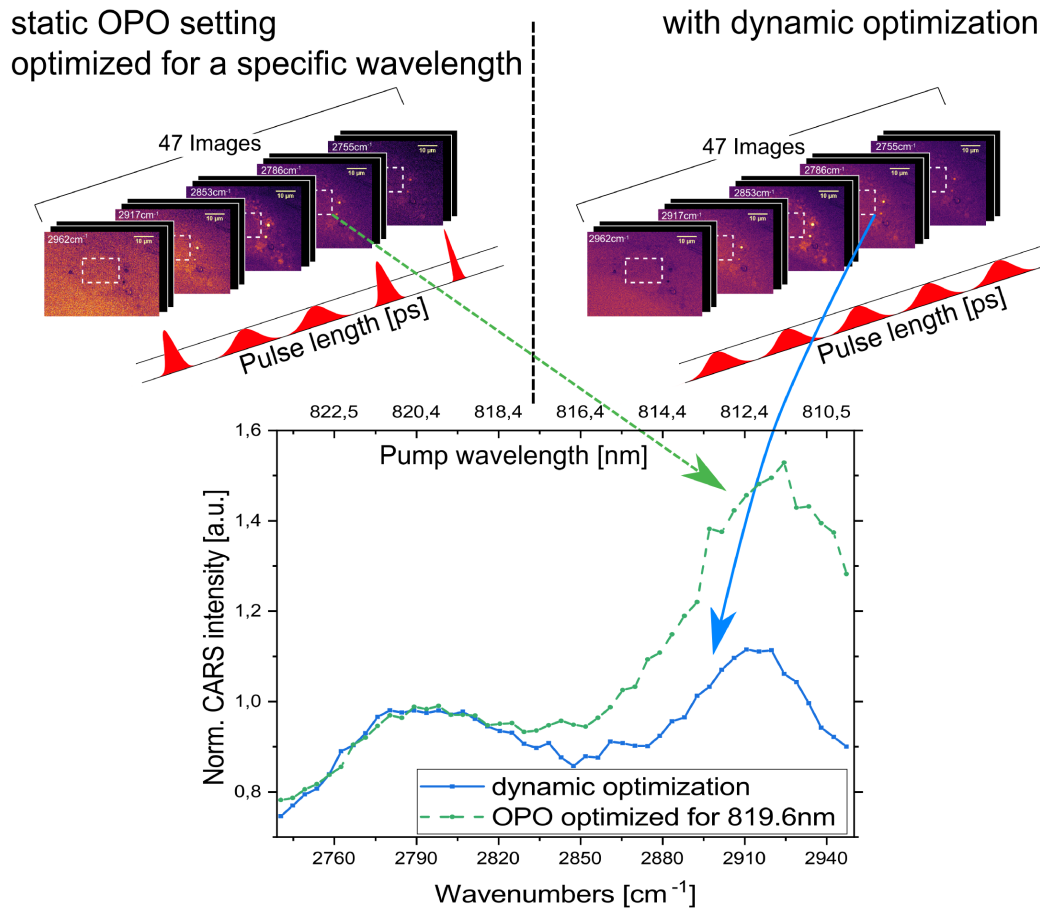


Figure 41 – HS-CARS imaging scheme: influence of the OPO operation mode on spectra due to pulse length variation

On the upper left the HS-CARS image stack of a U2OS cell sample is depicted using a static OPO optimization at 819,6nm pump wavelength. During the spectral scan the pulse length is not constant resulting in a distorted CARS spectrum depicted in green dashed line. On the upper right the dynamic optimization mode of the OPO is shown utilizing the home-built Matlab program. All OPO parameters are optimized during the HS-CARS acquisition, the pulse length is kept constant resulting in the undistorted spectrum depicted in the solid blue line. Both spectra are acquired of a ROI at the cellular nucleus, and were averaged of 3 repeated HS-CARS scans for each spectrum. Published in [Pilger et al. [2018]].

4.3.5. Identifying the OPO parameters influencing the pulse length during wavelengths scanning

In order to investigate the behavior of the OPO and to identify all involved parameters in the OPO tuning, which can affect the pulse length of the output beam of the OPO, additional experiments were performed. The aim of this study was to inform the community performing CRS-microscopy on the OPO's pulse length variation as well as to offer the customized, Matlab-based software for OPO control to avoid disturbed HS-CARS data. Up to the authors knowledge the pulse length of the OPO was considered in general as determined by the pump laser and, therefore, as constant and not a factor, which had to be further regarded or controlled in hyperspectral experiments. This is also the case for hyperspectral SRS due to the similar dependence on the pulse length of the pump beam. For the determination of the range of pulse lengths, which can occur with the present ps-OPO system, a pure DMSO (dimethyl sulfoxide) sample was prepared between two cover slides separated by thin Teflon ring probing the $C-H$ symmetric stretching mode at 2913cm^{-1} by using a constant wavelengths combination of 1064nm as Stokes and $812,3\text{nm}$ as pump beam. A constant focal power was applied of 12mW Stokes and 23mW pump beam correcting the OPO's power variations due to the settings by rotating the halfwave-plate in front of the polarizing beam splitter cube. The OPO's cavity length remained constant during the experiment. The OPO's LBO crystal temperature was then tuned over a range of $3,5^\circ\text{C}$ (see fig. 42 a) while measuring the pulse length as well as the CARS signal by acquiring images ($256 \times 256\text{px}$ using $15,6\mu\text{s}$ pixel dwell time). For the visualization of the CARS signal intensity all pixels were averaged and normalized on the lowest value coinciding with the longest pulse length (fig. 42 b). The pulse length varied in a range of $3,6 - 5,4\text{ps}$, while the highest possible output power of the OPO at that specific wavelength was observed at the longest pulse length defining the optimal crystal's temperature t_{opt} . The corresponding normalized CARS intensity showed a linear behavior indicated by the linear regression as a guide to the eye. A signal increase with a factor of up to 1,51 was observed in the CARS intensity. The behavior of the OPO was not entirely decoupled from setting a temperature below (red crosses) or above (blue circles) t_{opt} , indicated by the different gradients of the linear regressions. The linear dependence can be explained as an overlay of two competing effects: shortening the pulse length of the pump beam scales quadratic to the CARS intensity as already mentioned leading to a quadratic increase in CARS intensity. On the other hand the temporal overlap of the unaltered Stokes beam with the varying pump beam is decreasing with shorter pulse lengths of the pump beam, which can be understood as an "area matching" in temporal space of both pump and Stokes pulses. The combination of both counteract-

ing effects leads to the observed linear increase in CARS intensity.

Then the cavity length L_{Cav} of the OPO was tuned in the order of $\sim 20\mu m$ holding the LBO crystal temperature constant probing again the DMSO sample (fig. 43). The highest output power of the OPO was observed with the longest pulse length defining the optimal set point for the cavity length setting to L_{Cav}^{opt} . A change in pulse length in the range of $5,1 - 3,2ps$ was detected leading to a change in CARS intensity, which was non-linear (fig. 43 **a**). For investigating the unexpected non-linear behavior of the CARS intensity change two additional experiments were conducted: First, the repetition rate of the pump beam generated by the OPO was measured by detecting the laser pulses with a fast Si-photodiode (*Thorlabs*, DET10A) and a spectrum analyzer (*Tektronix*, MDO 4054 B-6, utilizing the $6GHz$ spectrum analyzer function). The repetition rate was constant while the cavity length was changed in a range of $17,5 - 25,5\mu m$ (data not shown). Second, the temporal overlap of Stokes and pump beam was investigated by feeding the monitor signal of the laser as reference signal of the Stokes beam into a real-time oscilloscope (*Tektronix*, MSO 71254C, $100GS/s$ $12,5GHz$). The pump beam was detected at a fixed position in the optical beam path with the fast Si-photodiode and directed into the second channel of the oscilloscope utilizing a differential SMA probe (*Tektronix*, P7313SMA). Both signals were compared by the 50% rising edge amplitude and by applying the delay measurement function of the oscilloscope. Then at least 35450 triggered events (caused by the single laser pulses) were detected and compared at two settings of the OPO cavity, elongating the cavity by $\sim 25,5\mu m$ lead to a change of temporal offset to the reference of $1,57 \pm 0,52ps$ by subtracting both data sets of each other. Hence, tuning the cavity length in a larger scale can lead to a temporal mismatch of Stokes and pump beam pulses in CARS experiments. This result lead to a repeat experiment changing the cavity length while probing a DMSO sample with CARS, but now the temporal overlap of both beams was manually adjusted to the highest CARS signal possible at one cavity length by tuning the delay stage behind the OPO beam exit (compare fig. 19). Now the expected linear dependence of pulse length alteration and normalized CARS signal was observed (fig. 43 **b**).

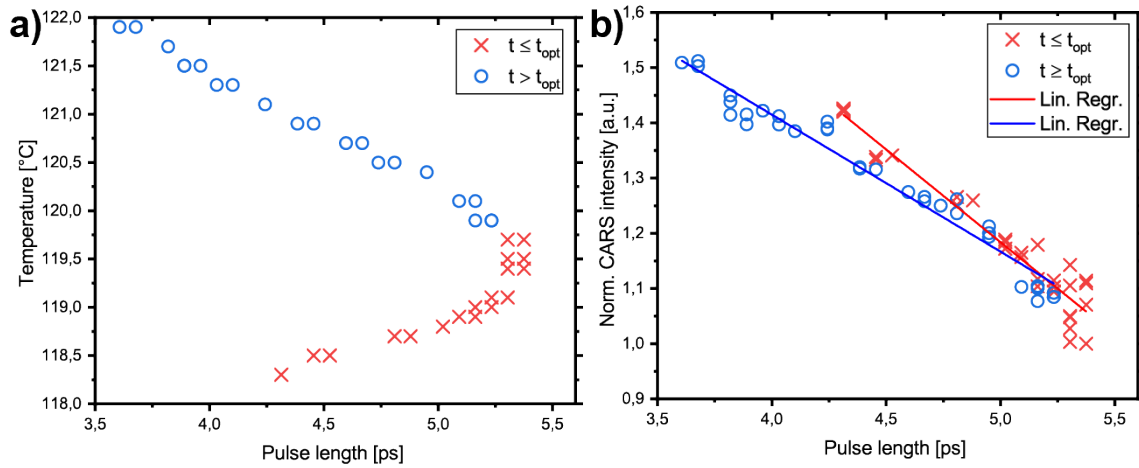


Figure 42 – OPO crystal temperature influences CARS intensity due to pulse length variation imaging a DMSO solution

a) depicts the dependence of the pulse length due to the OPO's crystal temperature t in a range of 3, 5°C: red crosses indicate t below the optimal temperature t_{opt} , blue circles above t_{opt} , respectively. t_{opt} coincides with the maximum output power of the OPO's signal beam as well as with the longest pulse length ($\sim 5,4ps$). The corresponding normalized CARS intensity probing the CH symmetric stretching mode at $2913cm^{-1}$ with a static pump wavelength of $812,3nm$ is shown in b): the pulse length varies due to the change of the crystal temperature in a range of 5, 4 – 3, 6ps leading to an increase of the CARS intensity of up to 1, 51. The data is normalized to the lowest CARS signal intensity, a linear regression is added as a guide to the eye. The OPO cavity length was kept constant. Published in [Pilger et al. [2018]].

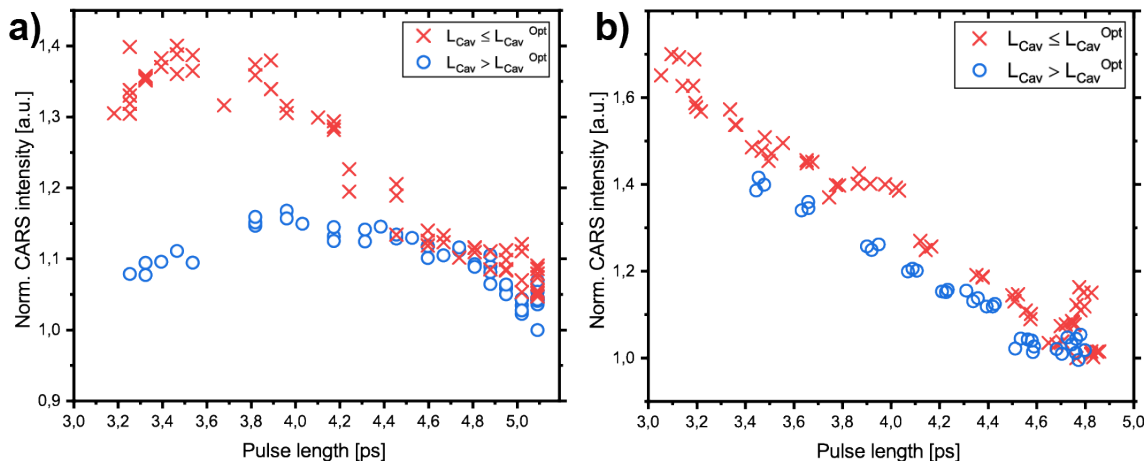


Figure 43 – Detuning of OPO cavity length leads to pulse length variation and temporal mismatch resulting in CARS intensity changes

In **a)** the cavity length of the OPO was de-tuned from the optimal value L_{Cav}^{opt} in a range of $\sim 20\mu\text{m}$ having a constant crystal temperature while a DMSO sample was investigated at 2913cm^{-1} . The pulse length varies from $5,1 - 3,2\text{ps}$, while a difference in normalized CARS intensity occurs. The CARS values can be separated into two groups: L_{Cav} below (red crosses) or above L_{Cav}^{opt} (blue circles). No linear behavior of CARS signal to pulse length was observed, which proved to be due to temporal mismatch of the pump to the Stokes laser pulses yielded by the change in cavity length. In **b)** the temporal overlap was manually optimized by a delay stage behind the OPO signal exit resulting in a linear behavior. The observed effect of the pulse length variation showed an increase of up to 71% of the normalized CARS intensity at a pulse length of $3,2\text{ps}$ compared to the longest pulse length of $5,1\text{ps}$ having the optimal cavity length L_{Cav}^{opt} . Published in [Pilger et al. [2018]].

4.3.6. Influence of pulse length induced distortions on HS-CARS spectra shown in methanol

For estimating the influence of the OPO induced pulse length variation in HS-CARS data sets a pure methanol sample was prepared in the same way as the DMSO sample between two thin cover slides. Then a HS-CARS scan was performed by probing $2800 - 2955\text{cm}^{-1}$ (corresponding pump wavelength was $809 - 818\text{nm}$) in two modes of operation: first, by utilizing the home-written Matlab program, and second, by using a fixed OPO setting optimized for one pump wavelength. Then the second mode was applied recording two spectra at two OPO optimization wavelengths ($819,8\text{nm}$ and $815,1\text{nm}$) for comparison to the dynamic mode and to indicate the effects on the spectra itself when changing the static optimization wavelengths, which is usually not a criterion mentioned in current hyperspectral CRS work but very likely affects the reproducibility (fig. 44 **a)**). In the scanned wavenumber range two prominent molecular resonances of methanol are visible: the symmetric $C - H$ stretching mode at 2830cm^{-1} as well as the anti-symmetric $C - H$ stretching mode at 2940cm^{-1} . The data was

normalized on 2823cm^{-1} for comparison reasons. The pulse length was simultaneously acquired for the entire wavelengths tuning range of 8nm and plotted in fig. 44 **b** showing a constant value for the dynamic optimization ($\sim 5\text{ps}$) while the static optimization induces a shift in the pulse length in the range of $5,0 - 3,6\text{ps}$ (blue curve, OPO optimization at $819,8\text{nm}$) and $5,0 - 4,0\text{ps}$ (red curve, OPO optimization at $815,1\text{nm}$), respectively. The longest pulse length is recorded at the wavelength of the initial OPO optimization. Due to the pulse length variation the hyperspectral CARS intensity is affected, the black curve (constant pulse length) serves as reference at the 2940cm^{-1} peak showing a difference to the static OPO optimization at $819,8\text{nm}$ (blue curve) of 41%, to the OPO optimization at $815,1\text{nm}$ (red curve) of 16%, respectively. Comparing the obtained spectra to a spontaneous Raman spectrum acquired of the methanol sample with a 785nm cw-laser system embedded in a home-built Raman micro-spectroscopy setup shows a good overlap of the molecular resonances of the HS-CARS spectrum to the spontaneous Raman spectrum (fig. 45). This indicates that the HS-CARS setup has a sound performance over the scanned wavelengths range as well as a good wavelengths calibration in the range of the probed resonances.

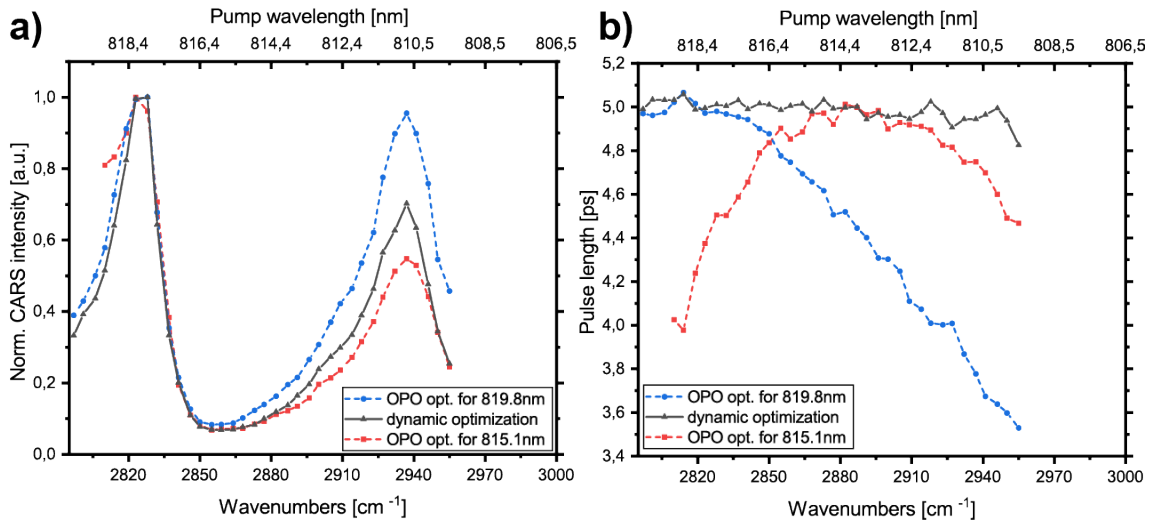


Figure 44 – OPO operation modes causing intensity distortions on HS-CARS spectra in methanol due to pulse length variations

HS-CARS spectra probing the range of $2800 - 2955\text{cm}^{-1}$ in pure methanol covering two molecular resonances at 2830cm^{-1} and 2940cm^{-1} . **a)** displays OPO operated by the dynamic optimization mode having a constant pulse length (black solid line), static OPO optimization at $819,8\text{nm}$ (2800cm^{-1}) (blue dashed line) and at $815,1\text{nm}$ (2870cm^{-1}), respectively. A normalization of all spectra is performed at 2823cm^{-1} for easy comparison. A distortion of the red and blue spectra compared to the reference becomes apparent at the 2940cm^{-1} methanol resonance. In **b)** the corresponding pulse lengths are depicted showing an unaltered value utilizing the dynamic optimization (black solid line), whereas the static OPO settings (red and blue dashed lines) show longest pulse length (5ps) at the wavelengths of the optimization, but a decrease during the wavelengths scan of up to $3,7\text{ps}$, leading to the observed distortion in the HS-CARS spectrum. Published in [Pilger et al. [2018]].

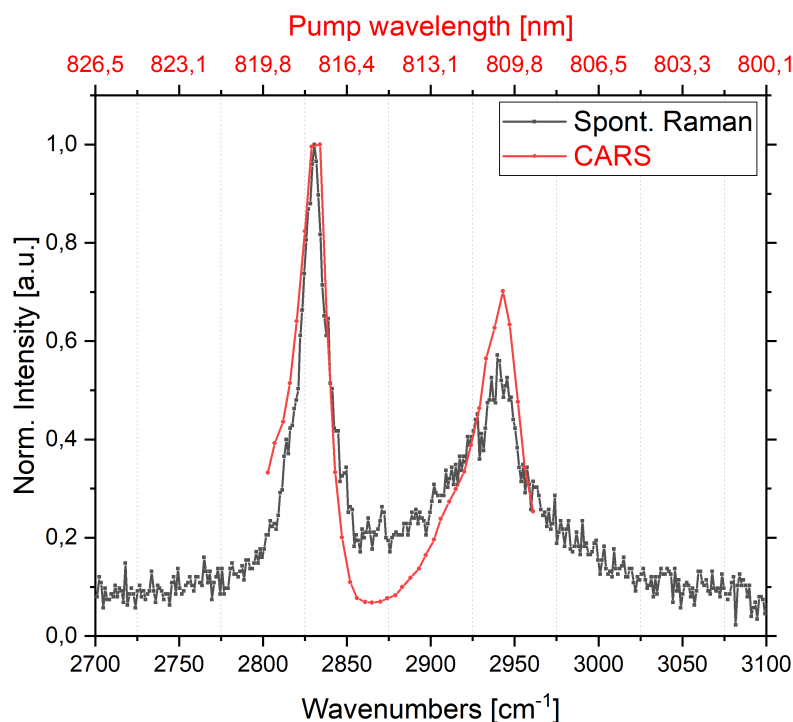


Figure 45 – Comparison of HS-CARS to spontaneous Raman spectrum acquired on pure methanol. The normalized CARS intensity during a hyperspectral scan ($2800 - 2955\text{cm}^{-1}$) (red line) of pure methanol is compared to a spontaneous Raman spectrum ($2700 - 3100\text{cm}^{-1}$) (black line) acquired by a home-built spectroscopy setup utilizing a 785nm cw-laser system. Two resonances are observed: the symmetric and anti-symmetric $C - H$ stretching mode at 2830cm^{-1} and 2940cm^{-1} , respectively. Both spectra are normalized to 2823cm^{-1} . HS-CARS shows good accordance to spontaneous Raman data; the spectral peaks are at the same Raman shift indicating a successful spectral calibration of the HS-CARS setup. The single acquired data points are linked by solid lines guiding the eye, the pump wavelength depicted in red is valid only for the CARS spectrum in combination with the unaltered 1064nm Stokes beam.

4.3.7. Investigating the effect of non-controlled OPO wavelengths tuning on HS-CARS spectra in U2OS cell sample

For the investigation of the spectral distortions due to the pulse length variation on more relevant biological samples a U2OS cell sample fixed with 4% para-formaldehyde solution¹⁵ was imaged. A hyperspectral CARS scan was performed in the range of $2738 - 2947\text{cm}^{-1}$ with a spectral width of $4,7\text{cm}^{-1}$ resulting in a data set of 47 images. Again the two previously discussed modes of OPO wavelengths tuning were performed while the HS-CARS scan was repeated for each mode 3 times in alternating order excluding any additional effects on only one mode due to temporal drifts. The duration of each HS-CARS scan was 27min resulting in 162min for all 6 scans. For

¹⁵The cell preparation was performed by Dr. Mathias Simonis.

the visualization of the data one set was chosen to be analyzed by a PCA analysis [Bonnier and Byrne [2012]], the first 3 loadings were selected for the false-color coding depicted in fig. 46 **a**. The corresponding pulse lengths are shown in fig. 46 **b**, the dynamic optimization has a constant pulse length of 4,9ps (solid blue line) and the static OPO optimization at 819,6nm (dashed green line) exhibits a variation from 4,8ps at 819,6nm to 3,5ps at 810,0nm. Two regions of interest are selected for further analysis, an area of a prominent lipid droplet (ROI A, yellow dot) and a larger area of the cellular nucleus (ROI B). In these areas the pixel values are averaged and the 3 repeated experiments are utilized to generate the mean spectrum of each OPO mode depicted in fig. 46 **c** (ROI A) and **d** (ROI B). The standard deviation is represented as the error bars of each spectral data point, indicating two different conclusions: first, in general the standard deviation is low for both methods indicating a high reproducibility due to a stable microscopy setup over time (maximal error $\delta_{max} < 10\%$ of the corresponding data point for ROI A static mode, mean error $\bar{\delta} < 4,2\%$; for ROI B $\delta_{max} < 4,5\%$, mean error $\bar{\delta} < 2,4\%$, respectively). Second, comparing dynamic and static OPO mode to each other we observe a lower error value of both ROIs using the dynamic optimization mode, (ROI A dynamic optimization: $\delta_{max} < 9,8\%$, $\bar{\delta} < 3,9\%$, for ROI B mean error $\delta_{max} < 2,8\%$, $\bar{\delta} < 1,5\%$, respectively). This indicates a even higher reproducibility of HS-CARS scans utilizing the home-written Matlab program.

The spectral distortions due to the pulse length variation become apparent comparing the blue solid lines to the green dashed lines in figs 46 **c**, **d**: for a better comparison the undistorted spectra were utilized as reference and the relative change in CARS intensity was calculated by dividing the distorted spectra by the undistorted (fig. 47 **a** for ROI A, **b** for ROI B, respectively). Here, a pulse length induced increase of CARS intensity with a factor of up to 1,52 in ROI A and of up to 1,49 in ROI B was found (both at $2940cm^{-1}$).

Summing up these findings the use of a controlled OPO tuning mode is crucial for undistorted HS-CARS data acquisition due to OPO induced pulse length variations during wavelengths tuning. The observed effects using a static OPO control mode can vary spectral components in a range of up to a factor of $\sim 1,5$. A custom-written OPO control software proved to be one possible solution excluding the OPO as a source for spectral distortions and can be of help to other research groups, who are active in the field. The experiments were performed with CARS as a contrast mechanism but are also valid for hyperspectral SRS spectra due to the similar dependence to the pulse length. During the experiments the pulse length was permanently recorded to show the contrast to a static OPO tuning mode. This is not necessary using the dynamic OPO control mode in daily HS-CARS data acquisition due to the coincidence of a repro-

ducible and constant pulse length of the OPO generated pump beam with the highest possible output power of the OPO at a specific wavelength. This relation was shown investigating the OPO behavior at pure samples, where the cavity length as well as the LBO crystal temperature were identified as main influence on the OPO tuning. These findings are exploited for the presented dynamic optimization mode via a home-written Matlab-based control program. Hence, also research groups without an autocorrelator are able to perform undistorted HS-CARS scanning utilizing our findings for their OPO control mode, if they use their own program, or adapt our proposed program for their setups. In addition to that the general performance of the microscopy setup in terms of precision of spectral calibration (comparison to spontaneous Raman spectroscopy) as well as in mechanical and focal stability (U2OS cell repeat experiments) were quantitatively evaluated and the reproducibility proved to be sound and solid.

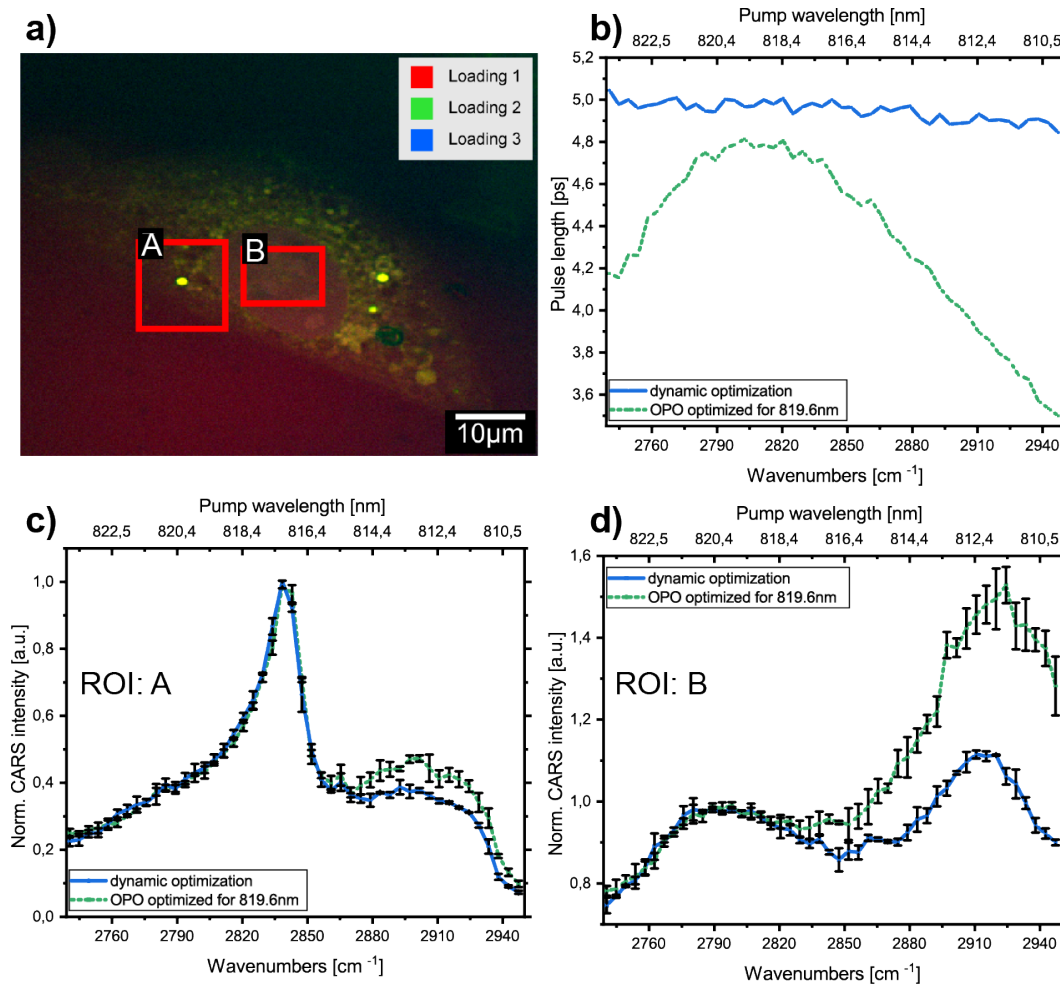


Figure 46 – OPO operation modes influence pulse length visualized in HS-CARS imaging of a U2OS cell

a) shows a PCA analysis of an HS-CARS image stack of 47 images acquired in a spectral range of $2738 - 2947\text{cm}^{-1}$ with a step size of $\sim 4,7\text{cm}^{-1}$ of a fixed U2OS sample; three characteristic PCA loadings are chosen for a false-color coding (right box). Two ROIs are selected for extracting the spectral response of the CARS intensity: ROI A contains a lipid droplet (yellow dot), ROI B covers a part of the cellular nucleus. During the repeated hyperspectral wavelengths scan two modes for OPO operation are realized sequentially: dynamic optimization mode and static optimization of the OPO at $819,6\text{nm}$. **b)** depicts the pulse length of the different scanning modes during hyperspectral tuning, a constant value of $\sim 4,9\text{ps}$ is achieved for the dynamic optimization (blue solid line), the static OPO setting leads to a change in pulse length from $4,8 - 3,5\text{ps}$ (green dashed line). This leads to a distortion of the HS-CARS spectra shown for ROI A (lipid droplet) in **c)** and for ROI B (nucleus) in **d)**: Normalizing the CARS intensity on one spectral resonance (2840cm^{-1} for **c)**, 2780cm^{-1} for **d)**) a clear difference between both modes can be observed in the spectra at the molecular resonance at 2920cm^{-1} . For each OPO mode the hyperspectral scan was repeated three times in alternating order, the error bars indicate the standard deviation of the different scans. Published in [Pilger et al. [2018]].

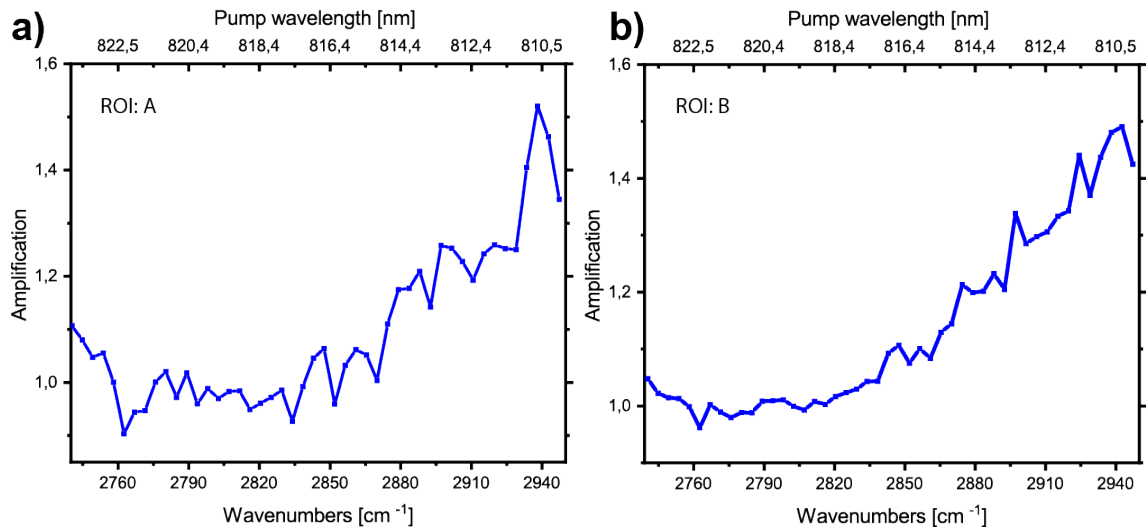


Figure 47 – Relative difference in CARS signal during hyperspectral scanning due to OPO induced pulse length variation

a) shows the relative variation of the normalized CARS signal of ROI A (fig. 46, lipid droplet) by dividing the curve with varying pulse length (fig. 46, green dashed line) by the spectrum having constant pulse length (fig. 46, blue solid line). An enhancement in CARS signal of up to 1.52 is observed at 2940cm^{-1} due to the OPO induced pulse length variation. **b)** shows the comparison for ROI B (nucleus area) indicating a change in relative CARS intensity of up to 1,49 at 2940cm^{-1} . Published in [Pilger et al. [2018]].

4.4. Applying HS-CARS imaging to biological research questions

In the following section the successful application of HS-CARS answering specific biological questions will be demonstrated emphasizing the comparison of the hyperspectral imaging in one image plane to data acquired at a fixed resonance imaging the entire volume of the sample by z-scanning.

4.4.1. Analyzing the influence of copper on the fitness parameters of *Caenorhabditis elegans*

In a collaboration with the research group of Prof. Walter Traunspurger, Bielefeld University, *Caenorhabditis elegans* were analyzed during a life history trait experiment under the influence of copper concerning their fitness parameters [Fueser et al. [2018]]. Here, the lipid storage is imaged by probing the 2845cm^{-1} resonance via CARS microscopy as an indicator of energy for cell survival, which is closely connected to the influence of toxic stress on the organism [den Hartigh et al. [2010], Yen et al. [2010]]. Changes in the lipid distribution due to aging are already reported to influence the lifespan of *C. elegans* [Hou and Taubert [2012]] and the correlation of fat storage, oxidative stress and lifespan is found [Yen et al. [2010]], showcasing the close relation of life history traits during the life cycle experiment and the lipid analysis utilizing CARS microscopy. The label-free manner of the image acquisition is especially beneficial to this problem, due to the already found misleading interpretations of the amount of lipid storage by utilizing fluorescent staining for microscopic imaging [Yen et al. [2010], Yi et al. [2014]] as well as a different behavior of *C. elegans* in the food uptake, metabolic rates and distribution properties [Hellerer et al. [2007]] and also the change in molecular physical properties [Cheng and Xie [2015]] due to the fluorescent dyes.

In the present study¹⁶ the life history trait was performed over 42 and 43 days on a control group (24 nematodes) as well as a group treated (24 nematodes) with low¹⁷ (EC5) and moderate (EC20) concentrations of copper based on the experimental design of [Muschiol et al. [2009]].

¹⁶Sample preparation and additional experiments were performed by Mr. H. Fuser during his master thesis [Fueser [2016]] in the research group of Prof. Traunspurger.

¹⁷Not investigated by (HS)-CARS.

4.4.2. Volumetric CARS imaging reveals changes of the lipid storage in *C. elegans*

For the investigation of the lipid storage utilizing CARS 4 adult nematodes of the control as well as from the EC20 group were fixed in a 4% para-form aldehyde solution after their natural death. Due to the absence of lipid droplets in the pharynx region of the *C. elegans* the vulva and the tail region were selected for the imaging (fig. 48 **a**). The $C-H_2$ stretching mode at 2845cm^{-1} was probed by $816,7\text{nm}$ as pump and 1064nm Stokes beam applying in total less than 30mW of focal power avoiding any damage to the sample having a pixel dwell time of $25,6\mu\text{s}$. The detected CARS signal at 660nm was isolated by the filter set already described in (4.2). For each region a volumetric z-scan was performed covering the entire diameter of the specimen of $13 - 32\mu\text{m}$ with a step size of 500nm (27 to 65 slices). The study contains 187 images of the control and 135 images of the EC20 group. The analysis of the CARS data was performed by applying a background subtraction and creating a composition of the z-stack into one single two-dimensional projection utilizing the *FIJI* plug-in *VolumeJ 1.8* [Abramoff et al. [2004]] for the final quantification of the lipid content for vulva (fig. 48 **b**) and tail region (fig. 48 **c**), respectively. After adaptive thresholding (range of 110-255 gray values) the images were converted into a binary form for the final identification of lipid areas of the nematodes by the *FIJI* tool *particle analyzer* [Schindelin et al. [2012], Rueden et al. [2017]]. This way the total area of lipids per nematode was calculated by summing up all voxels identified as lipids (fig. 49 **a**) and also the mean area per detected lipid increment was calculated (fig. 49 **b**). Dividing the total area of lipids by the nematodes' total area [after Hellerer et al. [2007]] the relative lipid area fraction was calculated (fig. 49 **c**). By sorting the identified average areas of lipids into area classes of 6 intervals ($2 - 10$, $10 - 20$, $20 - 30$, $30 - 40$, $40 - 50$, $> 50\mu\text{m}^2$) the distribution of the occurrences was studied (fig. 49 **d**). The data indicates a strong influence by the copper treatment on the lipid distribution of the nematodes; the lipid-filled areas as well as the body fraction, which is used for lipid storage, are reduced in adult nematodes of the EC20 group in comparison to the control group showing high significance. Considering the distribution of lipid area size the EC20 group shows the absence of larger lipid increments ($> 30\mu\text{m}^2$), instead the number of small lipid areas ($\leq 10\mu\text{m}^2$) was increased. This findings indicated, that CARS microscopy is a powerful tool to study the physiological mechanisms in *C. elegans* exposed to copper as a toxic substance. The life history trait experiment provides data on hatching time, lifespan, fertility and reproduction of the nematodes, which also proved to be strongly affected by the copper exposition. The detailed findings and conclusions of these experiments will not be included into this thesis.

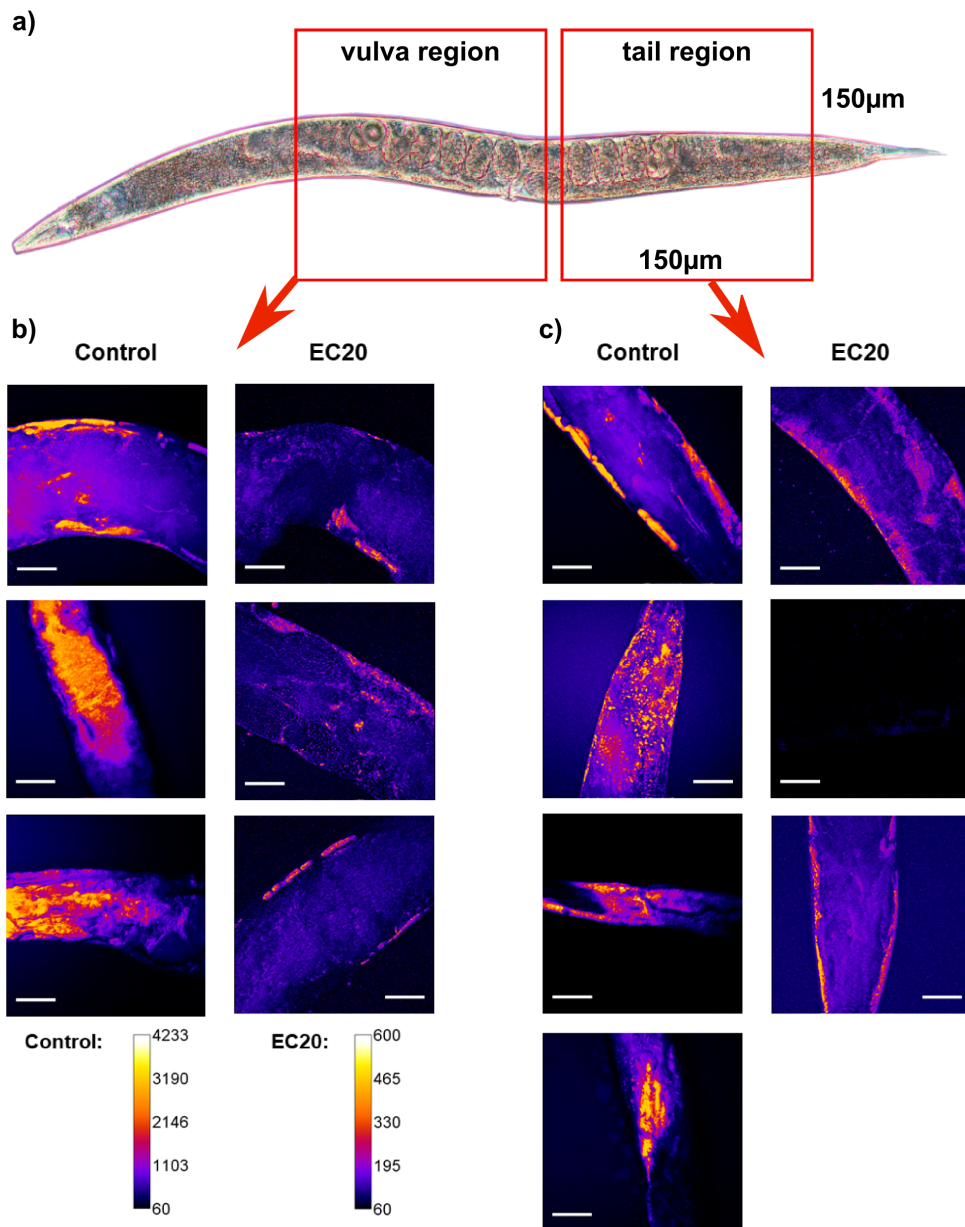


Figure 48 – 3D CARS imaging studying the lipid distribution in *C. elegans* during life history trait **a)** shows a bright-field image of an adult *C. elegans* depicting the areas selected for CARS microscopy (red boxes, vulva and tail region, respectively). In **b)** 3D projections of CARS probing the 2845cm^{-1} resonance are presented imaging the vulva region of nematodes of the control group (left column) and the EC20 treatment (right column, respectively). The corresponding data of the tail region is shown in **c)** highlighting lipid-rich structures such as tissue or lipid droplets of seven adults. Each image shows another replicate. The scale bar indicates $30\mu\text{m}$. Published in [Fueser et al. [2018]].

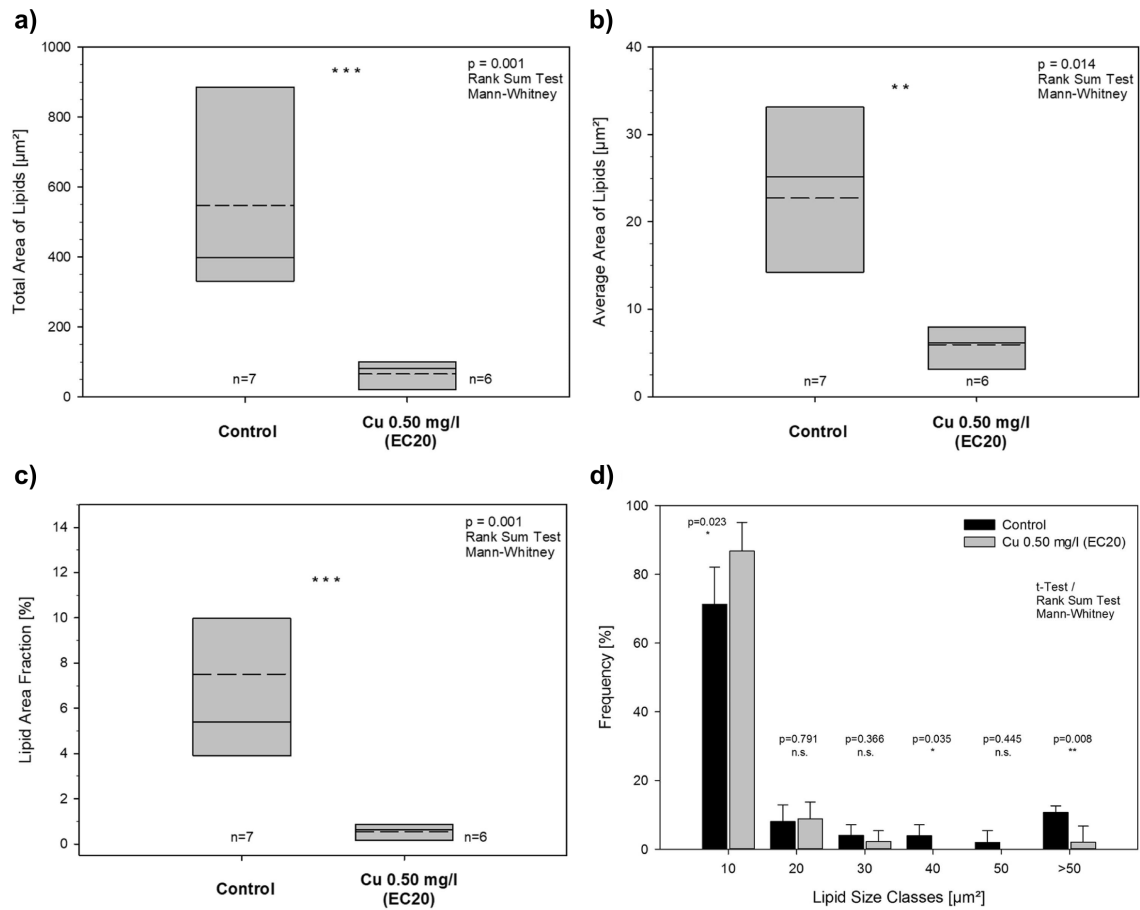


Figure 49 – Quantitative analysis of 3D CARS data determining lipid size and content of control and EC20 treatment

After summing the 3D-CARS data into two-dimensional arrays the area containing lipids is identified via thresholding; **a)** compares the total lipid area of control group and EC20 treatment, **b)** the average area of lipids, respectively. In **c)** the relative lipid area fraction is calculated by dividing the total area of lipids by the area of the nematode. By sorting the findings of the total lipid area into 6 size classes the relative size frequency was determined (**d**). Testing for significance: ***: $p < 0,001$, **: $p < 0,01$, n.s.: $p < 0,05$, $n = 7$, median depicted by solid line, mean by dashed line, respectively. Error bars represent standard deviation. Published in [Fueser et al. [2018]].

4.4.3. Hyperspectral CARS scanning assessing false positive identification of lipid contents

Following, the volumetric CARS data will be contrasted to hyperspectral CARS imaging in one focal plane covering the wavenumber range of $2664 - 3117\text{cm}^{-1}$ in terms of information content and applicability to the biological question. The specimen was an adult nematode of the control group fixed in 4% para-formaldehyde after the natural death. The overall focal power was set below 54mW while scanning the pump beam from $799 - 829\text{nm}$ in $0,3\text{nm}$ step size applying a pixel dwell time of $13\mu\text{s}$. During the hyperspectral scan 101 images were acquired and finally analyzed with a principal component analysis (PCA, compare Schie and Huser [2013]) in order to separate the different spectral components of the response of the specimen (fig. 50 a). The first 4 loadings of the PCA showed substantial information content and were selected for the illustration of the nematode, where the principal component 3 indicates the lipid response, PC4 showed predominantly the protein content (fig. 50 b). The lipid content in the body of the nematode can be clearly identified due to the characteristic spectral response, which leads to a clear separation to other parts such as the digestive system or the germ cells. Here, the full spectral response of all components of the nematode enables this clear separation, which is more difficult and reliable probing solely the 2845cm^{-1} resonance due to unspecific signal contributions by the non-resonant background of CARS microscopy. Here, a smaller mistake in false positive identification of lipid droplets can be expected. On the contrary, the extended time consumption of the hyperspectral CARS imaging ($\sim 30\text{mins}/z - \text{plane}$) in comparison to standard CARS imaging ($\sim 15\text{sec}/z - \text{plane}$) hinders a high number of replicates. Even one full volumetric analysis of one nematode assuming an average number of 35 z-slices results in a measuring time of $17,5\text{hours}$ in the case of hyperspectral CARS. In the conclusion a combination of both techniques is a promising strategy, where the hyperspectral data can evaluate the quality of the volumetric standard CARS images in terms of false positives at lipid droplet identification as well as to grant deeper insight into other parts of the nematode possibly affected by the copper treatment. Thus, future research on this specimen should likely combine both methods granting high data quality as well as high throughput.

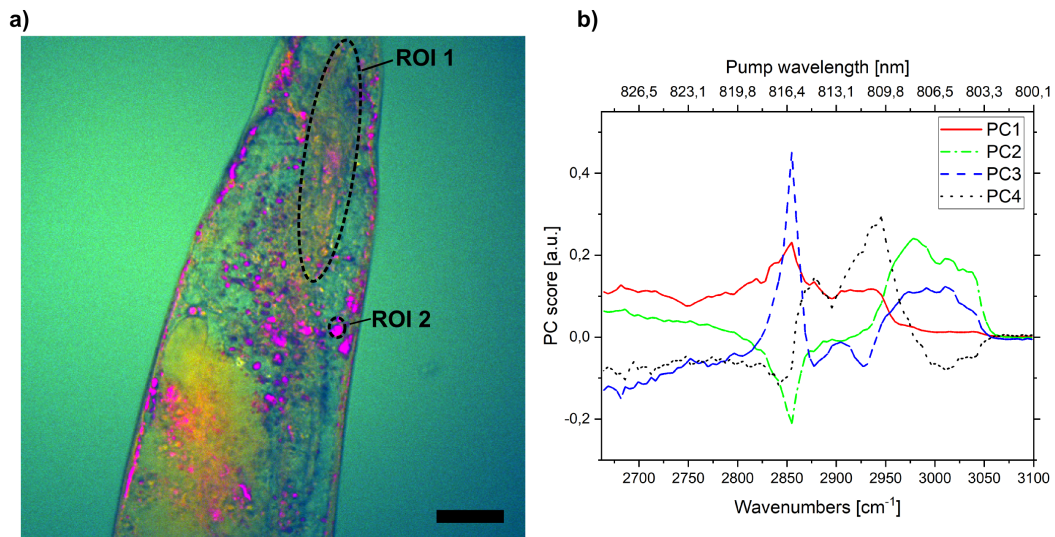


Figure 50 – PCA analysis of a hyperspectral CARS image scan of a *C. elegans* sample. An adult nematode was investigated by a hyperspectral CARS scan from $2664 - 3117\text{cm}^{-1}$ wavenumbers by tuning the OPO via a customized Matlab program. **a)** shows the image of a PCA analysis performed on the image stack of the 101 images, the first 4 loadings were selected as important contributions for the image and were color-coded for the final image. ROI 1 shows the digestive tract, ROI 2 shows a randomly selected lipid droplet. A clear separation is achieved between desired lipid contribution and other compartments of the *C. elegans*, especially the non-resonant background, inevitable in CARS imaging. The scale bar indicates $20\mu\text{m}$. **b)** shows the corresponding scores of the PCA's first 4 loadings according to the Raman resonance probed by the combination of the fixed Stokes beam at 1064nm and the tuned pump beam. PC3 (blue) indicates the lipid contribution (at $\sim 2845\text{cm}^{-1}$), PC4 (black) has a peak at 2940cm^{-1} , which corresponds to the protein contributions.

4.4.4. Visualizing the differentiation of primary human alveolar epithelial cells by label-free imaging techniques

As conclusion of the research on *C. elegans* combining standard CARS imaging with hyperspectral scanning this scheme of analysis is adapted to an other specimen of interest. In a collaboration with the research group of Prof. Maike Windbergs, Goethe University Frankfurt a. M., the differentiation of primary human alveolar epithelial cells was investigated with several imaging modalities such as fluorescence microscopy, spontaneous Raman microscopy as well as CARS and hyperspectral CARS microscopy [Vukosavljevic et al. [2019]]. The novelty of the study is the combination of spontaneous Raman microscopy and both CARS techniques as label-free imaging modalities for the comparison to classic fluorescence based microscopy. The differentiation of alveolar type II (ATII) cells located in the peripheral human lung into type I (ATI) cells is of interest because of the generation of the air-blood barrier. ATI cells are forming a cellular barrier to the respiratory tract while the ATII cells are producing, accumulating and secreting the alveolar surfactant, which is lining the cells in the deep lung area. In addition to that the ATII cells are responsible for replacing ATI cells via differentiation into type I, which is accompanied by morphological as well as molecular modifications in terms of cellular lipid content and expression of specific marker proteins studied already with confocal laser scanning microscopy, rt-PCR, flow cytometry and immunoblotting [Fuchs et al. [2003], Campbell et al. [1999]]. The morphological changes during the differentiation have been visualized in the past by scanning electron microscopy as well as transmission electron microscopy [Cheek et al. [1989], Fuchs et al. [2003]] showing the flattening and wide spreading of the cells. The spreading of up to 90% of the alveolar surface area allows the in vivo gas exchange of the blood. Summing up the prior work on the differentiation of ATII into ATI cell type the analysis methods required fixation and disruption of the cells [Pygall et al. [2007]]. Therefore, spontaneous Raman scattering was applied in imaging mode on this problem for gaining insight into the Raman shift of the cells during differentiation accessing their molecular changes [Kann et al. [2015]], which was performed with a commercial confocal Raman microscope (*WITec*, alpha 300R+)¹⁸. For backing up the conclusions of this study fluorescence microscopy (*Zeiss*, Zeiss LSM710) as a well-established standard was applied to ensure observing the differentiation process by utilizing Laurdan staining for the visualization of the lipid content. The data of spontaneous Raman microscopy as well as fluorescence microscopy will not be shown in this thesis.

¹⁸Spontaneous Raman and fluorescence microscopy were performed by Dr. B. Vukosavljevic as part of [Vukosavljević [2018]].

4.4.5. Volumetric CARS imaging enables z-sectioning and shows differentiation process over time

The combination of volumetric CARS microscopy showing the differentiation process probing the 2845cm^{-1} resonance for the visualization of the lipid content during a time period of 7 days as well as hyperspectral CARS imaging at selected regions of interest (ROIs) of samples at days 1, 2, 3 is centered in this paragraph. The volumetric CARS microscopy was performed by scanning the cell samples with a step size of 300nm in z-direction resulting in an image stack of 30 to 40 images per replicate and day covering the entire cellular volume (fig. 51). The focal power of the Stokes and pump beam were set to be below 30mW , isolating the CARS signal with the previously described optical filter set combination. By applying a twofold zoom the field of view was $75\mu\text{m} \times 75\mu\text{m}$ while acquiring $512 \times 512\text{px}$ with a pixel dwell time of $31,25\mu\text{s}$. This results in an acquisition time of 6mins for one 3D-CARS scan per replicate. For the visualization of the data *FIJI- Volume Viewer* [Schindelin et al. [2012], Rueden et al. [2017]] was utilized to generate a conversion summing up all z-slices into one top view. At the beginning of the experiments we observed cell diameters of $\sim 10\mu\text{m}$ at day 1. Over time cell growth started and more lipid vesicles could be found and the cells were grouped together after day 3. Days 5 and 7 show strongly enlarged, converging cell structures, which exceed even the field of view. These findings were also in good accordance to the other methods applied on the specimen such as spontaneous Raman microscopy as well as fluorescence microscopy (see also [Vukosavljevic et al. [2019]]). In order to back up the claim of applying CARS microscopy to image the differentiation process of the ATII type cells into ATI type repeat experiments of days 1 to 5 were performed on more replicates, while additional data of day 4 is presented fitting in the overall findings of the differentiation process (fig. 52). In the case of rather low CARS signals it proved useful to add dotted green lines marking the cellular border as well as blue dotted lines marking the cell nucleus as guide to the eye. For showing a sufficient z-sectioning capability of the setup, which is capable to differentiate between the nucleus and the lipid filled cellular volume, selected 3D data is provided showcasing single consecutive z-scans of cells of day 1 (fig. 53) and day 3 (fig. 54), respectively. In fig. 55 the 3D-CARS data of day 2 is presented in a 90° rotated side view illustrating the z-extent of the ATII cells. Here, also the z-sectioning capability can be evaluated due to the clear display of the cellular border. However this type of presentation of the 3D-CARS data is limited to a strong signal-to-background ratio occurring at high lipid contents in the cells, which were observed predominantly at the first 3 days of differentiation.

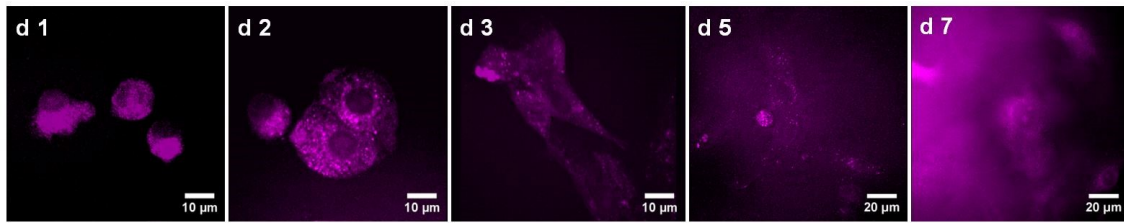


Figure 51 – Comparison of representative CARS images illustrating the differentiation process of ATII into ATI cells over 7 days

The differentiation process from ATII cells into ATI imaged by volumetric CARS imaging; 3D projections are utilized for the illustration of the lipid distribution and the extent of the cells, while probing the 2845cm^{-1} CH_2 stretching resonance. The projection made with *FIJI Volume Viewer* sums the volumetric data of every z-scan for a top view. The cellular extent at day 1 is rather small, the shape is round. Over time the cells flatten out and the number of lipid droplets is decreasing until at day 7 the field of view is filled completely by the ATI cell. Published in [Vukosavljevic et al. [2019]].

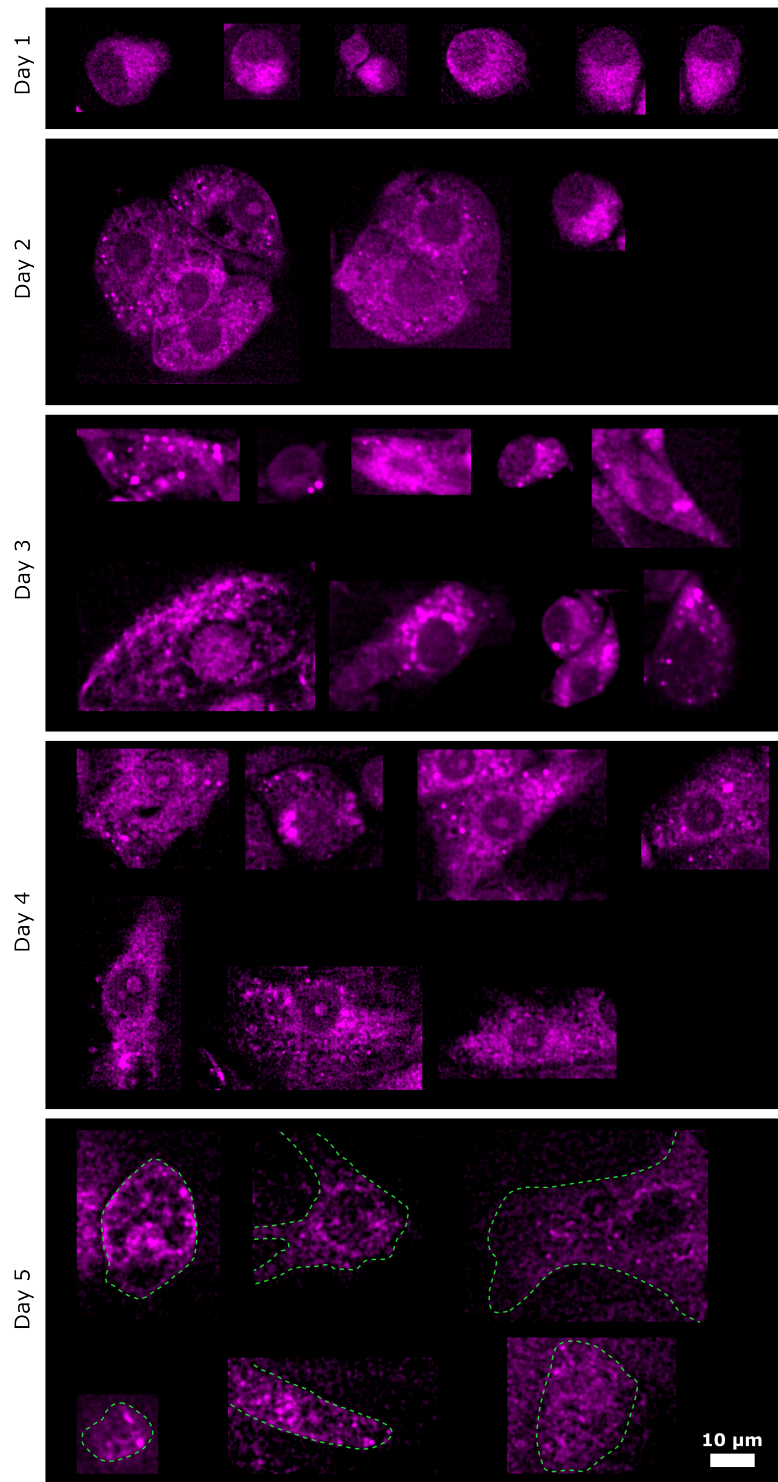


Figure 52 – Repeat experiments during the differentiation process of ATII cells applying CARS imaging at different time points

For backing up the claims on the differentiation process of the cell samples several replicates were imaged at the selected time points. Here, additional data on day 4 is included confirming the claim of the differentiation from ATII into ATI type. At day 5 the lipid content is already strongly reduced resulting in a rather weak CARS signal, therefore, the green dashed line is included for marking the cellular border and to guide the eye. Published in [Vukosavljevic et al. [2019]].

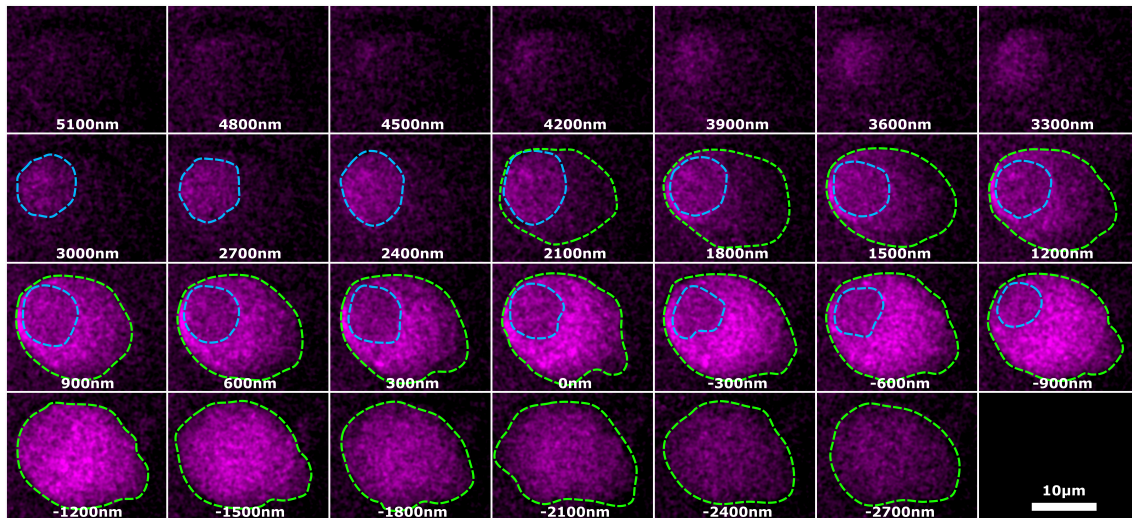


Figure 53 – Representative CARS z-scan on ATII cells at day 1

Volumetric imaging is performed for visualizing the lipid content of the cell samples by applying a step size of 300nm in z-direction. Here, a sample of day 1 is shown scanning a z-depth of $5,8\mu\text{m}$. Due to the low lipid content of that particular time point the green dotted line is added marking the cellular border as a guide to the eye, the blue dotted line marks the nucleus, respectively. The cell appears to be round and has an diameter of $\sim 19\mu\text{m}$. Published in [Vukosavljevic et al. [2019]].

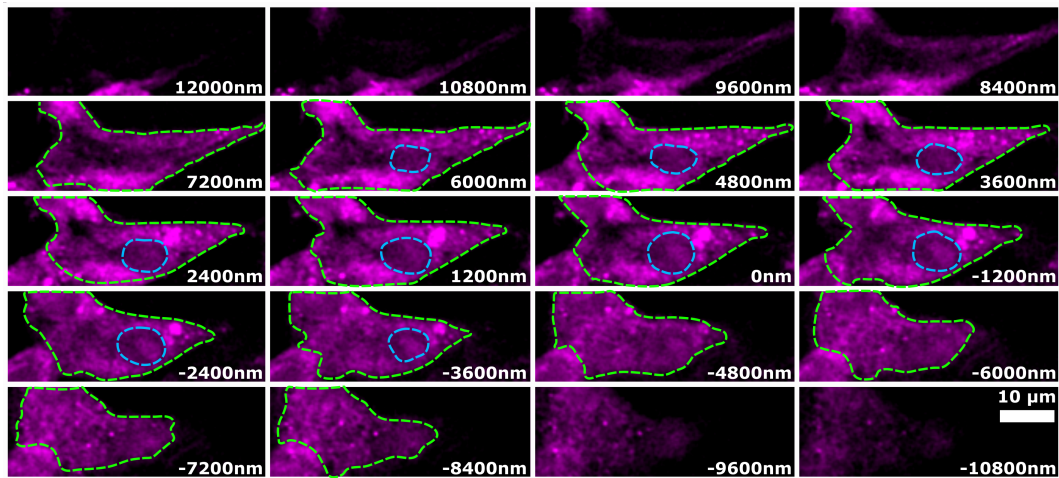


Figure 54 – Representative CARS z-scan on the differentiation of ATII cells into ATI at day 3

A representative sample after 3 days of differentiation is z-scanned in the range of $21\mu\text{m}$ with a step size of 300nm , while in the image a step size of $1,2\mu\text{m}$ is selected for presentation. The cellular area is larger compared to day 1 and the cell's shape is not round anymore, but has flattened out. The green dashed line depicts the cellular border guiding the eye, the blue line depicts the nucleus, respectively. Published in [Vukosavljevic et al. [2019]].

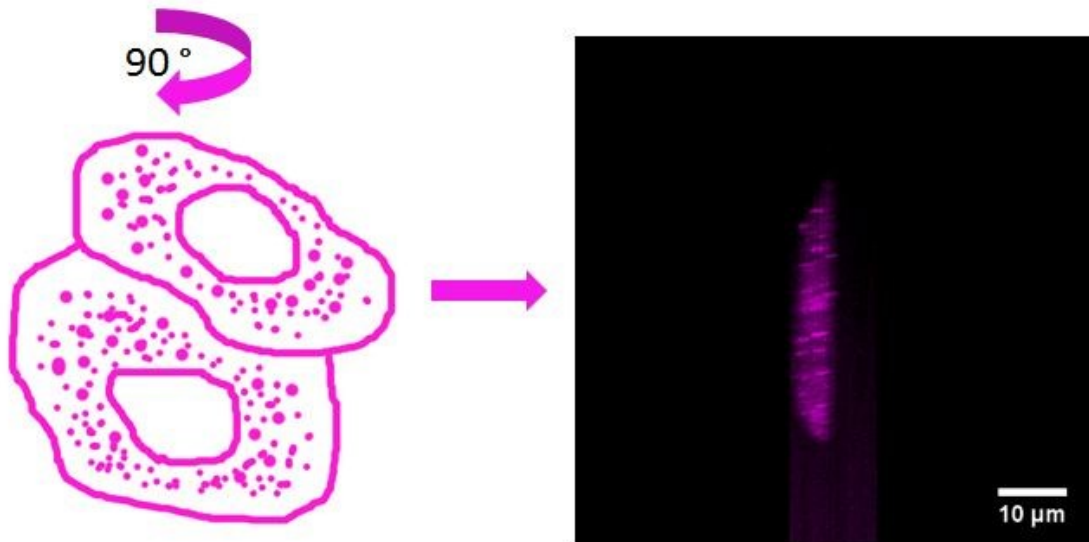


Figure 55 – 3D projection of volumetric CARS data at a rotation angle of 90° of ATII cell differentiation at day 2

An other way of presenting the volumetric CARS data of the cell samples is presented above: the *FIJI* plug-in *Volume Viewer* is utilized for enabling a 90° rotation of the viewing plane gaining insight into the z-expansion of the cells during the differentiation process. This method is only applicable having higher signal levels due to a high lipid content. The corresponding top view image can be found in fig. 51 d2. Published in [Vukosavljevic et al. [2019]].

4.4.6. Non-negative matrix factorization applied on HS-CARS scans reveals cellular compartments

To confirm the claims made due to the volumetric CARS imaging of distinguishing the lipid rich cellular volume from the nucleus hyperspectral CARS imaging was performed in one focal plane covering a range of $2700 - 3050\text{cm}^{-1}$ by tuning the pump beam from $826,5 - 803\text{nm}$ with a step size of $4,7\text{cm}^{-1}(0,3\text{nm})$, and applying a focal power of less than 30mW . The pixel dwell time was adapted to the signal to background due to the current lipid content of the particular day of differentiation as well as to the selected zoom level ($2\times$ or $3\times$) ranging from $6,4 - 12,8\mu\text{s}$ while the total scanning time per replicate was for days 1 and 3 37mins and for day 2 52mins . On the data sets the non-negative matrix factorization (NNMF) as a multivariate statistical analysis tool was performed by a Matlab-based custom written program¹⁹ based on the Matlab Statistics tool box [Matlab [2012]], which performed the differentiation of the different spectral components of the specimen, such as lipid rich vesicles (2845cm^{-1}) and cellular proteins (2930cm^{-1}) as well as the non-resonant background (fig. 56).

¹⁹The development of the NNMF analysis program was predominantly performed by Mr. Henning Hachmeister, also in supervision to the NNMF analysis related work in the master thesis of Mr. P. Greife.

For this purpose a ROI was selected, where an offset subtraction and a binning in a 4×4 *pixel* frame was performed reducing the arbitrary signal fluctuations, which can hinder the successful application of the NNMF algorithm by the non-relevant changes in intensity due to noise. In the ROI 4 image subsections were selected showing a characteristic spectral response, which were utilized as initial values inputted into the NNMF analysis. The NNMF analysis separates the original input data A , as the original matrix, into the two non-negative matrices W and H with the definite rank number k representing the unique vibrational signatures, which were as a prior knowledge inserted into the algorithm by selecting the subsets in the input data. This step also grants the reproducibility of the performed analysis. The NNMF works in an iterative manner in order to find W and H , while minimizing the root-mean-squared residual between A and $W \bullet H$ [Berry et al. [2007]]. Applied on the presented images W and H are representing k times a two-dimensional image and the corresponding vibrational response, respectively. Here, each two-dimensional image section of W is having a corresponding intensity distribution of the vibrational response imprinted on H . For the final visualization W is false-color coded and illustrated by *FIJI*. For the link to the spectral response indicated by the false-color coding the eigenvectors found by the NNMF for the entire image are shown next to the images. The successful separation of lipid-rich vesicles (depicted in magenta) in the cellular volume and the cell's nucleus (blue) can be observed, while the background is identified and depicted in black color. For the investigation on the signal-to-background level of the provided NNMF analysis the eigenvectors of the specific channels of interest are presented in a small sub-ROI, which show a characteristic area of the specimen such as e.g. the nucleus showcased in the data set of day 2 (fig. 57). The clear peak structure in the spectral behavior of the eigenvector indicates a sufficient signal-to-noise ratio of the input data. Comparing the eigenvector spectra of lipids (fig. 57 a) to proteins indicating the nucleus (fig. 57 c) a distinct spectral discriminability becomes apparent. The presented hyperspectral data showed good accordance to the volumetric CARS data in terms of nucleus identification and also fitted well to the spontaneous Raman data (not shown here). In general the study proved that the differentiation of ATII into ATI type primary human alveolar epithelial cells can be visualized with label-free techniques allowing to study morphological and biochemical changes as well as the storage and secretion of the lung surfactant without the labeling influences.

The benefits of the NNMF analysis utilized in this study over the prior presented PCA analysis are the always positive values of the NNMF eigenvectors as well as the input of prior defined spectral information, which enables an easier interpretation of the results. Furthermore, the NNMF analysis is less affected by undesired influences

of signal gradients, which can occur due to the rolling ball effect in CARS microscopy caused by the spatial mismatch of Stokes and pump beam at the outer regions of the image or due to a tilted sample plane in relation to the focal plane, which often occurs at imaging tissue sections prepared by a microcryotome on thin glass slides.

Summing up the results on the hyperspectral CARS imaging it was possible to apply these technique to relevant biomedical problems, while the volumetric CARS imaging at one particular molecular resonance enabling fast imaging for a high number of replicates in combination to the hyperspectral scanning proved to be a powerful tool. Here, both methods could play on their advantages, while their intrinsic drawbacks were balanced, especially the rather slow acquisition speed and lacking volumetric information of HS-CARS.

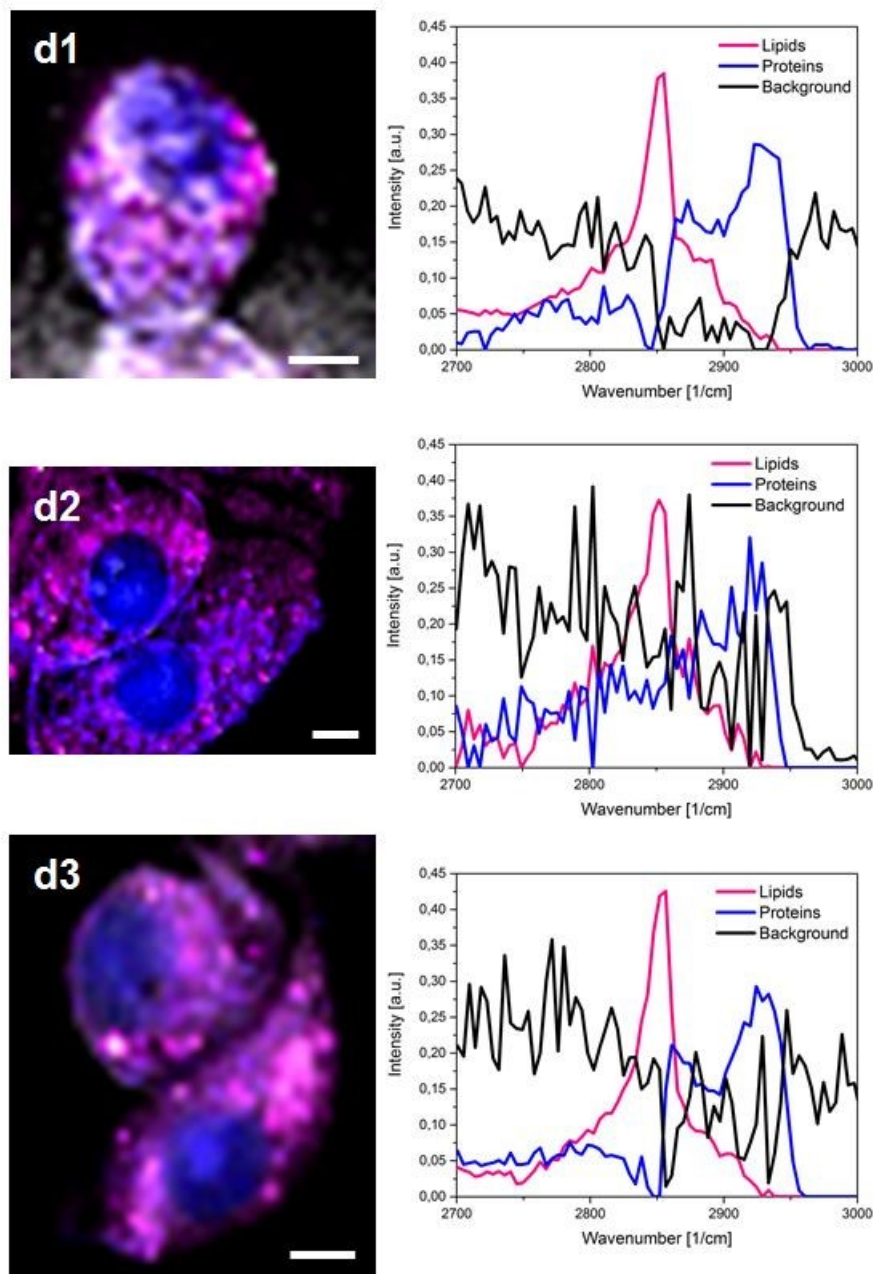


Figure 56 – Hyperspectral CARS imaging of ATII differentiation process utilizing NNMF for decoding spectral information

For the hyperspectral CARS imaging a range of $2700 - 3050\text{cm}^{-1}$ was scanned with a step size of $4,7\text{cm}^{-1}$ applying a total focal power of less than 30mW over time (days 1 to 3 - rows d1 to d3). A non-negative matrix factorization (NNMF) analysis was performed on each image stack producing three individual channels which correspond to the lipid rich environment (magenta), proteins (blue) indicating the nucleus and the background (black) used in the overlay images on the left. The scale bar indicates $1\mu\text{m}$. On the right the NNMF eigenvectors are shown, which are associated to the different spectral components averaged over the entire image. Increasing lipid droplet formation is observed on days 1 to 2. At day 3 the cellular volume starts to increase, while the size and number of the lipid droplets is continuously growing. Published in [Vukosavljevic et al. [2019]].

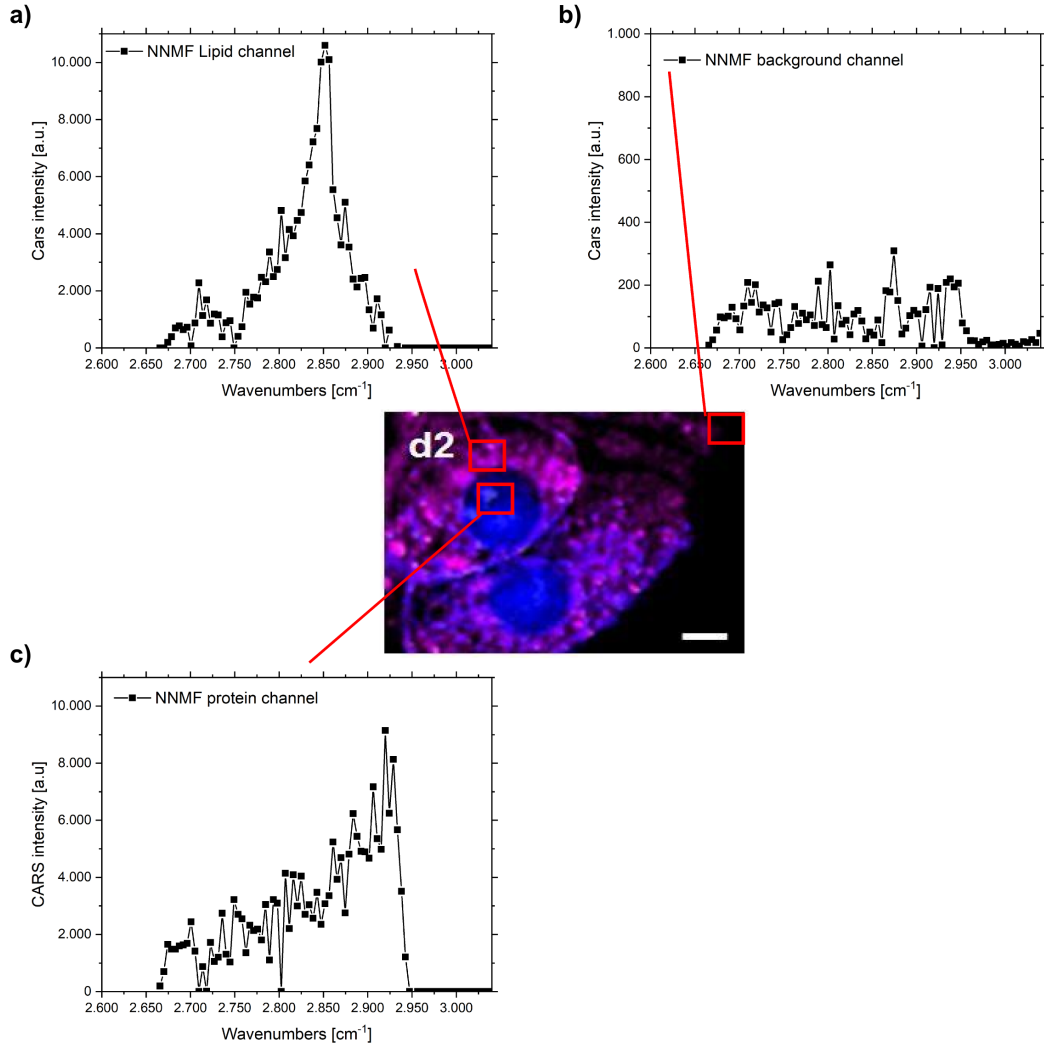


Figure 57 – Investigating the signal-to-background behavior at selected ROIs utilizing NMF analysis on hyperspectral CARS data at day 2

The data set of fig. 56 day 2 (d2 - false-color encoded image in the middle) is utilized to showcase the ability of the NMF analysis to distinguish between the different presented channels by the generation of eigenvectors with sufficient signal-to-background ratio. Therefore, three characteristic regions of interest (ROIs) are selected showing the predominant spectral eigenvector value for the ROI. In **a)** the ROI is chosen to be from a lipid rich cellular area (depicted in magenta), the eigenvector shows a strong peak at the 2845cm^{-1} CH_2 resonance. A ROI of the area outside of the cell is selected in **b)**, the eigenvector shows an even, slightly fluctuating spectral behavior representing the non-resonant background. **c)** is selected at the nucleus region of the cell (blue color coding), the eigenvector has a peak at the protein resonance at $\sim 2930\text{cm}^{-1}$. Note that the data points are connected as a guide to the eye. The scale bar indicates $1\mu\text{m}$. Published in [Vukosavljevic et al. [2019]].

4.5. Resolution enhancement utilizing structured illumination in scanning-based non-linear microscopy

Recently notable efforts were performed in biomedical research in order to circumvent the diffraction limit in super-resolution fluorescence microscopy by various methods such as **STED** (stochastic emission depletion) [Hell and Wichmann [1994], Klar and Hell [1999]], **d-STORM** (direct stochastic optical reconstruction microscopy) [Fölling et al. [2008], Wolter et al. [2010], Heilemann et al. [2008], Rust et al. [2006]] as well as **SIM** (structured illumination microscopy) [Lukosz and Marchand [1963], Gustafsson et al. [2008], Gustafsson, M. G. L. [2000, 2005]] to name just some major applications in this field. All have the need of a sufficient fluorescence label in common enabling the various methods a resolution of up to $\sim 20 - 50nm$ in stochastic-based and $\sim 180 - 200nm$ in linear structured illumination-based microscopy [Wu and Shroff [2018], Schermelleh et al. [2019], Sahl et al. [2017]]. In the following paragraph the combination of an enhanced resolution and a label-free contrast mechanism by CARS microscopy is explored trying to combine the benefits of the super-resolution fluorescence-based techniques without the need for fluorescent labels, which are laborious, toxic and depending on the specimen can not be applied at all due to rigid cell walls or undesired autofluorescence of cellular compartments. Approaches for a resolution enhancement in CRS-microscopy were demonstrated utilizing the saturation of the CARS signals or the beam shaping of the participating pump or Stokes beam [Betin et al. [1975], Duncan et al. [1981], Tolles et al. [1977], Yonemaru et al. [2015], Kim et al. [2012]]. More recently the saturation of the SRS signal was demonstrated by applying very high focal powers and, therefore, limiting the range of samples and increasing the phototoxicity [Gong et al. [2019], Gong and Wang [2014]].

For the realization of enhancing the resolution in the presented CRS-setup the combination of structured illumination with CARS as a heterodyne detected contrast mechanism was chosen. Here, two strategies are pursued in order to show the resolution enhancement: first, a scanning mirror-based striped illumination pattern generation for two-photon excited fluorescence is introduced showing significant enhancement in contrast and resolution. The selected specimen are fluorescent bead samples, stained murine tissue sections as well as auto-fluorescent *Convallaria majalis* sections imaged on the TriM Scope II in a collaborative effort with *LaVision Biotec*, Germany. The purpose of these measurements is showing the easy implementation of the scanning mirror-based structured illumination due to the use of almost all standard components in state of the art two-photon microscopes by just adding a sCMOS camera for the final detection of the images. Second, this concept is transferred to the presented CARS

microscopy setup: utilizing the experience in epi-CARS detection [Pilger [2014]] concerning the signal strength in combination with the use of a sCMOS camera instead of a PMT the final setup contains a 4π detection in order to maximize the signal by using forward CARS for the camera-based detection. Here, the mechanical stability (see 3.2) as well as the optimal setting of the pattern parameters turned out to be crucial. The presented data on pure samples such as polystyrene bead samples or DMSO solutions can be seen as the first successful realization of structured illumination in combination with CARS for resolution enhancement and contrast improvement.

4.5.1. Generating striped illumination pattern by addressing the galvanometric scanning mirrors

Realizing the striped illumination patterns by using the galvanometric scanning mirrors was explored at first on the CRS-microscope by synchronizing the AOM for rapid intensity switching due to the current position of the mirror (see also 3.2.1). Applying the patterns to pure dye solutions the accuracy and timing of the pattern was checked and first data were acquired on bead samples by using the $1064nm$ laser source for two-photon excitation. Here, the pattern fineness and the setting of suitable values for pattern line spacing and rotation angles were tested and evaluated for best modulation depth and signal-to-noise ratio in the raw data. The finer the pattern the lower the modulation depth of the illumination pattern will get due to scattering effects in the sample, which will illuminate also the non-illuminated areas to a certain extent. For best results a high fluorescence signal strength was required, which was realized by transferring the experiment to a setup capable of femto-second laser excitation of the fluorophores. Therefore, an industrial collaborative project was initiated with the company *LaVision Biotec*, which is developing the two-photon scanning microscope TriM Scope II. This system was specifically modified as platform for the presented two-photon excited fluorescence data sets in this paragraph²⁰. The excitation source was a $\sim 140fs$ pulsed laser system (*Coherent*, Chameleon Ultra I), with $690 - 1040nm$ tunable wavelengths range in combination with a dispersion compensation stage realized through a prism compressor. The generation of the striped illumination pattern at the TriM Scope II setup was realized by a specifically adapted software program²¹ written in *Python*, which allowed to change the line spacing, angle of rotation as well as the phase settings of the excitation pattern. In addition to that the program addressed an inbuilt EOM in order to block the excitation beam when the scanning mirrors were illuminating an undesired position in the sample. A $60\times$ oil immersion

²⁰The work was supported by Dr. H. Spiecker, Dr. M. Schütte, Mr. M. Ruoff, LaVision Biotec.

²¹Developed together with Mr. M. Ahlering, LaVision Biotec.

objective lens (*Olympus*, APON, $NA = 1,42$) focused the excitation laser beam into the sample. For detecting the images a home-built tube lens holder was utilized, which also mounted the sCMOS camera (*Andor*, Neo 5.5) on top of the microscope body. A $700nm$ SP beam splitter separated the excitation lasers at $780nm$ from the epi-detected fluorescence signals. Additional bandpass filters were used in front of the camera to avoid undesired signals or to separate the fluorescence signal of the staining of interest from others (if so the filter is mentioned in the figure caption). The tube lens was a $f = 300mm$ apochromatic $\varnothing = 50mm$ lens focusing the fluorescence signal onto the camera chip, which had a pixel size of $6,5\mu m$. In combination with the objective lens and tube lens pairing this lead to a pixel size in the image of $66nm$. In this approach a illumination pattern with three phases and three angles of rotation (separated by 60°) was used.

4.5.2. Enhancing the resolution and contrast by striped illumination of fluorescent bead samples in two-photon excitation

For determining the best pattern spacing a series of images were acquired on fluorescent bead samples (beads $\varnothing = 200nm$, *ThermoFisher*, TetraSpeck microspheres) by increasing the pattern fineness. The bead samples were created by diluting the stock solution by a factor of 1 : 5 with distilled water and letting a drop of $60\mu l$ dry on a cover slide, while the sample was placed overhead. By this preparation a single monolayer with the desired density of the fluorescent beads was created. For evaluating the best combination of modulation depth of the excitation pattern as well as a high fineness of the pattern for a high resolution enhancement the *FIJI* plugin FairSIM [Müller et al. [2016]] (fig. 58) was utilized in the reconstruction process. In the FairSIM plugin the Richardson-Lucy filtering algorithm on both input and output data of the reconstruction was applied setting 15 iterations. The apodization cut off was set to 1,2. The raw data set containing 9 images was averaged and used as the widefield image for the comparison to the reconstructed image. Fig. 59 shows a zoom into a ROI of a group of fluorescent beads. Here, the filtered widefield image is added to the comparison due to the enhancement of contrast by the necessary filtering steps in the reconstruction process. Hence, the filtered widefield image uses the averaged data of the widefield image but then performs the same filtering steps as the final reconstruction. In this way the comparison is more significant and one can make sure that observed improvements are arising from the striped illumination and not only due to filtering of the images, which is similar to a deconvolution step. In the presented reconstruction the contrast is clearly enhanced due to a larger range of intensity values compared to widefield and filtered widefield image, which can be seen by performing a line plot (fig. 60). Also a

group of beads presented in the ROI can not be resolved in the widefield images. Only the reconstruction shows a gap between single beads, also visible in the line plot by a clear drop of intensity (fig. 60, pink arrow).

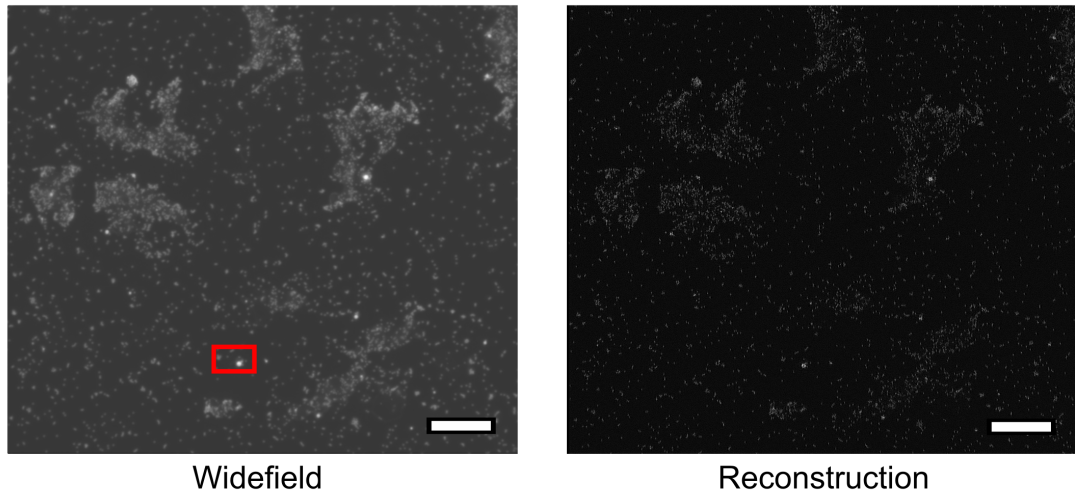


Figure 58 – Structured illumination applied on a $200nm$ TetraSpeck fluorescence bead sample using two-photon excitation

A mono layer of fluorescent beads $\varnothing = 200nm$ was illuminated with a striped illumination pattern using two-photon excitation by a $780nm$ femtosecond laser source having $\sim 140fs$ pulse length. Left hand side shows the average of all nine acquired raw images forming the widefield image, right shows the reconstruction using FairSIM applying a Richardson-Lucy filtering on the final image. The red box is selected as ROI for a zoom in (see fig. 59). The scale bar indicates $10\mu m$.

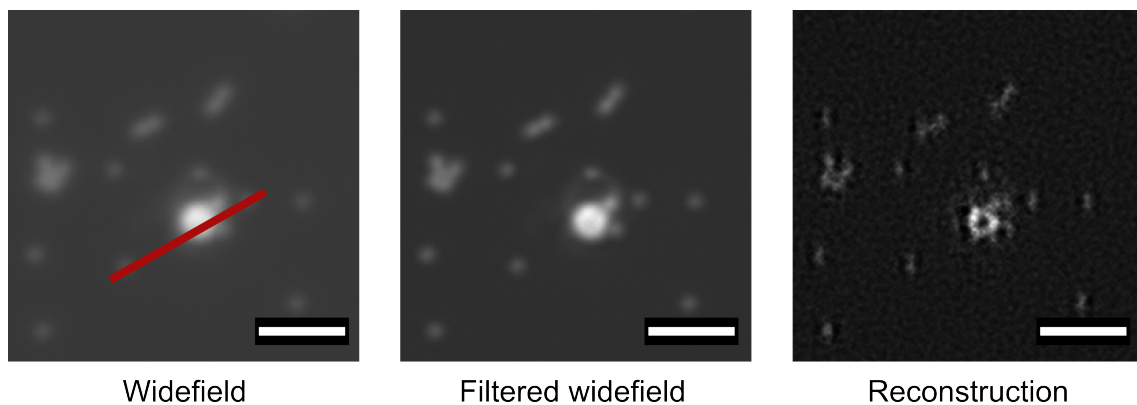


Figure 59 – Comparison of widefield images to the reconstruction in a region of interest of a $200nm$ bead sample

The selected ROI shows a constellation of several $200nm$ beads grouped together in a circle. Left hand side shows the widefield image, middle shows the filtered widefield, which corresponds to a deconvolved image, and right hand side shows the final reconstructed image by FairSIM. The red line indicates the location of a line plot performed for comparing all three images (fig. 60). The scale bar indicates $2\mu m$.

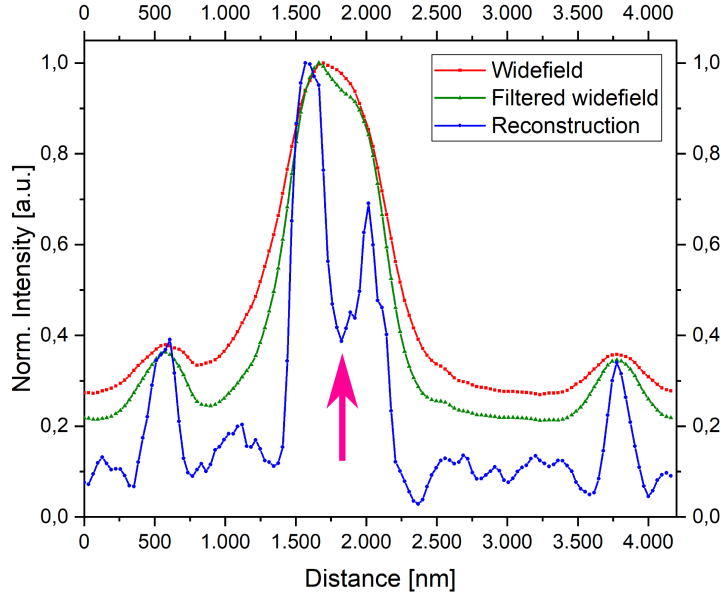


Figure 60 – Line plot of the 200nm bead sample: comparing widefield images to the reconstruction shows enhanced resolution and contrast

The line plot compares the normalized intensity values of widefield (red line), filtered widefield (green) and reconstruction (blue) of the 200nm TetraSpeck bead sample using a striped illumination pattern and two-photon excitation (compare red line in fig. 59). Widefield and filtered widefield are unable to resolve the gap in a group of the fluorescent beads, whereas the reconstructed image can separate between the single beads and shows a clear decrease of intensity (pink arrow). The increased contrast of the reconstruction becomes apparent due to the larger range of intensity values (0,06 – 1a.u.; reconstruction) in comparison to widefield and filtered widefield (0,2 – 1a.u.; filtered widefield).

4.5.3. Exploiting autofluorescence signals of *Convallaria majalis* for combining z-scanning with striped illumination pattern via MAP-SIM

In order to explore the performance of the presented striped illumination pattern generation in two-photon microscopy on a larger field of view as well as in a 3D scanning experiment the auto-fluorescent sample *Convallaria majalis* is investigated. Changing to a 25 \times air objective lens (*Nikon*, $NA = 1,1$; $WD = 2mm$) in combination with the $f = 300mm$ tube lens lead to a field of view of $\sim 360\mu m$ having a magnification factor of 41,6 and a camera pixel size of $1px \hat{=} 156,3nm$. A z-scan over $8\mu m$ with a step size of $0,5\mu m$ was sequentially performed by the built-in z-scanner of the TriM Scope II setup, based on a micro-motor drive. Nine images containing the tree angles of rotation with each three phase settings of the illumination pattern were recorded for each z-plane. Each z-plane data set was reconstructed by the Matlab-based reconstruction toolbox MAP-SIM²² [Lukeš et al. [2014], Křížek et al. [2015]], which has the ability to utilize even higher harmonics of the applied illumination pattern. By setting a relative

²²In collaboration with Mr. J. Pospisil.

coarse illumination pattern and by the intrinsic character of galvanometric scanning-based illumination patterns to be not sinusoidal higher harmonic contributions of the illumination pattern are observable in the Fourier spectra of the raw data sets. The FairSIM reconstruction algorithm is developed predominantly to operate on illumination patterns, whose frequencies are chosen to be at the edge of the detectable OTF for highest resolution enhancement. In the reverse conclusion a higher harmonic of the illumination pattern is arising artifacts in the final reconstructed image, because its frequency content is not separated from the first order contribution and is not shifted to the correct position in the image. This behavior of the reconstruction algorithm is reducing the possible pattern settings in the presented approach to be consisting only of one detectable frequency of the illumination pattern. In the MAP-SIM algorithm second or higher harmonics of the illumination pattern are utilized for the reconstruction process and contribute to the final image.

Hence, the MAP-SIM approach is applied to the *Convallaria majalis* sample, which showed a coarse pattern fineness. For each z-plane the reconstruction was performed and also an averaged widefield image is generated for comparison reasons. All acquired z-planes were then false color coded by the hyperstack function in *FIJI* (fig. 61), the color bar indicates the z-position. The contrast of the reconstruction as well as the z-sectioning capability of the reconstructed image stack is enhanced. Two ROIs are selected for a zoom image, indicated by the red boxes. ROI 1 shows an area with a thicker structure of the cell walls of the *Convallaria majalis* sample (fig. 62), while ROI 2 (fig. 63) shows a thinner cell wall structure. Both ROIs show a clearer z-sectioning capability as well as a clear enhancement in contrast in the reconstructed image. Due to the lower magnification and coarser structure of the sample no resolution enhancement beyond the diffraction limit can be expected, but nevertheless the striped illumination approach in combination with the MAP-SIM reconstruction improves the image quality and the data set was reconstructable in all recorded z-planes. Combining the scanning mirror-based striped illumination with MAP-SIM as reconstruction tool can be further optimized by finding optimal parameters for illumination angles and phase step size and choice of increments in order to fully exploit the second or higher harmonics of the striped illumination pattern in the reconstruction. Both reconstruction algorithms introduced in this paragraph are compared in their performances on the $\varnothing = 200nm$ fluorescent bead sample (compare fig. 58). MAP-SIM as well as FairSIM are optimized in its performance on this data set and the final images are compared to the averaged widefield image (fig. 64). Both reconstructions show the resolution improvement due to the applied structured illumination pattern in the two-photon excitation. The MAP-SIM approach has a better background removal whereas FairSIM shows at

the location of the beads a slightly increased performance in terms of resolution. A line plot indicated by the green line in fig. 64 shows that the dip between single beads is more prominent using FairSIM as well as the diameter of the left hand side bead is slightly smaller (fig. 65).

Scattering in the sample material is identified as major factor which still limits the detectable fineness of the illumination pattern. Applying a very fine illumination pattern on a fluorescent bead sample with a bead diameter of $\varnothing = 1\mu m$ shows this effect very prominent at the border of the illuminated area (fig. 66). Two effects are visible in this image: first a corona at each bead arising from out of focus light as well as the illumination of beads, which are outside of the excitation area (red arrows). The red line indicates the border between the area with excitation by the laser (left hand side) and the non illuminated area (right hand side). Beads in the non illuminated area are also visible due to scattering of laser light of the excitation or of the generated fluorescence light into the non illuminated area. This effect is also present in the area between single illuminated lines of the applied striped pattern, which is reducing the modulation depth of the pattern leading to the need of coarser patterns in the recorded raw images. Here, MAP-SIM can circumvent this challenge due to more freedom in the choice of pattern fineness.

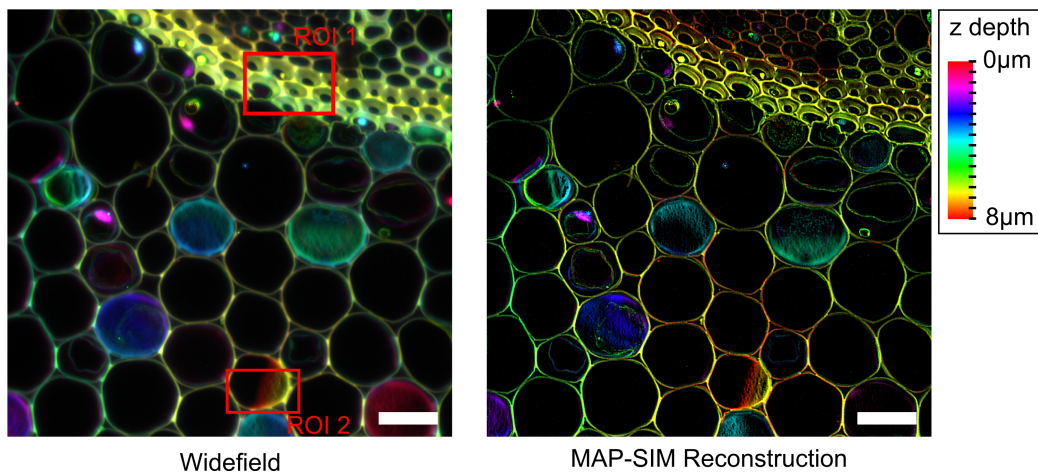


Figure 61 – MAP-SIM reconstruction performed on a z-scan image series of a *Convallaria majalis* sample

The two-photon excited autofluorescence of a *Convallaria majalis* sample was utilized for applying the structured illumination in addition to a z-scan over $8\mu m$ with a step size of $0,5\mu m$. In each z-plane nine images were recorded shifting the phase and angle of the illumination pattern. Each image stack per z-plane was reconstructed by the MAP-SIM toolbox and the results of all z-planes were false color coded according to the z-position by *FIJI* using the hyperstack functionality. Two regions of interest (ROI 1 and 2, red boxes) were selected for a more detailed comparison of the above shown averaged widefield images and the reconstruction (see figs 62 and 63). Note, that for this data set a $25\times$ objective lens (*Nikon*, $NA = 1,1$; $WD = 2mm$) was utilized. The scale bar shows $40\mu m$.

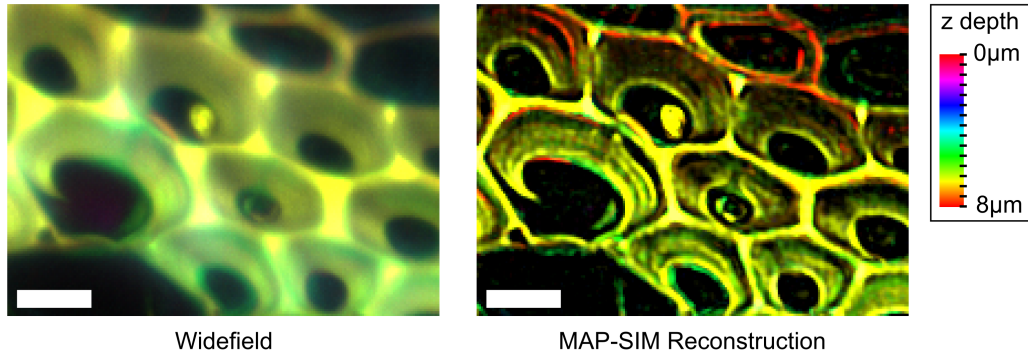


Figure 62 – ROI 1 of *Convallaria majalis* sample comparing widefield to MAP-SIM reconstruction. This ROI compares the averaged widefield (left hand side) and reconstructed image (right hand side) showing several linked cell walls of the sample. The contrast and z-sectioning is enhanced by the MAP-SIM approach, additional features are revealed in the reconstructed image. The color code bar (box) indicates the position during the z-scanning according to the false color in the image. The scale bar shows $10\mu m$.

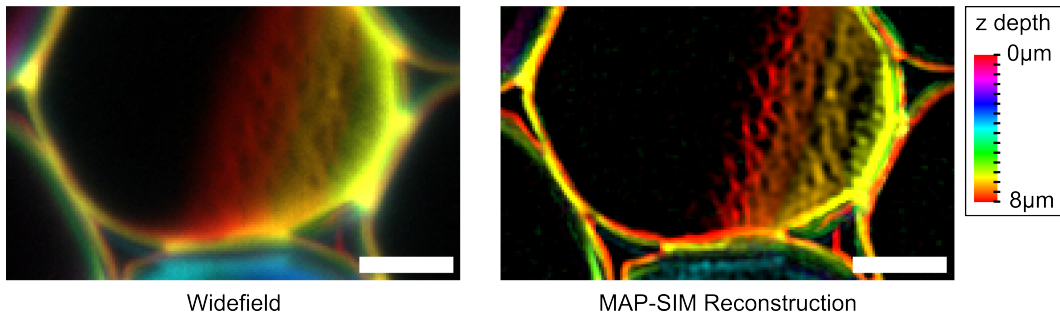


Figure 63 – ROI 2 of *Convallaria majalis* sample comparing widefield to MAP-SIM reconstruction. The second ROI compares the averaged widefield (left hand side) and reconstructed image (right hand side) of a single cell. The contrast and z-sectioning is enhanced performing the MAP-SIM reconstruction. The color code bar (box) indicates the position during the z-scanning according to the false color in the image. The scale bar indicates $10\mu m$.

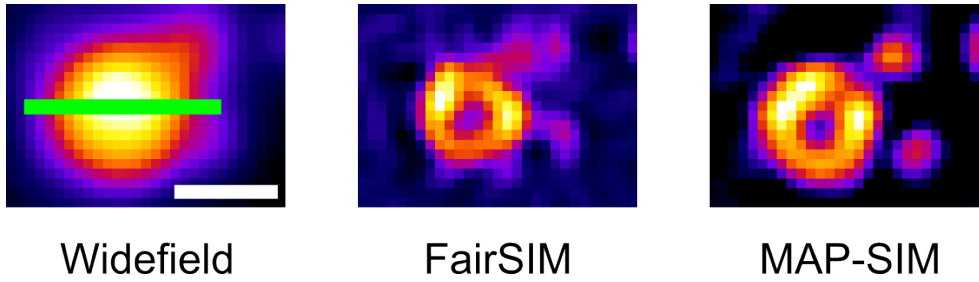


Figure 64 – Comparing the performance of FairSIM and MAP-SIM on fluorescent bead samples. Both reconstruction algorithms are tested on the $\varnothing = 200nm$ fluorescent bead data set showing a clear increase in resolution due to the ability to resolve a bead cluster, whereas in the averaged widefield image no single bead structures are visible. In FairSIM the same parameters are used as in fig. 58. The green line indicates the location of a comparing line plot. The background suppression is slightly better in the MAP-SIM reconstruction. The scale bar (white) indicates $500nm$.

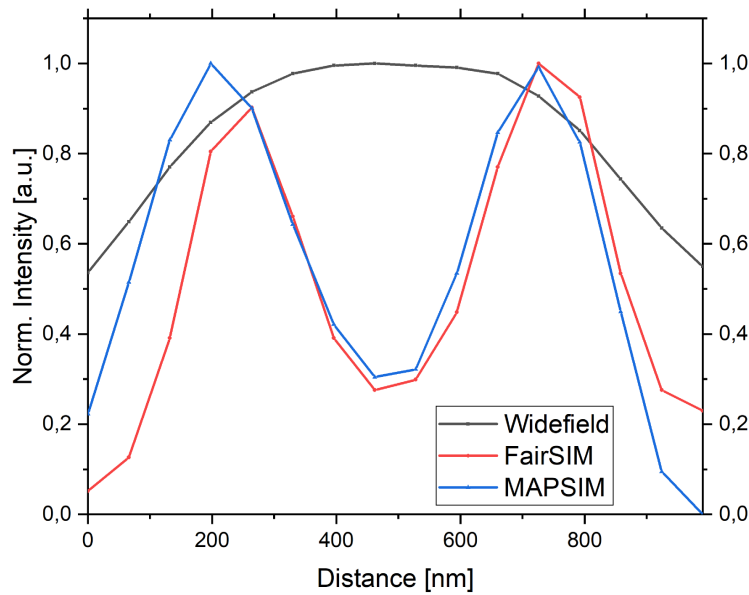


Figure 65 – Line plot comparing reconstruction algorithms on a fluorescent bead sample. Comparing both reconstruction algorithms (FairSIM red line, MAP-SIM blue line) to the averaged widefield image data (black line) a clear dip between single beads is apparent due to the applied structured illumination pattern in two-photon excitation. FairSIM has a slightly better performance compared to the MAP-SIM reconstruction due to the higher decrease of values in the gap between the beads as well as the slightly smaller diameter of the left hand side bead.

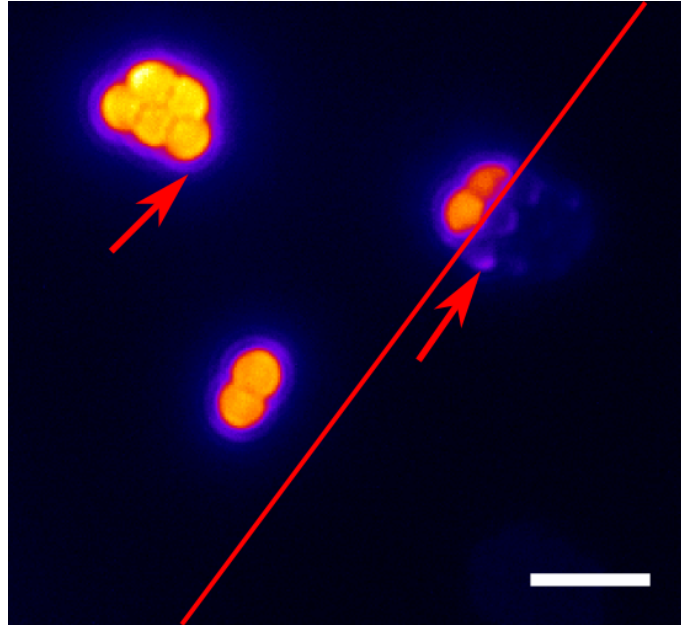


Figure 66 – Fluorescent $1\mu\text{m}$ bead sample imaged by fine illumination pattern investigating scattering effects

A sparse monolayer of $1\mu\text{m}$ fluorescent beads was illuminated with a very fine illumination pattern (single lines of the pattern can not be seen in the presented raw image). The selected cutout of the full image shows the border between illuminated (left hand side) and non-illuminated area (right side), indicated by the red diagonal line. This raw image shows two effects: first, a corona around each bead as well as, second, a fluorescent signal of the non-illuminated area showing the outline of additional beads (arrows). This is an example of the limitations of the striped illumination approach due to scattering events in the sample. The scale bar shows $2,5\mu\text{m}$.

4.5.4. Investigating the potential of a striped two-photon illumination in tissue utilizing a stained murine kidney section

In the next step a murine kidney tissue section (ThermoFisher, FluoCells prepared Slide #3) stained with three fluorescent dyes (Alexa Fluor 488 WGA, Alexa Fluor 568 and DAPI) was investigated utilizing a laser wavelength of 800nm for the two-photon excitation of the Alexa Fluor 568 dye, which stained the filamentous actin prevalent in the glomeruli and the brush border. A $595/40\text{BP}$ bandpass filter is set in front of the camera isolating the desired signal at $\sim 603\text{nm}$. Again the developed striped illumination scheme is applied to this sample while the reconstruction is performed in MAP-SIM for fig. 67 as well as in FairSIM using similar parameters as in the fluorescent bead sample for a cutout of the data set (fig. 69). Averaged widefield and reconstructed image are compared in fig. 67 showing an enhanced contrast and resolution. A line plot (fig. 68), whose location is indicated by the red line in fig. 67, is confirming the superior performance of the reconstruction over the widefield image. The range of intensity values is larger in the reconstruction indicating a better contrast, edges in

the reconstructed image are steeper showing the improvements in resolution (apparent in fig. 68). A ROI processed now with FairSIM (fig. 69) compares the performance of reconstruction to widefield in an overlay image, confirming that both reconstruction algorithms work well on the generated data sets.

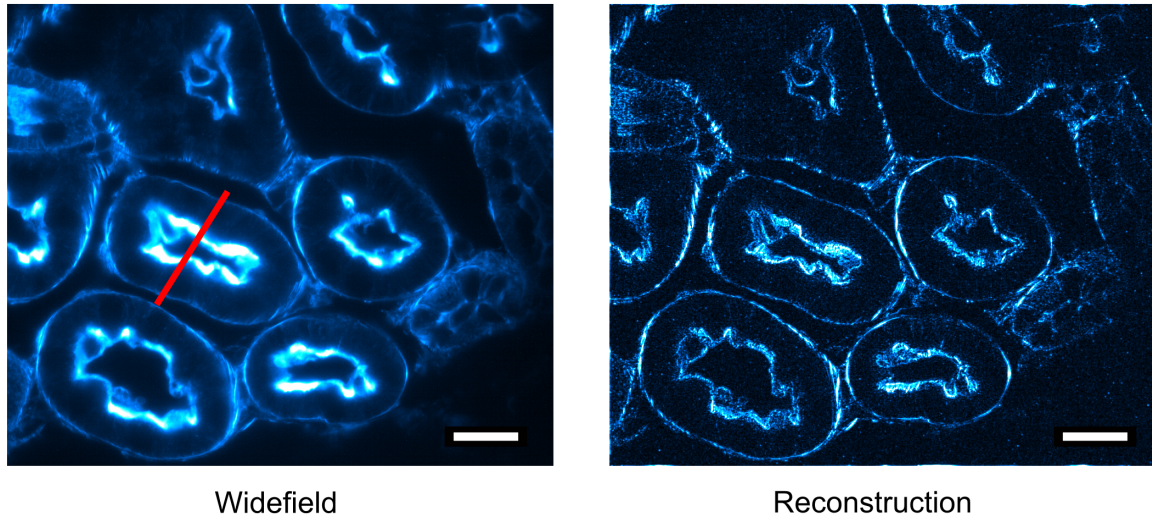


Figure 67 – Striped two-photon excited fluorescence imaging of a stained murine kidney tissue section comparing widefield to reconstruction

A wavelength of $800nm$ was utilized for the two-photon excitation of the Alexa Fluor 568 dye, which stains the filamentous actin prevalent in the glomeruli and the brush border in the tissue section [Wiederschain [2011]]. An additional $595/40BP$ bandpass filter isolated the detected signal in front of the camera. Generating averaged widefield (left hand side) and reconstructed image (right hand side) by the MAP-SIM algorithm allows the comparison: the reconstruction shows enhanced contrast and resolution. The red line marks the location of a line plot for comparing both images (see fig. 68). The scale bar indicates $25\mu m$.

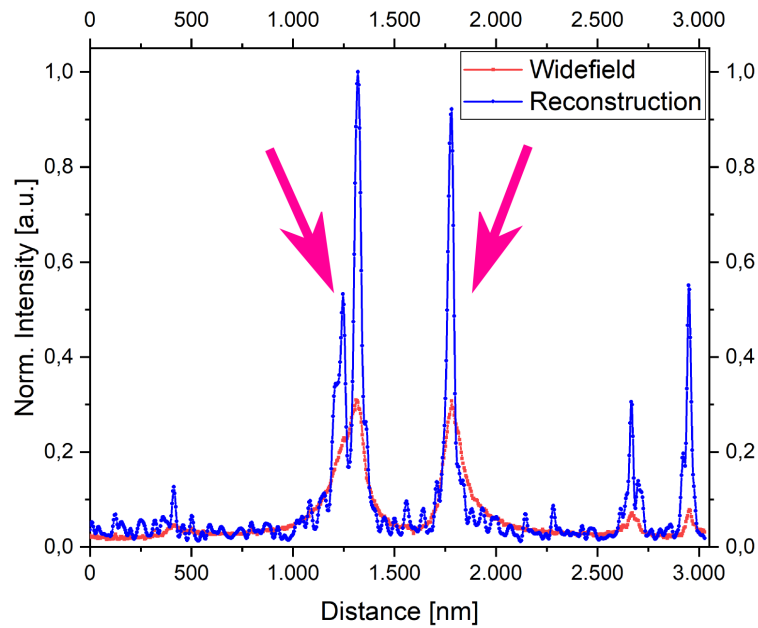


Figure 68 – Line plot at selected ROI of a kidney tissue section

The line plot compares the normalized intensity values of the widefield (red line) to the reconstructed image (blue line) at the ROI indicated by the red line in fig. 67. The reconstruction made with MAP-SIM shows an enhanced contrast due to the larger range of intensity values as well as an enhanced resolution indicated at the steep edges of the filamentous actin prevalent (pink arrows).

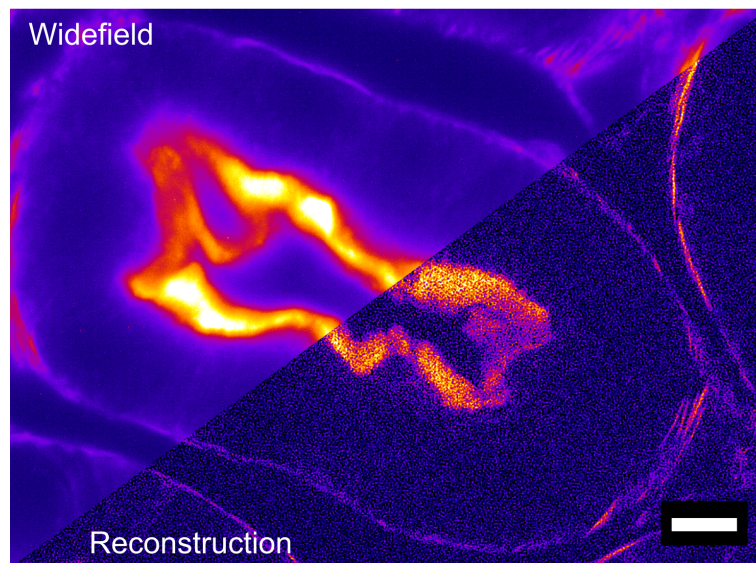


Figure 69 – Zoom image of a kidney tissue section comparing widefield to reconstructed image using FairSIM

A single cell of fig. 67 is selected for comparing the widefield to the reconstructed image utilizing the FairSIM algorithm with similar parameters determined on the bead samples. The reconstruction shows also an enhanced contrast and resolution confirming that the reconstruction process of the generated data sets is working well with both described algorithms. The scale bar indicates 5 μ m.

4.5.5. SI-CARS: investigating the potential of resolution enhancement by striped illumination patterns

For the generation of the striped illumination patterns utilizing CARS as contrast mechanism the Stokes beam was rapidly switched in its intensity according to the position of the galvanometric scanning mirrors (see 3.2.1). The parameters of the pattern such as spacing of the illuminated lines, angle of rotation and pixel dwell time were set by the scanning control program ScanImage. Finding the best setting of the pattern fineness was performed on pure samples such as butter, DMSO or olive oil. Here, the modulation depth of the detected illumination pattern was compared and balanced to the noise level in the raw images due to the camera exposure time as well as to the desired high fineness of the pattern, which finally generates the resolution enhancement in the reconstructed image. An example of a raw image with a coarse illumination pattern easy visible as bright stripes is presented in fig. 70. The 2913cm^{-1} $C - H$ symmetric stretching resonance was probed in pure DMSO, which was applied on a dried monolayer of polystyrene beads with a diameter of $\varnothing = 1,1\mu\text{m}$. The strong CARS signal of the DMSO generated an anti-contrast of the polystyrene beads, which was useful to evaluate the CARS signal strength on a sCMOS camera as well as to adjust the optics generating the final image on the camera chip. The red arrow indicates the scan direction of a single illuminated line.

For the reconstruction of a SI-CARS data stack nine images were acquired consisting of three different angles of the illumination pattern separated by $\sim 60^\circ$. For each angle of the pattern the phase is shifted in three steps in order to fully illuminate the sample area. An example of typical raw data is showcased in fig. 71. A monolayer of polystyrene beads with a diameter of $\varnothing = 2\mu\text{m}$ was prepared by letting a drop of the diluted stock solution dry out overhead on a cover slip. In the SI-CARS experiment the 3070cm^{-1} resonance of the polystyrene was probed generating the CARS signal with a wavelength of $643,6\text{nm}$, which was filtered by a stack of optical short-pass and bandpass filters and finally detected on the sCMOS camera. The reconstruction was performed by FairSIM generating again the averaged widefield and the filtered widefield images for the comparison to the reconstructed image (fig. 72). Due to a still rather coarse illumination line spacing the parameters in the reconstruction process were adapted to the applied illumination pattern. The apodization factor was set to 1,2 while a final Wiener filter of 0,056 delivered the best results on this data set. The red box indicates the position of a line plot showing the normalized intensity values of all three presented images (fig. 73). A better contrast as well as a resolution enhancement becomes apparent studying the gap between two beads due to the larger range of intensity values occurring in the reconstruction as well as a decrease of intensity at the

gap structure between two beads (indicated by the pink arrow in fig. 73). The power spectra of the reconstruction process as well as for the final images can be directly extracted from the FairSIM software (fig. 74). The spectra of the raw data for each angle of the illumination pattern show a clear peak of the frequency of the applied pattern, which is utilized for finding the correct length and angle of the k_0 parameter fitting routine (fig. 74, red circles and green arrow). Comparing widefield to the reconstructed image in Fourier space clearly shows additional spatial frequencies in the reconstruction, which becomes apparent in fig. 74, right hand side. The green circle in the Fourier space of the reconstruction indicates the maximum spatial frequencies of the widefield image, all values outside of this circle depict the additional spatial frequencies due to the applied structured illumination.

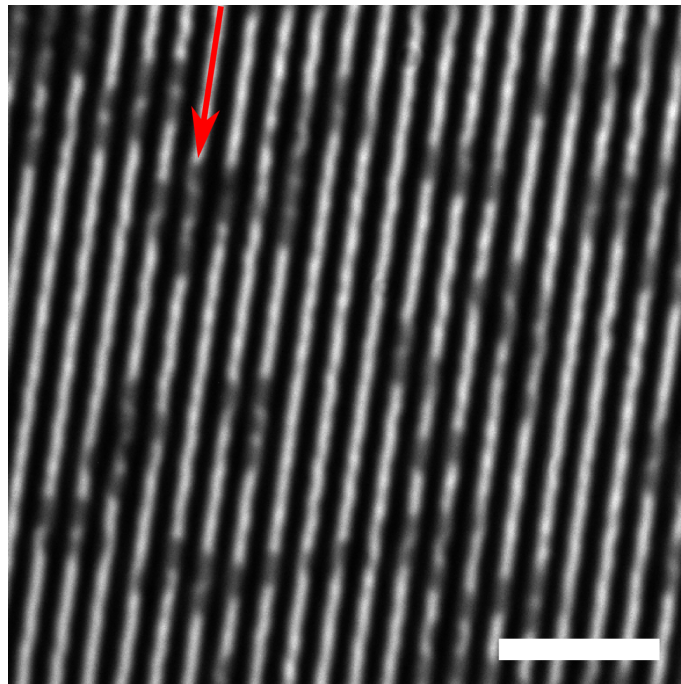


Figure 70 – $1, 1\mu m$ polystyrene beads in DMSO solution illuminated with coarse CARS illumination pattern

A coarse illumination pattern was generated probing the $2913cm^{-1}$ $C-H$ symmetric stretching mode of the DMSO solution in which $1, 1\mu m$ polystyrene beads were embedded. In this way an anti contrast of the beads was generated. The red arrow indicates the scan direction. The scale bar indicates $5\mu m$.

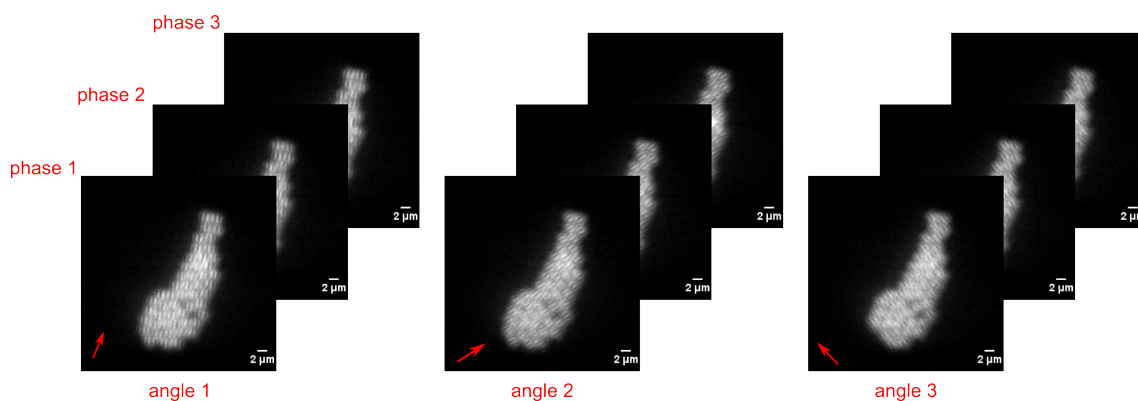


Figure 71 – Raw data set using striped CARS illumination pattern for imaging $2\mu\text{m}$ polystyrene beads

A suitable fineness of the CARS illumination pattern was chosen probing the 3070cm^{-1} polystyrene resonance. The raw image set consists of three angles separated by 60° rotation, while for each angle the illumination pattern is shifted in its phase by three increments in order to illuminate the entire sample space. The red arrows indicates the scan direction for each angle. The scale bars shows $2\mu\text{m}$.

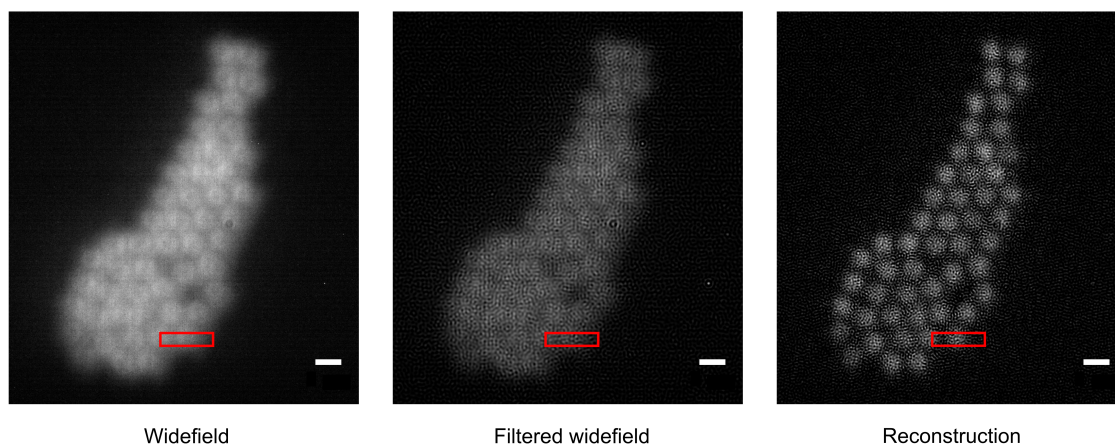


Figure 72 – SI-CARS: comparison of widefield to reconstruction in $2\mu\text{m}$ polystyrene beads

The SI-CARS raw data set (fig. 71) probing the 3070cm^{-1} polystyrene resonance is processed by the FairSIM plugin in *FIJI* using a Wiener-filter of 0,056 setting a apodization factor of 1,2. Left shows the widefield image in comparison to the filtered widefield (middle) and the reconstruction (right hand side). The red box shows the location of a line plot (fig. 73). The contrast and resolution of the reconstructed image is enhanced in comparison to both widefield and filtered widefield. The scale bar indicates $2\mu\text{m}$.

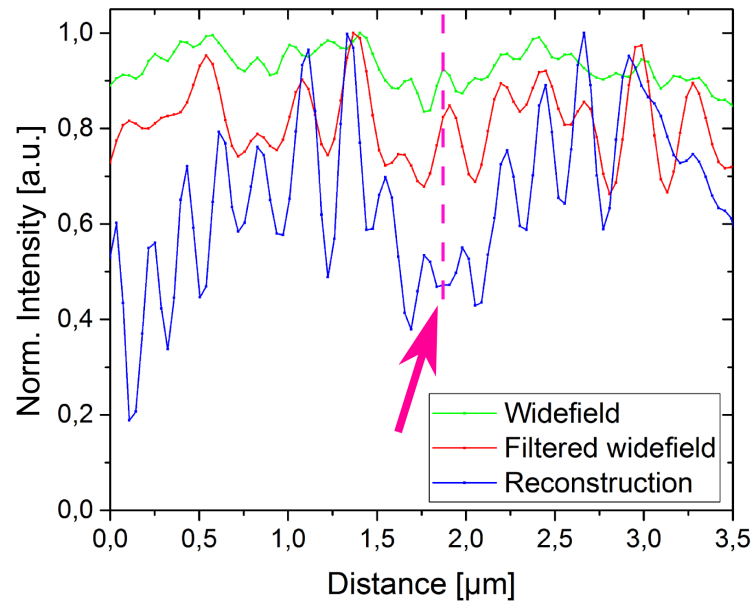


Figure 73 – SI-CARS: line plot of ROI comparing reconstruction to widefield image
 Comparing widefield (green) and filtered widefield (red) to the reconstructed image (blue) an enhanced contrast due to a higher range of intensity values as well as a higher drop in intensity at the area between the single beads can be observed (pink arrow and dashed vertical line). The intensity values were normalized for better comparison.

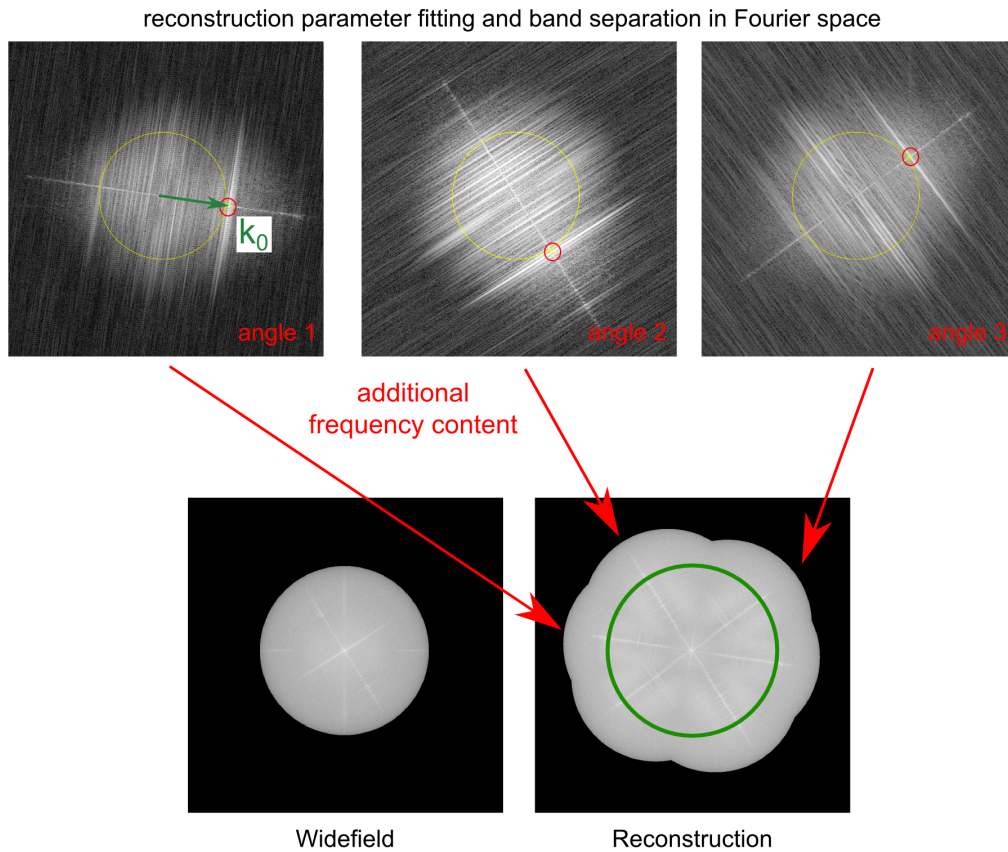


Figure 74 – Reconstruction parameter fitting and band separation in Fourier space using Fair-SIM. In the upper row the single power spectra in the Fourier space are shown for each angle of the illumination pattern. The inner area of the yellow circle indicates the setting of the excluded frequencies searching for the k_0 value in the parameter fitting routine in the FairSIM plugin. The red circles show the localized intensity maxima for the each angle of the illumination pattern determining the correct parameter fitting of k_0 (drawn in green) for the reconstruction step. In the lower row the Fourier spectra of the averaged widefield image (left hand side) is contrasted to the reconstruction (right hand side). The enhanced area in the Fourier space of the reconstruction is due to the additional information content generated by the striped illumination pattern according to each angle of the illumination pattern. The green circle added into the reconstruction indicates the maximum frequencies of the widefield image for comparison.

4.5.6. Structured illumination utilizing galvanometric scanning mirrors proves to be a versatile tool for two-photon fluorescence and CARS microscopy

In summary the performance of the newly developed structured illumination approach by utilizing the galvanometric scanning mirrors showed significant improvement in contrast and resolution in two-photon excited fluorescence microscopy. The presented data set acquired on fluorescent bead samples as well as on relevant tissue sections and biological applications such as a *Convallaria majalis* sample were successfully reconstructed. This concept has the appealing point of utilizing most of the standard components of a state-of-the-art two-photon scanning microscope by adding a sCMOS camera to the setup. This way a cost-efficient improvement of existing setups can be easily performed using free reconstruction software such as FairSIM as well as the MAP-SIM toolbox for the final image.

This concept is also applicable to CARS microscopy avoiding high excitation intensities as well as problems with the spatial overlap of pump and Stokes beam by avoiding the use of pattern generation by light interference. First successful data acquisition was performed on a polystyrene bead sample showing improvement in resolution and contrast. In future steps doubly-resonant CARS can be utilized as contrast mechanism for boosting the signal intensity [Weeks and Huser [2010]]. Thus a better modulation depth of the applied illumination patterns is expected and also finer patterns can be applied resulting in even higher resolution enhancement.

4.6. Developing a self-synchronized two-color fiber laser for fast, high contrast CRS-microscopy

CRS-microscopy is a versatile tool for biomedical research addressing questions closely related to clinical research because of the fast, non-invasive and chemical sensitive imaging modality [Yun and Kwok [2017]]. At the same time no fluorescent labels are needed in this technique while the excitation laser powers are moderate and are mostly not affecting the sample of interest [Zumbusch et al. [1999], Freudiger et al. [2008], Nandakumar et al. [2009], Ozeki et al. [2009]]. Hence, the preparation of the sample is minimal compared to fluorescence-based techniques and also in-vivo experiments can be performed even at human patients in the operating room [Evans et al. [2007], Ji et al. [2013, 2015], Lu et al. [2016], Orringer et al. [2017]]. Combining CRS-imaging with endoscopic approaches by utilizing optical fibers can allow live examinations in the human patients [Lukic et al. [2017], Lombardini et al. [2018], Latka et al. [2013]], which was performed utilizing CARS as contrast mechanism. Ongoing activities are trying to expand this modality also to SRS.

A major drawback of current state-of-the-art CRS-microscopy setups are the traditional solid-state lasers, typically Ti:sapphire or Nd:Van systems, mostly combined with optical parametric oscillators used for the required tunable laser wavelengths in the CRS imaging process. These laser systems have a large footprint, are cost-intensive, sensitive to influences of the environment such as vibrations, temperature changes, dust and humidity, they require large vibration-isolated optical tables as well as maintenance in terms of retuning the optical paths for granting the spatio-temporal overlap and thus can not be easily included into a medical, sterile operating room.

Recent efforts have been performed to exploit fiber laser technology for replacing the traditional laser systems in order to overcome their shortcomings mentioned above: fiber-Ti:sapphire hybrid sources [Ozeki et al. [2010], Wang et al. [2010]], all-fiber lasers based on the following techniques: active synchronization [Nose et al. [2012], Karpf et al. [2015]], parametric wavelength conversion [Zhai et al. [2011], Baumgartl et al. [2012a], Lefrancois et al. [2012]], soliton self-frequency shift [Andresen et al. [2007], Pegoraro et al. [2009], Krauss et al. [2009], Xie et al. [2014], Crisafi et al. [2018]], and supercontinuum (SC) light generation [Gambetta et al. [2010], Selm et al. [2010], Freudiger et al. [2014], Chen et al. [2016], Tu et al. [2016], Orringer et al. [2017]]. Fiber-lasers are robust and the components can be densely packed into sealed containment while they also offer the desired wavelengths tunability addressing the molecular resonance of interest. The recent progress in fiber laser technology allows to include most optical components into the fiber-based optical path [Sobon et al. [2015], Wei et al.

[2014a]], which reduces the footprint of the system as well as the need of free-space optics and their alignment as well as it improves the overall stability of the optical system. Nevertheless, previous implementations of the fiber laser technology had shown first promising results but still lacked the full performance of the traditional solid-state laser systems especially due to low power levels, a narrow wavelengths tuning range and high laser intensity noise. These shortcomings resulted in poor image quality, low scanning speeds and the need of special noise suppression schemes especially in the case of SRS. Here, the balanced detection is utilized to overcome the shortcomings of laser systems without high quality noise performance [Nose et al. [2012]], but the scheme relies on the delicate adjustment of balanced receivers subtracting the undesired laser noise, which results in obstacles of the systems in terms of continuous performance while wavelengths tuning over a wide range as well as it increases the complexity of the CRS-microscope and the overall costs.

In a collaborative project with the research group of Prof. Dr. K. K. Y. Wong, the University of Hong Kong, China a novel high-power self-synchronized two-color pulsed fiber laser system was developed²³ overcoming the described drawbacks of the fiber laser technology in recent implementations [Kong et al. [2019]]. The presented picosecond fiber laser provides high intensity stability (50db better performance than competitive systems), low timing jitter (24, 3fs), large wavelengths tuning range resulting in an addressable wavenumber range of $2700 - 3550\text{cm}^{-1}$, low average power fluctuation ($< 0, 5\%$), low pulse width variation during wavelengths tuning ($< 1, 8\%$) and a fiber-based intensity modulation scheme for SRS imaging with a excellent modulation depth of $> 99\%$. Due to the excellent noise performance and high intensity modulation depth the performed SRS microscopy shows high contrast and high chemical sensitivity without the need of an additional noise cancellation device such as a balanced detection scheme, while the imaging speed is still comparable to other fiber-based as well as solid-state laser systems.

The performance of the fiber laser system is demonstrated in two steps: first, both wavelengths branches are analyzed in terms of spectral and temporal performance by utilizing a real-time oscilloscope, a spectrum analyzer and power measuring devices. Second, the performance is demonstrated by simultaneous imaging with CARS and SRS contrast on several biomedical samples such as living human cell samples, murine arterial tissue sections, murine brain slices as well as pure substances for comparison to spontaneous Raman scattering spectra. In addition to that the introduced fiber-based laser system provides a femtosecond pulse length branch which extends the range of application also to second harmonic generation as well as to two-photon excited fluores-

²³Equal contribution with Mrs. C. Kong and Mr. H. Hachmeister.

cence imaging providing full multimodal imaging ability. This application is showcased on a mouse tail sample (SHG imaging) as well as on a stained murine kidney section and a stained murine brain section visualizing the pyramidal neurons (two-photon excited fluorescence). This fs-pulsed laser setup is also proposed as a stand-alone system with optimized pulse length, which is a powerful and cost-efficient tool for users of two-photon scanning systems [Kong et al. [2017]].

4.6.1. Utilizing highly doped ytterbium and erbium non-linear fibers for the low noise, high power two-color laser in CRS-microscopy

Stokes beam generation in the master oscillator branch

The presented two-color pulsed laser system for CRS-microscopy can be separated in two major branches due to the use as Stokes and pump pulses for the final experiment. The master oscillator consists of a passively mode-locked femtosecond laser cavity at $1000nm$ wavelength realized by pumping a $25cm$ long piece of ytterbium-doped (Yb) non-linear fiber (*Thorlabs*, YB1200-4/125) via a $976nm$ Cw-laser diode (*II-VI*, LC96Z400; **Pump**) (fig. 75, left upper corner) [Xu et al. [2011], Spiegelberg et al. [2004]]. A fiber-based optically integrated module (**OIM**), which provides polarization-sensitive isolation, signal extraction and pump/signal multiplexing, closes the cavity and is combined with a drop-in polarization controller (*General Photonics*, PolaRite; **PC**). It allows the passive mode-locking by nonlinear polarization rotation (NPR) granting the successful and reliable self-starting of the source with stable fs-pulses having the all-normal-dispersion regime [Chong et al. [2006]]. The wavelengths tuning is performed by placing a tunable filter (*Semrock*, LL01-1064-12,5; **F1**) inside the cavity, which is used as bandpass filter ($\sim 8nm$) and can be tuned by manual rotation (range $50nm$) allowing the adjustment of the laser wavelength from $1010 - 1060nm$ (fig. 81 a). For rapid automatic wavelengths tuning it can be easily replaced by a fiber-coupled tunable filter in later steps of the setup. Also a system trigger is generated by a fast photodiode, which detects the filtered out light. The master oscillator creates $\sim 20mW$ power at the systems fundamental repetition rate of $80MHz$ (fig. 78 a), which is the same as in conventional solid-state laser systems obtaining the advantages of a high repetition rate such as allowing the fast modulation of the laser intensity (typically at $10 - 20MHz$) for SRS imaging with high scanning speeds. The generated fs-laser pulse intensity is extracted through the OIM and then split up in two branches with equal intensity by a $50 : 50$ splitting fiber optic coupler (**OC**) feeding each the following Stokes and pump beam generation.

For the Stokes beam generation a fiber-based chirped pulse amplification (FCPA) scheme is applied [Strickland and Mourou [1985]]: first, linear chirp is applied to the

fs-pulses by a single mode fiber (*Corning*, HI60, 50m length; **SMF**) for reducing the peak power of the pulses. Then a core-pumped single-cladding Yb-doped fiber amplifier (**YDFA**) is creating $\sim 20mW$ of output power [Paschotta et al. [1997]]. It is comprised of a highly-doped Yb fiber (*Thorlabs*, YB1200-4/125; 25cm length) a 980/1030nm wavelength-division multiplexing coupler (*Haphit*; **WDM**) in combination with a fiber-coupled laser diode (again *II-VI*, LC96Z400) at 976nm for the Cw pump light generation. Then a fiber-based intensity modulator (*iXblue*, NIR-MX-LN-10; **FIM**) is placed behind the preamplifier stage and can be used for the fast frequency modulation at 20MHz used in SRS imaging. The modulation is synchronized with the 80MHz fundamental repetition rate of the master oscillator by processing the system trigger signal. The fiber modulator provides a modulation depth of $> 99\%$ (fig. 78 b), which is an excellent value compared to free-space devices such as e.g. a resonant EOM (electro-optic modulator) with $\sim 80 - 95\%$ modulation depth (compared e.g. to *APE*, EOM 1030). Second, a high power double-cladding YDFA (**DC-YDFA**) (similar to [Wei et al. [2016]]) is utilized to boost the Stokes beam to the final power of $> 1W$, which is then coupled out by a fiber collimator and directed to the grating compressor stage (black dotted box, right hand side of fig. 75). This last amplifier stage is composed of a double-cladding Yb fiber (*iXblue*, IXF-2CF-Yb-O-10-130-NH-V2.0, 1,5m length), which is pumped by a multimode fiber-coupled pump laser diode (*QPhotonics*, QSP-975-10) with a maximum power of 10W at 975nm wavelength (to generate a maximal Stokes beam power of $\sim 250mW$ in the experiment usually $< 4W$ pump power are used) [Yong Wang and Hong Po [2003], Zenteno [1993], Snitzer et al. [1988], Jeong et al. [2004]]. The undesired residual pump power after the non-linear double clad Yb fiber is extracted from the following beam path by removing the outer coating of the fiber and applying UV-curable optical adhesive (*Thorlabs*, NOA63), which removes the residual pump light due to the higher refractive index of 1,56.

Grating pulse compressor is optimizing the pulse length of the Stokes beam

The compressor stage is set up to generate the desired pulse length of the final Stokes beam of $\sim 3,2ps$ (see also fig. 78 c) by two high transmission grating pairs (*Lightsmyth* LSFSG-1000-13212-94) in combination with a telescope (lenses L1 and L2, *Thorlabs*, AC508-75-B). The telescope has the purpose to change the compression ratio by translation relative to the gratings as well as to allow spectral filtering by a translation slit placed in the focal plane of L1 (spectral bandwidth is 1nm during wavelengths tuning) [Weiner [2009, pp. 412]]. By rotating the polarization of the incoming and exiting light by half- and quarter-wave plates in combination with a polarizing beam splitter cube (**PBS**) the coupling in and out of the grating compressor

is performed with low intensity losses.

Slaved second laser cavity generates fundamental pump beam light at $1,5\mu\text{m}$ wavelengths

For creating the pump beam laser light the second half of the output of the master oscillator cavity at $1\mu\text{m}$ is injected into a second laser cavity exploiting the coherent wavelength generation process (CWG) utilizing a $1030/1580\text{nm}$ WDM. This second laser cavity is working at 1578nm using the principle of passive self-synchronization for synchronizing the repetition rate to the $1\mu\text{m}$ laser pulses [Rusu et al. [2004]]. The cavity is comprised of a fiber-based OIM and as the gain medium 50cm of a single-cladding erbium-doped fiber (*Thorlabs*, ER80-8/125; **Er**), which is pumped by a fiber-based Cw-laser diode at 976nm . The polarization of the laser light inside the cavity is controlled by the second drop-in polarization controller. A narrow optical bandpass filter (*BAAR*, bandwidth $< 1,0\text{nm}$; **F2**) placed between two fiber couplers is determining the central wavelength. The cavity length is optimized to match the repetition rate of the master cavity as good as possible by the use of a high precision translation stage mounting one fiber coupler. In this state the $1,5\mu\text{m}$ cavity can produce a self-sustained pulse train [Haus et al. [1994], Krausz et al. [1990], Tamura et al. [1993]], which is not synchronized to the master cavity.

Synchronization of both laser cavities by exploiting cross-phase modulation and group velocity dispersion effects

The synchronization of both laser cavities is performed by the passive self-synchronization, which can coherently generate two-color laser pulses. It relies in the interaction of cross-phase modulation (**XPM**) and group velocity dispersion (**GVD**), which can occur due to the use of active and passive single mode fibers in the $1,5\mu\text{m}$ cavity [Rusu et al. [2004], Yoshitomi et al. [2006], Hsiang et al. [2009]]. The XPM effect describes the nonlinear phase shift of an electromagnetic field, which occurs when high intensity optical fields of different wavelengths, direction or state of polarization meet in nonlinear optical fibers. The nonlinearity refers to the intensity dependence of the refractive index in the fiber material. XPM allows both wavelengths in the cavity the coupling to each other without an energy transfer between them, leading to an asymmetric spectral broadening of the center wavelength of the laser pulses in the case that both pulses are co-propagating in the fiber ([Agrawal [2012, pp. 13]]).

In the described setup the synchronization will start at the first collision of both pulses co-propagating in the fiber of the $1,5\mu\text{m}$ cavity (see fig. 76) e.g. at the position **A** to **B**. The XPM effect initiates a frequency shift of the $1,5\mu\text{m}$ pulses depending on the

timing of the pulses to each other (the $1,0\mu m$ pulses can be considered as temporal reference), leading to a redshift in the case of a faster timing, or a blueshift for a slower timing. This shift is exploited due to having anomalous dispersion at $1,5\mu m$ in the cavity by the used silica fiber (*Corning*, SMF-28e; normal dispersion at $1,0\mu m$) for connecting e.g. the OIM (compare also [Agrawal [2012, p. 8]]), which then slows down or speeds up the circulating pulse according to the wavelength shift of the XPM effect. By carefully choosing the dispersion coefficient of the fiber both effects lead to a stable range of operation due to the intrinsic mismatch of the repetition rates of both cavities due to the optical path length. Therefore, both cavities are matched in their repetition rate as good as possible to each other in the prior calibration process. Finally, the described method grants an excellent synchronization of both laser branches in this setup without any electronic devices, resulting in the low timing jitter of $\sim 24,3fs$ between the cavities determined by optical cross-correlation (see fig. 78 e).

For finding the desired material parameters numerical simulations of the XPM-induced wavelengths shifts were performed and finally the self-synchronization was simulated²⁴ including dispersion and XPM-induced effects (fig. 77) [Hult [2007], Wu et al. [2014], Fisher and Bischel [1973]]. **a)** and **b)** show the timing evolution of the $1,5\mu m$ pulses assuming the repetition rate of the slaved cavity is slightly lower than of the master cavity, without external injected pulses (**77 a)** the temporal mismatch is continuously increasing, no synchronization takes place. With injected pulses at $1\mu m$ less than 50 round trips ($\sim 625ns$) are enough to perform the synchronization and stabilize the slaved cavity at zero temporal offset (**77 b)**. **77 c)** and **d)** show the configuration, when a higher repetition rate in the slaved cavity is assumed. The gradient of the temporal mismatch is reversed, but the situation with and without the injection of the external $1\mu m$ pulses is similar, also resulting in a stable synchronized operation when the $1\mu m$ pulses are present in the slaved cavity.

Pump beam amplification and frequency doubling generate the final pump beam wavelengths

The $1,5\mu m$ laser light is extracted of the cavity by the OIM and then amplified by a heavily-doped double-cladding erbium/ytterbium-doped fiber amplifier (*CorActiv*, DCF-EY-10/128; **DC-EDFA**), which is pumped by a multimode fiber-coupled pump laser diode (similar to the DC-YDFA) at $975nm$. The amplified laser light is coupled out by a FC, which is mounted on a linear translation stage for tuning the temporal overlap to the Stokes beam (delay line, **DL**). After optimizing the polarization state of the $1,5\mu m$ beam by half- and quarter-wave plates it is focused (by lens

²⁴This work was performed by Dr. X. Wei.

L3, $f_{L3} = 75\text{mm}$, *Thorlabs*, AC508-075-C) into a temperature controlled periodically poled lithium niobate crystal (*Covesion*, MSHG1550-0.5, **PPLN**) for performing the frequency doubling to $789,6\text{nm}$ [Taverner et al. [1998]]. The bandwidth of the beam is determined to $0,35\text{nm}$ with a typical power of $\sim 160\text{mW}$, which is utilized as the pump beam in the CRS-experiments (fig. 81 **d**) after performing the collimation and beam diameter matching by an additional lens (*Thorlabs*, AC254-125-B, $f_{L4} = 125\text{mm}$; **L4**). Changing the central wavelength of the $1,5\mu\text{m}$ cavity in combination with temperature tuning of the PPLN crystal an additional wavelengths tuning range can be achieved also in this laser branch extending the addressable range of molecular resonances (fig. 81 **c**). Stokes and pump beam are spatially overlapped by the already described methods similar to the solid-state laser system (see 3.1.3) and can now be utilized for CRS-microscopy.

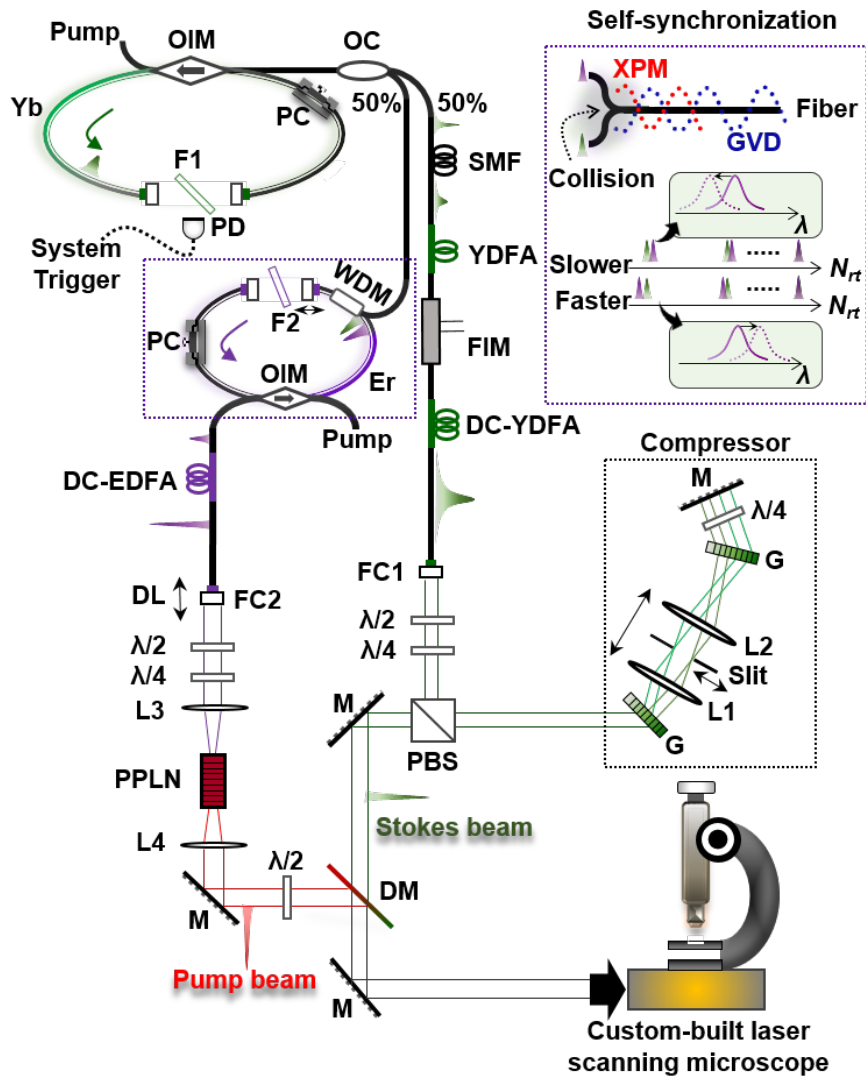


Figure 75 – Schematic diagram of the tunable two-color all fiber-based CRS-laser

The passively mode-locked laser cavity (left upper corner) generates the $1\mu\text{m}$ fs-pulse train with 80MHz repetition rate, which is then split into two branches. One half is amplified by two amplifier stages to generate the Stokes beam (green color), which is compressed by a grating compressor (right middle box) to ps-pulse length. The other half is utilized to synchronize the second slaved laser cavity at $1,5\mu\text{m}$ (violet color), which is amplified and then frequency doubled by a PPLN crystal to the final pump wavelength (red). Both Stokes and pump beam are spatio-temporally overlapped and then coupled into the scanning CRS-microscope. The right upper box shows a sketch of the self-synchronization utilizing cross-phase modulation and anomalous dispersion. See main text for detailed explanation. Abbreviations: **OC** - fiber optic coupler, **DM** - dichroic mirror, **DL** - delay line, **DC-EDFA** - double-cladding erbium-doped fiber amplifier, **DC-YDFA** - double-cladding ytterbium-doped fiber amplifier, **Er** - erbium doped fiber, **F** - filter, **FC** - fiber collimator, **FIM** - fiber coupled intensity modulator, **G** - grating, **GVD** - group velocity dispersion, **L** - lens, **M** - mirror, N_{rt} - round-trip number, **OIM** - fiber-based optically integrated module, **PBS** - polarizing beam splitter, **PC** - polarization controller, **PD** - photodiode, **PPLN** - periodically poled lithium niobate crystal, **SMF** - single-mode fiber, **YDFA** - ytterbium-doped fiber amplifier, $\frac{\lambda}{2}$ - half-wave plate, $\frac{\lambda}{4}$ - quarter-wave plate. Part of [Kong et al. [2019]].

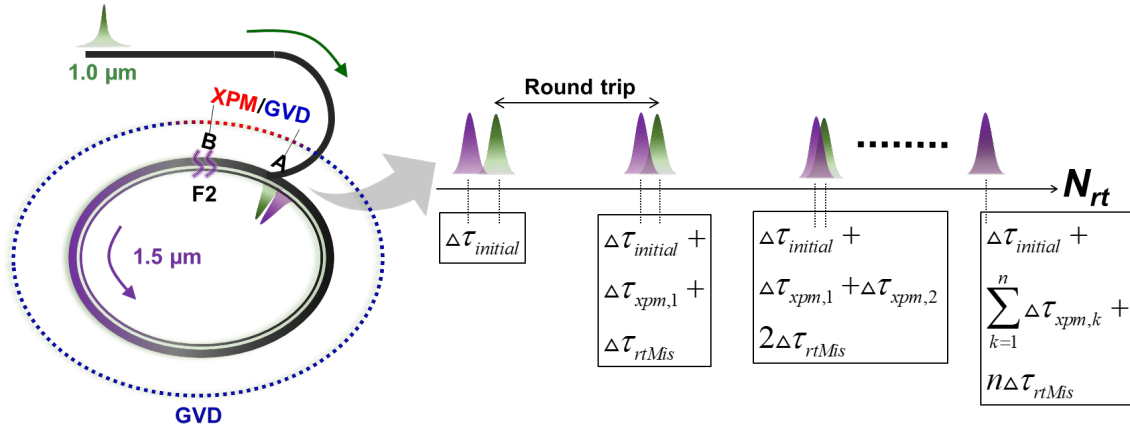


Figure 76 – Sketch of the passive self-synchronization mechanism utilized in the fiber laser setup. Half of the $1,0\mu\text{m}$ laser light (green) serving as master oscillator is coupled into the $1,5\mu\text{m}$ pump beam cavity (violet), whose repetition rate is already optimized to the value of the master oscillator in the self-sustained pulse train mode but has still a temporal offset ($\Delta\tau_{initial}$). In the optical path between points **A** and **B** a nonlinear fiber enables the interplay between both laser pulses via cross-phase modulation (**XPM**) inducing a shift of the center wavelength of the $1,5\mu\text{m}$ pulse train. Due to the anomalous dispersion in the cavity for the $1,5\mu\text{m}$ wavelength a slowing-down or speeding-up of the pulses is achieved by group velocity dispersion (**GVD**) according to the frequency shifts induced by XPM. On the right hand side the synchronization process is depicted showing the timing of both pulses to each other while the round-trip number N_{rt} is evolving from left to right. Due to the combined XPM/GVD effect the timing offset of both pulses is decreasing by each round-trip by $\Delta\tau_{xpm}$ up to the point of synchronization after n round trips. Part of [Kong et al. [2019]].

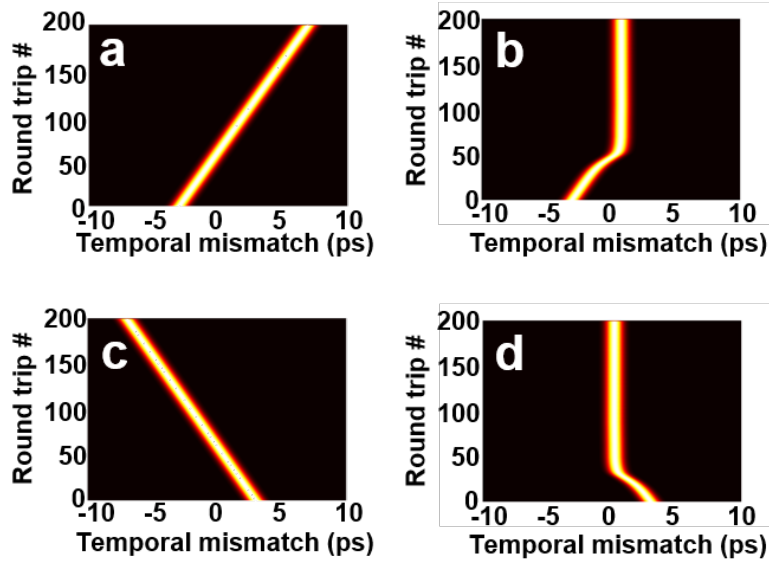


Figure 77 – Numerical simulations of the passive self-synchronization mechanism of the $1,5\mu\text{m}$ laser cavity

Timing evolution of the $1,5\mu\text{m}$ pulses in the cavity **a)** without injected $1,0\mu\text{m}$ pulses and **b)** with injected pulses, while the repetition rate of the $1,5\mu\text{m}$ cavity is assumed to be slightly lower than the master cavity in the simulation. The round-trip number is depicted over the temporal mismatch between both pulses. **c)** and **d)** show the same situation but having a slightly higher repetition rate of the $1,5\mu\text{m}$ cavity, respectively. Both simulated situations show a synchronization by the injected $1,0\mu\text{m}$ pulses after < 50 round trips (temporal mismatch = 0ps). The simulation assumes a initial timing delay of 3ps and a round trip time mismatch of 50fs . Part of [Kong et al. [2019]].

4.6.2. Characterizing the temporal and spectral properties of the all fiber-based CRS-laser source

For the characterization of the constructed fiber laser setup additional experiments were conducted in order to demonstrate the performance also for comparison to other competitive setups. The constant and synchronous repetition rate of both lasers is determined to $\sim 80\text{MHz}$, $12,5\text{ns}$ pulse-to-pulse timing by sequentially visualizing the pulse train of both laser wavelengths by a fast photodiode (*HP*, 11982 A, 10GHz bandwidth) and a 20GHz real-time oscilloscope (*LeCroy*, SDA-820Zi-B) (fig. 78 **a**). A long term measurement of the pulse train over $500\mu\text{s}$ proves a stable operation without any intensity fluctuations or Q-switching events (fig. 79), which also indicates the environmental insensitive operation of the system.

For demonstrating the capabilities of the fiber-based intensity modulator in the Stokes beam path a 20MHz sinusoidal modulation was applied and again the pulse train was measured showing a modulation depth of $> 99\%$ (fig. 78 **b**), which is an excellent value compared to state-of-the-art resonant EOM solutions in free-space optics (having $80 - 95\%$ modulation depth, compared to e.g. *APE*, EOM 1030). For comparison a

sinusoidal function is plotted as an envelope to the depicted pulse train of the Stokes beam as a guide to the eye. The pulse length of both laser wavelengths is also characterized by utilizing two autocorrelators (Stokes: *Femtochrome Research*, FR-103 MN; pump beam: *MesaPhotonics*, FROGscan) due to the different wavelengths. The Stokes beam has a pulse length of 3,2ps and 2,7ps for the pump beam, respectively. Due to the already described challenges of the pulse length dependence during wavelengths tuning in hyperspectral CRS-experiments utilizing OPO-based laser systems (compare 4.3) the pulse length of the Stokes beam was also monitored during wavelengths tuning (1015–1040nm) showing a variation of < 1,8% indicating further advantages of the all fiber-based system (green line in 78 c). The power stability performance is determined by detection via the photodiode and the real-time oscilloscope during a time period of 100mins for finally calculating the the root-mean-square value to be better than 0,5% for the Stokes (setting 550mW power) and 0,1% for the pump beam (at 100mW power), respectively (fig. 78 d). For testing the performance of the synchronization between pulse trains at these two wavelengths, their cross-correlation curve was measured through sum frequency generation (SFG) in a KTP (potassium titanyl phosphate) optical crystal. During the measurement, the temporal delay between both pulse trains was changed using the optical delay line in the optical path of one pulse train. The raw SFG signal is recorded over 10sec by an oscilloscope at the peak (gray curve, full temporal overlap) and 50% (black curve, 2ps delay) SFG intensity in (fig 78 e). The timing jitter between these two pulse trains is estimated by calculating the intensity fluctuation of the SFG signal and the rising/falling slope of the cross-correlation trace, both at half maximum, and then divided the former by the latter, yielding a timing jitter of 24,3fs (0,8% of the pulse length).

For comparing the noise performance of both laser branches (fig. 78 f, green and red curve) to other widely recognized laser systems the relative intensity noise (RIN) is measured by a fast photodiode (*HP*, 11982 A, 10GHz bandwidth) and an optical spectrum analyzer (*Agilent*, E4440 A, 26,5GHz bandwidth) and is compared to the values of a standard solid-state fs laser (*Spectra-Physics*, MaiTai, black solid curve) and a typical super continuum-based (SC, blue and purple curve) fiber laser (similar to [Freudiger et al. [2014]]) (fig. 78 f). At the Stokes beam modulation frequency of 20MHz for SRS imaging (black dotted box) the introduced fiber-laser system has in both branches similar performance ($-147dBc/Hz$ pump beam, $-148dBc/Hz$ Stokes beam) being a unique selling point of the new design offering $\sim 50dB$ better performance compared to other recent fiber-based laser systems. These systems suffer from the degraded noise performance due to nonlinear conversion processes of at least one laser wavelength [Dudley et al. [2006]], also apparent in (78 f, blue curve). Here,

the use of two laser cavities in the two-color laser system in combination with their synchronization by exploiting the XPM and GVD effects lead to the better performance. The solid-state laser system (black curve) performs close to the shot noise limit (black dotted curve), in this case at $-164dBc/Hz$, being the edge in terms of achievable noise performance. Further investigations were also performed concerning the frequency spectra at the fundamental repetition rate of the non-modulated Stokes laser (fig. 80 **a**) and by applying a modulation of the Stokes beam via the fiber-based intensity modulator at $\sim 20MHz$ (fig. 80 **b**) as well as of the repetition rate of the pump laser (80 **c**). The signal-to-noise performance of all acquired RF-spectra show a low laser noise (SNR at $80MHz$: Stokes $74db$, pump $73db$, respectively), the desired modulation of $20MHz$ in the Stokes beam has a SNR of $67dB$ without any additional frequency contents, which is beneficial for the lock-in amplification process.

The spectral properties of the fiber-based laser system are depicted in fig. 81, by coarse wavelengths tuning via rotation of the intracavity filter in the Stokes beam cavity (F1, bandwidth of $\sim 8nm$) the accessible wavelengths regime of $1005 - 1065nm$ is measured in (81 **a**) by the frequency analyzer. The final Stokes spectrum for CRS imaging is generated by the grating compressor (depicted in fig. 81 **b**) and has a bandwidth of $\sim 1,0nm$ offering a continuous wavelengths spectrum from $1010 - 1060nm$. Also the fundamental central wavelength of the pump beam branch can be tuned from $1540 - 1590nm$ by rotating filter F2 having a bandwidth of $< 1,0nm$ (fig. 81 **c**). The frequency doubling performed by the temperature controlled PPLN has a typical bandwidth of $0,35nm$ and is showcased at $1578nm$ doubled to $789nm$ in fig. 81 **d**, the transform-limited Gaussian pulse width is $2,6ps$.

The laser setup is capable of high-speed SRS imaging with high chemical sensitivity, which is appealing due to the lack of any non-resonant background contribution in contrast to CARS imaging. For proving the ability to access the Raman resonances by SRS without any shifts of the Raman peaks e.g. due to the dispersive line shapes in CARS, two pure samples are analyzed by wavelengths tuning of the Stokes beam (fig. 82). The Raman resonances of pure methanol and DMSO are acquired in the range of $2800 - 3050cm^{-1}$ by SRS as well as with spontaneous Raman scattering (SR) with a home-built spontaneous micro-Raman scattering setup utilizing a $785nm$ Cw diode laser (*Innovative Photonic Solutions*) in combination with a fiber-coupled grating spectrometer (*Princeton Instruments*, Acton 2300i) with camera detection (*Andor*, Newton DU 920p BR-DD). Comparing the SRS to the SR spectra show excellent peak overlap and the same line shapes, whereas in the case of methanol the spectral background between both Raman resonances in the probed wavenumber range is even better in SRS.

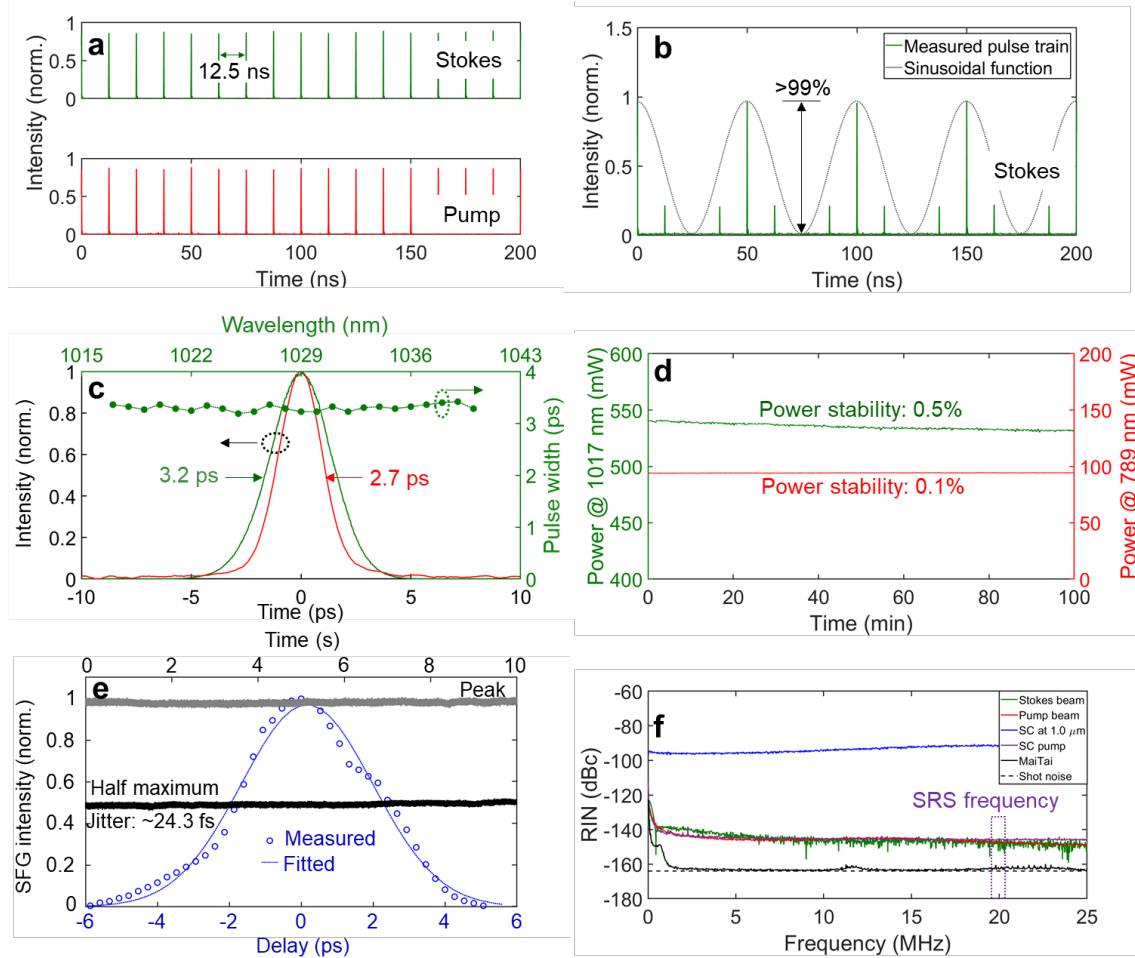


Figure 78 – Temporal characterization of the Stokes and pump laser pulses

a) shows the pulse train acquired with fast photodiodes and a 20GHz real-time oscilloscope at 1017nm (Stokes) and 789nm (pump beam), respectively. **b)** depicts the real-time pulse train of the Stokes beam while applying a 20MHz sinusoidal intensity modulation via the fiber-based modulator. The modulation depth shows $>99\%$. As a guide to the eye a sinusoidal function is plotted as an envelope to the modulated pulses. By performing an autocorrelation of both laser wavelengths the pulse length was determined to $3,2\text{ps}$ for the Stokes (green) and $2,7\text{ps}$ for the pump beam (red) in **c)**. Also the pulse length stability during wavelengths tuning was measured from $1015 - 1040\text{nm}$ showing $< 1,8\%$ variation (green line plot for the Stokes beam). The power stability was proven to be better than $0,5\%$ for Stokes (at $\sim 550\text{mW}$ output power) and $0,1\%$ for the pump beam (at $\sim 100\text{mW}$ output power) acquired over 100min calculating the RMS value (**d)**). By performing a sum-frequency generation (SFG) of both beams in a KTP crystal and an optical cross correlation by a spectrum analyzer while tuning the delay stage of the pump beam the timing jitter between both laser lines was analyzed (**e)**). The maximum SFG signal (gray line) as well as the half of the signal (black line) are showcased. By fitting a Gaussian function to all measured SFG intensities while tuning the delay between Stokes and pump beam the slope of the Gaussian fit was extracted to determine the jitter to be $\sim 24,3\text{fs}$. In **f)** the noise performance of the described home-built laser system (green and red lines) is compared to typical competing laser systems such as a super continuum fiber laser (SC) at $1,0\mu\text{m}$ (Stokes, blue line) and $1,5\mu\text{m}$ (as source for the pump beam, purple line), a fs-pulsed MaiTai laser (black solid line) as well as the shot noise limit as reference (black dashed line). The typical modulation frequency for SRS imaging is indicated by the black dotted box. Part of [Kong et al. [2019]].

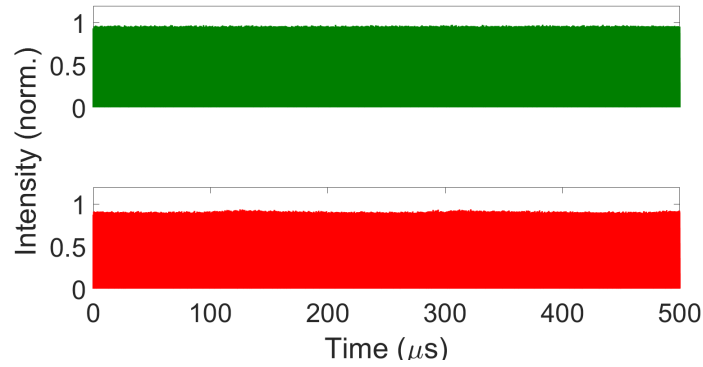


Figure 79 – Pulse train characterization of both laser wavelengths over long time period. The pulse train of Stokes (green) and pump beam (red) are analyzed by detecting the laser wavelength with fast photodiodes on a $20GHz$ real-time oscilloscope over a time period of $500\mu s$. The normalized intensity shows very low changes. Part of [Kong et al. [2019]].

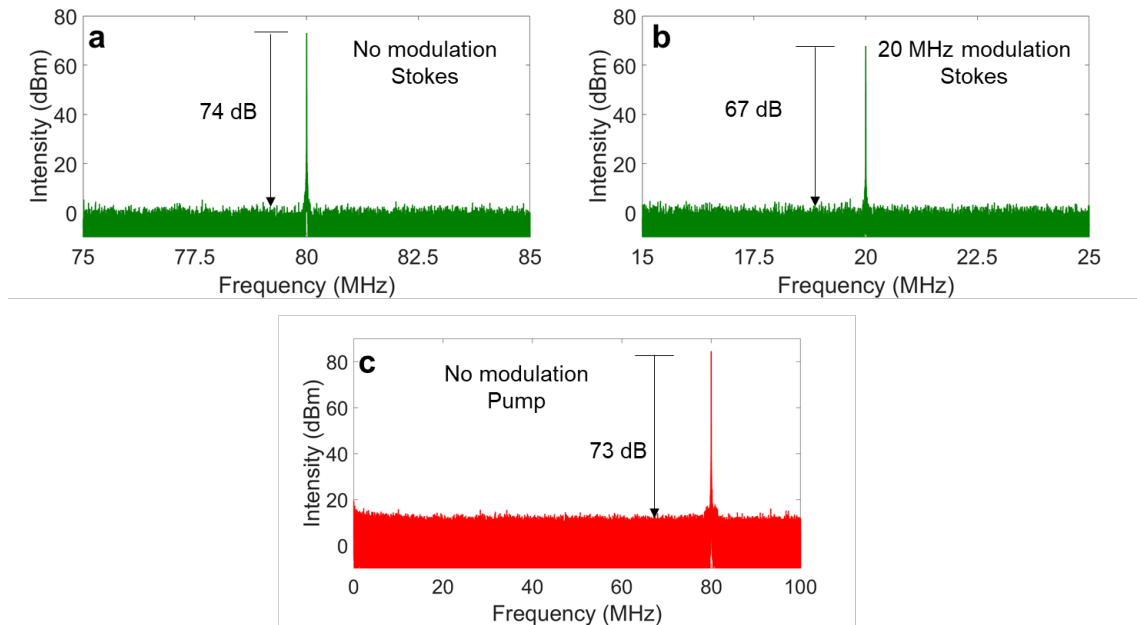


Figure 80 – Radio frequency (RF) spectra for characterizing the two-color pulsed fiber laser. **a)** shows the RF spectrum of the non-modulated Stokes beam centered at the fundamental repetition rate of the laser system at $\sim 80MHz$ showing the signal-to-noise characteristic of $74dB$. Applying the frequency modulation at $20MHz$ with the fiber-based modulator for SRS imaging (**b**) leads to a detected modulation performance of $67db$. In **c)** the frequency doubled pump beam is analyzed showing a SNR of $73db$ at $80MHz$. Part of [Kong et al. [2019]].

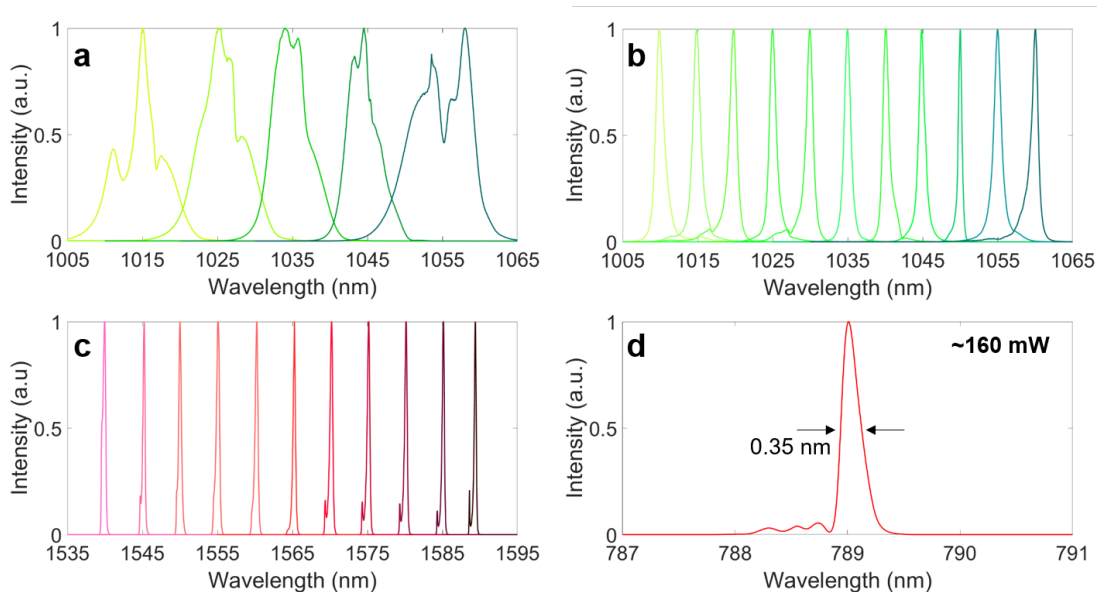


Figure 81 – Spectral characterization of the two-color fiber laser source

a) shows the accessible coarse tuning wavelengths of the $1,0\mu\text{m}$ master cavity by rotating the intracavity filter F1 (8nm bandwidth). In **b)** the slit-based filter scheme of the grating compressor is utilized for a fine tuning from $1010 - 1060\text{nm}$. **c)** depicts the tuning range of the fundamental pump beam from $1540 - 1590\text{nm}$ by rotating the intracavity filter F2 ($< 1\text{nm}$ bandwidth). **d)** showcases the final pump beam wavelength generated by the PPLN via frequency doubling with a central wavelength at 789nm having a bandwidth of $0,35\text{nm}$. All spectra were acquired by a spectrum analyzer and are normalized. Adapted from [Kong et al. [2019]].

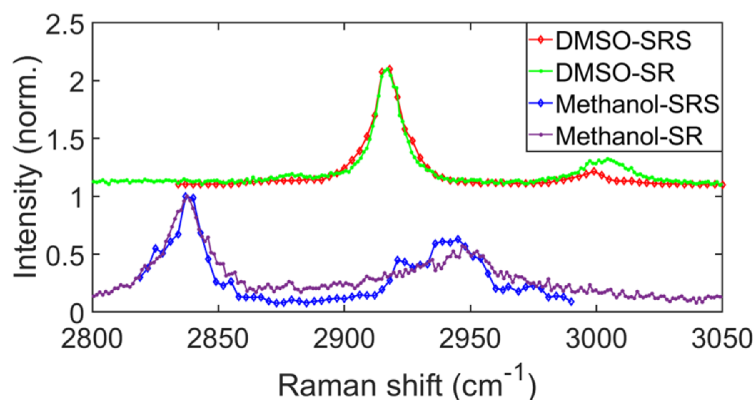


Figure 82 – Comparing SRS and spontaneous Raman spectra on pure samples

By wavelengths tuning of the Stokes beam the molecular resonance of two pure samples (DMSO - red line, methanol - blue line) is acquired from $2800 - 3050\text{cm}^{-1}$ and compared to spontaneous Raman spectra (SR, green DMSO and violet methanol, respectively). All intensities were normalized and vertically shifted for easy comparison. The SRS spectra were acquired by scanning $5\times$ zoomed images and averaging the intensity values of the pixels. The SR spectra were acquired by the home-built spontaneous Raman setup utilizing a 785nm Cw-laser. Adapted from [Kong et al. [2019]].

4.6.3. All fiber-based two-color laser system enables simultaneous SRS and CARS imaging on living human cells

For exploring the performance of the fiber laser system living osteosarcoma²⁵ (U2OS) cells are investigated by probing the 2845cm^{-1} CH_2 stretching mode in order to highlight the lipid distribution and the cellular border (fig. 83 **a** CARS and **b** SRS). The cells were cultivated in DMEM media (*ThermoFisher*) containing 10% fetal bovine serum (*ThermoFisher*) on a standard petri dish stored in a humidified incubator at 37°C , 5% O_2 and 5% CO_2 . Shortly before the imaging process the medium was replaced by phosphate buffered saline (*Sigma Aldrich*, PBS). The focal pump beam intensity was 33mW the modulated Stokes beam 74mW , respectively. The SRS images were acquired by setting a intensity modulation frequency of 20MHz of the Stokes beam (see also 3.1.6). The pump beam and the CARS signal were separated by a dichroic mirror (*Semrock*, LP02-785RU) and the CARS signal is further filtered (FF01-655/40-25). The pump beam is filtered by carefully suppressing the Stokes beam (*Semrock*, FF01-855/210-25, F01-950SP), detected on the fast SI-photodiode module and finally demodulated by a fast lock-in amplifier (LIA) (*APE Berlin*, SRS Detection Set). The integration time constant of the LIA was $2\mu\text{s}$ enabling a pixel dwell time of the laser scanner of $12,5\mu\text{s}$ for both contrast methods. No balanced detection scheme was needed for the SRS imaging. The CARS wavelengths were separated by the dichroic beam splitter and detected on the PMT. No stripes can be observed in the simultaneously acquired CARS images due to the slower response time of the PMT, which masks the 20MHz Stokes intensity modulation. For easy comparison all presented CARS images are processed with the look-up table (LUT) “cyan hot”, the SRS images are processed with the LUT “red hot” by the image software *FIJI* [Schindelin et al. [2012], Rueden et al. [2017]]. The intensity of each signal is color-coded in the LUT and optimized for best contrast for each image and can differ from image to image. Therefore, a color bar is depicted beside each image to keep the intensity distributions transparent. Single prominent lipid droplets in the cells are highlighted by arrows, the cellular border of a selected cells is indicated by a white dashed circle.

In the next step living primary myoblast cells (PMD) were imaged during their differentiation process by applying 25mW pump and 47mW modulated Stokes focal power setting a pixel dwell time of $51,2\mu\text{s}$ combined with a LIA time constant of $20\mu\text{s}$ (fig. 83 **c** CARS and **d** SRS). The PMD cells were cultivated in DMEM containing 5% horse serum (*ThermoFisher*) and prepared on petri dishes coated with an extracellular matrix (*Sigma Aldrich*) at 1 : 500. The cells contain less lipid contents and, therefore,

²⁵The human cell samples were provided by Prof. T. H. Cheung, Prof. C. S. W. Lai and Prof. N. P. Lee.

exhibited less signal at the 2845cm^{-1} Raman resonance in combination to the lower laser intensity applied to this sample the pixel dwell time had to be increased compared to the U2OS cells. Nevertheless, single lipid droplets (showcased by the arrows) as well as the cellular border (white dashed circle) are clearly discriminable. Also the advantages of SRS due to the lack of the non-resonant background contribution is apparent in the images: the nucleus area of the cell indicated by the white dashed circle in fig. 83 **c** shows an inner structure, which is not visible in the SRS channel. Here, the background-free SRS responds only to the aliphatic CH_2 groups, whereas the CARS channel generates also unspecific signals, which lowers the chemical specificity.

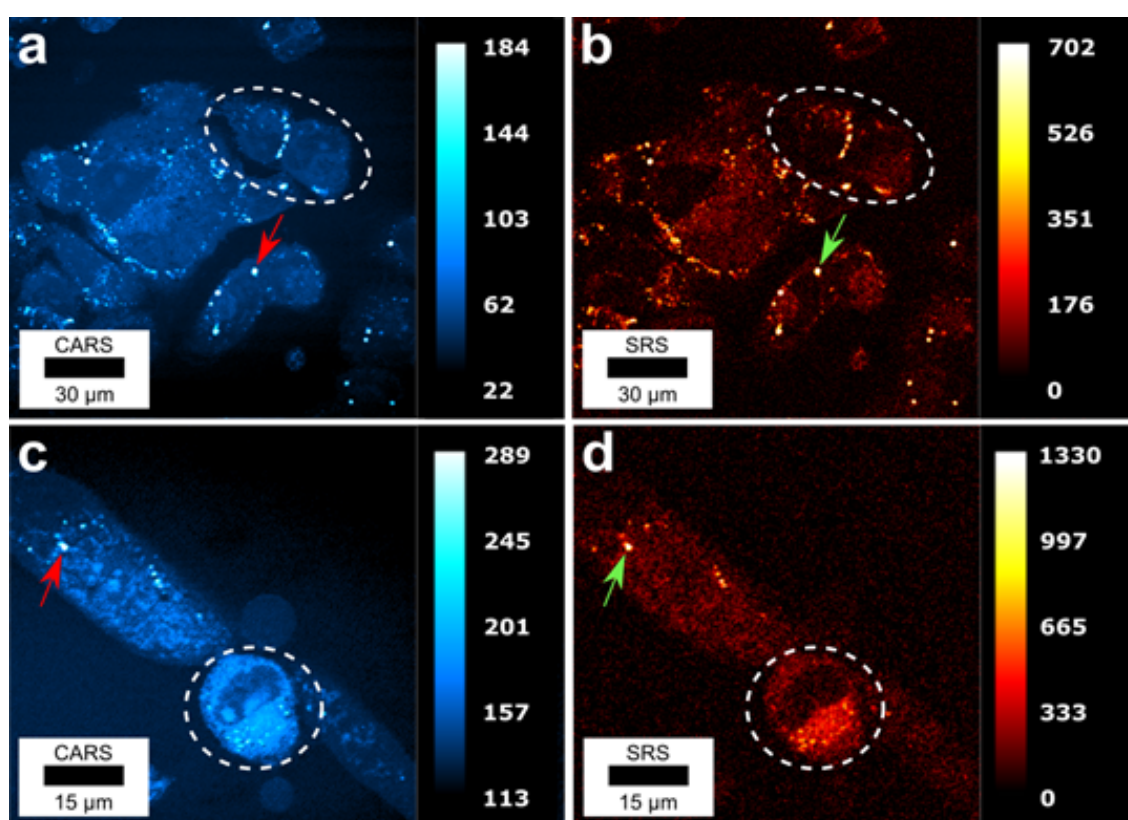


Figure 83 – Comparing SRS and CARS imaging performance on living human cells
 In **a**) and **b**) simultaneous acquired CARS and SRS images probing the 2845cm^{-1} resonance in living osteosarcoma cells (U2OS) are presented. The focal power was set to be 33mW pump and 74mW Stokes beam (20MHz modulation), respectively. The pixel dwell time was $12,5\mu\text{s}$ while setting the time constant of the lock-in amplifier (LIA) to $2\mu\text{s}$. **c**) and **d**) show living primary myoblast cells (PMD) in their differentiation process by again probing the 2845cm^{-1} resonance. The focal power of the pump beam was 25mW and 47mW for the Stokes beam, respectively. The pixel dwell time is $51,2\mu\text{s}$ in combination with a LIA time constant of $20\mu\text{s}$. The arrows indicate selected lipid droplets in the cellular area. Part of [Kong et al. [2019]].

4.6.4. Investigating the performance of the all fiber-based laser on tissue samples utilizing simultaneous SRS and CARS contrast

A tissue section of a 2-month-old mouse, which suffered of severe combined immunodeficiency, was imaged by the dual channel approach using CARS and SRS as described before. The tissue was embedded in paraffin and cut into $50\mu\text{m}$ thick sections by a cryo microtome and transferred to a thin cover slide. An overview of the investigated slide is created by a bright-light setup with $4\times$ magnification (fig. 84 a) showing the superior Vena cava (border indicated by the violet dotted lines). For the CRS experiments two ROIs were selected (red and green boxes) and a larger field of view is generated by moving the sample and then stitching the overlapping sequentially acquired images (fig. 84 b CARS and c SRS). The focal powers were set to 33mW pump and 74mW Stokes beam with 20MHz intensity modulation frequency. The pixel dwell time was set to $6,4\mu\text{s}$ and the lock-in amplifier time constant was $2\mu\text{s}$. In the images the border between Tunica media and Tunica intima can be observed, a violet dotted line is inserted to guide the eye. The yellow inset in fig. 84 b shows a zoom image of red blood cells forming a thrombus (yellow dotted circle), which was adherent to the vascular wall. The CRS images of ROI 2 are presenting a lipid rich area in the Tunica media (fig. 84 d and e, CARS and SRS, respectively). The green line indicates the location of a line scan comparing both imaging modalities to each other (fig. 84 f). The normalized intensity profiles show again the superior performance of SRS to CARS due to the small features visible in the SRS channel (indicated by red arrows), where in the CARS channel the non-resonant background masks them leading to a diminished chemical sensitivity.

In a further experiment a murine brain tissue sample²⁶ was investigated in the same manner. The sample was extracted of the mouse, cut by a cryo microtome into $50\mu\text{m}$ thick slices and was finally fixed by using a 4% para-form aldehyde solution. Two regions of interest are selected for the dual channel imaging via SRS and CARS investigating the neuron network as well as the distribution of the granule cells in the hippocampus (fig. 85). During the imaging the focal power of the pump beam was set to 33mW the Stokes beam to 67mW by using a pixel dwell time of $12,8\mu\text{s}$ and a LIA time constant of $2\mu\text{s}$. The image contrast and sensitivity is very satisfactory and will be exploited to perform large area scans in future projects [Ruiz-Perera et al. [2018], Klenke et al. [2013]], enabling the identification of the individual brain sections and following the transitions into each other, especially the formation of the granule cells.

²⁶The samples are provided by Prof. B. Kaltschmidt and Prof. C. Kaltschmidt.

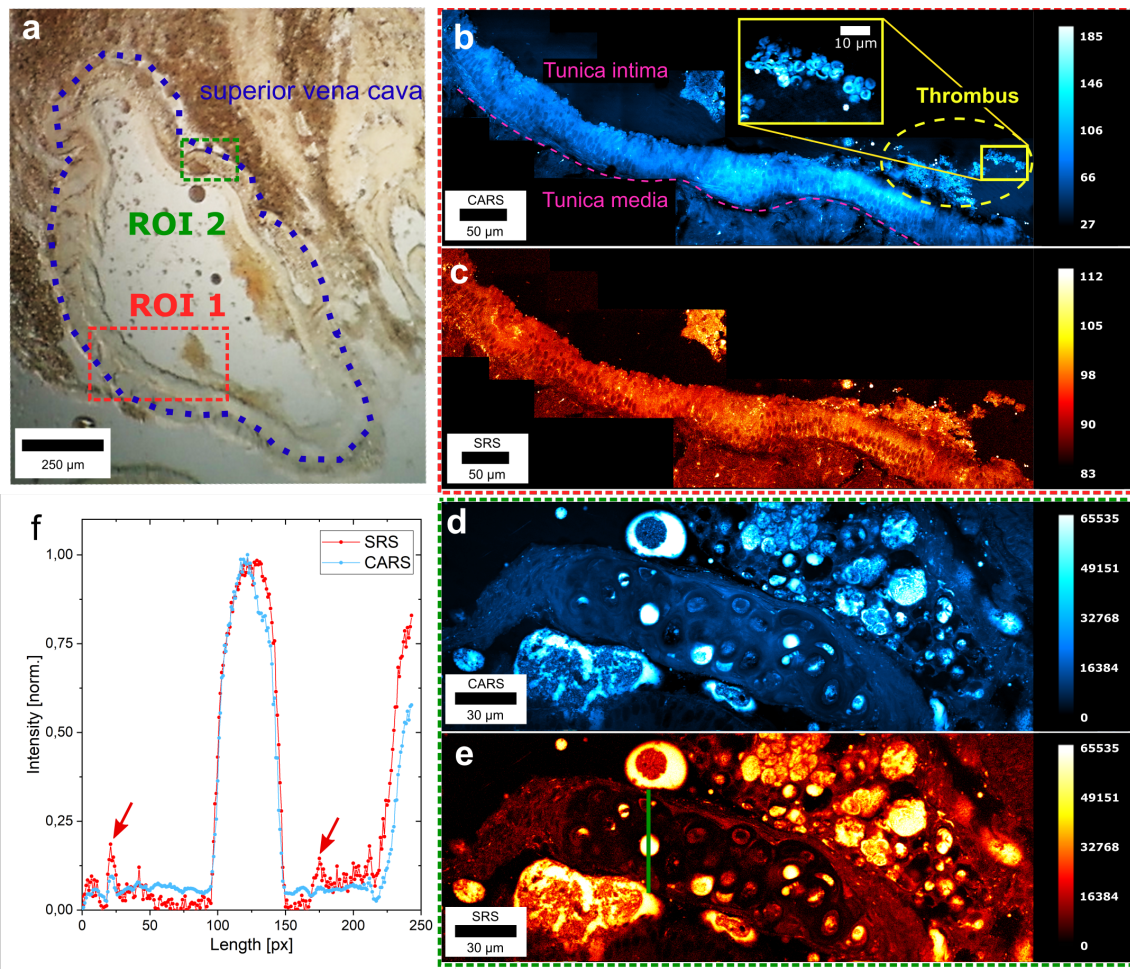


Figure 84 – CRS-imaging of murine superior Vena cava tissue cryosection

a) shows a bright-field overview image of the analyzed cryosection. For further analysis with simultaneous SRS and CARS imaging two ROIs are selected (red and green boxes). The violet dotted line indicates the location of the superior Vena cava. **b)** shows the CARS and **c)** the SRS images of ROI 1, which were stitched showing a large field-of-view. They allow the discrimination of Tunica media and Tunica intima. The border between them is indicated by the added pink dotted line. The yellow inset shows a zoom image visualizing a thrombus persisting of red blood cells adhering to the vascular wall. **d)** and **e)** show the stitched CARS and SRS images of ROI 2 detailing the Tunica media with lipid rich structures. The green line in **e)** depicts the location of a comparing line plot, which is presented in **f)**. Here, small lipid rich structures are revealed by SRS, due to the higher chemical contrast (red arrows) by the advantage of having no non-resonant background in SRS. For all images the focal pump power was set to $33mW$ and $74mW$ for the Stokes beam, having a pixel dwell time of $6,4\mu s$. The LIA time constant is set to be $2\mu s$ in combination with the applied $20MHz$ modulation frequency in the Stokes branch. Part of [Kong et al. [2019]].

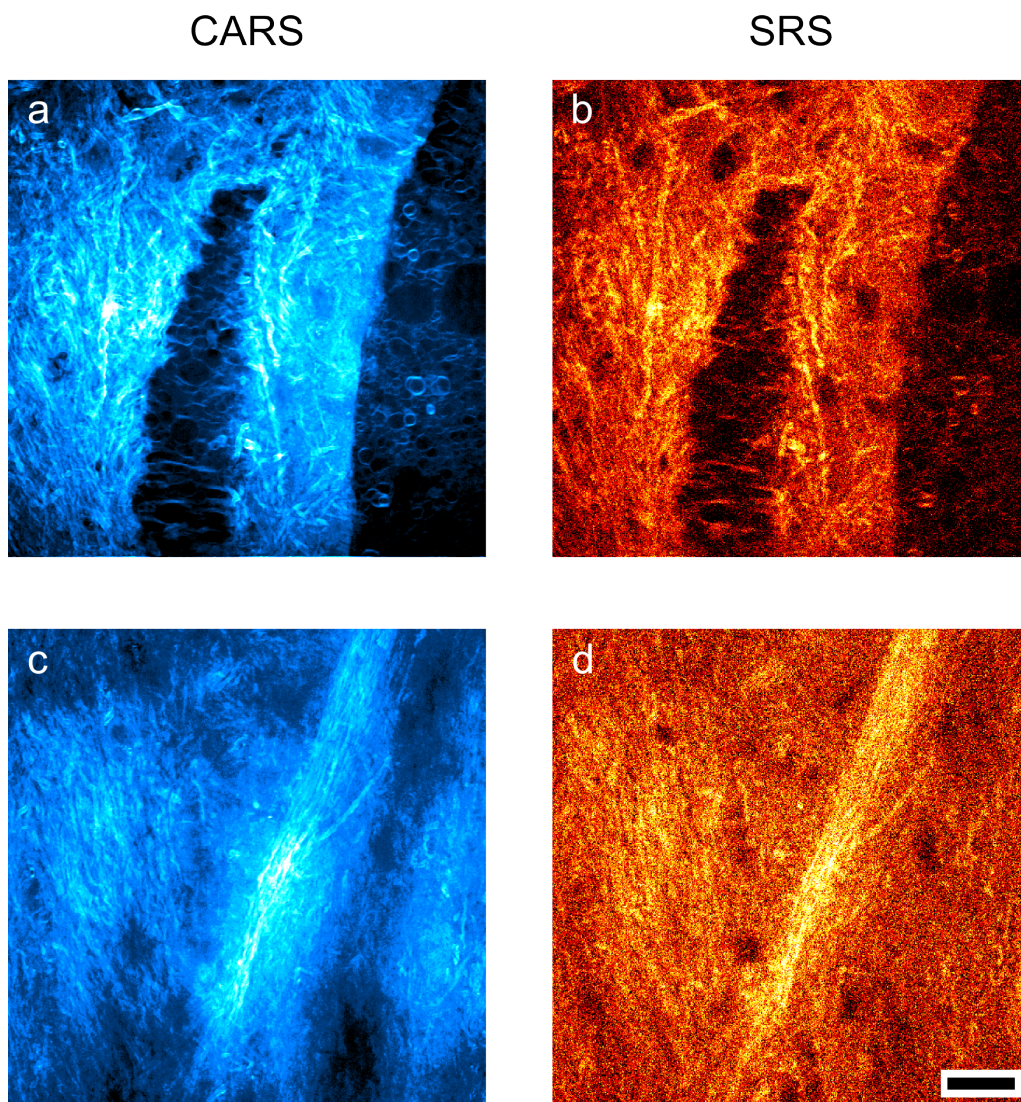


Figure 85 – CRS-imaging of murine brain sections

Murine brain sections are investigated by simultaneous CARS and SRS imaging at two different locations on a $50\mu\text{m}$ thick cryo-section (**a** CARS and **b** SRS of ROI 1 as well as **c** and **d** of ROI 2, respectively). The focal power was set to 33mW and 67mW for the pump and Stokes beam, respectively. The pixel dwell time was $12,8\mu\text{s}$, while having a LIA time constant of $2\mu\text{s}$ in combination with the applied 20MHz modulation frequency in the Stokes branch. The scale bar depicts $20\mu\text{m}$.

4.6.5. Fs-laser pulses of Stokes cavity are utilized for SHG and two-photon excited fluorescence imaging broadening the range of application

The multimodal imaging capability of the introduced laser system is demonstrated by generating $\sim 200fs$ pulsed laser light by removing the filtering slit in the grating compressor stage of the Stokes beam generation, which then provides a spectral bandwidth of $\sim 8nm$ with a central frequency of $\sim 1025nm$. An unstained mouse tail sample²⁷ was harvested from a 3-month old C57BL/6²⁸ mouse and selected for demonstrating SHG generation at $\sim 512,5nm$ (fig. 86 a) by applying $\sim 20mW$ focal power and controlling the polarization of the fs-laser beam by a combination of a half- and a quarter-wave plate (one state of polarization is shown in the image). The collagen in the tendon tissue of the sample generates the detected SHG signal, while the surrounding muscle tissue remains without signal contributions. Two-photon excited fluorescence imaging was performed using $20mW$ focal power on a murine kidney section (*ThermoFisher*, FluoCells prepared slide #3), which is stained with three individual fluorescent dyes. Two optical bandpass filters (centered at $519nm$ and $600nm$) are separating two fluorescent stains in the experiments for sequential imaging: Alexa Fluor 568 phalloidin is detected labeling the filamentous actin cytoskeleton prevalent in the glomeruli and brush border (fig. 86 b) as well as Alexa Fluor 488 wheat germ agglutinin labeling elements of the glomeruli and the convoluted tubules (fig. 86 c) (interpretation based on [Wiederschain [2011]]).

For demonstrating the z-sectioning capabilities of the system a z-scan over $145\mu m$ range with a step size of $5\mu m$ is acquired of a $200\mu m$ thick mouse brain tissue²⁹ prepared between two thin cover slides. The mouse is expressing the yellow fluorescent protein (YFP) in layer-V pyramidal neurons (Thy1-YFP H-line) [Lai et al. [2012]], which was excited by $\sim 50mW$ focal power, indicating the neuron distribution in the tissue. Fig. 86 d shows a 3D montage of the data stack generated by *FIJI volume viewer* as well as in fig. 86 e a selected single xy-slice of the stack showcasing the neurons and, thereby, the good z-sectioning of the two-photon excitation.

The application of the Stokes-laser branch as a versatile and low-cost source for SHG and two-photon excited fluorescence was also proposed in a stand-alone version [Kong et al. [2017]]. In general also 3-photon excited fluorescence [Wang et al. [2018], Horton et al. [2013]] can be performed by this laser source utilizing the fundamental pump beam cavity laser light ($1578nm$), but due to the lack of sufficient optics (e.g. objective lens corrected for $\sim 1500 - 1700nm$, mirrors and telescope lenses in sufficient

²⁷Provided by T.H. Cheung, C.S.W. Lai and N.P. Lee.

²⁸Transgenic mouse model.

²⁹Provided by Prof. T. H. Cheung, Prof. C. S. W. Lai.

anti-reflective coating in this range) this modality has not been pursued so far.

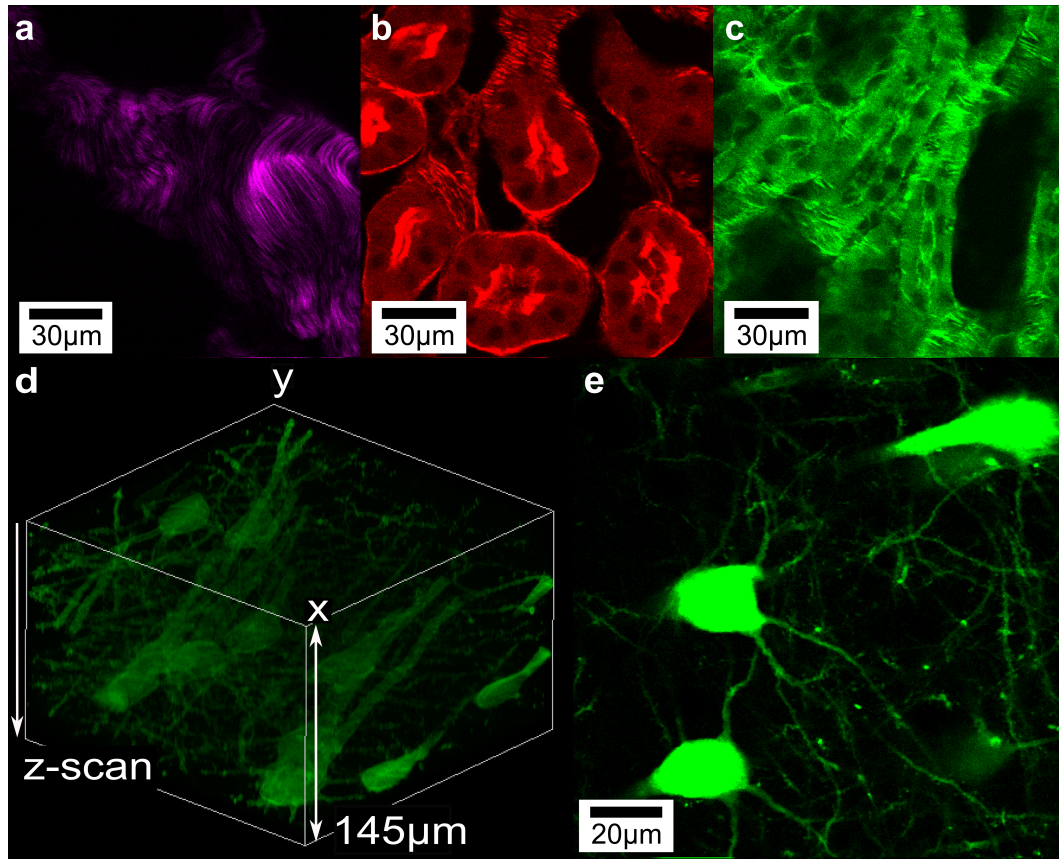


Figure 86 – SHG imaging of mouse tail sample and two-photon excited fluorescence imaging of kidney and brain tissue sections

The fs-pulsed Stokes beam (bandwidth $\sim 8nm$, $\sim 200fs$ pulse length) can be utilized for e.g. SHG imaging (a) of a mouse tail sample by applying $\sim 20mW$ focal power. The polarization of the laser was controlled by a stack of half- and quarter-wave plate. Two-photon excitation is demonstrated with the same source and focal power on a mouse kidney section (*ThermoFisher*, FluoCells prepared slide #3) visualizing two different fluorescent stains of the sample sequentially by using a suitable optical filter set (b, Alexa Fluor 568 phalloidin labeling the filamentous actin cytoskeleton prevalent in glomeruli and the brush border; c, Alexa Fluor 488 wheat germ agglutinin labeling elements of the glomeruli and the convoluted tubules [Wiederschain [2011]]). In d) and e) the two-photon excitation of a $200\mu m$ thick mouse brain tissue section prepared between two cover slides is demonstrated in 3D imaging modality. The mouse was expressing the yellow fluorescent protein (YFP) in layer-V pyramidal neurons (Thy1-YFP H-line) [Lai et al. [2012]]. The z-stage was utilized for scanning a range of $145\mu m$ with $5\mu m$ step size. d) shows a 3D montage (performed via *FIJI volume viewer*) indicating the distribution of the neurons in the tissue. e) showcases a single frame of the stack, the focal power was set to $\sim 50mW$. Part of [Kong et al. [2019]].

4.6.6. Extending the range of accessible wavenumbers with a third laser cavity enabling the visualization of alkyne tagged samples in the future

The introduced all fiber-based CRS laser source has been characterized and compared to state-of-the-art fiber-based and traditional solid-state laser systems determining the unique selling point of this laser system in having a superior noise performance, which allows the rapid SRS imaging without the need of a balanced detection scheme for laser noise cancellation. The abilities were demonstrated by imaging relevant living human cells as well as different tissue sections by a dual SRS and CARS contrast in simultaneous rapid acquisition manner. For proving the versatility of the setup also SHG and two-photon excited fluorescence imaging are showcased on several samples combined with z-scanning. In table 1 the demonstrated properties of the two-color all fiber-based laser system are compared to other laser systems using fiber-laser technology for generating one or both laser wavelengths for CRS microscopy known from literature. Here, the novelty of the introduced approach becomes apparent.

The next steps in the development of the all fiber-based laser system are inserting an AOTF (acousto-optic tunable filter) into the Stokes beam cavity for enabling rapid automated wavelengths tuning in order to allow a hyperspectral image scan similar to the previously described modality based on the solid-state laser system (compare 4.4). Also the use of all fiber-based electronically controlled Fabry-Pérot wavelengths filters inside the laser cavities can replace the manual wavelengths tuning and enable tuning speeds of up to $100kHz$ [Huber et al. [2006]].

In addition to that the range of accessible Raman shifts will be further extended by adding a third oscillator cavity as alternative second pump beam for CRS-microscopy. Especially samples with alkyne tags such as e.g. EdU (ethynyl deoxyuridine) are of particular interest due to their Raman resonance in the range of $\sim 2100cm^{-1}$, which is located in the “Raman-silent region” ($1800 - 2600cm^{-1}$) [Zhao et al. [2017]]. Here, no Raman resonances of the typical chemical compounds inside biological cells are active. Therefore, also very small concentrations of alkyne-tagged molecules are accessible by CRS-microscopy. Several studies have been performed utilizing the method of introducing alkyne-tagged molecules into the cells metabolism and finally tracing their distribution by using the label-free CRS-imaging [Shi et al. [2018], Chen et al. [2014], Wei et al. [2014a]]. Still, up to now the use of fiber-based laser sources is hindered in the range of the desired Raman shifts due to the lack of sufficient material combinations for the fiber doping and the connected pumping schemes. In the ongoing project new gain materials will be explored combined with the use of additional fiber-based SESAM mirrors (semi-saturable absorber mirrors) in the laser cavity [Qi et al. [2016]] for improving the mode locking ability of the laser cavity in the case of more

problematic gain media. Promising candidates are e.g. neodymium-doped ($\sim 900nm$), bismuth-doped ($1100 - 1500nm$) and thulium-doped ($1700 - 2000nm$) fibers. When a sufficient combination is identified a third laser oscillator can be added for generating a second pump laser wavelength, which then can be directed into an additional branch for the frequency doubling to the desired final pump beam wavelength. This way a dual contrast of e.g the lipid distribution in a cell by probing the $2845cm^{-1}$ CH_2 resonance and the alkyne tagged molecules, e.g. $2120cm^{-1}$ in the case of EdU, can be exploited for studying the distribution of chemicals during the cells live metabolism. For optimizing the robustness of the source while at the same time minimizing the foot print of the setup, the frequency doubling can also be performed by using fiber-integrated PPLN modules, which would allow a sealed one box system ideal for clinical application [Runcorn et al. [2015]].

	HFL	ASFL	PWCFL	SSFSFL	SCFL	Current work
Pulse length [ps]	< 1, 1 – 10	1 – 10, CW	1 – 10, 10 – 100	< 1	< 1, 1 – 10	~ 3ps
Pump beam power [mW]	> 1000	~ 10, ~ 500	< 100, 100 – 200	1 – 10, 10 – 100	< 10, 10 – 200, > 200	> 160
Stokes beam power [mW]	100 – 500	~ 3, 15	< 100, 100 – 200, > 200	< 1, 1 – 10, > 10	< 10, 10 – 200, > 200	> 1000
Spectral range [cm ⁻¹]	1600 – 2850, 2700 – 3100	2610 – 3430, 750 – 3150	1000 – 2000, 2700 – 3100, 1000 – 5000	0 – 2500, 2300 – 3300, 700 – 4000	1000 – 2000, 2700 – 3100, 1000 – 5000	2700 – 3550
Noise level*	low	high	high	high	high	low
SRS imaging capability	yes	yes	no	yes	yes	yes
SRS imaging speed [$\mu\text{m}/\text{pixel}$]	2, > 200	3000, > 5000	NA	3000, 30000	< 5	> 6, 4
Need of balanced detection	no	yes	NA	yes	yes	no
Use of solid-state laser	yes	no	no	no	no	no
Demonstration of biological samples	Tobacco BY-2 cell, HeLa cells, mouse brain, mouse skin, PC3 cells	Geranium phaenum stem, HeLa cells	NA	Aquatic plant, mouse brain, blood cells	Mouse skin, human surgical specimens	living U2OS cells, living PMD cells, mouse superior Vena cava tissue, mouse brain tissue

Table 1 – Comparison of CRS laser sources

HFL: hybrid fiber laser [Ozeki et al. [2010], Wang et al. [2010, 2013], Ozeki et al. [2012]], ASFL: actively synchronized fiber laser [Karpf et al. [2015], Nose et al. [2012]], PWCFL: parametric wavelength conversion fiber laser [Zhai et al. [2011], Baumgartl et al. [2012a], Lefrancois et al. [2012], Yang et al. [2018], Baumgartl et al. [2012b], Chemnitz et al. [2012], Lamb et al. [2013], Gottschall et al. [2014]], SSFSFL: soliton self-frequency shift fiber laser [Andresen et al. [2007], Pegoraro et al. [2009], Krauss et al. [2009], Xie et al. [2014], Crisafi et al. [2018]], SCFL: super continuum fiber laser [Gambetta et al. [2010], Selm et al. [2010], Freudiger et al. [2014], Chen et al. [2016], Tu et al. [2016], Orringer et al. [2017], Riek et al. [2016], Coluccelli et al. [2014]], *: referring to solid-state lasers. Red color highlights drawbacks compared to the introduced home-built fiber-based laser system (shown in blue).

5. Summary and outlook

This PhD thesis describes the development of a coherent Raman scattering microscope and its use for multimodal imaging of several biomedically relevant samples. This instrument enables the simultaneous acquisition of images with SRS and CARS contrast in addition to second harmonic generation and two-photon excited fluorescence imaging in forward and epi-detection. The sample can be moved in all three spatial dimensions allowing volumetric imaging and large fields of view by automated sample movement and image stitching [Hofemeier et al. [2016]]. By utilizing rapid intensity modulation in combination with lock-in amplification undesired fluorescence signals can be successfully excluded from the desired CARS contrast, which was demonstrated with different samples for quantitative analysis [Jaeger et al. [2016]]. The setup can address a wide range of molecular resonances due to the use of two optical parametric oscillators, which also allow hyperspectral scanning by automated wavelength tuning of the pump beam in the CRS experiment. Here, it was possible to introduce a substantially improved level of reproducibility due to the optimization of the mechanical stability of the setup by customizing optomechanical components and by developing a specifically adapted control software, which was shared with other research groups [Pilger et al. [2018]].

This hyperspectral scanning capability was successfully applied to a range of biomedical samples. The combination of rapid volumetric imaging addressing a single molecular resonance in addition to hyperspectral CARS at selected sample positions was found to be a useful match to answer specific research questions that could not be analyzed by other means [Vukosavljevic et al. [2019], Fueser et al. [2018]]. For exploring the possibility of enhancing the spatial resolution of CARS microscopy in a gentle and bio-compatible way the concept of structured illumination was introduced in the setup. This was realized by rapid intensity switching and the precise control of the scanning mirrors in order to generate a striped illumination pattern in the sample. By simply adding a modern sCMOS camera for detection most of the components are already part of modern CRS or two-photon scanning microscopes, which offers enhanced resolution by low additional costs. This technique was successfully demonstrated with fluorescent samples by two-photon excitation as well as on polystyrene bead samples with CARS contrast.

For the support of CRS microscopy in clinical applications a novel low noise two-color all-fiber-based laser source was developed in a collaboration with the University of Hong Kong [Kong et al. [2019]]. This source provides very low relative intensity noise in combination with superior laser power compared to other, fiber-based sources, which makes

it a perfect tool for CRS microscopy, especially for SRS. Here, several biomedical samples were investigated by simultaneously acquiring SRS and CARS signals showcasing the superior performance of the laser source without the need for balanced detection in the SRS detection path. The laser source is characterized in additional experiments and its performance is compared to other fiber laser setups reported in the literature. It also offers multimodal imaging capability through minor changes in the setup allowing SHG and two-photon excited fluorescence imaging by acting as femtosecond pulsed laser source. This solution is also proposed as a stand-alone setup, making it a cost-effective source for two-photon scanning microscopes [Kong et al. [2017]].

In the future, the CRS microscope will be further enhanced through the development and implementation of an additional laser oscillator into the fiber laser setup, which extends the range of addressable wavenumbers to the Raman-silent region ($1800 - 2600\text{cm}^{-1}$), where in typical biomedical samples no natural molecular resonances are present. This can be exploited for imaging alkyne-tagged or deuterated samples, which offer a unique molecular signature and, thereby, lead to an enhanced sensitivity [Shi et al. [2018], Wei et al. [2014a], Chen et al. [2014]].

Also, this technique can be applied in time-lapsed experiments to the tracking of alkyne-tagged virus particles or circulating tumor cells, which would address a topic of high interest in biomedical research [Hübner et al. [2009]]. The SI-CARS approach can be further explored to allow for the imaging of virus particles, the size of which is well below the typical spatial resolution of a CRS microscope. Here, the low non-resonant background in the Raman-silent region will lead to an optimized signal to noise performance, which is beneficial for the SI-CARS application. Ultimately, the use of doubly-resonant CARS, which is actively probing two molecular resonances at the same time leading to a strongly enhanced signal strength [Weeks and Huser [2010]], can be utilized at specifically designed molecules. This will enable investigating the metabolic incorporation of these molecules into living cells. With these tools it will then be possible to follow the distribution of the molecule of interest over time, unlimited by bleaching effects and without the side-effects of fluorescence labeling.

6. List of publications

- *High contrast, fast chemical imaging by coherent Raman scattering using a self-synchronized two-color fiber laser*; Kong†, C., **Pilger†, C.**, Hachmeister†, H., Wei, X., Cheung, T. H., Lai, C. S. W., Lee, N. P., Tsia, K. K., Wong, K. K. Y., Huser, T., submitted to peer reviewed journal, (2019) {†: equal contribution}
- *Pulse length variation causing spectral distortions in OPO-based hyperspectral coherent Raman scattering microscopy*; **Pilger C.**, Hachmeister H., Greife P., Weiß A., Wiebusch G., Huser T., *Optics Express*: 26, 28312-28322, (2018)
- *Compact high-power fs ytterbium fiber laser at 1010nm for biomedical applications*; Kong†, C., **Pilger†, C.**, Hachmeister†, H., Wei, X., Cheung, T., Lai, C., Huser, T., Tsia, K. K., Wong, K. K. Y., *Biomedical Optics Express*: 8(11), 4921-4932, (2017) {†: equal contribution}
- *Vibrational spectroscopic imaging and live cell video microscopy for studying differentiation of primary human alveolar epithelial cells*; Vukosavljevic, B., Hittinger, M., Hachmeister, H., **Pilger, C.**, Murgia, X., Gepp, M., Gentile, L., Huwer, H., Schneider-Daum, N., Huser, T., Lehr, C-M., Windbergs, M., *Journal of Biophotonics*: 311, e201800052, (2018)
- *Analyzing life-history traits and lipid storage using CARS microscopy for assessing effects of copper on the fitness of *Caenorhabditis elegans**; Fuser, H., Majdi, N., Hägerbäumer, A., **Pilger, C.**, Hachmeister, H., Greife, P., Huser, T., Traunspurger, W., *Ecotoxicology and Environmental Safety*: 156, 255-262, (2018)
- *Label-free in vivo analysis of intracellular lipid droplets in the oleaginous microalga *Monoraphidium neglectum* by coherent Raman scattering microscopy*; Jaeger, D., **Pilger, C.**, Hachmeister, H., Oberländer, E., Wördenweber, R., Wichmann, J., Mussnug, J.H., Huser, T., Kruse, O., *Scientific Reports*: 6, 35340, (2016)
- *Label-free nonlinear optical microscopy detects early markers for osteogenic differentiation of human stem cells*; Hofemeier, A. D., Hachmeister, H., **Pilger, C.**, Schürmann, M., Greiner, J., Nolte, L., Sudhoff, H., Kaltschmidt, C., Huser, T., Kaltschmidt, B., *Scientific Reports*: 6, 6716, (2016)

A. Statutory declaration

I hereby declare that I completed the submitted thesis with no other help and literature than the one known to the reviewers. Sentences or parts of sentences quoted literally are marked as quotations, identification of other references with regards to the statement and scope of this work is quoted.

Bielefeld, 24. 06. 2019

Christian Pilger

B. Acknowledgments

I would like to thank Prof. Thomas Huser for the chance to produce this thesis and for his mentoring and continuous interest in all things related to the CARS lab and the work we did there.

Thomas, I really enjoyed the amount of freedom you allowed me during the realization of all tasks in the lab and the great and steady input of new ideas, which seemed to come in a steady natural flow to you. A big additional “Thank you!” for the great and fruitful idea of forming our collaboration with the University of Hong Kong and the financial support you provided for this work, which also allowed me to experience a new fascinating city and find new friends.

I also want to thank Prof. Anselmetti, Prof. Hütten and Prof. Borghini for joining the examination committee of this thesis.

Furthermore, I thank Dr. Gerd Wiebusch for the support with his experience during the work in the lab, providing good council when there was a problem to be solved. Also I want to express my gratitude for proofreading this thesis, which is always a laborious task.

Special thanks go to Henning Hachmeister: we started the study of physics together a long time ago and shared a great part of the last 10 years solving problems together while acting as our sparring partners. I really enjoyed our time in the lab, building our own setup and you keeping the spirits up during long measurement sessions, while we always had joint interests besides the work. Thank you so much!

Really big thanks go to Prof. Kenneth Wong and his research group at the HKU for providing the chance for the fruitful collaboration. I enjoyed the heartfelt hospitality you always provided me during the visits in Hong Kong very much.

In addition to that I would like to thank Sherry Kong and Dr. Xiaoming Wei for the great time we had together during the entire collaboration applying fiber lasers to CRS microscopy, which took a longer time than initially expected. I want to thank both of you for the friendship we formed and also for introducing me to the “very local” places in Hong Kong, which a European tourist would never find on his own.

I’m thanking Alex Weiß and Paul Greife for the great collaboration during their master theses, it was a pleasure to work with you.

I thank Prof. Olaf Kruse and Dr. Daniel Jäger for the well planned and structured collaboration on the microalgae-related work. Daniel, I really appreciated our joint time in the lab.

I also want to thank Prof. Maike Windbergs and Dr. Branko Vukosavljevic for the collaboration on the human lung cell differentiation: Branko, we had a tough long week

of measurements and an even tougher way until the paper was accepted, but finally it worked out for all of us.

I want to thank Prof. Barbara and Prof. Christian Kaltschmidt for the collaboration on multiple topics and the great interest they showed during our collaboration in the CRS-technique, always being generous with their time to come in our lab for having a look at things and also for providing so many various samples.

Many thanks go to Prof. Walter Traunspurger and to Hendrik Fuser for the collaboration on *C. elegans*, which was a very interesting task and worked well when our laser was not making trouble.

Dr. Marcel Müller I want to thank for his the support on topics related to structured illumination and FairSIM.

I also thank Jakub Pospíšil for the collaboration concerning MAP-SIM and all the nice discussions on related topics.

Additional thanks go to Dr. Mathias Simonis for always being generous providing cell samples.

I'm thanking all collaborators from LaVision Biotec for the exciting time during the collaboration; it was a great experience to get insight into industrial-related research. Your support was very generous and friendly!

To all my office mates I say thanks a lot for the fruitful atmosphere and the nice conversations about not work-related topics.

My thanks also go to all members of the research group *Biomolecular Photonics* for the good working atmosphere and the team spirit, which I enjoyed very much!

I thank Dr. Mark Schüttpeitz for his support concerning MatLab and also for nice conversations on brewing techniques.

Furthermore, I'm thanking Reinhild Pätzmann for all her labors concerning the administration matters such as contracts, travel expenses or even custom matters. You always supported the scientific work, many thanks for that.

Also big thanks go to all members of the mechanical and electronic workshop of the faculty of physics, University of Bielefeld, especially to Karl-Heinz Eichner, Wolfgang Gronemeyer, Uwe Walkenhorst, Herbert Bergmeier and Dieter Gollay; without them many technical nice and home-made solutions and devices utilized in this thesis would have not been realized or at least not with that high quality and love to the detail.

Special thanks go to my family, who supported me with their love, encouragement and their interest in my studies! An additional "Thank you!" I want to direct to my sister Diana for proofreading of this thesis while being not an expert on the topic but instead on the language. This fact turned out to be beneficial for finding errors but

also laborious sizing “our physicist” terms.

Finally, my biggest heartfelt thanks go to my wife Nadine Pilger for keeping me grounded all the time with her love and endurance!

References

- E. Abbe. Beiträge zur Theorie des Mikroskops und der mikroskopischen Wahrnehmung. *Archiv für Mikroskopische Anatomie*, 9(1):413–418, 1873. ISSN 0176-7364. doi: 10.1007/BF02956173.
- M. D. Abramoff, Paulo J. Magalhães, and Sunanda J. Ram. Image processing with ImageJ. *Biophotonics international*, 11(7):36–42, 2004.
- Govind Agrawal. *Nonlinear Fiber Optics*. Elsevier Science & Technology Books, San Diego, CA, USA, 2012. ISBN 9780123973078.
- Esben R. Andresen, Carsten K. Nielsen, Jan Thøgersen, and Søren R. Keiding. Fiber laser-based light source for coherent anti-Stokes Raman scattering microspectroscopy. *Optics Express*, 15(8):4848–4856, 2007. ISSN 1094-4087. doi: 10.1364/OE.15.004848.
- Gian-Luca Anselmetti. *Korrektur von Laserfluktuationen in Bildern eines Kohärente Anti-Stokes-Raman-Streuung (CARS) Mikroskops*. Bachelor Thesis, University of Bielefeld, Bielefeld, 2016.
- APE. Manual Levante Emerald: Synchronously pumped OPO. 2009.
- Martin Baumgartl, Mario Chemnitz, Cesar Jauregui, Tobias Meyer, Benjamin Dietzek, Jürgen Popp, Jens Limpert, and Andreas Tünnermann. All-fiber laser source for CARS microscopy based on fiber optical parametric frequency conversion. *Optics Express*, 20(4):4484–4493, 2012a. ISSN 1094-4087. doi: 10.1364/OE.20.004484.
- Martin Baumgartl, Thomas Gottschall, Javier Abreu-Afonso, Antonio Díez, Tobias Meyer, Benjamin Dietzek, Manfred Rothhardt, Jürgen Popp, Jens Limpert, and Andreas Tünnermann. Alignment-free, all-spliced fiber laser source for CARS microscopy based on four-wave-mixing. *Optics Express*, 20(19):21010–21018, 2012b. ISSN 1094-4087. doi: 10.1364/OE.20.021010.
- Willem P. Beeker, Petra Gross, Chris J. Lee, Carsten Cleff, Herman L. Offerhaus, Carsten Fallnich, Jennifer L. Herek, and Klaus-Jochen Boller. A route to sub-diffraction-limited CARS Microscopy. *Optics Express*, 17(25):22632–22638, 2009. ISSN 1094-4087. doi: 10.1364/OE.17.022632.
- Antonio P. Beltrami, Laura Barlucchi, Daniele Torella, Mathue Baker, Federica Li-mana, Stefano Chimenti, Hideko Kasahara, Marcello Rota, Ezio Musso, Konrad Urbanek, Annarosa Leri, Jan Kajstura, Bernardo Nadal-Ginard, and Piero Anversa.

- Adult Cardiac Stem Cells Are Multipotent and Support Myocardial Regeneration. *Cell*, 114(6):763–776, 2003. ISSN 00928674. doi: 10.1016/S0092-8674(03)00687-1.
- Michael W. Berry, Murray Browne, Amy N. Langville, V. Paul Pauca, and Robert J. Plemmons. Algorithms and applications for approximate nonnegative matrix factorization. *Computational Statistics & Data Analysis*, 52(1):155–173, 2007. ISSN 01679473. doi: 10.1016/j.csda.2006.11.006.
- A. A. Betin, G. A. Pasmanik, and L. V. Piskunova. Stimulated Raman scattering of light beams under saturation conditions. *Soviet Journal of Quantum Electronics*, 5(11):1309–1313, 1975. ISSN 0049-1748. doi: 10.1070/QE1975v005n11ABEH012117.
- E. Betzig. Proposed method for molecular optical imaging. *Optics letters*, 20(3):237–239, 1995.
- E. Betzig, G. H. Patterson, R. Sougrat, O. W. Lindwasser, S. Olenych, J. S. Bonifacino, M. W. Davidson, J. Lippincott-Schwartz, and H. F. Hess. Imaging Intracellular Fluorescent Proteins at Nanometer Resolution. *Science*, 313(5793):1642–1645, 2006. doi: 10.1126/science.1127344.
- Christian Bogen, Arwa Al-Dilaimi, Andreas Albersmeier, Julian Wichmann, Michael Grundmann, Oliver Rupp, Kyle J. Lauersen, Olga Blifernez-Klassen, Jörn Kalinowski, Alexander Goesmann, Jan H. Mussnug, and Olaf Kruse. Reconstruction of the lipid metabolism for the microalga *Monoraphidium neglectum* from its genome sequence reveals characteristics suitable for biofuel production. *BMC genomics*, 14:926, 2013a. doi: 10.1186/1471-2164-14-926.
- Christian Bogen, Viktor Klassen, Julian Wichmann, Marco La Russa, Anja Doebbe, Michael Grundmann, Pauliina Uronen, Olaf Kruse, and Jan H. Mussnug. Identification of *Monoraphidium contortum* as a promising species for liquid biofuel production. *Bioresource Technology*, 133:622–626, 2013b. ISSN 09608524. doi: 10.1016/j.biortech.2013.01.164.
- F. Bonnier and H. J. Byrne. Understanding the molecular information contained in principal component analysis of vibrational spectra of biological systems. *The Analyst*, 137(2):322–332, 2012. ISSN 0003-2654. doi: 10.1039/c1an15821j.
- M. Born and R. Oppenheimer. Zur Quantentheorie der Molekeln. *Annalen der Physik*, 389(20):457–484, 1927. ISSN 00033804. doi: 10.1002/andp.19273892002.
- R. W. Boyd. *Nonlinear optics*. Academic Press, San Diego, CA, 2nd ed edition, 2003. ISBN 978-0121216825.

- L. Campbell, A. J. Hollins, A. Al-Eid, G. R. Newman, C. von Ruhland, and M. Gumbleton. Caveolin-1 expression and caveolae biogenesis during cell transdifferentiation in lung alveolar epithelial primary cultures. *Biochemical and biophysical research communications*, 262(3):744–751, 1999. ISSN 0006-291X. doi: 10.1006/bbrc.1999.1280.
- Lillie Cavonius, Helen Fink, Juris Kiskis, Eva Albers, Ingrid Undeland, and Annika Enejder. Imaging of Lipids in Microalgae with Coherent Anti-Stokes Raman Scattering Microscopy. *Plant Physiology*, 167(3):603–616, 2015. ISSN 0032-0889. doi: 10.1104/pp.114.252197.
- J. M. Cheek, M. J. Evans, and E. D. Crandall. Type I cell-like morphology in tight alveolar epithelial monolayers. *Exp Cell Res.*, (184):375, 1989.
- Mario Chemnitz, Martin Baumgartl, Tobias Meyer, Cesar Jauregui, Benjamin Dietzek, Jürgen Popp, Jens Limpert, and Andreas Tünnermann. Widely tuneable fiber optical parametric amplifier for coherent anti-Stokes Raman scattering microscopy. *Optics Express*, 20(24):26583–26595, 2012. ISSN 1094-4087. doi: 10.1364/OE.20.026583.
- Kun Chen, Tao Wu, Tian Zhou, Haoyun Wei, and Yan Li. Cascaded Dual-Soliton Pulse Stokes for Broadband Coherent Anti-Stokes Raman Spectroscopy. *IEEE Photonics Journal*, 8(6):1–8, 2016. doi: 10.1109/JPHOT.2016.2629084.
- Zhixing Chen, Daniel W. Paley, Lu Wei, Andrew L. Weisman, Richard A. Friesner, Colin Nuckolls, and Wei Min. Multicolor live-cell chemical imaging by isotopically edited alkyne vibrational palette. *Journal of the American Chemical Society*, 136(22):8027–8033, 2014. ISSN 0002-7863. doi: 10.1021/ja502706q.
- J.-X. Cheng and X. S. Xie. *Coherent Raman scattering microscopy*, volume [1]. CRC Press, Boca Raton, FL, 2013. ISBN 978-1-4398-6765-5.
- J.-X. Cheng and X. S. Xie. Vibrational spectroscopic imaging of living systems: An emerging platform for biology and medicine. *Science*, 350(6264):aaa8870, 2015. doi: 10.1126/science.aaa8870.
- J.-X. Cheng, A. Volkmer, and X. S. Xie. Theoretical and experimental characterization of coherent anti-Stokes Raman scattering microscopy. *Optical Society of America*, (Vol. 19, No. 6):1368–1375, 2002.
- Jakub Chojnacki and Christian Eggeling. Super-resolution fluorescence microscopy studies of human immunodeficiency virus. *Retrovirology*, 15(1):41, 2018. doi: 10.1186/s12977-018-0424-3.

- Andy Chong, Joel Buckley, Will Renninger, and Frank Wise. All-normal-dispersion femtosecond fiber laser. *Optics Express*, 14(21):10095–10100, 2006. ISSN 1094-4087. doi: 10.1364/OE.14.010095.
- Nicola Coluccelli, Vikas Kumar, Marco Cassinero, Gianluca Galzerano, Marco Marangoni, and Giulio Cerullo. Er/Tm: fiber laser system for coherent Raman microscopy. *Optics Letters*, 39(11):3090–3093, 2014. ISSN 0146-9592. doi: 10.1364/OL.39.003090.
- Francesco Crisafi, Vikas Kumar, Antonio Perri, Marco Marangoni, Giulio Cerullo, and Dario Polli. Multimodal nonlinear microscope based on a compact fiber-format laser source. *Spectrochimica acta. Part A, Molecular and biomolecular spectroscopy*, 188: 135–140, 2018. doi: 10.1016/j.saa.2017.06.055.
- Adam P. Croft, Joana Campos, Kathrin Jansen, Jason D. Turner, Jennifer Marshall, Moustafa Attar, Loriane Savary, Corinna Wehmeyer, Amy J. Naylor, Samuel Kemble, Jenefa Begum, Kerstin Dürholz, Harris Perlman, Francesca Barone, Helen M. McGettrick, Douglas T. Fearon, Kevin Wei, Soumya Raychaudhuri, Ilya Korsunsky, Michael B. Brenner, Mark Coles, Stephen N. Sansom, Andrew Filer, and Christopher D. Buckley. Distinct fibroblast subsets drive inflammation and damage in arthritis. *Nature*, 570(7760):246–251, 2019. doi: 10.1038/s41586-019-1263-7.
- Brandon M. Davis, Amanda J. Hemphill, Derya Cebeci Maltaş, Michael A. Zipper, Ping Wang, and Dor Ben-Amotz. Multivariate Hyperspectral Raman Imaging Using Compressive Detection. *Analytical Chemistry*, 83(13):5086–5092, 2011. ISSN 0003-2700. doi: 10.1021/ac103259v.
- Justin Demmerle, Cassandravictoria Innocent, Alison J. North, Graeme Ball, Marcel Müller, Ezequiel Miron, Atsushi Matsuda, Ian M. Dobbie, Yolanda Markaki, and Lothar Schermelleh. Strategic and practical guidelines for successful structured illumination microscopy. *Nature Protocols*, 12:988 EP –, 2017. doi: 10.1038/nprot.2017.019.
- Laura J. den Hartigh, Jaime E. Connolly-Rohrbach, Samantha Fore, Thomas R. Huser, and John C. Rutledge. Fatty acids from very low-density lipoprotein lipolysis products induce lipid droplet accumulation in human monocytes. *Journal of immunology (Baltimore, Md. : 1950)*, 184(7):3927–3936, 2010. doi: 10.4049/jimmunol.0903475.
- G. Donnert, J. Keller, R. Medda, M. A. Andrei, S. O. Rizzoli, R. Luhrmann, R. Jahn, C. Eggeling, and S. W. Hell. Macromolecular-scale resolution in biological fluores-

- cence microscopy. *Proceedings of the National Academy of Sciences*, 103(31):11440–11445, 2006. ISSN 0027-8424. doi: 10.1073/pnas.0604965103.
- Druet, S. A. J. and Taran, J. P. E. CARS spectroscopy. *prog. Quantum Electron*, (7): 1–72, 1981.
- John M. Dudley, Goëry Genty, and Stéphane Coen. Supercontinuum generation in photonic crystal fiber. *Optics Express*, 78(4):1135–1184, 2006. ISSN 1094-4087. doi: 10.1103/RevModPhys.78.1135.
- M. D. Duncan, P. Oesterun, F. König, and Robert L. Byer. Observation of saturation broadening of the coherent anti-stokes raman spectrum (cars) of acetylene in a pulsed molecular beam. *Chemical Physics Letters*, 80(2):253–256, 1981. ISSN 00092614. doi: 10.1016/0009-2614(81)80103-0.
- C. L. Evans and X. S. Xie. Coherent Anti-Stokes Raman Scattering Microscopy: Chemical Imaging for Biology and Medicine. *Annual Review of Analytical Chemistry*, 1(1):883–909, 2008. ISSN 1936-1327. doi: 10.1146/annurev.anchem.1.031207.112754.
- Conor L. Evans, Xiaoyin Xu, Santosh Kesari, X. Sunney Xie, Steven T. C. Wong, and Geoffrey S. Young. Chemically-selective imaging of brain structures with CARS microscopy. *Optics Express*, 15(19):12076–12087, 2007. ISSN 1094-4087. doi: 10.1364/OE.15.012076.
- Erik Fällman and Ove Axner. Design for fully steerable dual-trap optical tweezers. *APPLIED OPTICS*, 36(10):2107, 1997. ISSN 0003-6935. doi: 10.1364/AO.36.002107.
- Robert A. Fisher and W. Bischel. The role of linear dispersion in plane-wave self-phase modulation. *IEEE Journal of Quantum Electronics*, 23(12):661–663, 1973. ISSN 00189197. doi: 10.1063/1.1654782.
- J. Folch, M. Lees, and S. GH. Sloane. A simple Method for the Isolation and Purification of Total Lipids from Animal Tissues. *J. Biol. Chem.*, (226):497–509, 1957.
- Jonas Fölling, Mariano Bossi, Hannes Bock, Rebecca Medda, Christian A. Wurm, Birka Hein, Stefan Jakobs, Christian Eggeling, and Stefan W. Hell. Fluorescence nanoscopy by ground-state depletion and single-molecule return. *Nature Methods*, 5(11):943–945, 2008. ISSN 1548-7091. doi: 10.1038/nmeth.1257.
- C. W. Freudiger, W. Min, B. G. Saar, S. Lu, G. R. Holtom, C. He, J. C. Tsai, J. X. Kang, and X. S. Xie. Label-Free Biomedical Imaging with High Sensitivity

- by Stimulated Raman Scattering Microscopy. *Science*, 322(5909):1857–1861, 2008. doi: 10.1126/science.1165758.
- Christian W. Freudiger, Wenlong Yang, Gary R. Holtom, Nasser Peyghambarian, X. Sunney Xie, and Khanh Q. Kieu. Stimulated Raman Scattering Microscopy with a Robust Fibre Laser Source. *Nature photonics*, 8(2):153–159, 2014. ISSN 1749-4885. doi: 10.1038/nphoton.2013.360.
- J. T. Frohn, H. F. Knapp, and A. Stemmer. True optical resolution beyond the Rayleigh limit achieved by standing wave illumination. *Proceedings of the National Academy of Sciences*, 97(13):7232–7236, 2000. ISSN 0027-8424.
- Dan Fu, Gary Holtom, Christian Freudiger, Xu Zhang, and Xiaoliang Sunney Xie. Hyperspectral Imaging with Stimulated Raman Scattering by Chirped Femtosecond Lasers. *The Journal of Physical Chemistry B*, 117(16):4634–4640, 2012. ISSN 1520-6106. doi: 10.1021/jp308938t.
- Dan Fu, Wenlong Yang, and Xiaoliang Sunney Xie. Label-free Imaging of Neurotransmitter Acetylcholine at Neuromuscular Junctions with Stimulated Raman Scattering. *Journal of the American Chemical Society*, 139(2):583–586, 2017. ISSN 0002-7863. doi: 10.1021/jacs.6b10727.
- Sabine Fuchs, Andrew John Hollins, Michael Laue, Ulrich Friedrich Schaefer, Klaus Roemer, Mark Gumbleton, and Claus-Michael Lehr. Differentiation of human alveolar epithelial cells in primary culture: morphological characterization and synthesis of caveolin-1 and surfactant protein-C. *Cell and tissue research*, 311(1):31–45, 2003. ISSN 0302-766X. doi: 10.1007/s00441-002-0653-5.
- Hendrik Fueser. *Effects of copper on life history traits and lipid storage in Caenorhabditis elegans combining life-cycle experiments with coherent anti-Stokes Raman spectroscopy (CARS)*. Masters thesis, University of Bielefeld, Bielefeld, 2016.
- Hendrik Fueser, Nabil Majdi, Arne Haegerbaeumer, Christian Pilger, Henning Hachmeister, Paul Greife, Thomas Huser, and Walter Traunspurger. Analyzing life-history traits and lipid storage using CARS microscopy for assessing effects of copper on the fitness of *Caenorhabditis elegans*. *Ecotoxicology and Environmental Safety*, 156:255–262, 2018. ISSN 01476513. doi: 10.1016/j.ecoenv.2018.03.037.
- Andrew Fussell, Erik Garbacik, Herman Offerhaus, Peter Kleinebudde, and Clare Strachan. In situ dissolution analysis using coherent anti-Stokes Raman scattering (CARS) and hyperspectral CARS microscopy. *European Journal of Phar-*

- maceutics and Biopharmaceutics*, 85(3):1141–1147, 2013. ISSN 09396411. doi: 10.1016/j.ejpb.2013.08.012.
- Alessio Gambetta, Vikas Kumar, Giulia Grancini, Dario Polli, Roberta Ramponi, Giulio Cerullo, and Marco Marangoni. Fiber-format stimulated-Raman-scattering microscopy from a single laser oscillator. *Optics Letters*, 35(2):226–228, 2010. ISSN 0146-9592. doi: 10.1364/OL.35.000226.
- Feruz Ganikhanov, Silvia Carrasco, X. Sunney Xie, Mordechai Katz, Wolfgang Seitz, and Daniel Kopf. Broadly tunable dual-wavelength light source for coherent anti-Stokes Raman scattering microscopy. *Optics Letters*, 31(9):1292, 2006. ISSN 0146-9592. doi: 10.1364/OL.31.001292.
- Erik T. Garbacik, Roza P. Korai, Eric H. Frater, Jeroen P. Kortarik, Cees Otto, and Herman L. Offerhaus. In planta imaging of Δ^9 -tetrahydrocannabinolic acid in *Cannabis sativa* L. with hyperspectral coherent anti-Stokes Raman scattering microscopy. *Journal of Biomedical Optics*, 18(4):046009, 2013. ISSN 1083-3668. doi: 10.1117/1.JBO.18.4.046009.
- Li Gong and Haifeng Wang. Breaking the diffraction limit by saturation in stimulated-Raman-scattering microscopy: A theoretical study. *Physical Review A*, 90(1), 2014. ISSN 1050-2947. doi: 10.1103/PhysRevA.90.013818.
- Li Gong, Wei Zheng, Ying Ma, and Zhiwei Huang. Saturated Stimulated-Raman-Scattering Microscopy for Far-Field Superresolution Vibrational Imaging. *Physical Review Applied*, 11(3), 2019. doi: 10.1103/PhysRevApplied.11.034041.
- Thomas Gottschall, Tobias Meyer, Martin Baumgartl, Benjamin Dietzek, Jürgen Popp, Jens Limpert, and Andreas Tünnermann. Fiber-based optical parametric oscillator for high resolution coherent anti-Stokes Raman scattering (CARS) microscopy. *Optics Express*, 22(18):21921–21928, 2014. ISSN 1094-4087. doi: 10.1364/OE.22.021921.
- Paul Greife. *Implementation of a Hyper-Spectral Image Scan Capability in a Coherent Anti-Stokes Raman Scattering (CARS) Microscope*. Masters Thesis, University of Bielefeld, Bielefeld, 2017.
- J. F.W. Greiner, D. Widera, J. Müller, F. Qunneis, C. Zander, I. Martin, J. Malah, D. Schuetzmann, C. Prante, H. Schwarze, W. Prohaska, A. Beyer, K. Rott, A. Hütten, A. Gölzhäuser, H. Sudhoff, C. Kaltschmidt, and B. Kaltschmidt. Efficient animal-serum free 3D cultivation method for adult human neural crest-derived

- stem cell therapeutics. *European Cells and Materials*, 22:403–419, 2011. doi: 10.22203/eCM.v022a30.
- Greiner, Johannes F. W., Lena-Marie Grunwald, Janine Müller, Holger Sudhoff, Darius Widera, Christian Kaltschmidt, and Barbara Kaltschmidt. Culture bag systems for clinical applications of adult human neural crest-derived stem cells. *Stem Cell Research & Therapy*, 5(2):34, 2014. ISSN 1757-6512. doi: 10.1186/scrt422.
- John M. Guerra. Super-resolution through illumination by diffraction-born evanescent waves. *Applied Physics Letters*, 66(26):3555–3557, 1995. ISSN 0003-6951. doi: 10.1063/1.113814.
- M. G.L. Gustafsson, Shao, P. M. Carlton, Wang, C. J. R., I. N. Golubovskaya, W. Z. Cande, D. A. Agard, and J. W. Sedat. Three-Dimensional Resolution Doubling in Wide-Field Fluorescence Microscopy by Structured Illumination. *Biophysical Journal*, 94(12):4957–4970, 2008. ISSN 00063495. doi: 10.1529/biophysj.107.120345.
- Gustafsson, M. G. L. Surpassing the lateral resolution limit by a factor of two using structured illumination microscopy. SHORT COMMUNICATION. *Journal of microscopy*, 198(2):82–87, 2000. doi: 10.1046/j.1365-2818.2000.00710.x.
- Gustafsson, M. G. L. Nonlinear structured-illumination microscopy: Wide-field fluorescence imaging with theoretically unlimited resolution. *Proceedings of the National Academy of Sciences*, 102(37):13081–13086, 2005. ISSN 0027-8424. doi: 10.1073/pnas.0406877102.
- Gustafsson, M. G. L., D. A. Agard, and J. W. Sedat. Doubling the lateral resolution Doubling the lateral resolution of wide-field fluorescence microscopy using structured illumination. *P Soc Photo-Opt Ins*, 1(13):141–150, 2000.
- H. Haken and H. C. Wolf. *Molekulphysik und Quantenchemie*. Springer, Berlin, 5. edition, 2006. ISBN 978-3-54030314-5.
- Hamamatsu Photonics. OrcaFlash 4.0 vers. 1.1, C11440-22C. *Instruction manual*, 2012.
- H. A. Haus, E. P. Ippen, and K. Tamura. Additive-pulse modelocking in fiber lasers. *IEEE Journal of Quantum Electronics*, 30(1):200–208, 1994. ISSN 00189197. doi: 10.1109/3.272081.
- Stefan Hauser, Darius Widera, Firas Qunneis, Janine Müller, Christin Zander, Johannes Greiner, Christina Strauss, Patrick Lüningschrör, Peter Heimann, Hartmut

- Schwarze, Jörg Ebmeyer, Holger Sudhoff, Marcos J. Araúzo-Bravo, Boris Greber, Holm Zaehres, Hans Schöler, Christian Kaltschmidt, and Barbara Kaltschmidt. Isolation of Novel Multipotent Neural Crest-Derived Stem Cells from Adult Human Inferior Turbinate. *Stem Cells and Development*, 21(5):742–756, 2012. ISSN 1547-3287. doi: 10.1089/scd.2011.0419.
- X. N. He, J. Allen, P. N. Black, T. Baldacchini, X. Huang, H. Huang, L. Jiang, and Y. F. Lu. Coherent anti-Stokes Raman scattering and spontaneous Raman spectroscopy and microscopy of microalgae with nitrogen depletion. *Biomedical Optics Express*, 3(11):2896, 2012. ISSN 2156-7085. doi: 10.1364/BOE.3.002896.
- E. Hecht. *Optics*. Addison-Wesley, Reading, Mass, 4. ed., internat. ed edition, 2002. ISBN 0-8053-8566-5.
- M. Heilemann, E. Margeat, R. Kasper, M. Sauer, and P. Tinnefeld. Carbocyanine Dyes as Efficient Reversible Single-Molecule Optical Switch. *Journal of the American Chemical Society*, 127(11):3801–3806, 2005. ISSN 0002-7863. doi: 10.1021/ja044686x.
- Mike Heilemann, Sebastian van de Linde, Mark Schüttpelz, Robert Kasper, Britta Seefeldt, Anindita Mukherjee, Philip Tinnefeld, and Markus Sauer. Subdiffraction-resolution fluorescence imaging with conventional fluorescent probes. *Angewandte Chemie (International ed. in English)*, 47(33):6172–6176, 2008. doi: 10.1002/anie.200802376.
- R. Heintzmann and C. Cremer. Laterally modulated excitation microscopy: Improvement of resolution by using a diffraction grating. *Proceedings Of Optical Biopsies and Microscopic Techniques III*, (3568):185–196, 1999.
- R. Heintzmann, T. M. Jovin, and C. Cremer. Saturated patterned excitation microscopy—a concept for optical resolution improvement. *Journal of the Optical Society of America A*, 19(8):1599, 2002. ISSN 1084-7529. doi: 10.1364/JOSAA.19.001599.
- Rainer Heintzmann and Thomas Huser. Super-Resolution Structured Illumination Microscopy. *Chemical reviews*, 117(23):13890–13908, 2017. doi: 10.1021/acs.chemrev.7b00218.
- S. W. Hell and J. Wichmann. Breaking the diffraction resolution limit by stimulated emission: stimulated-emission-depletion fluorescence microscopy. *Optics Letters*, 19(11):780, 1994. ISSN 0146-9592. doi: 10.1364/OL.19.000780.

- Thomas Hellerer, Claes Axäng, Christian Brackmann, Per Hillertz, Marc Pilon, and Annika Enejder. Monitoring of lipid storage in *Caenorhabditis elegans* using coherent anti-Stokes Raman scattering (CARS) microscopy. *Proceedings of the National Academy of Sciences*, 104(37):14658–14663, 2007. ISSN 0027-8424. doi: 10.1073/pnas.0703594104.
- Samuel T. Hess, Thanu P.K. Girirajan, and Michael D. Mason. Ultra-High Resolution Imaging by Fluorescence Photoactivation Localization Microscopy. *Biophysical Journal*, 91(11):4258–4272, 2006. ISSN 00063495. doi: 10.1529/biophysj.106.091116.
- HighQ. Instruction Manual, piccoTRAIN (IC-1064-15000 / 532-10000 ps Nd:VAN). 2012.
- HighQ. Lasersource picoTRAIN (IC-1064-15000 / 532-10000 ps Nd:VAN): picture, 2013.
- L. M. Hirvonen, K. Wicker, O. Mandula, and R. Heintzmann. Structured illumination microscopy of a living cell. *European Biophysics Journal*, 38(6):807–812, 2009. ISSN 0175-7571. doi: 10.1007/s00249-009-0501-6.
- Arne D. Hofemeier. *Detection of osteogenic differentiation of human inferior turbinate stem cells by CARS microscopy*. Bachelor thesis, University of Bielefeld, Bielefeld, 2014.
- Arne D. Hofemeier, Henning Hachmeister, Christian Pilger, Matthias Schürmann, Greiner, Johannes F. W., Lena Nolte, Holger Sudhoff, Christian Kaltschmidt, Thomas Huser, and Barbara Kaltschmidt. Label-free nonlinear optical microscopy detects early markers for osteogenic differentiation of human stem cells. *Scientific Reports*, 6(1):57, 2016. ISSN 2045-2322. doi: 10.1038/srep26716.
- Nicholas G. Horton, Ke Wang, Demirhan Kobat, Catharine G. Clark, Frank W. Wise, Chris B. Schaffer, and Chris Xu. In vivo three-photon microscopy of subcortical structures within an intact mouse brain. *Nature photonics*, 7:205 EP –, 2013. ISSN 1749-4885. doi: 10.1038/nphoton.2012.336.
- Nicole Shangming Hou and Stefan Taubert. Function and Regulation of Lipid Biology in *Caenorhabditis elegans* Aging. *Frontiers in physiology*, 3:143, 2012. doi: 10.3389/fphys.2012.00143.
- Wei-Wei Hsiang, Chia-Hao Chang, Chien-Po Cheng, and Yinchieh Lai. Passive synchronization between a self-similar pulse and a bound-soliton bunch in a two-color

- mode-locked fiber laser. *Optics Letters*, 34(13):1967, 2009. ISSN 0146-9592. doi: 10.1364/OL.34.001967.
- Qiang Hu, Milton Sommerfeld, Eric Jarvis, Maria Ghirardi, Matthew Posewitz, Michael Seibert, and Al Darzins. Microalgal triacylglycerols as feedstocks for biofuel production: perspectives and advances. *The Plant Journal*, 54(4):621–639, 2008. ISSN 09607412. doi: 10.1111/j.1365-313X.2008.03492.x.
- Bin Huang, Shuai Yan, Lin Xiao, Rong Ji, Liuyan Yang, Ai-Jun Miao, and Ping Wang. Label-Free Imaging of Nanoparticle Uptake Competition in Single Cells by Hyperspectral Stimulated Raman Scattering. *Small*, 14(10):1703246, 2018. ISSN 16136810. doi: 10.1002/smll.201703246.
- Linzhang Huang, Ken L. Chambliss, Xiaofei Gao, Ivan S. Yuhanna, Erica Behling-Kelly, Sonia Bergaya, Mohamed Ahmed, Peter Michaely, Kate Luby-Phelps, Anza Darehshouri, Lin Xu, Edward A. Fisher, Woo-Ping Ge, Chieko Mineo, and Philip W. Shaul. SR-B1 drives endothelial cell LDL transcytosis via DOCK4 to promote atherosclerosis. *Nature*, 569(7757):565–569, 2019. doi: 10.1038/s41586-019-1140-4.
- R. Huber, M. Wojtkowski, and J. G. Fujimoto. Fourier Domain Mode Locking (FDML): A new laser operating regime and applications for optical coherence tomography. *Optics Express*, 14(8):3225–3237, 2006. ISSN 1094-4087. doi: 10.1364/OE.14.003225.
- Wolfgang Hübner, Gregory P. McNERney, Ping Chen, Benjamin M. Dale, Ronald E. Gordon, Frank Y. S. Chuang, Xiao-Dong Li, David M. Asmuth, Thomas Huser, and Benjamin K. Chen. Quantitative 3D video microscopy of HIV transfer across T cell virological synapses. *Science (New York, N.Y.)*, 323(5922):1743–1747, 2009. doi: 10.1126/science.1167525.
- Johan Hult. A Fourth-Order Runge–Kutta in the Interaction Picture Method for Simulating Supercontinuum Generation in Optical Fibers. *J. Lightwave Technol.*, 25(12):3770–3775, 2007.
- Thomas Huser and James Chan. Raman spectroscopy for physiological investigations of tissues and cells. *Advanced Drug Delivery Reviews*, 89:57–70, 2015. ISSN 0169409X. doi: 10.1016/j.addr.2015.06.011.
- Daniel Jaeger. *Establishing Monoraphidium neglectum as a novel oleaginous research model for the process of triacylglycerol accumulation in microalgae*. PhD-Thesis, University of Bielefeld, Bielefeld, 2017.

- Daniel Jaeger, Christian Pilger, Henning Hachmeister, Elina Oberländer, Robin Wördenweber, Julian Wichmann, Jan H. Mussnug, Thomas Huser, and Olaf Kruse. Label-free in vivo analysis of intracellular lipid droplets in the oleaginous microalga *Monoraphidium neglectum* by coherent Raman scattering microscopy. *Scientific Reports*, 6(1):217, 2016. ISSN 2045-2322. doi: 10.1038/srep35340.
- Y. Jeong, J. Sahu, D. Payne, and J. Nilsson. Ytterbium-doped large-core fiber laser with 1.36 kW continuous-wave output power. *Optics Express*, 12(25):6088–6092, 2004. ISSN 1094-4087. doi: 10.1364/OPEX.12.006088.
- Minbiao Ji, Daniel A. Orringer, Christian W. Freudiger, Shakti Ramkissoon, Xiaohui Liu, Darryl Lau, Alexandra J. Golby, Isaiah Norton, Marika Hayashi, Nathalie Y. R. Agar, Geoffrey S. Young, Cathie Spino, Sandro Santagata, Sandra Camelo-Piragua, Keith L. Ligon, Oren Sagher, and X. Sunney Xie. Rapid, label-free detection of brain tumors with stimulated Raman scattering microscopy. *Science translational medicine*, 5(201):201ra119, 2013. doi: 10.1126/scitranslmed.3005954.
- Minbiao Ji, Spencer Lewis, Sandra Camelo-Piragua, Shakti H. Ramkissoon, Matija Snuderl, Sriram Veneti, Amanda Fisher-Hubbard, Mia Garrard, Dan Fu, Anthony C. Wang, Jason A. Heth, Cormac O. Maher, Nader Sanai, Timothy D. Johnson, Christian W. Freudiger, Oren Sagher, Xiaoliang Sunney Xie, and Daniel A. Orringer. Detection of human brain tumor infiltration with quantitative stimulated Raman scattering microscopy. *Science translational medicine*, 7(309):309ra163, 2015. doi: 10.1126/scitranslmed.aab0195.
- Minbiao Ji, Michal Arbel, Lili Zhang, Christian W. Freudiger, Steven S. Hou, Dongdong Lin, Xinju Yang, Brian J. Bacsikai, and X. Sunney Xie. Label-free imaging of amyloid plaques in Alzheimer’s disease with stimulated Raman scattering microscopy. *Science advances*, 4(11):eaat7715, 2018. doi: 10.1126/sciadv.aat7715.
- Birthe Kann, Herman L. Offerhaus, Maike Windbergs, and Cees Otto. Raman microscopy for cellular investigations—From single cell imaging to drug carrier uptake visualization. *Advanced Drug Delivery Reviews*, 89:71–90, 2015. ISSN 0169409X. doi: 10.1016/j.addr.2015.02.006.
- Sebastian Karpf, Matthias Eibl, Wolfgang Wieser, Thomas Klein, and Robert Huber. A Time-Encoded Technique for fibre-based hyperspectral broadband stimulated Raman microscopy. *Nature Communications*, 6:6784, 2015. ISSN 2041-1723. doi: 10.1038/ncomms7784.

- Hyunmin Kim, Garnett W. Bryant, and Stephan J. Stranick. Superresolution four-wave mixing microscopy. *Optics Express*, 20(6):6042–6051, 2012. ISSN 1094-4087. doi: 10.1364/OE.20.006042.
- Tae Kyung Kim and James H. Eberwine. Mammalian cell transfection: the present and the future. *Analytical and bioanalytical chemistry*, 397(8):3173–3178, 2010. doi: 10.1007/s00216-010-3821-6.
- Thomas A. Klar and Stefan W. Hell. Subdiffraction resolution in far-field fluorescence microscopy. *Optics Letters*, 24(14):954, 1999. ISSN 0146-9592. doi: 10.1364/OL.24.000954.
- Christin Klenke, Darius Widera, Thomas Engelen, Janine Müller, Thomas Noll, Karsten Niehaus, M. Lienhard Schmitz, Barbara Kaltschmidt, and Christian Kaltschmidt. Hsc70 is a novel interactor of NF-kappaB p65 in living hippocampal neurons. *PLoS one*, 8(6):e65280, 2013. doi: 10.1371/journal.pone.0065280.
- P. Kner, B. B. Chhun, E. R. Griffis, L. Winoto, and Gustafsson, M. G. L. Super-resolution video microscopy of live cells by structured illumination. *Nature Methods*, 6(5):339–342, 2009. ISSN 1548-7091. doi: 10.1038/nmeth.1324.
- Cihang Kong, Christian Pilger, Henning Hachmeister, Xiaoming Wei, Tom H. Cheung, Lai, Cora S. W., Thomas Huser, Kevin. K. Tsia, and Wong, Kenneth K. Y. Compact fs ytterbium fiber laser at 1010 nm for biomedical applications. *Biomedical Optics Express*, 8(11):4921, 2017. ISSN 2156-7085. doi: 10.1364/BOE.8.004921.
- Cihang Kong, Christian Pilger, Henning Hachmeister, Xiaoming Wei, Tom H. Cheung, Lai, Cora S. W., Nikki P. Lee, Kevin. K. Tsia, and Wong, Kenneth K. Y., Huser, Thomas. High contrast, fast chemical imaging by coherent Raman scattering using a self-synchronized two-color fiber laser. *submitted to peer reviewed journal*, 2019.
- Lingjie Kong, Minbiao Ji, Gary R. Holtom, Dan Fu, Christian W. Freudiger, and X. Sunney Xie. Multicolor stimulated Raman scattering microscopy with a rapidly tunable optical parametric oscillator. *Optics Letters*, 38(2):145, 2013. ISSN 0146-9592. doi: 10.1364/OL.38.000145.
- K. König, H. G. Breunig, R. Bückle, M. Kellner-Höfer, M. Weinigel, E. Büttner, W. Sterry, and J. Lademann. Optical skin biopsies by clinical CARS and multiphoton fluorescence/SHG tomography. *Laser Physics Letters*, 8(6):465–468, 2011. ISSN 16122011. doi: 10.1002/lapl.201110014.

- Günther Krauss, Tobias Hanke, Alexander Sell, Daniel Träutlein, Alfred Leitenstorfer, Romedi Selm, Martin Winterhalder, and Andreas Zumbusch. Compact coherent anti-Stokes Raman scattering microscope based on a picosecond two-color Er: fiber laser system. *Optics Letters*, 34(18):2847–2849, 2009. ISSN 0146-9592. doi: 10.1364/OL.34.002847.
- F. Krausz, Ch. Spielmann, T. Brabec, E. Wintner, and A. J. Schmidt. Self-starting additive-pulse mode locking of a Nd:glass laser. *Optics Letters*, 15(19):1082, 1990. ISSN 0146-9592. doi: 10.1364/OL.15.001082.
- Pavel Křížek, Tomáš Lukeš, Martin Ovesný, Karel Fliegel, and Guy M. Hagen. SIM-Toolbox: a MATLAB toolbox for structured illumination fluorescence microscopy. *Bioinformatics*, 3568:btv576, 2015. ISSN 1367-4803. doi: 10.1093/bioinformatics/btv576.
- Cora Sau Wan Lai, Thomas F. Franke, and Wen-Biao Gan. Opposite effects of fear conditioning and extinction on dendritic spine remodelling. *Nature*, 483(7387):87–91, 2012. doi: 10.1038/nature10792.
- Man Kee Lam and Keat Teong Lee. Microalgae biofuels: A critical review of issues, problems and the way forward. *Biotechnology Advances*, 30(3):673–690, 2012. ISSN 07349750. doi: 10.1016/j.biotechadv.2011.11.008.
- Erin S. Lamb, Simon Lefrancois, Minbiao Ji, William J. Wadsworth, X. Sunney Xie, and Frank W. Wise. Fiber optical parametric oscillator for coherent anti-Stokes Raman scattering microscopy. *Optics Letters*, 38(20):4154–4157, 2013. ISSN 0146-9592. doi: 10.1364/OL.38.004154.
- Ines Latka, Sebastian Dochow, Christoph Krafft, Benjamin Dietzek, and Jürgen Popp. Fiber optic probes for linear and nonlinear Raman applications - Current trends and future development. *Laser & Photonics Reviews*, 7(5):698–731, 2013. ISSN 18638880. doi: 10.1002/lpor.201200049.
- Simon Lefrancois, Dan Fu, Gary R. Holtom, Lingjie Kong, William J. Wadsworth, Patrick Schneider, Robert Herda, Armin Zach, X. Sunney Xie, and Frank W. Wise. Fiber four-wave mixing source for coherent anti-Stokes Raman scattering microscopy. *Optics Letters*, 37(10):1652–1654, 2012. ISSN 0146-9592. doi: 10.1364/OL.37.001652.
- Yonghua Li-Beisson, Fred Beisson, and Wayne Riekhof. Metabolism of acyl-lipids in *Chlamydomonas reinhardtii*. *The Plant Journal*, 82(3):504–522, 2015. ISSN 09607412. doi: 10.1111/tpj.12787.

- Alberto Lombardini, Vasyl Mytskaniuk, Siddharth Sivankutty, Esben Ravn Andresen, Xueqin Chen, Jérôme Wenger, Marc Fabert, Nicolas Joly, Frédéric Louradour, Alexandre Kudlinski, and Hervé Rigneault. High-resolution multimodal flexible coherent Raman endoscope. *Light, science & applications*, 7:10, 2018. doi: 10.1038/s41377-018-0003-3.
- Fa-Ke Lu, David Calligaris, Olutayo I. Olubiyi, Isaiah Norton, Wenlong Yang, Sandro Santagata, X. Sunney Xie, Alexandra J. Golby, and Nathalie Y. R. Agar. Label-Free Neurosurgical Pathology with Stimulated Raman Imaging. *Cancer research*, 76(12): 3451–3462, 2016. doi: 10.1158/0008-5472.CAN-16-0270.
- Tomáš Lukeš, Pavel Křížek, Zdeněk Švindrych, Jakub Benda, Martin Ovesný, Karel Fliegel, Miloš Klíma, and Guy M. Hagen. Three-dimensional super-resolution structured illumination microscopy with maximum a posteriori probability image estimation. *Optics Express*, 22(24):29805, 2014. ISSN 1094-4087. doi: 10.1364/OE.22.029805.
- Aleksandar Lukic, Sebastian Dochow, Hyeonsoo Bae, Gregor Matz, Ines Latka, Bernhard Messerschmidt, Michael Schmitt, and Jürgen Popp. Endoscopic fiber probe for nonlinear spectroscopic imaging. *Optica*, 4(5):496, 2017. ISSN 2334-2536. doi: 10.1364/OPTICA.4.000496.
- W. Lukosz and M. Marchand. Optischen Abbildung Unter Überschreitung der Beugungsbedingten Auflösungsgrenze. *Optica Acta: International Journal of Optics*, 10(3):241–255, 1963. ISSN 0030-3909. doi: 10.1080/713817795.
- O. Mandula, M. Kielhorn, K. Wicker, G. Krampert, I. Kleppe, and R. Heintzmann. Line scan - structured illumination microscopy super-resolution imaging in thick fluorescent samples. *Optics Express*, 20(22):24167, 2012. ISSN 1094-4087. doi: 10.1364/OE.20.024167.
- Teresa M. Mata, António A. Martins, and Nidia. S. Caetano. Microalgae for biodiesel production and other applications: A review. *Renewable and Sustainable Energy Reviews*, 14(1):217–232, 2010. ISSN 13640321. doi: 10.1016/j.rser.2009.07.020.
- Matlab. MATLAB and Statistics Toolbox. 2012.
- Srikanth Reddy Medipally, Fatimah Md. Yusoff, Sanjoy Banerjee, and M. Shariff. Microalgae as Sustainable Renewable Energy Feedstock for Biofuel Production. *BioMed Research International*, 2015(3):1–13, 2015. ISSN 2314-6133. doi: 10.1155/2015/519513.

- J. Mertz. *Introduction to optical microscopy*. Roberts, Greenwood Village, Colo, 2010. ISBN 978-0-9815194-8-7.
- Leonardo A. Meza-Zepeda, Agate Noer, John Arne Dahl, Francesca Micci, Ola Myklebost, and Philippe Collas. High-resolution analysis of genetic stability of human adipose tissue stem cells cultured to senescence. *Journal of Cellular and Molecular Medicine*, 12(2):553–563, 2008. ISSN 1582-1838. doi: 10.1111/j.1582-4934.2007.00146.x.
- Miloš Miljković, Tatyana Chernenko, Melissa J. Romeo, Benjamin Bird, Christian Matthäus, and Max Diem. Label-free imaging of human cells: algorithms for image reconstruction of Raman hyperspectral datasets. *The Analyst*, 135(8):2002, 2010. ISSN 0003-2654. doi: 10.1039/c0an00042f.
- Marcel Müller, Viola Mönkemöller, Simon Hennig, Wolfgang Hübner, and Thomas Huser. Open-source image reconstruction of super-resolution structured illumination microscopy data in ImageJ. *Nature Communications*, 7(1):82, 2016. ISSN 2041-1723. doi: 10.1038/ncomms10980.
- Daniel Muschiol and Walter Traunspurger. Life cycle and calculation of the intrinsic rate of natural increase of two bacterivorous nematodes, *Panagrolaimus* sp. and *Poikilolaimus* sp. from chemoautotrophic Movile Cave, Romania. *Nematology*, 9(2): 271–284, 2007. doi: 10.1163/156854107780739117.
- Daniel Muschiol, Fabian Schroeder, and Walter Traunspurger. Life cycle and population growth rate of *Caenorhabditis elegans* studied by a new method. *BMC ecology*, 9:14, 2009. doi: 10.1186/1472-6785-9-14.
- P. Nandakumar, A. Kovalev, and A. Volkmer. Vibrational imaging based on stimulated Raman scattering microscopy. *New Journal of Physics*, 11(3):033026, 2009. doi: 10.1088/1367-2630/11/3/033026.
- Robert P. J. Nieuwenhuizen, Keith A. Lidke, Mark Bates, Daniela Leyton Puig, David Grünwald, Sjoerd Stallinga, and Bernd Rieger. Measuring image resolution in optical nanoscopy. *Nature Methods*, 10(6):557–562, 2013. ISSN 1548-7091. doi: 10.1038/nmeth.2448.
- Keisuke Nose, Yasuyuki Ozeki, Tatsuya Kishi, Kazuhiko Sumimura, Norihiko Nishizawa, Kiichi Fukui, Yasuo Kanematsu, and Kazuyoshi Itoh. Sensitivity enhancement of fiber-laser-based stimulated Raman scattering microscopy by collinear

- balanced detection technique. *Optics Express*, 20(13):13958–13965, 2012. ISSN 1094-4087. doi: 10.1364/OE.20.013958.
- Elina Oberländer. *Raman-Spektroskopie in Biomedizin und an nahfeldgekoppelten Nanosystemen*. PhD-Thesis, University of Bielefeld, Bielefeld, 2016.
- Daniel A. Orringer, Balaji Pandian, Yashar S. Niknafs, Todd C. Hollon, Julianne Boyle, Spencer Lewis, Mia Garrard, Shawn L. Hervey-Jumper, Hugh J. L. Garton, Cormac O. Maher, Jason A. Heth, Oren Sagher, D. Andrew Wilkinson, Matija Snuderl, Sriram Veneti, Shakti H. Ramkissoon, Kathryn A. McFadden, Amanda Fisher-Hubbard, Andrew P. Lieberman, Timothy D. Johnson, X. Sunney Xie, Jay K. Trautman, Christian W. Freudiger, and Sandra Camelo-Piragua. Rapid intraoperative histology of unprocessed surgical specimens via fibre-laser-based stimulated Raman scattering microscopy. *Nature biomedical engineering*, 1, 2017. ISSN 2157-846X. doi: 10.1038/s41551-016-0027.
- Yasuyuki Ozeki, Fumihiko Dake, Shin’ichiro Kajiyama, Kiichi Fukui, and Kazuyoshi Itoh. Analysis and experimental assessment of the sensitivity of stimulated Raman scattering microscopy. *Optics Express*, 17(5):3651–3658, 2009. ISSN 1094-4087. doi: 10.1364/OE.17.003651.
- Yasuyuki Ozeki, Yuma Kitagawa, Kazuhiko Sumimura, Norihiko Nishizawa, Wataru Umemura, Shin’ichiro Kajiyama, Kiichi Fukui, and Kazuyoshi Itoh. Stimulated Raman scattering microscope with shot noise limited sensitivity using subharmonically synchronized laser pulses. *Optics Express*, 18(13):13708–13719, 2010. ISSN 1094-4087. doi: 10.1364/OE.18.013708.
- Yasuyuki Ozeki, Wataru Umemura, Kazuhiko Sumimura, Norihiko Nishizawa, Kiichi Fukui, and Kazuyoshi Itoh. Stimulated Raman hyperspectral imaging based on spectral filtering of broadband fiber laser pulses. *Optics Letters*, 37(3):431–433, 2012. ISSN 0146-9592. doi: 10.1364/OL.37.000431.
- R. Paschotta, J. Nilsson, A. C. Tropper, and D. C. Hanna. Ytterbium-doped fiber amplifiers. *IEEE Journal of Quantum Electronics*, 33(7):1049–1056, 1997. ISSN 00189197. doi: 10.1109/3.594865.
- James B. Pawley. *Handbook of biological confocal microscopy*. Springer, New York, NY, 3. ed. edition, 2006. ISBN 9780387259215. doi: 10.1007/978-0-387-45524-2.
- Pegasus Optik. AOM MT 200-A0.4-1064: Opto Electronic. *Manual*, 2007.

- Adrian F. Pegoraro, Andrew Ridsdale, Douglas J. Moffatt, John Paul Pezacki, Brian K. Thomas, Libin Fu, Liang Dong, Martin E. Fermann, and Albert Stolow. All-fiber CARS microscopy of live cells. *Optics Express*, 17(23):20700–20706, 2009. ISSN 1094-4087. doi: 10.1364/OE.17.020700.
- Christian Pilger. *Construction of a Coherent Raman Scattering-microscope with resolution enhancement by structured illumination*. Masters Thesis, University of Bielefeld, Bielefeld, 2014.
- Christian Pilger, Henning Hachmeister, Paul Greife, Alex Weiß, Gerd Wiebusch, and Thomas Huser. Pulse length variation causing spectral distortions in OPO-based hyperspectral coherent Raman scattering microscopy. *Optics Express*, 26(22):28312, 2018. ISSN 1094-4087. doi: 10.1364/OE.26.028312.
- G. Placzek. *Rayleigh-Streuung und Raman Effekt: in Handbuch der Radiologie*. Akademische Verlagsgesellschaft, Leipzig, 1934.
- E. Ploetz, S. Laimgruber, S. Berner, W. Zinth, and P. Gilch. Femtosecond stimulated Raman microscopy. *Applied Physics B*, 87(3):389–393, 2007. ISSN 0946-2171. doi: 10.1007/s00340-007-2630-x.
- T. A. Pologruto, B. L. Sabatini, and K. Svoboda. ScanImage: Flexible software for operating laser scanning microscopes. *BioMedical Engineering OnLine*, 2(1):13, 2003. ISSN 1475925X.
- K. I. Popov, . Pegoraro, A. F., A. Stolow, and L. Ramunno. Image formation in CARS microscopy: effect of the Gouy phase shift. *Optics Express*, 19(7), 2011.
- Eric O. Potma, Wim P. de Boeij, and Douwe A. Wiersma. Nonlinear coherent four-wave mixing in optical microscopy. *Journal of the Optical Society of America B*, 17(10):1678, 2000. ISSN 0740-3224. doi: 10.1364/JOSAB.17.001678.
- Peter E. Powers. *Fundamental Nonlinear Optics*. CRC Pr, Boca Raton, 2011. ISBN 978-1-4200-9351-3.
- Samuel R. Pygall, Joanne Whetstone, Peter Timmins, and Colin D. Melia. Pharmaceutical applications of confocal laser scanning microscopy: the physical characterisation of pharmaceutical systems. *Advanced Drug Delivery Reviews*, 59(14):1434–1452, 2007. ISSN 0169409X. doi: 10.1016/j.addr.2007.06.018.
- Xue Qi, Sheng-Ping Chen, Hai-Yue Sun, Bing-Ke Yang, and Jing Hou. 1016nm all fiber picosecond MOPA laser with 50W output. *Optics Express*, 24(15):16874–16883, 2016. ISSN 1094-4087. doi: 10.1364/OE.24.016874.

- C. V. Raman and K. S. Krishnan. A New Type of Secondary Radiation. *Nature*, 121 (3048):501–502, 1928. doi: 10.1038/121501c0.
- F.R.S. Rayleigh. XXXI. Investigations in optics, with special reference to the spectroscope. *Philosophical Magazine Series 5*, 8(49):261–274, 1879. ISSN 1941-5982. doi: 10.1080/14786447908639684.
- F.R.S. Rayleigh. X. On the electromagnetic theory of light. *Philosophical Magazine Series 5*, 12(73):81–101, 1881. ISSN 1941-5982. doi: 10.1080/14786448108627074.
- F.R.S. Rayleigh. XXXIV. On the transmission of light through an atmosphere containing small particles in suspension, and on the origin of the blue of the sky. *Philosophical Magazine Series 5*, 47(287):375–384, 1899. ISSN 1941-5982. doi: 10.1080/14786449908621276.
- E. H. Rego, L. Shao, J. J. Macklin, L. Winoto, G. A. Johansson, N. Kamps-Hughes, M. W. Davidson, and Gustafsson, M. G. L. Nonlinear structured-illumination microscopy with a photoswitchable protein reveals cellular structures at 50-nm resolution. *Proceedings of the National Academy of Sciences*, 109(3):E135–E143, 2012. ISSN 0027-8424. doi: 10.1073/pnas.1107547108.
- E. Hesper Rego and Lin Shao. Practical structured illumination microscopy. *Methods in molecular biology (Clifton, N.J.)*, 1251:175–192, 2015. doi: 10.1007/978-1-4939-2080-8{\textunderscore}10.
- Claudius Riek, Claudius Kocher, Peyman Zirak, Christoph Kölbl, Peter Fimpel, Alfred Leitenstorfer, Andreas Zumbusch, and Daniele Brida. Stimulated Raman scattering microscopy by Nyquist modulation of a two-branch ultrafast fiber source. *Optics Letters*, 41(16):3731–3734, 2016. ISSN 0146-9592. doi: 10.1364/OL.41.003731.
- Curtis T. Rueden, Johannes Schindelin, Mark C. Hiner, Barry E. DeZonia, Alison E. Walter, Ellen T. Arena, and Kevin W. Eliceiri. ImageJ2: ImageJ for the next generation of scientific image data. *BMC bioinformatics*, 18(1):529, 2017. doi: 10.1186/s12859-017-1934-z.
- Lucia M. Ruiz-Perera, Lennart Schneider, Beatrice A. Windmüller, Janine Müller, Greiner, Johannes F. W., Christian Kaltschmidt, and Barbara Kaltschmidt. NF- κ B p65 directs sex-specific neuroprotection in human neurons. *Scientific Reports*, 8(1):16012, 2018. ISSN 2045-2322. doi: 10.1038/s41598-018-34394-8.

- T. H. Runcorn, T. Legg, R. T. Murray, E. J. R. Kelleher, S. V. Popov, and J. R. Taylor. Fiber-integrated frequency-doubling of a picosecond Raman laser to 560 nm. *Optics Express*, 23(12):15728–15733, 2015. ISSN 1094-4087. doi: 10.1364/OE.23.015728.
- Jens Rupprecht. From systems biology to fuel—*Chlamydomonas reinhardtii* as a model for a systems biology approach to improve biohydrogen production. *Journal of Biotechnology*, 142(1):10–20, 2009. ISSN 01681656. doi: 10.1016/j.jbiotec.2009.02.008.
- M. J. Rust, M. Bates, and X. Zhuang. Sub-diffraction-limit imaging by stochastic optical reconstruction microscopy (STORM). *Nature Methods*, 3(10):793–796, 2006. ISSN 1548-7091. doi: 10.1038/nmeth929.
- Matei Rusu, Robert Herda, and Oleg Okhotnikov. Passively synchronized two-color mode-locked fiber system based on master-slave lasers geometry. *Optics Express*, 12(20):4719–4724, 2004. ISSN 1094-4087. doi: 10.1364/OPEX.12.004719.
- B. G. Saar, C. W. Freudiger, J. Reichman, C. M. Stanley, G. R. Holtom, and X. S. Xie. Video-Rate Molecular Imaging in Vivo with Stimulated Raman Scattering. *Science*, 330(6009):1368–1370, 2010. doi: 10.1126/science.1197236.
- Brian G. Saar, Richard S. Johnston, Christian W. Freudiger, X. Sunney Xie, and Eric J. Seibel. Coherent Raman scanning fiber endoscopy. *Optics letters*, 36(13):2396–2398, 2011. doi: 10.1364/OL.36.002396.
- Steffen J. Sahl, Stefan W. Hell, and Stefan Jakobs. Fluorescence nanoscopy in cell biology. *Nature reviews. Molecular cell biology*, 18(11):685–701, 2017. doi: 10.1038/nrm.2017.71.
- Peer M. Schenk, Skye R. Thomas-Hall, Evan Stephens, Ute C. Marx, Jan H. Mussnug, Clemens Posten, Olaf Kruse, and Ben Hankamer. Second Generation Biofuels: High-Efficiency Microalgae for Biodiesel Production. *BioEnergy Research*, 1(1):20–43, 2008. ISSN 1939-1234. doi: 10.1007/s12155-008-9008-8.
- L. Schermelleh, R. Heintzmann, and H. Leonhardt. A guide to super-resolution fluorescence microscopy. *The Journal of Cell Biology*, 190(2):165–175, 2010. ISSN 0021-9525. doi: 10.1083/jcb.201002018.
- Lothar Schermelleh, Alexia Ferrand, Thomas Huser, Christian Eggeling, Markus Sauer, Oliver Biehlmaier, and Gregor P. C. Drummen. Super-resolution microscopy demystified. *Nature cell biology*, 21(1):72–84, 2019. doi: 10.1038/s41556-018-0251-8.

- I. W. Schie, J. Wu, T. Weeks, M. A. Zern, J. C. Rutledge, and T. Huser. Label-free imaging and analysis of the effects of lipolysis products on primary hepatocytes. *Journal of Biophotonics*, 4(6):425–434, 2011. ISSN 1864063X. doi: 10.1002/jbio.201000086.
- Iwan W. Schie and Thomas Huser. Methods and Applications of Raman Microspectroscopy to Single-Cell Analysis. *Applied Spectroscopy*, 67(8):813–828, 2013. ISSN 0003-7028. doi: 10.1366/12-06971.
- J. Schindelin, I. Arganda-Carreras, E. Frise, V. Kaynig, M. Longair, T. Pietzsch, S. Preibisch, C. Rueden, S. Saalfeld, B. Schmid, J.-Y. Tinevez, D. J. White, V. Hartenstein, K. Eliceiri, P. Tomancak, and A. Cardona. Fiji: an open-source platform for biological-image analysis. *Nature Methods*, 9(7):676–682, 2012. ISSN 1548-7091. doi: 10.1038/nmeth.2019.
- A. Schmoldt, H. F. Benthe, and G. Haberland. Digitoxin metabolism by rat liver microsomes. *Biochemical pharmacology*, 24(17):1639–1641, 1975. ISSN 1873-2968.
- M. Schüttpelz, T. Huser, and D. L. Andrews, editors. *Biomedical photonics, spectroscopy, and microscopy Chapter: Imaging and Probing Cells beyond the Optical Diffraction Limit*. John Wiley, Hoboken, 2014. ISBN 978-1118225554.
- Caroline Seebach, Dirk Henrich, Christopher Kähling, Kerstin Wilhelm, Andrea E. Tami, Mauro Alini, and Ingo Marzi. Endothelial Progenitor Cells and Mesenchymal Stem Cells Seeded onto β -TCP Granules Enhance Early Vascularization and Bone Healing in a Critical-Sized Bone Defect in Rats. *Tissue Engineering Part A*, 16(6):1961–1970, 2010. ISSN 1937-3341. doi: 10.1089/ten.tea.2009.0715.
- Romedi Selm, Martin Winterhalder, Andreas Zumbusch, Günther Krauss, Tobias Hanke, Alexander Sell, and Alfred Leitenstorfer. Ultrabroadband background-free coherent anti-Stokes Raman scattering microscopy based on a compact Er: fiber laser system. *Optics Letters*, 35(19):3282–3284, 2010. ISSN 0146-9592. doi: 10.1364/OL.35.003282.
- J. Sheehan, T. Dunihay, J. Benemann, and P. Roessler. A look back at the US Department of Energy’s aquatic species program: biodiesel from algae: Vol. 328 (National Renewable Energy Laboratory Golden. Vol. 328 (National Renewable Energy Laboratory Golden, 1998.
- Lingyan Shi, Yihui Shen, and Wei Min. Invited Article: Visualizing protein synthesis

- in mice with in vivo labeling of deuterated amino acids using vibrational imaging. *APL Photonics*, 3(9):092401, 2018. doi: 10.1063/1.5028134.
- E. Snitzer, H. Po, F. Hakimi, R. Tumminelli, and B. C. McCollum. Double clad, offset core Nd fiber laser in Optical Fiber Sensors. *Optical Fiber Sensors*, (Vol. 2):paper PD5 of OSA Technical Digest Series, 1988. doi: 10.1364/OFS.1988.PD5.
- Grzegorz Sobon, Jaroslaw Sotor, Iwona Pasternak, Aleksandra Krajewska, Wlodek Strupinski, and Krzysztof M. Abramski. 260 fs and 1 nJ pulse generation from a compact, mode-locked Tm-doped fiber laser. *Optics Express*, 23(24):31446–31451, 2015. ISSN 1094-4087. doi: 10.1364/OE.23.031446.
- C. M. Sparrow. On Spectroscopic Resolving Power. *The Astrophysical Journal*, 44:76, 1916. ISSN 0004-637X. doi: 10.1086/142271.
- Christine Spiegelberg, Jihong Geng, Yongdan Hu, Yushi Kaneda, Shibin Jiang, and Nasser Peyghambarian. Low-Noise Narrow-Linewidth Fiber Laser at 1550 nm (June 2003). *J. Lightwave Technol.*, 22(1):57, 2004.
- Donna Strickland and Gerard Mourou. Compression of amplified chirped optical pulses. *Optics Communications*, 56(3):219–221, 1985. ISSN 00304018. doi: 10.1016/0030-4018(85)90120-8.
- J. W. Strutt. XV. On the light from the sky, its polarization and colour. *Philosophical Magazine Series 5*, 41(271):107–120, 1871. ISSN 1941-5982. doi: 10.1080/14786447108640452.
- K. Tamura, J. Jacobson, E. P. Ippen, H. A. Haus, and J. G. Fujimoto. Unidirectional ring resonators for self-starting passively mode-locked lasers. *Optics Letters*, 18(3):220, 1993. ISSN 0146-9592. doi: 10.1364/OL.18.000220.
- D. Y. Tang, L. M. Zhao, B. Zhao, and A. Q. Liu. Mechanism of multisoliton formation and soliton energy quantization in passively mode-locked fiber lasers. *Optics Express*, 72(4):3304, 2005. ISSN 1094-4087. doi: 10.1103/PhysRevA.72.043816.
- D. Taverner, P. Britton, P. G. R. Smith, D. J. Richardson, G. W. Ross, and D. C. Hanna. Highly efficient second-harmonic and sum-frequency generation of nanosecond pulses in a cascaded erbium-doped fiber:periodically poled lithium niobate source. *Optics Letters*, 23(3):162, 1998. ISSN 0146-9592. doi: 10.1364/OL.23.000162.
- D. Lansing Taylor and Yu-Li Wang. Fluorescently labelled molecules as probes of the structure and function of living cells. *Nature*, 284(5755):405–410, 1980. doi: 10.1038/284405a0.

- R. W. Terhune, P. d. Maker, and C. M. Savage. Measurements of Nonlinear Light Scattering. *Physical Review Letters*, 14(17):681–684, 1965. ISSN 0031-9007. doi: 10.1103/PhysRevLett.14.681.
- Ronald Terjung, Iwan W. Schie, and Thomas Huser. *Comprehensive Physiology*. 206: 716, 2013. doi: 10.1002/cphy.c120025.
- W. M. Tolles, J. W. Nibler, J. R. McDonald, and A. B. Harvey. A Review of the Theory and Application of Coherent Anti-Stokes Raman Spectroscopy (CARS). *Applied Spectroscopy*, 31(4):253–271, 1977. ISSN 0003-7028. doi: 10.1366/000370277774463625.
- Adam J. Trewin, Brandon J. Berry, Alicia Y. Wei, Laura L. Bahr, Thomas H. Foster, and Andrew P. Wojtovich. Light-induced oxidant production by fluorescent proteins. *Free radical biology & medicine*, 128:157–164, 2018. doi: 10.1016/j.freeradbiomed.2018.02.002.
- Haohua Tu, Yuan Liu, Dmitry Turchinovich, Marina Marjanovic, Jens Lyngsø, Jesper Lægsgaard, Eric J. Chaney, Youbo Zhao, Sixian You, William L. Wilson, Bingwei Xu, Marcos Dantus, and Stephen A. Boppart. Stain-free histopathology by programmable supercontinuum pulses. *Nature photonics*, 10(8):534–540, 2016. ISSN 1749-4885. doi: 10.1038/nphoton.2016.94.
- A. Volkmer, J.-X. Cheng, and X. S. Xie. Vibrational Imaging with High Sensitivity via Epidetected Coherent Anti-Stokes Raman Scattering Microscopy. *Physical Review Letters*, 87(2), 2001. ISSN 0031-9007. doi: 10.1103/PhysRevLett.87.023901.
- Branko Vukosavljević. Tracing physicochemical and structural changes in drug delivery systems and human cells by confocal Raman microscopy: PhD-Thesis. 2018. doi: 10.22028/D291-27167.
- Branko Vukosavljevic, Marius Hittinger, Henning Hachmeister, Christian Pilger, Xabier Murgia, Michael M. Gepp, Luca Gentile, Hanno Huwer, Nicole Schneider-Daum, Thomas Huser, Claus-Michael Lehr, and Maike Windbergs. Vibrational spectroscopic imaging and live cell video microscopy for studying differentiation of primary human alveolar epithelial cells. *Journal of Biophotonics*, 311:e201800052, 2019. ISSN 1864063X. doi: 10.1002/jbio.201800052.
- S. Wachsmann-Hogiu, T. Weeks, and T. Huser. Chemical analysis in vivo and in vitro by Raman spectroscopy—from single cells to humans. *Current Opinion in Biotechnology*, 20(1):63–73, 2009. ISSN 09581669. doi: 10.1016/j.copbio.2009.02.006.

- Sina Wäldchen, Julian Lehmann, Teresa Klein, Sebastian van de Linde, and Markus Sauer. Light-induced cell damage in live-cell super-resolution microscopy. *Scientific Reports*, 5:15348 EP –, 2015. ISSN 2045-2322. doi: 10.1038/srep15348.
- Ke Wang, Christian W. Freudiger, Jennifer H. Lee, Brian G. Saar, X. Sunney Xie, and Chris Xu. Synchronized time-lens source for coherent Raman scattering microscopy. *Optics Express*, 18(23):24019–24024, 2010. ISSN 1094-4087. doi: 10.1364/OE.18.024019.
- Ke Wang, Delong Zhang, Kriti Charan, Mikhail N. Slipchenko, Ping Wang, Chris Xu, and Ji-Xin Cheng. Time-lens based hyperspectral stimulated Raman scattering imaging and quantitative spectral analysis. *Journal of Biophotonics*, 6(10):815–820, 2013. ISSN 1864063X. doi: 10.1002/jbio.201300005.
- Tianyu Wang, Dimitre G. Ouzounov, Chunyan Wu, Nicholas G. Horton, Bin Zhang, Cheng-Hsun Wu, Yanping Zhang, Mark J. Schnitzer, and Chris Xu. Three-photon imaging of mouse brain structure and function through the intact skull. *Nature Methods*, 15(10):789–792, 2018. ISSN 1548-7091. doi: 10.1038/s41592-018-0115-y.
- J. Warth and J. F. Desforges. Determinants of intracellular pH in the erythrocyte. *British journal of haematology*, 29(3):369–372, 1975. ISSN 0007-1048.
- T. Weeks and T. Huser. Differential Imaging of Biological Structures with Doubly-resonant Coherent Anti-stokes Raman Scattering (CARS). *Journal of Visualized Experiments*, (44), 2010. ISSN 1940-087X. doi: 10.3791/2085.
- Lu Wei, Fanghao Hu, Yihui Shen, Zhixing Chen, Yong Yu, Chih-Chun Lin, Meng C. Wang, and Wei Min. Live-cell imaging of alkyne-tagged small biomolecules by stimulated Raman scattering. *Nature Methods*, 11(4):410–412, 2014a. ISSN 1548-7091. doi: 10.1038/NMETH.2878.
- Xiaoming Wei, Jingjiang Xu, Yiqing Xu, Luoqin Yu, Jianbing Xu, Bowen Li, Andy K. S. Lau, Xie Wang, Chi Zhang, Kevin K. Tsia, and Wong, Kenneth K. Y. Breathing laser as an inertia-free swept source for high-quality ultrafast optical bioimaging. *Optics Letters*, 39(23):6593–6596, 2014b. ISSN 0146-9592. doi: 10.1364/OL.39.006593.
- Xiaoming Wei, Cihang Kong, Samuel Sy, Ho Ko, Kevin K. Tsia, and Wong, Kenneth K. Y. Ultrafast time-stretch imaging at 932 nm through a new highly-dispersive fiber. *Biomedical Optics Express*, 7(12):5208–5217, 2016. ISSN 2156-7085. doi: 10.1364/BOE.7.005208.

- Andrew Marc Weiner. *Ultrafast optics*. Wiley series in pure and applied optics. Wiley-Blackwell, Oxford, 2009. ISBN 978-0-471-41539-8.
- Alex Weiß. *Background-Free Coherent Anti-Stokes Raman Scattering Microscopy by High Frequency Modulation*. Masters Thesis, University of Bielefeld, Bielefeld, 2017.
- G. Ya. Wiederschain. The Molecular Probes handbook. A guide to fluorescent probes and labeling technologies. *Biochemistry (Moscow)*, 76(11):Sect. 23.1, 2011. ISSN 0006-2979. doi: 10.1134/S0006297911110101.
- S. Wolter, M. Schüttpelz, M. Tscherepanow, S. van de Linde, M. Heilemann, and M. Sauer. Real-time computation of subdiffraction-resolution fluorescence images. *Journal of microscopy*, 237(1):12–22, 2010. doi: 10.1111/j.1365-2818.2009.03287.x.
- Woodbury E. J. and Ng W. K. Ruby laser operation in the near IR. *Proceedings of the IRE*, (50):2347–2348, 1962.
- Shang-Ying Wu, Wei-Wei Hsiang, and Yinchieh Lai. Laser dynamics and relative timing jitter analysis of passively synchronized Er- and Yb-doped mode-locked fiber lasers. *J. Opt. Soc. Am. B*, 31(7):1508, 2014. doi: 10.1364/JOSAB.31.001508.
- Yicong Wu and Hari Shroff. Faster, sharper, and deeper: structured illumination microscopy for biological imaging. *Nature Methods*, 15(12):1011–1019, 2018. ISSN 1548-7091. doi: 10.1038/s41592-018-0211-z.
- Ruxin Xie, Jue Su, Eric C. Rentchler, Ziyang Zhang, Carey K. Johnson, Honglian Shi, and Rongqing Hui. Multi-modal label-free imaging based on a femtosecond fiber laser. *Biomedical Optics Express*, 5(7):2390–2396, 2014. ISSN 2156-7085. doi: 10.1364/BOE.5.002390.
- Shanhui Xu, Zhongmin Yang, Weinan Zhang, Xiaoming Wei, Qi Qian, Dongdan Chen, Qinyuan Zhang, Shaoxiong Shen, Mingying Peng, and Jianrong Qiu. 400 mW ultrashort cavity low-noise single-frequency Yb-doped phosphate fiber laser. *Optics Letters*, 36(18):3708–3710, 2011. ISSN 0146-9592. doi: 10.1364/OL.36.003708.
- Kangwen Yang, Shikai Zheng, Yuxing Wu, Pengbo Ye, Kun Huang, Qiang Hao, and Heping Zeng. Low-repetition-rate all-fiber integrated optical parametric oscillator for coherent anti-Stokes Raman spectroscopy. *Optics Express*, 26(13):17519–17528, 2018. ISSN 1094-4087. doi: 10.1364/OE.26.017519.
- Wenlong Yang, Ang Li, Yuanzhen Suo, Fa-Ke Lu, and X. Sunney Xie. Simultaneous two-color stimulated Raman scattering microscopy by adding a fiber amplifier to a 2

- ps OPO-based SRS microscope. *Optics letters*, 42(3):523–526, 2017a. doi: 10.1364/OL.42.000523.
- Yifan Yang, Lingchao Chen, and Minbiao Ji. Stimulated Raman scattering microscopy for rapid brain tumor histology. *Journal of Innovative Optical Health Sciences*, 10(05):1730010, 2017b. ISSN 1793-5458. doi: 10.1142/S1793545817300105.
- Kelvin Yen, Thuc T. Le, Ankita Bansal, Sri Devi Narasimhan, Ji-Xin Cheng, and Heidi A. Tissenbaum. A comparative study of fat storage quantitation in nematode *Caenorhabditis elegans* using label and label-free methods. *PloS one*, 5(9), 2010. doi: 10.1371/journal.pone.0012810.
- Yung-Hsiang Yi, Cheng-Hao Chien, Wei-Wen Chen, Tian-Hsiang Ma, Kuan-Yu Liu, Yu-Sun Chang, Ta-Chau Chang, and Szecheng J. Lo. Lipid droplet pattern and nondroplet-like structure in two fat mutants of *Caenorhabditis elegans* revealed by coherent anti-Stokes Raman scattering microscopy. *Journal of Biomedical Optics*, 19(1):011011, 2014. ISSN 1083-3668. doi: 10.1117/1.JBO.19.1.011011.
- Yasuo Yonemaru, Almar F. Palonpon, Shogo Kawano, Nicholas I. Smith, Satoshi Kawata, and Katsumasa Fujita. Super-Spatial- and -Spectral-Resolution in Vibrational Imaging via Saturated Coherent Anti-Stokes Raman Scattering. *Physical Review Applied*, 4(1), 2015. doi: 10.1103/PhysRevApplied.4.014010.
- Yong Wang and Hong Po. Dynamic Characteristics of Double-Clad Fiber Amplifiers for High-Power Pulse Amplification. *J. Lightwave Technol.*, 21(10):2262, 2003. doi: 10.1109/JLT.2003.818166.
- A. G. York, S. H. Parekh, D. D. Nogare, R. S. Fischer, K. Temprine, M. Mione, A. B. Chitnis, C. A. Combs, and H. Shroff. Resolution doubling in live, multicellular organisms via multifocal structured illumination microscopy. *Nature Methods*, 9(7):749–754, 2012. ISSN 1548-7091. doi: 10.1038/nmeth.2025.
- A. G. York, P. Chandris, D. D. Nogare, J. Head, P. Wawrzusin, R. S. Fischer, A. Chitnis, and H. Shroff. Instant super-resolution imaging in live cells and embryos via analog image processing. *Nature Methods*, 10(11):1122–1126, 2013. ISSN 1548-7091. doi: 10.1038/nmeth.2687.
- Dai Yoshitomi, Yohei Kobayashi, Masayuki Kakehata, Hideyuki Takada, Kenji Torizuka, Taketo Onuma, Hideki Yokoi, Takuro Sekiguchi, and Shinki Nakamura. Ultralow-jitter passive timing stabilization of a mode-locked Er-doped fiber laser by

- injection of an optical pulse train. *Optics Letters*, 31(22):3243, 2006. ISSN 0146-9592. doi: 10.1364/OL.31.003243.
- Seok Hyun Yun and Sheldon J. J. Kwok. Light in diagnosis, therapy and surgery. *Nature biomedical engineering*, 1, 2017. ISSN 2157-846X. doi: 10.1038/s41551-016-0008.
- L. Zenteno. High-power double-clad fiber lasers. *J. Lightwave Technol.*, 11(9):1435–1446, 1993. doi: 10.1109/50.241933.
- Yan-Hua Zhai, Christiane Goulart, Jay E. Sharping, Huifeng Wei, Su Chen, Weijun Tong, Mikhail N. Slipchenko, Delong Zhang, and Ji-Xin Cheng. Multimodal coherent anti-Stokes Raman spectroscopic imaging with a fiber optical parametric oscillator. *Applied Physics Letters*, 98(19):191106, 2011. ISSN 0003-6951. doi: 10.1063/1.3589356.
- Delong Zhang, Ping Wang, Mikhail N. Slipchenko, Dor Ben-Amotz, Andrew M. Weiner, and Ji-Xin Cheng. Quantitative Vibrational Imaging by Hyperspectral Stimulated Raman Scattering Microscopy and Multivariate Curve Resolution Analysis. *Analytical Chemistry*, 85(1):98–106, 2012. ISSN 0003-2700. doi: 10.1021/ac3019119.
- Zhilun Zhao, Yihui Shen, Fanghao Hu, and Wei Min. Applications of vibrational tags in biological imaging by Raman microscopy. *The Analyst*, 142(21):4018–4029, 2017. ISSN 0003-2654. doi: 10.1039/c7an01001j.
- Andreas Zumbusch, Gary R. Holtom, and X. Sunney Xie. Three-Dimensional Vibrational Imaging by Coherent Anti-Stokes Raman Scattering. *Physical Review Letters*, 82(20):4142–4145, 1999. ISSN 0031-9007. doi: 10.1103/PhysRevLett.82.4142.

Gedruckt auf alterungsbeständigem Papier °° ISO 9706